A Photophysical Investigation on the Role of Complexity on Controlling the Functions of Pluronic F127 and Sodium Deoxycholate Supramolecular Hydrogels

by

Ankur A. Awasthi
B.Sc, University of Mumbai, India, 2014
M.Sc, University of Mumbai, India, 2016

A Dissertation Submitted in Partial Fulfillment
of the Requirements for the Degree of

DOCTOR OF PHILOSOPHY

in the Department of Chemistry

University of Victoria

We acknowledge and respect the lək̓ʷəŋən peoples on whose traditional territory the university stands and the Songhees, Esquimalt and W̱SÁNEĆ peoples whose historical relationships with the land continue to this day.

Supervisory Committee

A Photophysical Investigation on the Role of Complexity on Controlling the Functions of Pluronic F127 and Sodium Deoxycholate Supramolecular Hydrogels

by

Ankur A. Awasthi

Bachelor of Science, University of Mumbai, India, 2014

Master of Science, University of Mumbai, India, 2016

Supervisory Committee

Dr. Cornelia Bohne (Department of Chemistry)

Supervisor

Dr. Dennis Hore (Department of Chemistry)

Departmental Member

Dr. Mohsen Akbari (Department of Mechanical Engineering)

Outside Member

Abstract

Colloidal states of matter, where a solid three-dimensional network entraps a liquid mobile phase are known as gels. Based on the nature of the interactions between the building blocks that constitute the solid matrix, gels can be classified into chemical or supramolecular gels. The covalent linkages involved in chemical gels make them irreversible and functionally rigid in nature. The non-covalent nature of the interactions between the building blocks in supramolecular gels makes them more reversible and susceptible to external stimuli. However, the involvement of non-covalent interactions in the formation of supramolecular gels, increases the complexity associated with such systems and makes it difficult to predict their function.

The primary objective of this dissertation was to understand the essential theoretical concepts that could facilitate the prediction of function in supramolecular gels. With respect to hydrogels, function can have various meanings depending on the type of application intended. For example, the release kinetics of loaded drugs from hydrogels can be considered one kind of function for a hydrogel. Another kind of function for a hydrogel could be its mechanical strength that can impact the different kinds of application a particular gel can be employed for. An additional outcome the work done in this dissertation seeks to emphasize is the significance of increased complexity in the designing of functional systems. Complexity is defined by the interconnected relationships between the various molecules involved in functional systems. By investigating systems where the complexity is gradually increased, my aim is to show that this increased complexity can be harnessed to design better functional hydrogel systems.

The first project involved using known theoretical concepts around the self-assembly of polymeric F127 hydrogels. The micellar microstructures of the hydrogel allow for guest localization in either the hydrophobic core or the hydrophilic corona. By choosing a water insoluble fluorophore like *N, N*′-bis(salicylidene)-(2-(3′,4′-diaminophenyl)benzothiazole (BTS), the hydrophobic effect was exploited to confine BTS to the core of the F127 micelles. This fluorophore confinement to the hydrophobic core of the micelles allowed us to generate an emissive hydrogel whose emission color was seen to be unaffected by changes in its environmental pH. This emission is seen to be a result of all three forms of BTS, i.e., the neutral, tautomer and dianionic forms, existing in the excited state. Additionally, by changing the

concentration of BTS localized within the hydrogels, the emission color from F127 hydrogels can be modulated.

The second project utilized the technique of fluorescence quenching to gain a detailed understanding of the microstructures present in sodium deoxycholate (NaDC) hydrogels. Pyrene was used as a polarity sensitive fluorophore to investigate this hydrogel system. The ratio between peak I and III (I/III) of pyrene steady-state emission spectra revealed details around the polarity of pyrene localization within the hydrogels. The accessibility of two different quenchers, an ionic quencher, iodide anion and a neutral quencher, nitromethane to excited pyrene was studied using steady-state and time-resolved fluorescence. Steady-state results indicate that pyrene in the hydrophilic parts of the gel is quenched more efficiently than in the hydrophobic parts of the gel, irrespective of the quencher used. However, time-resolved studies indicate that among the three possible microenvironments available for pyrene localization, there exists a microenvironment that allows access to nitromethane but not to iodide anions. These results indicate the availability of microstructures in the hydrogel that have a high negative charge density, which is responsible for the lack of access to iodide anions due to electrostatic repulsions.

The addition of cucurbit[6]uril (CB[6]) to these hydrogels results in a relocation of pyrene from the hydrophilic region to the hydrophobic regions of the hydrogel, indicated by the lack of alteration to the I/III ratio with increasing quencher concentration as well as the decreased access of the quencher. Moreover, the time-resolved studies indicate an increased heterogeneity for pyrene, which is a result of its complexation to CB[6]. Using the information from this project and previous work in the group, a molecular image of the hydrogel is successfully created that can explain the difference in release kinetics of pyrene and rhodamine 6G from NaDC-CB[6] hydrogels.

The last project was designed to investigate if the release kinetics of guests from a hydrogel system would be dependent on the binding kinetics between the building blocks of a multi component hydrogel. This involved the design and synthesis of a monourea derivative, and studying its gelation behavior and binding kinetics with CB[6]. The gelation studies involved the use of inversion vial tests to observe how the gelation behaviour of the urea is affected due to the presence of salts and CB[6]. The study of the binding kinetics showed the presence of both fast

(0–50 s) and slow kinetic processes (5-30 min). The information from the kinetic studies confirm the presence of binding interactions of the urea with NaCl and CB[6], which are possibly responsible for the changes in its gelation behaviour. Using the available information from the preliminary studies done in this work, prospective new functionalized ureas that may possess better gelation properties in aqueous solvents in presence of CB[6] are proposed.

Table of Contents

List of Tables

List of Equations

List of Figures

List of Charts

List of Schemes

List of Abbreviations

2D	Two dimensional
3D	Three dimensional
4-AP	4-aminopyridine
Å	Ångstrom
A	Absorbance
A	Adenine
A	Ground-state dianionic form
A	Integrated area under emission
A_0	Integrated area under emission in absence of quencher
A*	Excited-state dianionic form
A_i	pre-exponential factor
API	4-(1H-imidazol-1-yl)aniline
BAMB	1-aminium 4-methylbenzenesulphonate
BTS	*N, N*′-bis(salicylidene)-(2-(3′,4′-diaminophenyl)benzothiazole
C	Cytosine
°C	degree Celsius
Ca^{2+}	Calcium ion
$CaCl_2$	Calcium chloride
CB[n]	Cucurbit[n]uril
CB[5]	Cucurbit[5]uril
CB[6]	Cucurbit[6]uril
CB[7]	Cucurbit[7]uril
CB[8]	Cucurbit[8]uril
CB[10]	Cucurbit[10]uril
CDI	1,1’-carbonyldimidazole
$\chi 2$	Reduced chi-squared
CH_3NO_2	Nitromethane

CIE	Commission Internationale de l'Eclairage
CLSM	Confocal laser scanning microscopy
Cl^-	Chloride ion
cm	centimeter
CMC	Critical micellar concentration
CMT	Critical micellar temperature
°	degree (angular)
Da	Dalton
DAH	Diaminohexane
DCM	Dichloromethane
DMSO-d_6	Dimethylsulfoxide-d_6
DNA	Deoxyribonucleic acid
EG	Ethylene glycol
EOR	Enhanced oil recovery
Eq	Equation
ESIPT	Excited-state intramolecular proton transfer
ξ	Mesh size
F	Fluorophore
F.Q	Fluorophore-quencher complex
ESI-MS	Electrospray ionization mass-spectrometry
FCS	Fluorescence correlation spectroscopy
Fe^{2+}	Ferrous ion
Fe^{3+}	Ferric ion
FWHM	Full width half maximum
G	Guanine
g	gram
GSIPT	Ground-state intramolecular proton transfer
h	Planck's constant

h	hour
H^+	Proton
H_2SO_4	Sulfuric acid
HCl	Hydrochloric acid
HCOOH	Formic acid
HPLC	High performance liquid chromatography
Hz	Hertz
I	Fluorescence Intensity
I^-	Iodide anion
IRF	Instrument response function
iCB[n]	Inverted cucurbit[n]uril
K^+	Potassium ion
K	binding constant
k_f	Rate constant for fluorescence
k_{ic}	Rate constant for internal conversion
k_{isc}	Rate constant for intersystem crossing
k_{obs}	Observed rate constant
k_q	Bimolecular quenching rate constant
K_{SV}	Stern-Volmer constant for dynamic quenching
K_S	Stern-Volmer constant for static quenching
LMW	Low molecular weight
LMWG	Low molecular weight gel
λ_{em}	Emission wavelength
λ_{exc}	Excitation wavelength
M	Molar
MB	Methylene blue
MEM	Maximum entropy method
MΩ	Megaohm

Mg^{2+}	Magnesium ion
mg	milligram
MHz	Megahertz
min	minute
mL	millilitre
mM	millimolar
mmol	millimoles
μM	micromolar
μL	microlitre
MV	Methyl viologen
N	Ground-state normal form
N*	Excited-state normal form
Na^{+}	Sodium ion
NaBr	Sodium bromide
NaC	Sodium cholate
NaCl	Sodium chloride
NaDC	Sodium deoxycholate
Na_2HPO_4	Disodium phosphate
NaH_2PO_4	Monosodium phosphate
NaI	Sodium iodide
NaTC	Sodium taurocholate
NBS	National Bureau of Standards
NH_4^{+}	Ammonium ion
nm	nanometer
NMR	Nuclear magnetic resonance
Np	Naphthyl
ns	nanosecond
ν	wavenumber

OLED	Organic light emitting diode
P4VBAM	Poly(*N*-(4-vinylbenzyl)-4,4′-bipyridinium dichloride-*co*-acrylamide)
PEG	Polyethylene glycol
PEO	Poly(ethylene oxide)
PET	Photoinduced electron transfer
PLA	Polylactic acid
PLGA	Poly(lactic-c*o*-glycolic acid)
PPBEN	4,4′-{(1E,1′E)-[2-(3-aminopropoxy)pyrimidine-4,6-diyl]bis(ethene-2,1-diyl)}-bis(*N*,*N*-diethylaniline)
PPO	Poly(propylene oxide)
PTA	Phosphotungstic acid
PVA	Polyvinyl alcohol
Q	Quencher
R6G	Rhodamine 6G
RNA	Ribonucleic acid
s	second
S_0	Singlet ground state
S_1	Singlet excited state
SAR	Structure activity relationship
SDS	Sodium dodecylsulfate
τ	Fluorescence lifetime
τ_0	Fluorescence lifetime in absence of quencher
$<\tau>_{avg}$	Amplitude averaged fluorescence lifetime
τ_{obs}	Observed fluorescence lifetime
T	Ground-state tautomeric form
T*	Excited-state tautomeric form
T	Thymine
T	Temperature
T_1	Triplet excited state

TFA	Trifluoroacetic acid
THF	Tetrahydrofuran
TRIS	Tris(hydroxymethyl)aminomethane
TOF	Time of flight
UpCB[n]	Ultrapure cucurbit[n]urils
v	Volume
w	Weight

Acknowledgements

I would like to express my gratitude to my supervisor Dr. Cornelia Bohne, for pushing me to always being a better version of myself. Her approach to science has been a valuable perspective that has allowed me to grow not only as a scientist but as a human being. I would like to extend my deepest appreciation to Luis Netter, Dr. Stanislav Konorov and Jessy Oake, for their support with instruments and software, as well as thought provoking discussions on non-academic related topics such as politics and sports.

I would like to thank all past and present members of the Bohne group especially, Dr. Alessandra Menandro, Dr. Amilcar Machulek, Darius Amini, Guanqiao Wang, Gustavo Lopes Camelo, Helia Hosseini Nejad, Dr. Karina Argüello, Dr. Kevin Vos, Dr. Sree Gayatri Talluri, Dr. Suma Thomas, Victor Toledo and Nikoo Rahbari Asr for lending their ears to my whacky ideas and providing me invaluable perspectives that have enabled me to broaden my scientific viewpoint. To Guan and Gustavo, I would like to extend my deepest gratitude for sharing and indulging in one of my favourite hobbies, gaming. My appreciation and gratitude also extend to Dr. Luís Gustavo Teixeira Alves Duarte and Dr. Teresa Dib Zambon Atvars with whom I had a chance to collaborate during my research. I would also like to thank Dr. Prabhat K. Singh and Dr. Neeraj Agarwal for providing me with an opportunity to develop my supramolecular chemistry and photochemistry skills, as well as encouraging me to pursue a PhD.

I would like to use this opportunity to thank my friends back in India as well as in Canada for being there through the various ups and down experienced during my PhD as well as making life easier during the lockdown. I would like to thank my Mom and Dad without whose support and encouragement, this thesis would not be possible. My younger brother, Aayush deserves my greatest gratitude for allowing me to pursue academics while taking over the caretaking duties in the family. A special thank you also goes to my grandfather Dr. U. S. Awasthi and uncle, Ajay Pandey for his support and encouragement during my early academic years. A special thanks to my partner Dr. Janhavi Damani, for staying with me through thick and thin times during both of our respective PhDs.

Finally, I would like to thank the NSERC CREATE PoND program, NSERC, CAMTEC, ACS PRF, and UVic for financial and technical support.

Dedication

To Mom, Dad, and my brother Aayush.

Family gives you the roots to stand tall and strong.

Chapter 1: Introduction

1.1 Supramolecular Chemistry

Chemistry has evolved from the simple combination of atoms yielding intricately crafted molecules, to harnessing the intermolecular forces between molecules to yield elaborately designed supramolecular systems.[1-3] Thus, supramolecular chemistry is commonly known as the chemistry beyond the molecule.[4] Supramolecular structures can range from host-guest complexes to much larger complex molecular assemblies.[3-4] The intermolecular forces responsible for the assembly of supramolecular structures are reversible, causing supramolecular assemblies to be dynamic.[5] The intermolecular forces involved in the formation of supramolecular systems are non-covalent interactions like ionic, π-π and dipole-dipole interactions, hydrogen bonding, and Van der Waals dispersion interactions.[2, 4, 6-8] The hydrophobic effect, although not an interaction, can play a large role in the assembly of supramolecular structures in aqueous systems.[9-10] The hydrophobic effect is a phenomenon when two non-polar entities associate with each other in polar solvents, thereby decreasing their interactions with the polar solvent molecules.[9-10]

1.2 Self-sorting and Self-assembly

Self-sorting and self-assembly are terms that are often used interchangeably in the literature. Self-sorting is defined as the mutual recognition of complementary components in a complex mixture.[11-14] These complementary components can either be self- or non-self-binding motifs within the mixture. Self-assembly is the spontaneous assembling of ‘disorganized’ components of a system into ‘organized’ assemblies.[3, 15-16] Nature has provided us with a wonderful example in deoxyribonucleic acid (DNA) to understand the definition of self-sorting

and self-assembly.[17] Four bases (adenine (A), cytosine (C), guanine (G) and thymine (T)) self-sort to form A-T and G-C base pairs. The integration of these base pairs onto the polymeric backbone of DNA results in a self-assembled double helix structure, which stores information as well as allows cells to transcribe this stored information.[18] Thus, self-assembly can be imagined as the thermodynamic minimum of the system, whereas self-sorting is the process that takes this system towards this thermodynamic minimum (figure 1.1).

Biology uses self-sorting and self-assembly astoundingly to construct and modify nanoscale assemblies. Thus, self-sorting and self-assembly should be the strategic choice for chemists wishing to synthesize and design functional supramolecular systems. Understanding the nature of non-covalent interactions responsible for stabilizing supramolecular assemblies is highly important in such an approach. In terms of energetics, the favorable interactions within the self-assembled structure must be sufficient to overcome the entropic penalty for the arrangement of the assembly's components into an organized state.[19-20] This knowledge has allowed chemists to use self-sorting and self-assembly to fabricate diverse nanostructured materials such as self-assembled urea structures,[21-22] polymeric structures,[23] metal-organic cages[24-26] and mechanically interlocked molecular architectures, namely, rotaxanes,[27-29] knots[30-31] and catenanes[28, 32-33] to be used in a variety of fields like catalysis,[34-35] molecular separation,[36] energy storage[37-38] and nanotherapeutics.[39-41]

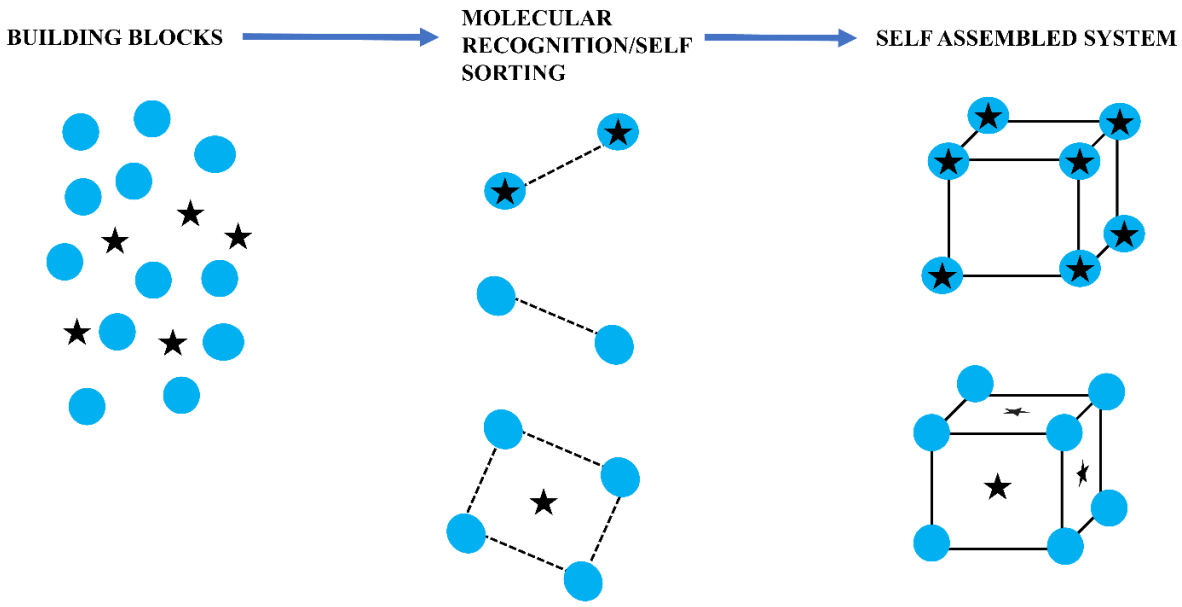

Figure 1.1: Schematic representation showing self-sorting and self-assembly.

1.3 Gels

Chemists have always been fascinated by nature and try to replicate it in a laboratory. One such fascination of chemists, is a living organism made up of 96% water and 1% organic matter, the jellyfish, a classic example of a functional hydrogel. Gels are colloid states of matter where a solid three-dimensional (3D) network entraps the solvent molecules (mobile phase).[42-43] Thus, gels are referred to as viscoelastic materials that possess liquid like properties, such as the ability to be deformed, along with solid like characteristics, such as the ability to maintain shape.[42-43]

1.3.1 Gels as functional materials/applications of gels

A transparent material formed by the slow hydrolysis of an ester and silicic acid is one of the earliest reported gels.[44] Ever since, the interest in gels and their properties has increased exponentially, and these emergent materials are now becoming a part of our everyday life like food and cosmetics.[45] One of most well-known uses of gels is as a stationary phase in separation

techniques such as size-exclusion chromatography and electrophoresis.[46-47] By using size-controlled porous gels as the stationary phase, a mixture of molecules having different sizes are passed through the gel. The smaller molecules will travel faster, whereas the larger molecules will take more time to pass through the gel, thereby resulting in the separation based on size.

Enhanced oil recovery (EOR) is a process where oil production in reservoirs is increased by reducing the water content. Excess water in oil reservoirs is a well-known problem caused by water flooding.[48-49] Presence of water increases the weight of the fluid column, thereby increasing the demand for lifting equipment, while also aggravating corrosion, scales, and degradation of field facilities.[48-49] This causes an increase in operational costs, environmental concerns as well as early shut-off of the wells that may still have significant amount of oil left in them.[49-50] Injection of a gel has emerged as a prospective methodology to implement EOR. The properties of the gel such as viscosity of the gel, nature of the gel phase, density of the gel, and injection time are modulated appropriately for the specific reservoirs.[50-51] The gelator is then injected into the injection well, where it forms hydrogels to block the pores in high-permeability regions. By appropriately designing the hydrogels, more water is allowed to diffuse into the gel than oil, in turn increasing the viscosity of water and reducing its permeability to the more porous area of the well. This allows for separation of water and oil, resulting in a uniform oil layer making oil production more efficient.[51]

Emissive gels have emerged as prospective materials for chemical or biological sensing.[52-53] These gels can be incorporated with known fluorophores that give a designated response such as increase in fluorescence or a quenching of fluorescence, when interacting with the analyte under study. Fluorescent organogels have shown great prospect in detection of nitroaromatic explosives.[54-55] The presence of nitroaromatics causes a photoinduced electron

transfer (PET) process, resulting in fluorescence quenching of the gel. Emissive hydrogels have also been used to develop molecular array chips that have enabled fluorescent high-throughput assays for multiple analytes.[56] Takeuchi and co-workers have also presented a platform for long term in-vivo glucose monitoring sensors.[57] A fibrous hydrogel that anchored the fluorophore was fabricated, wherein the length of the gel was controlled to control the amount of fluorescent sensors implanted.

Organ or tissue transplant is a medical technique administered on a patient when the failure of an organ or tissue occurs. This medical procedure relies heavily on donors, with donor shortages being a major problem for this approach. Engineering of artificial tissues, known as tissue engineering, is an alternative methodology that may overcome this challenge. In tissue engineering, the hydrogels are designed for the purpose of repair or regeneration of tissue or organ function.[58] The desired cells are isolated and grown in vitro within a 3D scaffold. This scaffold allows for the formation of tissue and controls the growth and shape of the tissue. The mobility of small molecules is controlled to allow the transportation of nutrients, oxygen, and drugs into the implanted tissues. With tissue engineering being used on a variety of tissues such as bladder, cartilage, skin and artery, the properties of the hydrogel being used need to be properly considered.[59] The mechanical properties of the hydrogel dictate adhesion and gene expression, wherein, the variation in adhesion of cells to the hydrogel can cause disparity in growth of different cells.[60] The degradation rate of the hydrogel also needs to be considered as it needs to match the rate of growth of the tissues being repaired. Most importantly, the biocompatibility of the hydrogel with the tissue is of paramount importance, as the scaffold may damage the cells or trigger an undesired immune response.[61]

Drug delivery is another avenue where gels have found prospective applications. The gel can be loaded with a drug of interest, and this gel now acts as a protective layer for the drugs, shielding it within the body from degradation by enzymes or low pH environments.[62] Furthermore, by modulating the biodegradability of the gel to external stimuli, the release of the loaded drug can be controlled using "smart hydrogels" sensitive to their environment.[63] The release of the drug from the porous gel depends on the drug-gel interaction, and thus, by modulating the gel structure and tuning the diffusion of small molecules within the gel, the drug release rate can be controlled.[64]

1.3.2 Types of hydrogels (chemical and supramolecular)

Gels can be classified based on their origin, chemical and physical properties (chart 1.1).[42] The simplest way to classify a gel is to classify them as artificial or natural based on their origin. Naturally occurring hydrogels can be found in soft tissues of the human body and include mucus, cartilage, tendons, blood clots and vitreous humor of the eye. Other examples of naturally occurring gels can be found in the long-finned pilot whale, that secretes an enzymatic gel on its outer surface that prevents other organisms from establishing colonies.

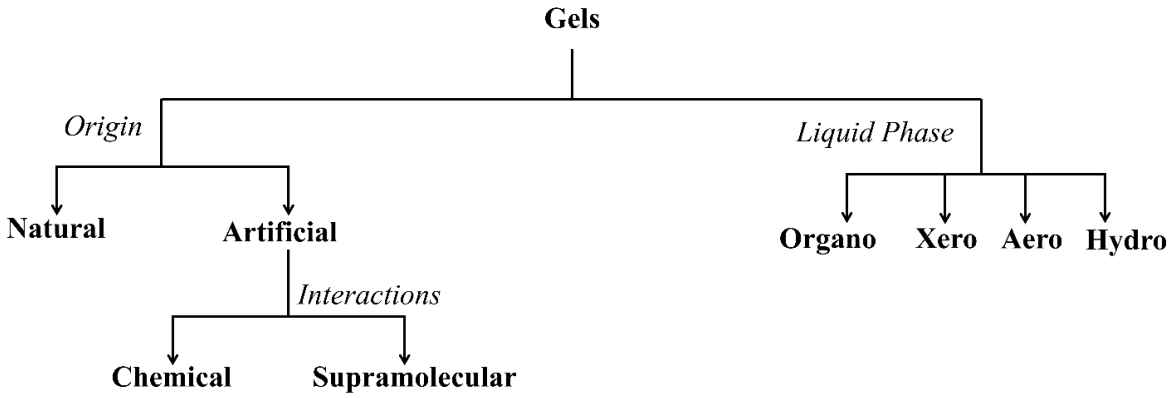

Chart 1.1: Schematic representation of the classification of different types of gels.

Since gels are made of a solid gel network that entraps the liquid mobile phase, changing the mobile phase results in different kind of gels. Most of the naturally occurring gels contain water or aqueous solvents as the mobile phase and are hence known as hydrogels. Due to the high-water content in hydrogels, they possess a degree of flexibility very similar to natural tissue making them suitable for tissue engineering purposes.[42] If the liquid mobile phase is changed to an organic solvent, the gels are now referred to as organogels, which have gained attention for their use as shock absorbing materials in tennis shoes.[42] Lastly, if the gel is dried without hindering the structural integrity of the gel it is known as a xerogel whereas if the liquid phase is replaced with air they are known as aerogels. These two kinds of gels are not normally considered as gels and include examples such as dried agar, silica gels or freeze-dried tofu.[42]

Artificial gels are further classified based on the interactions between the building blocks of the gel system. Chemical gels are formed by covalently crosslinking the building blocks to form the gel network. This crosslinking makes the structure of the gel permanent and irreversible.[65-66] The crosslinking between the gelators can be achieved by either crosslinking water-soluble monomers with bifunctional crosslinkers or by directly crosslinking the water-soluble monomers using heat, radiation or reaction with crosslinkers. The crosslinkers used in this process can often be toxic and may affect the stability of the material loaded into the gel, creating a need for them to be extracted.[67-68] Unlike chemical gels, supramolecular gels are formed through weak non-covalent interactions between the building blocks.[69] The kind of interactions involved in the formation of supramolecular gels makes them dynamic and reversible in nature. The involvement of non-covalent interactions in the formation of theses gels makes them excellent prospects in designing smart gel systems that are responsive to external stimuli like pH, temperature, or ionic strength.[69]

1.4 Supramolecular Gels

Supramolecular gels are further categorized based on the nature of the linkage between the gelators. Physical gels involve long chain molecules, typically polymers or biopolymers, that undergo physical entanglement under specific conditions resulting in a solid matrix that entraps the solvent. The other category that supramolecular gels are characterized into are low molecular weight gels (LMWG).[70-71] LMWGs are formed via weak non-covalent interactions between the low molecular building blocks of the gel. These LMWGs can be obtained via two methodologies. In the first methodology, the LMW gelator molecules are covalently attached to a long chain molecule (polymer/biomolecule). Under the desired conditions, these LMW molecules form non-covalent crosslinks resulting in what are commonly known as physical LMWGs.[72-73] In the other methodology, the LMW gelators are mixed in solution and under specific conditions they non-covalently link together to give rise to a 3D gel network that is capable on entrapping the solvent molecules.[69-71]

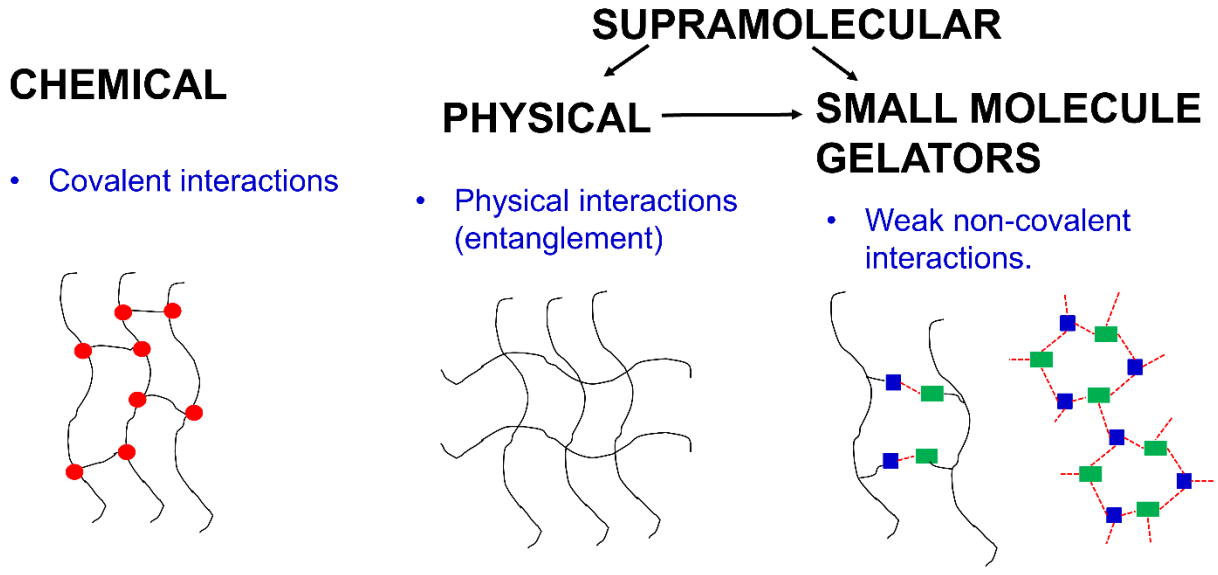

Figure 1.2: Schematic representation of difference in properties of gels based on their type.

1.4.1 Physical Gels

The subtle interplay between solubility of the polymer and its aggregation in the solvent plays an important role in dictating the overall mechanism of physical gelation.[74] Through a combination of several factors such as temperature, concentration and molar mass of polymer, pH and ionic strength, the solubility of the polymer within the solvent medium can be reduced.[74] The reduction in solubility of the polymer would ideally produce a precipitate, crystallization or two-phase-liquid-droplet morphology. However, in physical gels, the polymers still maintain interconnectivity within the polymer-rich domains through physical crosslinks or entanglements.

Crystallization through freeze-thaw cycles is one of the ways to form physical hydrogels in homopolymeric systems.[42] The crystallization and degree of crystallinity determine the properties of the hydrogel in this scenario. The freeze-thaw crystallization process involves the formation of microcrystals in the structure that act as physical crosslinks for the gel network. An example of this kind of hydrogelation is seen in the formation of polyvinyl alcohol (PVA) hydrogels, where the properties of the hydrogel depended on the concentration and molecular weight of PVA, number of freeze/thaw cycles, addition of alginate and temperature.[75-77]

Another strategy involves the use of amphiphilic copolymers containing both hydrophobic and hydrophilic subunits.[74] In aqueous medium, these copolymers self-assemble into organized structures like micelles and hydrogels, where the hydrophobic units of the copolymer are aggregated. These hydrogels are typically obtained from multiblock copolymers or graft copolymers, with the later typically composed of a polysaccharide backbone onto which hydrophobic units or chains are attached. Examples of such hydrogels include hydrogels made from the copolymerization of polyethylene glycol (PEG) and polylactic acid (PLA) or the hydrogels obtained from poly(lactic-c*o*-glycolic acid) (PLGA) grafted chitosan.[78-79]

Amphiphilic block copolymers can also crosslink in aqueous environments via reverse thermal gelation.[64] Such amphiphilic polymers are generally soluble in water at low temperatures. As the temperature is increased, the hydrophobic domains aggregate to reduce the amount of structured water around them which eventually results in a hydrogel. The gelation temperature for such hydrogels is highly dependent on polymer concentration, hydrophobic block length and chemical structure of the polymer. Some of the known hydrophobic segments that undergo this kind of reverse thermal gelling are PLGA, polyurethane and polyorganophosphazene.[64]

1.4.2 Low Molecular Weight Gels (LMWG)

LMWGs are formed via the self-assembly of small molecules into a solid matrix that traps solvent molecules by surface tension. These kinds of gels are typically prepared by dissolving the gelator molecules in a solvent at high temperature (above the sol-gel transition temperature) followed by cooling to room temperature. Exceptions to this methodology where gelation occurs at higher temperatures also exist.[80-81] The solvent and structure of LMW gelators involved play a key role in facilitating aggregation and interaction between the gelator molecules to induce gelation.

The weak non-covalent interactions in LMWG are highly dependent on external stimuli such as temperature, pH or ionic strength. This imparts a unique stimuli responsive characteristic to LMWGs. This stimuli response makes these gels highly reversible allowing for the design of gels where a molecule of interest can be entrapped and released when required, based on the application of an external stimuli. The reversible nature of these non-covalent interactions also allows for these gels to possess properties such as thixotropy or self-healing. Thixotropy refers to

the property of a gel to deform or transition to its sol phase on application of an external mechanical stress and regain its elastic properties on the removal of the stress.[73, 82]

1.5 Function in supramolecular gels

Function is defined as the ability of something to perform a specific task. At the molecular level, function is the action carried out by molecules via interactions with other molecular entities. Methylene blue (MB) serves as an ideal example to display how molecular function can be varied to perform a specific task (figure1.3).[83] The use MB in medicinal chemistry to treat methemoglobinemia is well documented.[84-86] Methemoglobinemia is a life-threatening condition characterized by the inability of hemoglobin to carry oxygen in the blood. This occurs as the ferrous form (Fe^{2+}) of the hemoglobin is oxidized to the ferric form (Fe^{3+}) to produce methemoglobin. When introduced in the body, MB is reduced to leucomethylene blue, which further interacts with the excess methemoglobin to reduce it back to hemoglobin to restore its ability to carry oxygen.[87-88]

Within biology itself, MB has shown to serve diverse functions apart from using it for treatment of a medical condition. Another function served by MB in biology is as a staining agent for bacterial identification or visualization of cellular structures in plant or animal cells.[89-91] MB is a blue dye that is positively charged and binds to the negatively charged components of a cell such as the nucleus, RNA and DNA present in the cytoplasm. In case of a healthy cell, the enzymes within the cell can degrade the MB resulting in the stain becoming colourless, and thus MB selectively stains only the non-healthy cells.

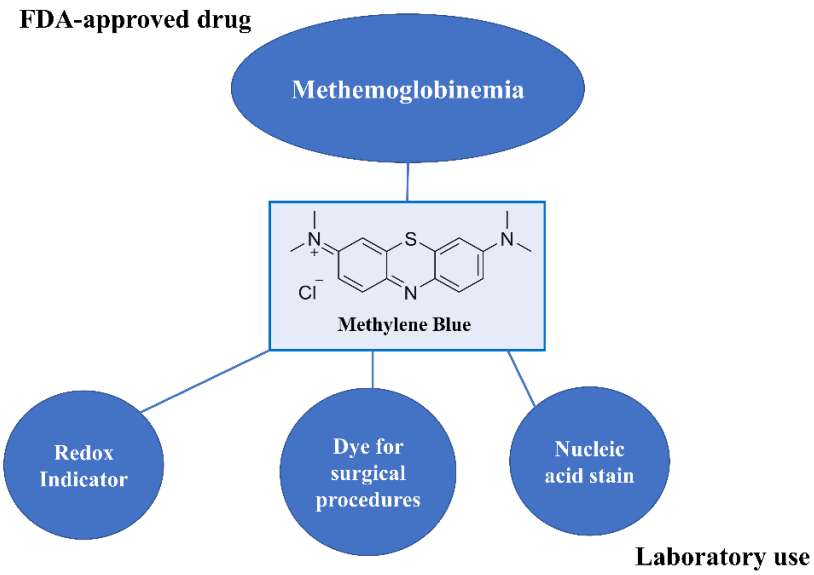

Figure 1.3: Schematic illustration of the various functions served by methylene blue.

In analytical chemistry, MB has been extensively used as a redox indicator.[92-94] A redox, or reduction-oxidation reaction, involves transfer of electrons from one species to another. When a chemical species is reduced, it gains electrons or loses oxygen, whereas when it is oxidized it loses an electron or combines with oxygen. A classical demonstration of this process in chemical kinetics is done via the "blue bottle" experiment where MB, dextrose and sodium hydroxide are mixed in solution.[95-97] On shaking the bottle, the solution turns blue due to oxidization of MB by oxygen, however, it gradually turns colourless over time since the MB is reduced to its colourless form by dextrose. Another way MB has been utilized is as a photosensitizer. Photosensitizers are molecules that absorb light, typically in the visible region of the absorption spectrum, and transfer the energy from the incident light to nearby molecules. Photosensitizers do this process by remaining unchanged after the energetic exchange has taken place, like photocatalysts. MB as a photosensitizer has been actively used to generate reactive oxygen species for photodynamic therapy to treat cancers.[98-99] The photosensitizing ability of MB has also been utilised in

developing dye sensitized solar cells, where MB absorbs the light and transfers this energy to a semiconductor that then produces electrical energy.[100-101]

Similarly, the concept of molecular function can be imagined and expanded to systems such as supramolecular gels. Depending on the properties of the hydrogel obtained, the same hydrogel could be utilized differently based on the task to be served. For example, a polymeric hydrogel that is capable of loading drugs for drug delivery purposes could be loaded with a stimuli-sensitive molecule, such as a fluorophore, to now serve as a sensor rather than its original function of drug release.

1.6 Prediction of function

Predictions have formed the basis of scientific research for a long time. Scientists have imagined an outcome, attempted to reach this outcome, and then investigated why their predicted outcomes were achieved or not. This trial-and-error method has formed the building block for predictive modelling as it has allowed the generation of sufficient knowledge which can be used to design systems and molecules to serve a particular purpose. The most prominent example of the success of this trial-and-error approach leading to predictive modelling is the use of structure activity relationships (SARs) to predict the molecular function of prospective drug molecules. SAR refers to a design technology where the relationship between chemical structure and biological activity of a particular molecule is studied.[102] The analysis of SAR enables to determine the chemical group responsible for inducing a desired biological effect in an organism. This knowledge then allows for chemical modifications of prospective drug molecules to enhance their potency or effect.[102]

1.6.1 Empirical and semi-empirical models for hydrogel drug release

With the advancement of information technology, mathematical modelling of drug delivery and predicting of drug release is a field of increasing importance. Using mathematical models, drug dosage formulations can be optimized to the type of drug administered and its targeted release profile. Mathematical modelling will allow us to save time and reduce costs in terms of the number of experimental studies needed to develop a new formulation and/or optimize an existing drug product. One of the most frequently used models to describe drug release is the Ritger-Peppas equation:[103-104]

$$\frac{M_t}{M_\infty} = kt^n \qquad \text{(Eq. 1.1)}$$

where, M_t is the mass of released drug at time t, M_∞ is total mass of released drug, k is a kinetic rate constant, and n is the release exponent which may be indicative of the mechanism of drug release. The power n depends on the type of transport, hydrogel geometry and polymer polydispersity: $n = 0$ .5 indicates Fickian diffusion drug release, $n = 1$ indicates surface erosion drug release, while if n is between 0.5 and 1, more than one mechanism of drug release may be involved in such systems.

An interesting semi-empirical model was also proposed by Hopfenberg, allowing for a quantitative description of drug release from a system where the release rate was assumed to be proportional to the time-dependent surface area of the device.[105] All mass transfer process involved in the release of the drug were assumed to add up to a single zero order process, confined to the surface area of the system. This zero-order process can be a single physical or chemical phenomenon or a result of a superimposition of several processes like swelling,

dissolution, or cleavage of polymer chains. Cooney has also presented a model based on the assumption of a single zero-order kinetic process confined to the surface area of the drug delivery system.[106] However, Cooney's model was limited to drug delivery systems with spherical or cylindrical geometries, whereas the Hopfenberg model could be applied to spherical, cylindrical and slab geometries.

All these models required the hydrogel systems to be developed, drug loaded, release experiments to be carried out and then fitting the release kinetics with the model of choice to investigate the mechanism of release. Thus, by providing theoretical support to these empirical models through the elucidation of the factors that affect drug release from a hydrogel, more accurate predictive models could be developed to accelerate the development of new hydrogel formulations for drug delivery purposes.

1.6.2 Factors governing the control of function around chemical and physical gels

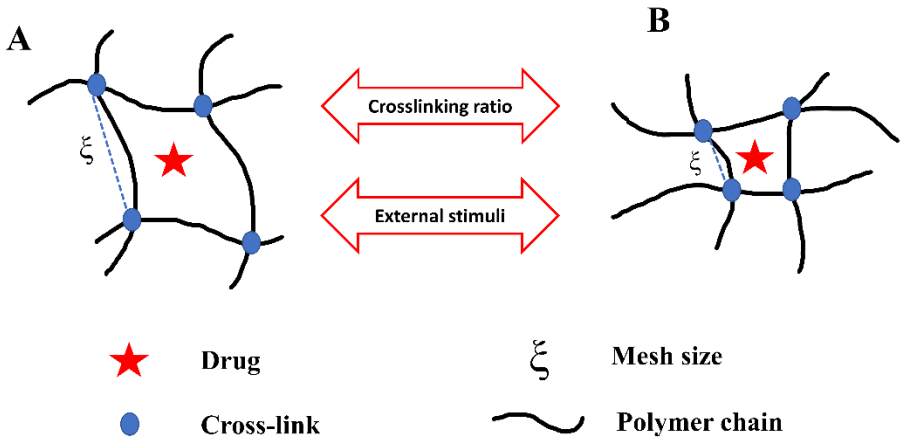

Figure 1.4: Schematic representation of mesh size in a chemical hydrogel in the A) swollen state and B) unswollen state.

Chemical and physical gels are predominantly formed through the same kind of building blocks, i.e., polymers. In chemical gels, the polymers are covalently crosslinked resulting in a gel. For chemical gels, the crosslinking ratio is the most important parameter that directly affects

the release kinetics of a loaded drug.[107-108] This is because the release of a drug from chemical gels can happen either through the degradation of the polymer network or through swelling of the hydrogel. The degradation mechanism of drug release involves designing of covalent crosslinks that either cleave over time or in response to external stimuli to release the drug. These cleavable linkages can include amide bonds, ester bonds, disulfide bonds or even macromolecular linkages such as peptide sequences. By modulating the amount of these cleavable crosslinks within the chemical gel, the release rate of the loaded drug can be optimized. The other strategy to release entrapped drugs from a chemical gel involves the swelling of the hydrogel. Swelling is defined as the penetration of a solvent into the polymer network that cause an abrupt change in its volume.[108-110] The swelling ability of a chemical hydrogel is highly dependent on its mesh size, which can be directly controlled by modulating the crosslinking ratio in the hydrogel (figure 1.4). Highly crosslinked hydrogels have tighter structures resulting in the drug being held tightly within the polymer network and reduced swelling ability of the hydrogel. By decreasing the crosslinking ratio, the movement of solvent into the mesh of the polymer is facilitated which in turn aides the release of the trapped drug.

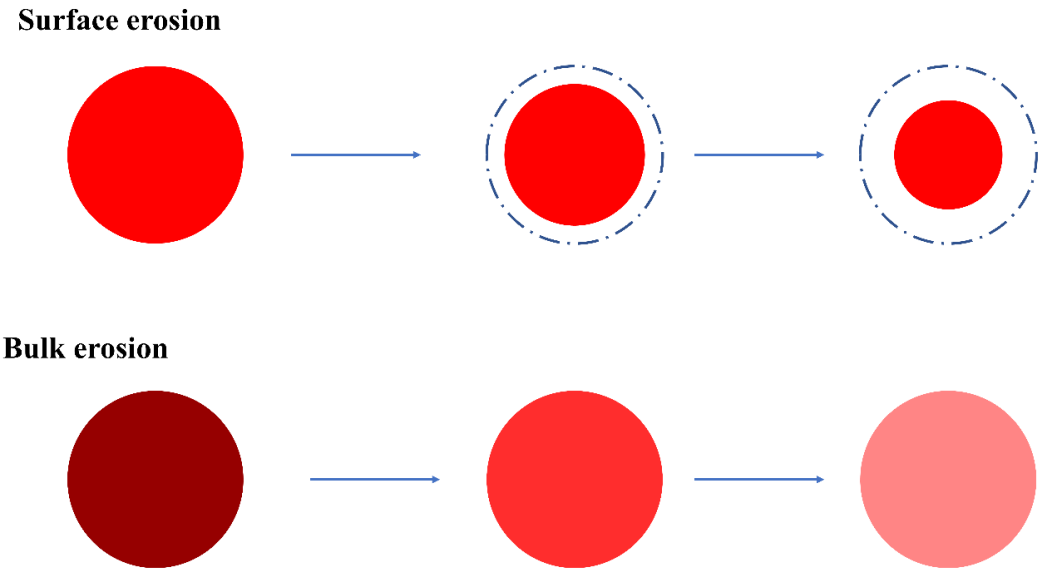

Figure 1.5: Schematic representation of surface and bulk erosion.

In physical hydrogels, the release of the drug is dictated by erosion. It is important to note that erosion is different to degradation discussed previously. Degradation is defined as the cleavage of polymer crosslinks, whereas erosion is defined as the loss of material from the polymer bulk. In degradation, the material lost on the cleaving of crosslinks results in formation of monomers and oligomers, whereas in erosion, the material lost can be either monomers, oligomers or even parts of the polymer backbone. Erosion can be of two types, namely, surface erosion and bulk erosion (figure 1.5), with the type of erosion dependent on the penetration rate of the solvent (water). In physical hydrogels, bulk erosion is typically observed, wherein the penetration rate of water into the polymer matrix is much faster than the rate of polymer relaxation.[110-111] The rate of solvent penetration for physical gels can be controlled by modifying the structure of the polymer.[110-111] Physical gels are typically formed using amphiphilic block copolymers that contain a hydrophilic and hydrophobic unit as part of the polymeric chain. By tuning the ratio of the hydrophilic and hydrophobic subunits of the polymer, the penetration rate of water into the polymer matrix can be modulated. Addition of more hydrophilic groups

increases the rate of water penetration, thereby releasing more drug from the hydrogel. On the other hand, the addition of hydrophobic groups decreases water penetration into the polymer matrix, since the hydrophobic groups collapse in presence of water to minimize their interaction with water molecules. This decrease in water penetration in turn results in a decrease in the release rate of drugs from physical hydrogels.

1.6.3 Factors governing control of function around supramolecular gels

When moving to supramolecular gels, the level of complexity increases drastically since these gels are formed through a self-sorting process that involves weak non-covalent interactions. These interactions can either be self-interactions between the gelator building blocks, between the drug and gel network (drug-gelator) or even involve the gelator interacting with the solvent (gelator-solvent). The modulation of these interactions by external stimuli such as pH or temperature has been used to control the release of drug molecules from such systems.[110] However, as mentioned previously, these non-covalent interactions tend to be reversible and dynamic in nature unlike the static interactions involved in chemical or physical gels. Moreover, the self-assembly of these systems may differ when going from a solution phase to the gel phase. This self-assembly process is highly dependent on external factors such as pH, ionic strength and temperature resulting in structural differences in the hydrogel network if any of these mentioned factors are affected. These microscopic structural differences when going from the sol phase to the gel phase may affect the localization ability of the drug within the hydrogel, which in turn affects rate of drug release. The intricate nature of the self-assembly process involved in supramolecular gel formation, dynamic and reversible nature of the various interactions and the complex interplay of the interactions between the different species involved in making a supramolecular gel, makes the modelling and prediction of function for

supramolecular hydrogels a significant challenge. By understanding and elucidating the parameters that affect the function of a supramolecular hydrogel, systems showing best predicted function could be designed and investigated to save time and money.

1.7 Background Information

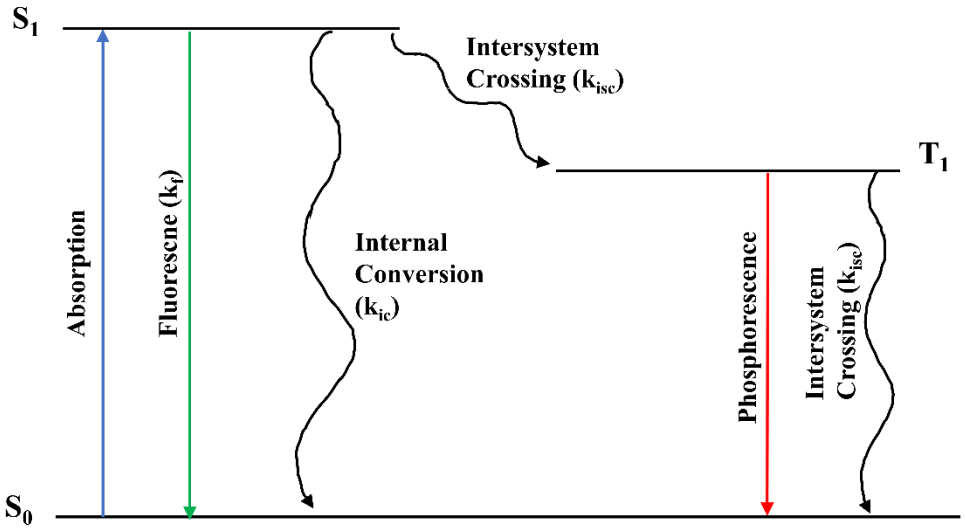

Figure 1.6: Simplified version of the Jablonski diagram.

The photophysical and photochemical processes that occur in a molecule after light absorption can be explained through the Jablonski diagram (figure 1.6). The Jablonski diagram provides a schematic representation of the different energy levels of the molecule, including the ground- and excited-states, and the transitions that occur between them either through radiative or non-radiative pathways.[112] The ground state and singlet excited-state are depicted by S_0 and S_1 respectively. The transition from the S_0 to the S_1 state, via light absorption is instantaneous and typically occurs within 10^{-15} s. Following light absorption, several processes can occur. One of the non-radiative processes that can occur is known as internal conversion. In internal conversion, the molecule can relax back to the ground-state from the singlet excited state without any emission of light. Another possible non-radiative transition possible is when the molecules in the S_1 state undergo spin inversion to the triplet state T_1. This process is known as intersystem

crossing. The transition from the T_1 to the S_0 is forbidden, and therefore emission from this state, called phosphorescence, is rarely observed at room temperature. Finally, the relaxation process from the S_1 to S_0 state that proceeds with the emission of light is known as fluorescence.[113]

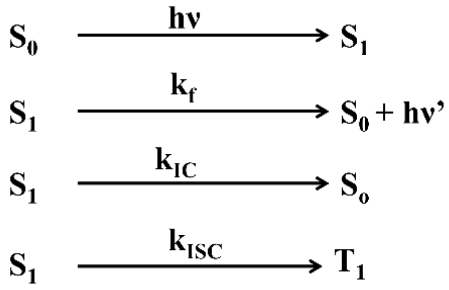

$$k_{obs} = k_f + k_{IC} + k_{ISC}$$

$$k_{obs} = \frac{1}{\tau_{obs}}$$

Figure 1.7: Mathematical representation of the deactivation pathways for an excited-state molecule.

Steady-state emission studies use the Jablonski diagram to understand the different mechanistic pathways for the decay of an excited molecule. As the molecule can undergo relaxation either through radiative or non-radiative pathways upon light excitation, the Jablonski diagram can help to better visualize and understand the efficiency of these pathways. Measuring the time-dependent fluorescence emission allows for the determination of the rate constants of the various relaxation pathways. The lifetimes (τ_{obs}) obtained in time-resolved studies are a reciprocal of the observed rate constant (k_{obs}), which is turn a sum of the rate constants of all the possible relaxation pathways for the singlet excited molecule (figure 1.7) to return to the ground state. The determination of these various rate constants for the different relaxation pathways can be used to interpret the observed kinetics and understand the relaxation mechanism, providing insights into the dynamics of the system.

1.8 Objectives

The objective of this thesis was to understand what different parameters would be needed to be considered when designing a supramolecular hydrogel system whose function can be controlled. In chapter 2, the inherent nature of the two microenvironments in Pluronic hydrogels is exploited to design a light emitting hydrogel system, where the emission is insensitive to pH. This insensitivity of emitted color from the hydrogel is attained by the selective localization of the fluorophore in the microenvironment impervious to H^+ ions. In chapter 3, the availability of different microenvironments within a supramolecular hydrogel for guest localization is explored. The hydrogel explored is sodium deoxycholate (NaDC) where the different binding sites for guests are known in the sol phase. By correlating the nature of the different microenvironments available in the gel to the available binding sites in the sol state, the basis of modulating hydrogel function can be postulated through controlling of the partition of guests within the different microenvironments. In chapter 4, the role played by specific guest interactions with an additive, cucurbit[6]uril (CB[6]) added to NaDC hydrogels is explored. The specific nature of the interactions of the guests with the building blocks of NaDC-CB[6] are seen to have characteristic impact on the guest's release kinetics from the gel. Hydrophobic guests capable of interacting with the external walls of CB[6] added to NaDC hydrogels are seen to show a slow down in their release kinetics, whereas this is not the case for cationic guests as they show no change in their release kinetics with increasing CB[6] concentration. This understanding of guest-CB[6] interactions in chapter 4 not only allows us to portray a molecular picture of the multi-component NaDC-CB[6] hydrogel network, but also explains the difference in release kinetics observed previously for two different guests from NaDC hydrogels.[114] Lastly, in chapter 5,

preliminary studies to understand the role of building block interactions on the release kinetics of guests were undertaken.

1.9 References

(1) Lehn, J.-M. Towards Complex Matter: Supramolecular Chemistry and Self-organization. *Eur. Rev.* **2009,** *17*, 263–280.
(2) Steed, J. W.; Atwood, J. L. *Supramolecular Chemistry*, John Wiley & Sons: 2013.
(3) Menger, F. M. Supramolecular Chemistry and Self-assembly. *Proc. Natl. Acad. Sci. USA* **2002,** *99*, 4818–4822.
(4) Ariga, K.; Kunitake, T. *Supramolecular Chemistry – Fundamentals and Applications : Advance Textbook*, Springer: Berlin, 2006.
(5) Schneider, H.-J.; Yatsimirsky, A. K. *Principles and Methods in Supramolecular Chemistry*, J. Wiley: New York, 2000.
(6) Lehn, J.-M. Supramolecular Chemistry: Receptors, Catalysts, and Carriers. *Science* **1985,** *227*, 849–856.
(7) Lehn, J.-M. Toward Self-organization and Complex Matter. *Science* **2002,** *295*, 2400–2403.
(8) Lehn, J.-M. Supramolecular Chemistry—Scope and Perspectives Molecules, Supermolecules, and Molecular Devices (Nobel Lecture). *Angew. Chem. Int. Ed. Engl.* **1988,** *27*, 89–112.
(9) Pratt, L. R.; Chandler, D. Theory of the Hydrophobic Effect. *J. Chem. Phys.* **1977,** *67*, 3683–3704.
(10) Tanford, C. The Hydrophobic Effect and the Organization of Living Matter. *Science* **1978,** *200*, 1012–1018.
(11) Jiang, W.; Schalley, C. A. Integrative Self-sorting is a Programming Language for High Level Self-assembly. *Proc. Natl. Acad. Sci.* **2009,** *106*, 10425–10429.
(12) Wu, A.; Isaacs, L. Self-sorting: The Exception or the Rule? *J. Am. Chem. Soc.* **2003,** *125*, 4831–4835.
(13) Saha, M. L.; Schmittel, M. Degree of Molecular Self-sorting in Multicomponent Systems. *Org. Biomol. Chem.* **2012,** *10*, 4651–4684.
(14) Zheng, Y.-R.; Yang, H.-B.; Northrop, B. H.; Ghosh, K.; Stang, P. J. Size Selective Self-sorting in Coordination-driven Self-assembly of Finite Ensembles *Inorg. Chem.* **2008,** *47*, 4706–4711.
(15) Whitesides, G. M.; Grzybowski, B. S. Self-assembly at all Scales. *Science* **2002,** *295*, 2418–2421.
(16) Philp, D.; Stoddart, J. F. Self-assembly in Natural and Unnatural Systems. *Angew. Chem. Int. Ed. Engl.* **1996,** *35*, 1154–1196.
(17) Watson, J. D.; Crick, F. H. C. Molecular Structure of Nucleic Acids. *Nature* **1953,** *171*, 737–738.
(18) Voet, D.; Voet, J. G. *Biochemistry, 3rd ed.*, J. Wiley & Sons: Hoboken, NJ, 2004.
(19) Packwood, D. M.; Han, P.; Hitosugi, T. Chemical and Entropic Control on the Molecular Self-assembly Process. *Nat. Commun.* **2017,** *8*, 1–8.
(20) Frenkel, D. Order Through Entropy. *Nat. Mater.* **2015,** *14*, 9–12.

(21) Shimizu, L. S.; Smith, M. D.; Hughes, A. D.; Shimizu, K. D. Self-assembly of a Bis-urea Macrocycle into a Columnar Nanotube. *Chem. Commun.* **2001**, 1592–1593.
(22) Shimizu, L. S.; Salpage, S. R.; Korous, A. A. Functional Materials from Self-Assembled Bis-urea Macrocycles. *Acc. Chem. Res.* **2014,** *47*, 2116–2127.
(23) Lehn, J.-M. Supramolecular Polymer Chemistry- Scope and Perspectives. *Polym. Int.* **2002,** *51*, 825–839.
(24) Taylor, L. K.; Andrews, R.; Sung, A. C. Y.; Vitorica-Yrezabal, I. J.; Riddell, I. A. Synthesis and Characterisation of an Integratively Self-sorted $[Fe4L6]^{8+}$ Tetrahedron. *Chem. Commun.* **2022,** *58*, 12301–12304.
(25) Holloway, L. R.; Bogie, P. M.; Hooley, R. J. Controlled Self-sorting in Self-assembled Cage Complexes. *Dalton Trans.* **2017,** *46*, 14719–14723.
(26) Johnson, A. M.; Hooley, R. J. Steric Effects Control Self-sorting in Self-assembled Clusters. *Inorg. Chem.* **2011,** *50*, 4671–4673.
(27) Santra, S.; Bej, S.; Nandi, M.; Mondal, P.; Ghosh, P. Syntheses of Metallo-pseudorotaxanes, Rotaxane and Post-synthetically Functionalized Rotaxane: A Comprehensive Spectroscopic Study and Dynamic Properties. *Dalton Trans.* **2017,** *46*, 13300–13313.
(28) Jamieson, E. M. G.; Modicom, F.; Goldup, S. M. Chirality in Rotaxanes and Catenanes. *Chem. Soc. Rev.* **2018,** *47*, 5266–5311.
(29) Chen, L.; Sheng, X.; Li, G.; Huang, F. Mechanically Interlocked Polymers Based on Rotaxanes. *Chem. Soc. Rev.* **2022,** *51*, 7046–7065.
(30) Ashbridge, Z.; Knapp, O. M.; Kreidt, E.; Leigh, D. A.; Pirvu, L.; Schaufelberger, F. Social Self-sorting Synthesis of Molecular Knots. *J. Am. Chem. Soc.* **2022,** *144*, 17232−17240.
(31) Lewis, J. E. M. Metallo-supramolecular Self-assembly with Reduced-symmetry Ligands. *Chem.* **2020,** *6*, 14–15.
(32) Fernando, I. R.; Frasconi, M.; Wu, Y.; Liu, W.-G.; Wasielewski, M. R.; Goddard, W. A., III; Stoddart, J. F. Sliding-ring Catenanes. *J. Am. Chem. Soc.* **2016,** *138*, 10214–10225.
(33) Rodríguez-Rubio, A.; Savoini, A.; Modicom, F.; Butler, P.; Goldup, S. M. A Co-conformationally "Topologically" Chiral Catenane. *J. Am. Chem. Soc.* **2022,** *144*, 11927–11932.
(34) Niemeyer, J. Functional Interlocked Molecules: Applications of Rotaxanes, Catenanes and Molecular Knots in Supramolecular Catalysis. In *Supramolecular Catalysts*; Wang, L.; Su, C.-Y., Eds.; 2020; pp 193–224.
(35) Jiao, Y.; Đorđević, L.; Mao, H.; Young, R. M.; Jaynes, T.; Chen, H.; Qiu, Y.; Cai, K.; Zhang, L.; Chen, X.-Y.; Feng, Y.; Wasielewski, M. R.; Stupp, S. I.; Stoddart, J. F. A Donor−acceptor [2]Catenane for Visible Light Photocatalysis. *J. Am. Chem. Soc.* **2021,** *143*, 8000–8010.
(36) Zhang, D.; Ronson, T. K.; Zou, Y.-Q.; Nitschke, J. R. Metal–organic Cages for Molecular Separations. *Nat. Rev. Chem.* **2021,** *5*, 168–182.
(37) Ge, X.; He, Y.; Liang, X.; Wu, L.; Zhu, Y.; Yang, Z.; Hu, M.; Xu, T. Thermally Triggered Polyrotaxane Translational Motion Helps Proton Transfer. *Nat. Commun.* **2018,** *9*, 1–7.
(38) Sluysmans, D.; Stoddart, J. F. The Burgeoning of Mechanically Interlocked Molecules in Chemistry. *Trends Chem.* **2019,** *1*, 185–197.
(39) Ornelas-Megiatto, C.; Becher, T.; Megiatto, J. Interlocked Systems in Nanomedicine. *Curr. Top. Med. Chem.* **2015,** *15*, 1236–1256.
(40) Benyettou, F.; Prakasam, T.; Ramdas Nair, A.; Witzel, I.-I.; Alhashimi, M.; Skorjanc, T.; Olsen, J.-C.; Sadler, K. C.; Trabolsi, A. Potent and Selective In Vitro and In Vivo Antiproliferative Effects of Metal–organic Trefoil Knots. *Chem. Sci.* **2019,** *10*, 5884–5892.

(41) August, D. P.; Borsley, S.; Cockroft, S. L.; della Sala, F.; Leigh, D. A.; Webb, S. J. Transmembrane Ion Channels Formed by a Star of David [2]Catenane and a Molecular Pentafoil Knot. *J. Am. Chem. Soc.* **2020,** *142*, 18859–18865.
(42) Osada, Y.; Kajiwara, K. *Gels Handbook: The Fundamentals*, Academic Press: San Diego, 2001.
(43) Demirci, U.; Khademhosseini, A. *Gels Handbook : Fundamentals, Properties and Applications (in 3 Volumes) Volume 1: Fundamentals of Hydrogels Volume 2: Applications of Hydrogels in Regenerative Medicine Volume 3: Application of Hydrogels in Drug Delivery and Biosensing*, World Scientific: Singapore, 2016.
(44) Dimitriev, Y.; Ivanova, Y.; Iordanov, R. History of Sol-gel Science and Technology (Review). *J. Chem. Technol. Metall.* **2008,** *43*, 181–192.
(45) Jones, C. D.; Steed, J. W. Gels with Sense: Supramolecular Materials that Respond to Heat, Light and Sound. *Chem. Soc. Rev.* **2016,** *45*, 6546–6596.
(46) Determann, H. *Gel Chromatography, Gel Filtration, Gel Permeation, Molecular Sieves; A Laboratory Handbook*, Springer-Verlag: Berlin, 1968.
(47) Magdeldin, S. *Gel Electrophoresis - Principles and Basics*, IntechOpen: Rijeka, Croatia, 2012.
(48) Tongwa, P.; Nygaard, R.; Bai, B. Evaluation of a Nanocomposite Hydrogel for Water Shut-off in Enhanced Oil Recovery Applications: Design, Synthesis, and Characterization. *J. Appl. Polym. Sci.* **2013,** *128*, 787–794.
(49) Taha, A.; Amani, M. Overview of Water Shutoff Operations in Oil and Gas Wells; Chemical and Mechanical Solutions. *ChemEngineering* **2019,** *3*, 51.
(50) Thomas, F. B.; Bennion, D. B.; Anderson, G. E.; Meldrum;, B. T.; Heaven, W. J. J. o. C. P. T. Water Shut-off Treatments - Reduce Water and Accelerate Oil Production. *J. Can. Pet. Technol.* **2000,** *39*, 25–29.
(51) Pinho De Aguiar, K. L. N.; Frias De Oliveira, P.; Elias Mansur, C. R. A Comprehensive Review of *In Situ* Polymer Hydrogels for Conformance Control of Oil Reservoirs. *Oil Gas Sci. Technol.* **2020,** *75*, 1–14.
(52) Li, Y.; Young, D. J.; Loh, X. J. Fluorescent Gels: A Review of Synthesis, Properties, Applications and Challenges. *Mater. Chem. Front.* **2019,** *3*, 1489–1502.
(53) Ghosh, S.; Praveen, V. K.; Ajayaghosh, A. The Chemistry and Applications of π-Gels. *Annu. Rev. Mater. Res.* **2016,** *46*, 235–262.
(54) Kartha, K. K.; Babu, S. S.; Srinivasan, S.; Ajayaghosh, A. Attogram Sensing of TNT with a Self-assembled Molecular Gelator. *J. Am. Chem. Soc.* **2012,** *134*, 4834–4841.
(55) Kartha, K. K.; Sandeep, A.; Praveen, V. K.; Ajayaghosh, A. Detection of Nitroaromatic Explosives with Fluorescent Molecular Assemblies and π-gels. *Chem. Rec.* **2015,** *15*, 252–265.
(56) Yoshimura, I.; Miyahara, Y.; Kasagi, N.; Yamane, H.; Ojida, A.; Hamachi, I. Molecular Recognition in a Supramolecular Hydrogel to Afford a Semi-wet Sensor Chip. *J. Am. Chem. Soc.* **2004,** *124*, 12204–12205.
(57) Heo, Y. J.; Shibata, H.; Okitsu, T.; Kawanishi, T.; Takeuchi, S. Long-term In Vivo Glucose Monitoring using Fluorescent Hydrogel Fibers. *Proc. Natl. Acad. Sci. USA* **2011,** *108*, 13399–13403.
(58) Lee, K. Y.; Mooney, D. J. Hydrogels for Tissue Engineering. *Chem. Rev.* **2001,** *101*, 1869–1879.
(59) Marler, J. J.; Upton, J.; Langer, R.; Vacanti, J. P. Transplantation of Cells in Matrices for Tissue Regeneration. *Adv. Drug Deliv. Rev.* **1998,** *33*, 165–182.

(60) Huang, S.; Ingber, D. E. The Structural and Mechanical Complexity of Cell-growth Control. *Nature Cell. Biol.* **1999,** *1*, E131–E138.
(61) Mikos, A. G.; McIntire, L. V.; Anderson, J. M.; Babensee, J. E. Host Response to Tissue Engineered Devices. *Adv. Drug Deliv. Rev.* **1998,** *33*, 111–139.
(62) Qiu, Y.; Park, D. Environment-sensitive Hydrogels for Drug Delivery. *Adv. Drug Deliv. Rev.* **2001,** *53*, 321–339.
(63) Soppimath, K. S.; Aminabhavi, T. M.; Dave, A. M.; Kumbar, S. G.; Rudzinski, W. E. Stimulus-responsive "Smart" Hydrogels as Novel Drug Delivery Systems. *Drug. Dev. Ind. Pharm.* **2002,** *28*, 957–974.
(64) Hoare, T. R.; Kohane, D. S. Hydrogels in Drug Delivery: Progress and Challenges. *Polymer* **2008,** *49*, 1993–2007.
(65) de Gennes, P.-G. *Scaling Concepts in Polymer Physics*, Cornell University Press: Ithaca, 1979.
(66) Parhi, R. Cross-linked Hydrogel for Pharmaceutical Applications: A Review *Adv. Pharm. Bull.* **2017,** *7*, 515–530.
(67) Bustamante-Torres, M.; Romero-Fierro, D.; Arcentales-Vera, B.; Palomino, K.; Magaña, H.; Bucio, E. Hydrogels Classification According to the Physical or Chemical Interactions and as Stimuli-sensitive Materials. *Gels* **2021,** *7*, 182.
(68) Ullah, F.; Othman, M. B. H.; Javed, F.; Ahmad, Z.; Akil, H. M. Classification, Processing and Application of Hydrogels: A Review. *Mater. Sci. Eng., C* **2015,** *57*, 414–433.
(69) Sangeetha, N. M.; Maitra, U. Supramolecular Gels: Functions and uses. *Chem. Soc. Rev.* **2005,** *34*, 821–836.
(70) Draper, E. R.; Adams, D. J. Low-molecular-weight gels: The State of the Art. *Chem.* **2017,** *3*, 390–410.
(71) Adams, D. J. Personal Perspective on Understanding Low Molecular Weight Gels. *J. Am. Chem. Soc.* **2022,** *144*, 11047–11053.
(72) Huang, X.; Li, R.; Duan, Z.; Xu, F.; Li, H. Supramolecular Polymer Gels: From Construction Methods to Functionality. *Soft Matter, 2022,18,* **2022,** *18*, 3828–3844.
(73) Chivers, P. A.; Smith, D. K. Shaping and Structuring Supramolecular Gels. *Nat. Rev. Mater.* **2019,** *4*, 463–478.
(74) Djabourov, M.; Nishinari, K.; Ross-Murphy, S. B. *Physical Gels from Biological and Synthetic Polymers*, Cambridge University Press: New York, 2013.
(75) Yokoyama, F.; Masada, I.; Shimamura, K.; Ikawa, T.; Monobe, K. Morphology and Structure of Highly Elastic Poly(vinyl alcohol) Hydrogel Prepared by Repeated Freezing-and-melting. *Colloid Polym. Sci.* **1986,** *264*, 595–601.
(76) Hassan, C. M.; Peppas, N. A. Structure and Morphology of Freeze/Thawed PVA Hydrogels. *Macromolecules* **2000,** *33*, 2472–2479.
(77) Xie, L.; Jiang, M.; Dong, X.; Bai, X.; Tong, J.; Zhou, J. Controlled Mechanical and Swelling Properties of Poly(vinyl alcohol)/Sodium Alginate Blend Hydrogels Prepared by Freeze–thaw Followed by Ca^{2+} Crosslinking. *J. Appl. Polym. Sci.* **2012,** *124*, 823–831.
(78) Jeong, B.; Bae, Y. H.; Kim, S. W. Thermoreversible Gelation of PEG-PLGA-PEG Triblock Copolymer Aqueous Solutions. *Macromolecules* **1999,** *32*, 7064–7069.
(79) Bhattarai, N.; Ramay, H. R.; Gunn, J.; Matsen, F. A.; Zhang, M. Q. PEG-grafted Chitosan as an Injectable Thermosensitive Hydrogel for Sustained Protein Release. *J. Controlled Release* **2005,** *103*, 609–624.

(80) Basit, H.; Pal, A.; Sen, S.; Bhattacharya, S. Two-component Hydrogels Comprising Fatty Acids and Amines: Structure, Properties, and Application as a Template for the Synthesis of Metal Nanoparticles. *Chem. – Eur. J.* **2008,** *14*, 6534–6545.
(81) Suzuki, M.; Hanabusa, K. L-lysine-based Low-molecular-weight Gelators. *Chem. Soc. Rev.* **2009,** *38*, 967–975.
(82) Mukhopadhyay, P.; Fujita, N.; Takada, A.; Kishida, T.; Shirakawa, M.; Shinkai, S. Regulation of a Real-time Self-healing Process in Organogel Tissues by Molecular Adhesives. *Angew. Chem. Int. Ed.* **2010,** *49*, 6338–6342.
(83) Khan, I.; Saeed, K.; Zekker, I.; Zhang, B.; Hendi, A. H.; Ahmad, A.; Ahmad, S.; Zada, N.; Ahmad, H.; Shah, L. A.; Shah, T.; Khan, I. Review on Methylene Blue: Its Properties, Uses, Toxicity and Photodegradation. *Water* **2022,** *14*, 242.
(84) Boylston, M.; Beer, D. Methemoglobinemia: A Case Study. *Crit. Care Nurse* **2002,** *22*, 50–55.
(85) Ginimuge, P. R.; Jyothi, S. D. Methylene Blue: Revisited. *J. Anaesthesiol. Clin. Pharmacol.* **2010,** *26*, 517–520.
(86) II, C. J.; B., L. J. Methylene Blue. *Am. J. Ther.* **2003,** *10*, 289–291.
(87) DiSanto, A. R.; Wagner, J. G. Pharmacokinetics of Highly Ionized Drugs II: Methylene Blue—Absorption, Metabolism, and Excretion in Man and Dog after Oral Administration. *J. Pharm. Sci.* **1972,** *61*, 1086–1090.
(88) Curry, S. Methemoglobinemia. *Ann. Emerg. Med.* **1979,** *11*, 214–221.
(89) Kiuchi, K. Rapid Alkaline Methylene Blue Supravital Staining for Assessment of Anterior Segment Infections. *Clin. Ophthalmol.* **2016,** *10*, 1971–1975.
(90) Hu, X.; Laguerre, V.; Packert, D.; Nakasone, A.; Moscinski, L. A Simple and Efficient Method for Preparing Cell Slides and Staining without Using Cytocentrifuge and Cytoclips. *Int. J. Cell Biol.* **2015,** *2015*, 813216.
(91) Wilson, T. M. On the Chemisty and Staining Properties of Certain Derivatives of the Methylene Blue Group when Combined with Eosin. *J. Exp. Med.* **1907,** *9*, 645–670.
(92) Farjami, E.; Clima, L.; Gothelf, K. V.; Ferapontova, E. E. DNA Interactions with a Methylene Blue Redox Indicator Depend on the DNA Length and are Sequence Specific. *Analyst.* **2010,** *135*, 1443-1448.
(93) Ksenzhek, O. S.; Petrova, S. A.; Kolodyazhny, M. V. Electrochemical Properties of Some Redox Indicators. *Bioelectrochem. Bioenerg.* **1977,** *4*, 346–357.
(94) Ziółkowski, R.; Jarczewska, M.; Górski, L.; Malinowska, E. Oligonucleotide-based Electrochemical Biosensor for Hg^{2+} Using Methylene Blue as a Redox Indicator. *J. Electrochem. Soc.* **2013,** *160*, B152–B155.
(95) Dutton, F. B. Methylene Blue - Reduction and Oxidation. *J. Chem. Educ.* **1960,** *37*, A799.
(96) Campbell, J. A. Kinetics—Early and Often. *J. Chem. Educ.* **1963,** *40*, 578–583.
(97) Anderson, L.; Wittkopp, S. M.; Painter, C. J.; Liegel, J. J.; Schreiner, R.; Bell, J. A.; Shakhashiri, B. Z. What Is Happening When the Blue Bottle Bleaches: An Investigation of the Methylene Blue-catalyzed Air Oxidation of Glucose. *J. Chem. Educ.* **2012,** *89*, 1425–1431.
(98) Tardivoa, J. P.; Giglio, A. D.; de Oliveirab, C. S.; Gabrielli, D. S.; Junqueira, H. C.; Tada, D. B.; Severino, D.; de Fátima Turchiello, R.; Baptista, M. S. Methylene Blue in Photodynamic Therapy: From Basic Mechanisms to Clinical Applications. *Photodiagn. Photodyn. Ther.* **2005,** *2*, 175–191.

(99) Kofler, B.; Romani, A.; Pritz, C.; Steinbichler, T. B.; Schartinger, V. H.; Riechelmann, H.; Dudas, J. Photodynamic Effect of Methylene Blue and Low Level Laser Radiation in Head and Neck Squamous Cell Carcinoma Cell Lines. *Int. J. Mol. Sci.* **2018,** *19*, 1107.
(100) Nurhidayani.; Muzakkar, M. Z.; Maulidiyah.; Wibowo, D.; Nurdin, M. A Novel of Buton Asphalt and Methylene Blue as Dye-sensitized Solar Cell using TiO_2/Ti Nanotubes Electrode. *IOP Conf. Ser.: Mater. Sci. Eng.* **2017,** *267*, 012035.
(101) Reda, S. M.; El-Sherbieny, S. A. Dye-sensitized Nanocrystalline CdS and ZnS Solar Cells with Different Organic Dyes. *J. Mater. Res.* **2010,** *25*, 522–528.
(102) Guha, R. On Exploring Structure-activity Relationships. *Methods Mol. Biol.* **2013,** *993*, 81–94.
(103) Ritger, P. L.; Peppas, N. A. A Simple Equation for Description of Solute Release I. Fickian and Non-Fickian Release from Non-swellable Devices in the Form of Slabs, Spheres, Cylinders or Discs. *J. Controlled Release* **1987,** *5*, 23–36.
(104) Ritger, P. L.; Peppas, N. A. A Simple Equation for Description of Solute Release II. Fickian and Anomalous Release from Swellable Devices. *J. Controlled Release* **1987,** *5*, 37–42.
(105) Hopfenberg, H. B. Controlled Release from Erodible Slabs, Cylinders, and Spheres. In *ACS Symposium Series*; Paul, D. R.; Haris, F. W., Eds.; American Chemical Society: Washington DC, 1976; pp 26–32.
(106) Cooney, D. O. Effect of Geometry on the Dissolution of Pharmaceutical Tablets and Other Solids: Surface Detachment Kinetics Controlling. *AIChE J.* **1972,** *18*, 446–449.
(107) Lin, C.-C.; Metters, A. T. Hydrogels in Controlled Release Formulations: Network Design and Mathematical Modeling. *Adv. Drug Deliv. Rev.* **2006,** *58*, 1379–1408.
(108) Peppas, N. A.; Bures, P.; Leobandung, W.; Ichikawa, H. Hydrogels in Pharmaceutical Formulations. *Eur. J. Pharm. Biopharm.* **2000,** *50*, 27–46.
(109) Siepmann, J.; Siepmann, F. Mathematical Modeling of Drug Delivery. *Int. J. Pharm.* **2008,** *364*, 328–343.
(110) Li, J.; Mooney, D. J. Designing Hydrogels for Controlled Drug Delivery. *Nat. Rev. Mater.* **2016,** *1*, 16071.
(111) Siepmann, J.; Göpferich, A. Mathematical Modeling of Bioerodible, Polymeric Drug Delivery Systems. *Adv. Drug Deliv. Rev.* **2001,** *48*.
(112) Jablonski, A. Efficiency of Anti-Stokes Fluorescence in Dyes. *Nature* **1933,** *131*, 839–840.
(113) Jaffe, H. H.; Miller, A. L. The Fates of Electronic Excitation Energy. *J. Chem. Edu.* **1966,** *43*, 469–473.
(114) Talluri, S. G. Effect of Cucurbit[6]uril on the Structure and Dynamics of NaDC Gels. PhD University of Victoria, 2021. http://hdl.handle.net/1828/13847

Chapter 2: Designing a Stimuli-robust White Light Emitting Hydrogel

This work was done in collaboration between researchers at the University of Victoria (Canada), University of Campinas (Brazil) and Universidade Federal do Rio Grande do Sul (Brazil).

Luís Gustavo Teixeira Alves Duarte, Teresa Dib Zambon Atvars and Cornelia Bohne formulated the conceptual framework of the project. LGTAD synthesized the BTS molecule that was used for the fluorescence measurements. Ankur Awasthi performed the experiments and data analysis involved in the project. LGTAD was also involved in the preliminary analysis of the data. Fabiano Severo Rodembusch, TDZA and CB were involved in the acquisition of funds and in a supervisory capacity.

2.1 Introduction

Stimuli responsive emissive hydrogels have found applications as chemo- and biosensors as well as drug delivery systems. The application of an external stimuli leads to a change in the emission response of the system resulting in the chemo- or biosensing properties of the hydrogel. With a drug-loaded hydrogel, the loaded drug is released from within the hydrogel into the body on the application of external stimuli. The mechanism of drug release or sensing involves degradation of either the gel network or fluorophore resulting in a shorter shelf life for the hydrogel system, suitable for short term applications. By designing emissive hydrogels that are resistant to the external stimulus, hydrogel systems for long term applications can be obtained.

2.1.1 Pluronic F127

Pluronic polymers, also referred to as poloxamers are a class of amphiphilic, water soluble, ABA triblock copolymers composed of hydrophilic poly(ethylene oxide) (PEO) subunits and hydrophobic poly(propylene oxide) (PPO) subunits (chart 2.1). The nomenclature system of Pluronics starts with a letter that denotes the texture of the polymer, where *F* represent flakes, *L* represents liquid, and *P* represent paste. The subsequent one or two numbers following the letter

indicate approximately 1/300 of the molar mass of the PPO chain, followed by the last number, which indicates 1/10 of the relative percentage of PEO chains.[1-3] For example, P103 and P123 both exists as paste with the same molar mass percentage of the PEO group indicated by the same letter and last digit. However, P123 has longer PPO units than P103 indicated by the difference in the first two digits of their names. The alteration of molar mass of either of the two subunits within the polymers, results in polymers with vastly different properties, making them ideal templates for the design of triblock copolymer systems for specific applications.

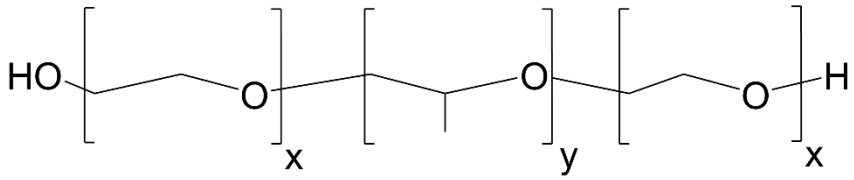

Chart 2.1: General structure of PEO-PPO-PEO Pluronic triblock copolymers.

In aqueous solutions, at sufficiently low temperature and concentrations, Pluronics exist as unimers. However, as the concentration or temperature is increased, these copolymers self-assemble to form a micelle. The micelle consists of a PPO dominated hydrophobic core and a PEO dominated hydrophilic corona (figure 2.1).[4] The concentration at which the copolymers form micelles is known as the critical micellar concentration (CMC) and the temperature at which micellization occurs is known as the critical micellization temperature (CMT).[5-6] The CMC and CMT for Pluronics are interdependent, i. e., CMC changes with temperature and CMT changes with concentration. As the polymer concentration is increased, the CMT decreases. Similarly, as temperature is increased, CMC decreases indicating that heating induces the micellization process.[4] The micellization process for Pluronic unimers is an entropy-driven process. The micelles are formed by the aggregation of the hydrophobic PPO blocks of the unimers to reduce their interaction with water molecules. Thus, when temperature is increased,

micellization is favored because the hydrophobic chains become de-solvated due to the breaking of hydrogen bonds between the hydrophobic PPO units and the surrounding water molecules. This de-solvation favors the aggregation of the PPO blocks to form the core of the micelles, with the solvated PEO chains forming the hydrated corona.[4, 7-8]

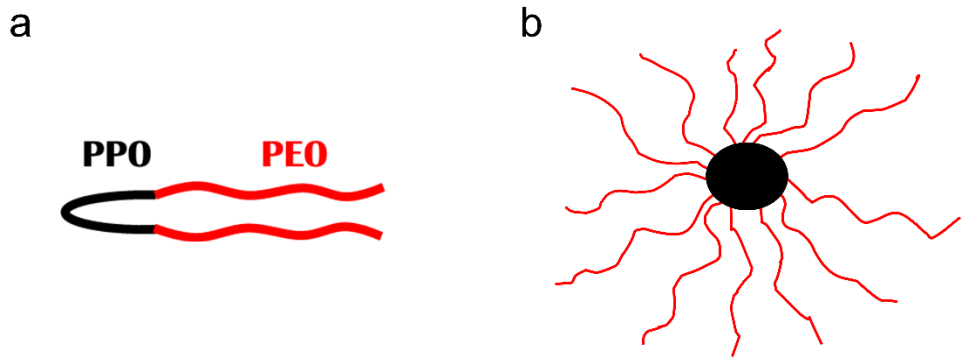

Figure 2.1: Structure for Pluronic polymers: a) free unimer b) micelle.

At sufficiently high concentrations, some Pluronics form a thermoreversible hydrogel. For example, F127 at 20% (w/v) concentration in water, forms a hydrogel at temperatures above 24–26 °C. The gelation in F127 is a result of the PEO blocks being dehydrated with an increase in temperature. This dehydration leads to chain friction and entanglement of the micellar chains, giving rise to an ordered cubic phase packing within F127 hydrogels.[9-10] This thermoreversible nature of F127 hydrogels make them prospective candidates for drug delivery, with F127 gels having been used for the topical administration of indomethacin and docetaxel.[11-12] Additionally, the transparent appearance of F127 hydrogels is highly suitable for developing luminescent hydrogels.

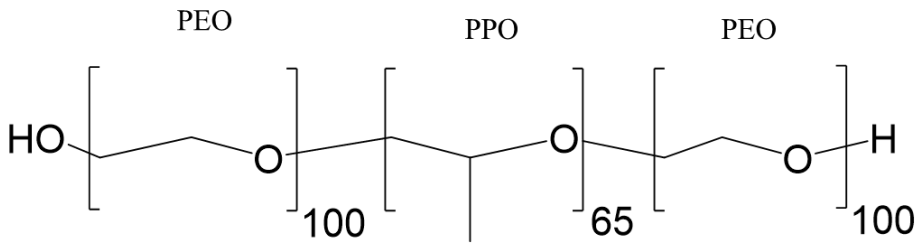

Chart 2.2: Molecular structure of F127.

2.1.2 White light emitting hydrogels.

Luminescent hydrogels have exhibited tremendous potential for applications in chemical and biosensing,[13-15] imaging,[16-17] anti-counterfeiting[18] and in fabrication of displays.[19-20] Different approaches can be used for the development of luminescent hydrogels. In a synthetic approach, the gelator is synthetically modified to attain the desired luminescent properties.[21-23] In a supramolecular approach, luminophores are incorporated as non-bonded guests within the hydrogels.[24-25] These luminophores include quantum[26-28] or carbon dots,[29-31] dyes,[17, 32] metal ions and their complexes,[33-35] showing that the luminescent properties in hydrogels can be altered without the requirement of a tailored synthetic effort for the desired modification.

A major motivation behind obtaining luminescent hydrogels is to obtain white light emitting hydrogels as they might turn into suitable alternatives for wearable optoelectronics devices. White light is a polychromatic beam of light, i.e., it is light made up of different wavelengths. Thus, the simplest and most common way for obtaining white light is by integrating three fluorophores, each with emissions corresponding to the three primary colors,[36-38] or by integrating two complementary colors,[39] within the hydrogel (figure 2.2). In this strategy, the color of the emitted light is dictated by the concentration ratio between the fluorophores incorporated within the hydrogel.[38-40] This incorporation of fluorophores within the hydrogel can either be through covalent binding

of the fluorophore to the gelator,[41-43] coordination to the gel matrix,[44-45] or physical entrapment within the gel.[36, 45-46] One of the disadvantages of this approach is that, as the concentration ratio between the fluorophore changes, the distribution of these fluorophores between the microenvironments of the hydrogel such as the immobile gel structures and the entrapped aqueous phase may change, which in turn can lead to changes in the photophysics of one or more of the fluorophores.

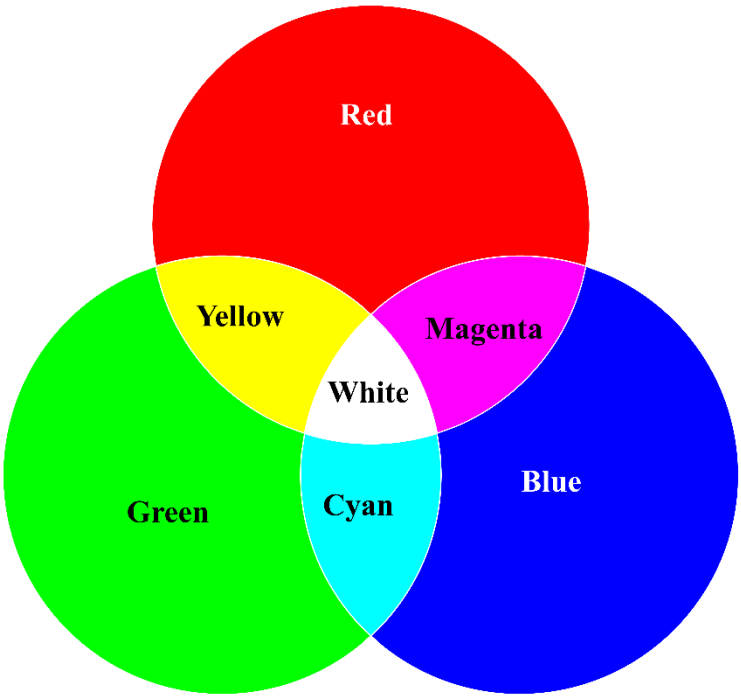

Figure 2.2: Schematic representation of the white light emission.

A viable alternative to the multi-molecule approach mentioned earlier is by using a single molecule approach. Herein, a single molecule, which can reversibly form other emitting species is incorporated within the hydrogel to achieve the desired color of light. Moreover, the use of a single molecule offers an avenue towards easier fabrication, better color reproducibility and improved stability for the luminescent hydrogel.[47-49] Examples of the single molecule approach include the copolymerization of a single molecule fluorophore with acrylamide,[50] or the modulation of the ground-state acid-base equilibrium of a fluorophore within a hydrogel.[46]

2.1.3 Excited-state intramolecular proton transfer (ESIPT)

Excited-state proton transfer (ESPT) is an important reaction that controls function in a variety of biological systems.[51-55] Molecules that have both proton (hydrogen) donating and accepting groups can undergo excited-state intramolecular proton transfer (ESIPT) due to increased acidity or basicity in the excited-state. A schematic representation of ESIPT is shown in scheme 2.1, where N and T are the ground-state normal and tautomer forms of a molecule and the N* and T* are its excited-state analogues respectively. In ESIPT, the T* form of the molecule is formed from the intramolecular proton transfer of the excited-state isomer (N*) as N is the only stable isomer in the ground-state. Once T* decays to the ground-state (T), the isomer is readily converted to N via a ground-state intramolecular proton transfer () process.[56-57] This four-level system ensures that only the N isomer of the molecule is prevalent in the ground-state, while in the excited-state N* and T* coexist. This leads to a broadening of the emission spectrum since both N* and T* forms of the molecule emit. Molecules undergoing ESIPT have found application in various fields such as in chemical sensors,[58-61] humidity sensors,[62-63] photo stabilizers,[64] proton transfer lasers,[65-69] photochromic switches[70-71] as well as in development of white light generation[72-74] and organic light-emitting diodes (OLED).[75-76]

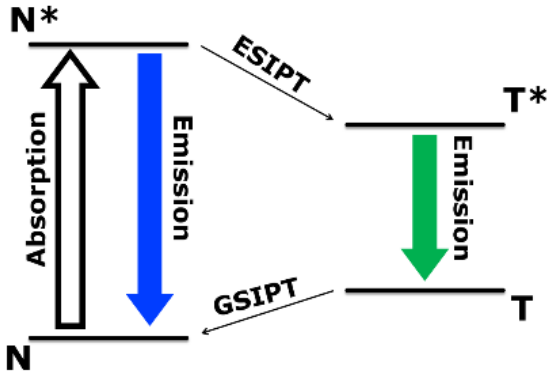

Scheme 2.1: Four-level diagram of the ESIPT process.

2.1.4 Objective

The objective of this chapter was to develop a white light emitting hydrogel where primarily one species of a fluorophore exists in the ground state and is located in a specific environment of the hydrogel. In contrast to ground state molecules, the singlet excited states of organic fluorophores are short lived, precluding any relocation of excited states within the different environments of supramolecular systems,[77-79] before decay to the fluorophore's ground-state. The design of the system relies on the ESIPT of *N,N′*-bis(salicylidene)-(2-(3′,4′-diaminophenyl)benzothiazole, (BTS) incorporated into Pluronic F127 hydrogels. BTS was chosen as it had shown drawbacks with respect to its light-colour stability in solid-state devices.[80-81] The choice of BTS served an additional purpose as being an indicator for the localization of the dye within the hydrogel. As BTS has been shown to possess an emissive dianion form,[82] the ground-state equilibrium of BTS incorporated F127 hydrogels would be sensitive to pH (chart 2.3). However, the pH sensitivity of BTS would be dependent on the localization of BTS within the hydrogel. For example, if BTS is localized within the hydrophobic core of the micelles it is assumed that the BTS molecules would be insensitive to pH, whereas if

they localize within the hydrophilic parts of the hydrogel, they will show a pH dependent change in the emission color of the hydrogel. Thus, this chapter details how the knowledge of different microenvironments for guest localization within F127 hydrogels was exploited to obtain a pH-insensitive white light emitting hydrogel.

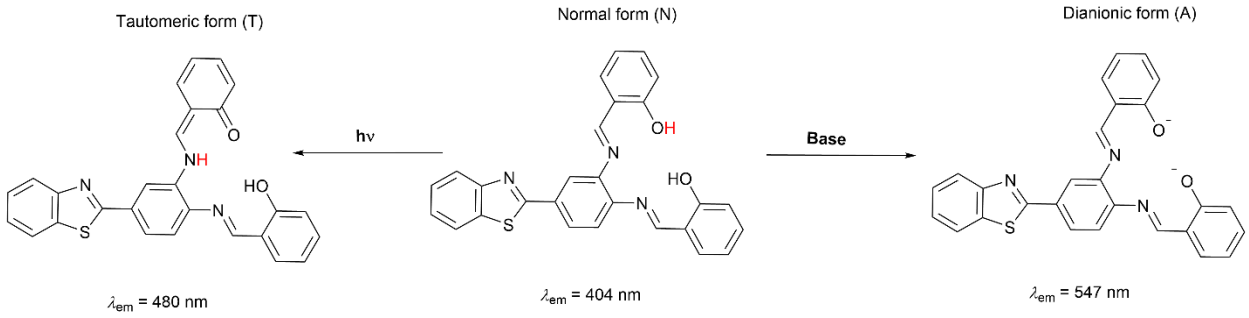

Chart 2.3: Isomers of BTS and its reported emission maxima in dichloromethane (DCM).

2.2 Experimental

2.2.1 Materials

Pluronic F127 (Sigma-Aldrich, M_W = 12,600 Da, 70 wt.% PEO) and dichloromethane (DCM, Fischer, HPLC grade > 99.8%) were used as received. Deionized water (Barnstead NANOpure deionizing system ≥ 17.8 MΩ cm) was used for preparation of all aqueous solutions. BTS was synthesized and purified according to reported literature procedures (appendix A2.1).[80]

2.2.2 Sample Preparation

All hydrogel samples were made using 17% (w/w) F127 by adding 4.0 g of F127 to 20 mL of water in an ice bath with stirring until all solid F127 dissolved. For solutions prepared at different pH values, the pH of water was first adjusted using HCl or NaOH to obtain the desired pH value and this water was then used to prepare the 17% (w/w) F127 samples. BTS was solubilized in DCM yielding an 800 μM stock solution. An aliquot of BTS in DCM was added to a glass vial, after which DCM was evaporated under a gentle air flow. After DCM evaporation, 4

mL of the 17% (w/w) F127 solution was added to the vial. This solution was then stirred for a week in an ice bath to ensure complete dissolution of BTS into 17% (w/w) F127. After a week, 3 mL of this BTS/F127 solution was transferred to a 10 mm × 10 mm quartz cell to carry out the photophysical studies.

2.2.3 Instrumentation

^{1}H NMR spectra were acquired using DMSO-d_6 as the solvent, on a Varian 400 MHz or a Bruker 400 MHz spectrometer. A VWR SympHony B10P pH meter was used to measure the pH of the solutions. Absorption spectra were collected on a CARY 100 Varian spectrometer at a scan rate of 600 nm/min. Emission spectra were measured using a PTI QM-40 spectrofluorometer using slits corresponding to 2.0 nm bandwidths for the excitation and emission monochromators. Samples were excited between 340 nm and 480 nm (figure S2.2). For the determination of the colour of the fluorescence, two emission spectra were collected to cover the full spectral range, with the exception of a 20 nm gap. This gap of 20 nm corresponds to double the excitation wavelength which was excluded to eliminate the collection of any scattered excitation light. The spectrum was interpolated linearly for the gap. The emission of a control sample containing the F127 gel but not the fluorophore, measured using the same experimental conditions, was subtracted from the BTS/gel spectrum to correct for the emission of impurities in F127 and any light scattering (figure 2.3). The presence of F127 emission was seen to not alter the shape of the BTS emission spectra (figure S2.3). The F127 sample shows a sharp peak around 400 nm which corresponds to the Raman scattering for water, since all samples were made in aqueous media. The Colour Calculator from Osram Sylvania was used to obtain the chromaticity diagram and to determine the Commission Internationale de l'Eclairage (CIE 1931) coordinates of chromaticity.[83]

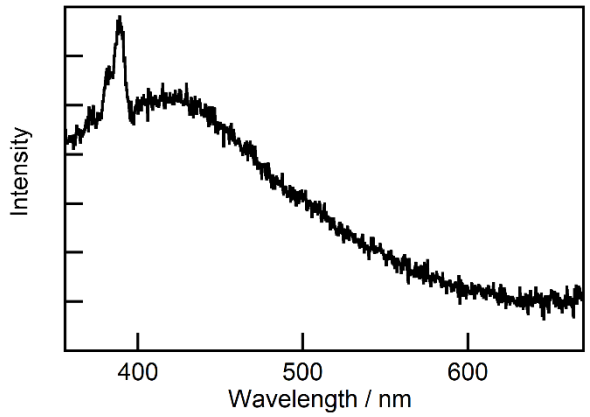

Figure 2.3: Steady-state emission (λ_{exc} = 340 nm) of 17% (w/w) F127 (w/v) at 30 °C.

Time-resolved emission decays were collected using an Edinburgh Instruments OB920 single photon counting system. A light emitting diode was used to excite the samples at 335 nm (EPLED-330, Edinburgh Instruments) and the emission was collected at specific wavelengths using a monochromator bandwidth of 16 nm. The instrument response function (IRF) was collected using an aqueous Ludox solution which scattered the excitation light. The data were collected until the highest intensity in the collecting channels reached 5,000 counts. The time-resolved decays were fit to a sum of exponentials (eq 2.1) using the software provided by Edinburgh Instruments, where A_i corresponds to the pre-exponential factor of species "*i*" and τ_i corresponds to the lifetime of species "*i*". The sum of the A_i values is equal to unity. To account for the IRF, a re-convolution of the IRF with the calculated decay was performed during the fitting of the experimental data.

$$I(t) = I_o \sum_{1}^{i} A_i \, e^{-\frac{t}{\tau_i}}$$

(Eq. 2.1)

The goodness of the fit was judged by the χ^2 values recovered from the fit of the experimental data to equation. 2.1 and by the visual inspection of the residuals. Fits with χ^2 values between 0.9 and 1.2 and having a random distribution of residuals around zero were deemed adequate.

2.3 Results

2.3.1 Steady-state emission results

BTS has been shown to have white light emission when incorporated as an active layer in an OLED because of the simultaneous emission from the normal (N*) and tautomeric forms of the dye (T*).[80] At a concentration of 17% (w/w) in water, F127 exists as a thermoreversible hydrogel, i.e., at a temperature of 20 °C, F127 exists as a sol, whereas on increasing the temperature to 30 °C, F127 transitions to a gel. This sol-gel transition for F127 could lead to a relocalization of BTS within the different microenvironments offered by F127 hydrogels. However, that is not the case, as seen in figures 2.4 and 2.5. The BTS emission is seen to be independent of the F127 phase transition, no matter the concentration of BTS that is incorporated within the hydrogels. The spectral features observed for BTS in F127 hydrogels are different from those observed previously in DCM.[80] Shoulders are observed for the N* and T* form of BTS in F127, which were absent in solution.

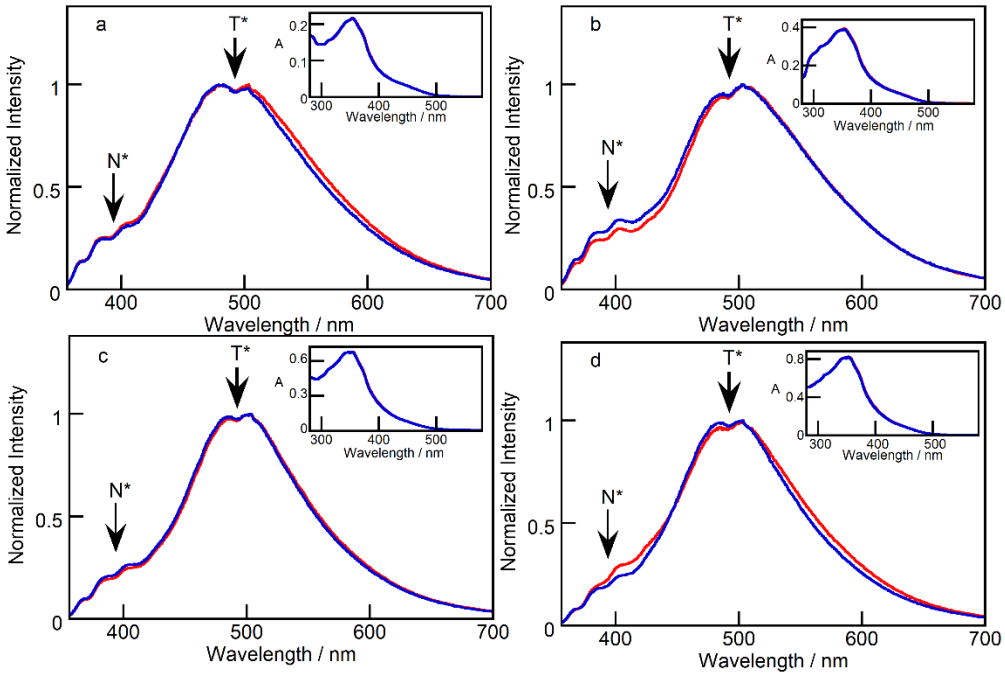

Figure 2.4: Normalized steady-state emission (λ_{exc} = 340 nm) of various BTS concentrations **(a)** A_{335} = 0.2, **(b)** A_{335} = 0.4, **(c)** A_{335} = 0.6 and **(d)** A_{335} = 0.8 in 17% (w/w) F127 at 20 °C (red, sol) and 30 °C (blue, gel). Inset: Absorption spectra of BTS in 17% (w/w) F127 at 20 °C (red, sol) and 30 °C (blue, gel).

The concentration of BTS was quantified using its absorption at 335 nm (A_{335}). This approach was adopted as the low solubility of BTS in water precluded the determination of the molar absorptivity for BTS. Moreover, the absorption spectra were also used to monitor changes in the ground-state equilibrium between the normal (N) and dianionic (A) form of BTS within the hydrogel. Similar to the steady-state emission results, the absorption spectra in BTS were seen to be independent of F127 phase transition.

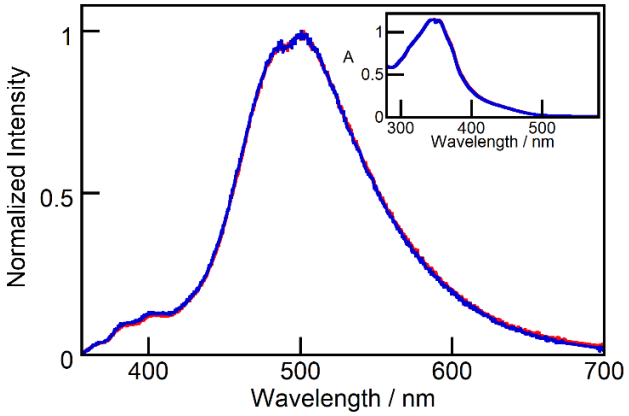

Figure 2.5: Normalized steady-state emission (λ_{exc} = 340 nm) of highest BTS concentrations (A_{335} = 1.1) in 17% (w/w) F127 at 20 °C (red, sol) and 30 °C (blue, gel). Inset: Absorption spectra of BTS in 17% (w/w) F127 at 20 °C (red, sol) and 30 °C (blue, gel).

2.3.2 Quantification of emission colour (chromaticity diagram)

Chromaticity is an objective specification for the color of light irrespective of its luminance. The CIE system for the perception of color is based on the trichromacy of human vision. Since the human eye has three different type of color sensitive cones, the response of the eye is best described in terms of tristimulus values which are used to make a chromaticity diagram. Any color on the chromaticity diagram can be considered a mixture of tristimulus CIE primaries X, Y and Z. The CIE system transforms these tristimulus values into the chromaticity coordinates x and y which signify hue and saturation, and a brightness parameter z that is independent of color.[84]

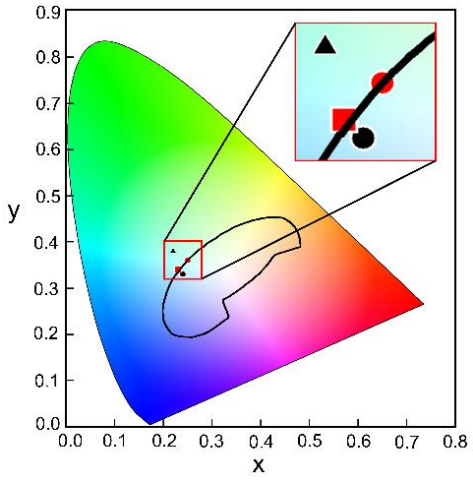

Figure 2.6: Chromaticity diagram (x, hue and y, saturation) of the emission (λ_{exc} = 340 nm) from 17% (w/w) F127 hydrogels with varying BTS concentrations. **(a)** A_{335} = 0.2 (black circle), **(b)** A_{335} = 0.4 (red circle), **(c)** A_{335} = 0.6 (black square), **(d)** A_{335} = 0.8 (red square) and **(e)** A_{335} = 1.1 (black triangle). The red and black squares have the same chromaticity coordinates (table S2.1) and overlap with each other.

Using the widely adopted 1931 CIE chromaticity diagram described by the National Bureau of Standards (NBS),[85] the color of BTS containing F127 hydrogels was quantified (figure 2.6 and table S2.1). At the lowest BTS concentration, the chromaticity coordinates for the hydrogels were seen to lie well within the perceived white light region. The white light region is any point lying within the black shape shown in figure 2.6, and any point lying within this region is considered to be emitting white light.[85] As the BTS concentration was increased in F127 gels, the color of the light emitted shifted towards the boundary of what is considered white light emission. At a high enough concentration corresponding to an absorbance of 1.1, the color of emitted light from BTS/F127 hydrogels became light blue with chromaticity coordinates that are no longer within the acceptable white region.

2.3.3 Insensitivity of white light emitting F127 hydrogels to pH

The presence of a ground-state equilibrium between the normal and dianion form of BTS presents an opportunity for BTS/F127 hydrogels to show sensitivity to pH.[82] Based on BTS'

properties in solution, the normal and dianion form of BTS have distinct absorption and emission maxima, that are sensitive to the polarity of the solvent.[80] The absorption spectra for the N form of BTS has been seen to shift from 346 nm in DCM to 384 nm in trifluoroacetic acid (TFA). Similarly, the emission maximum was seen to shift from 404 nm in DCM to 434 nm in DCM/TFA. When BTS is excited at 340 nm, the emission is predominantly seen from the N* and T* forms of BTS, however, if BTS is excited at longer wavelengths, we should see emission predominantly from the A* form. Therefore, the use of different excitation wavelengths to selectively excite the A form of BTS can indicate for the presence of the dianionic form of BTS.

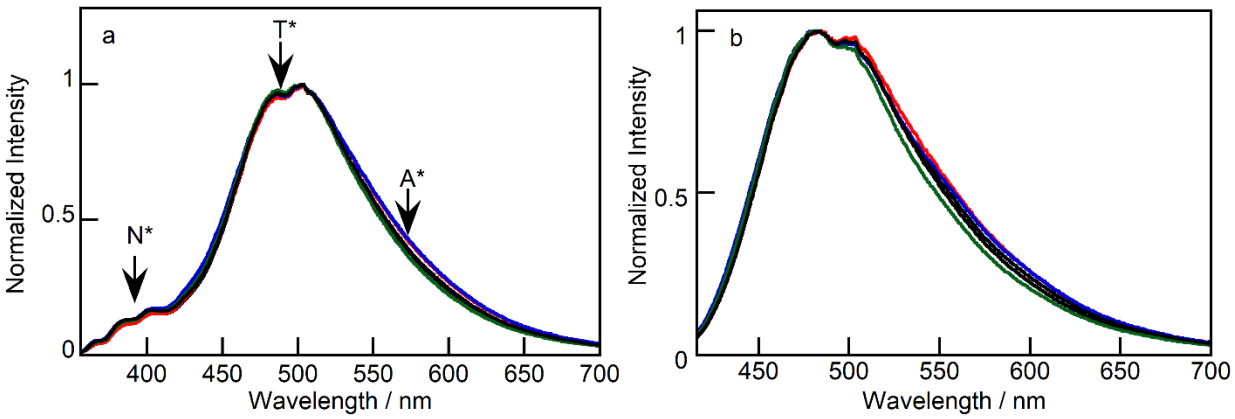

Figure 2.7: Normalized steady-state emission spectra of BTS in 17% (w/w) at 30 °C at various pH values: pH 4 (black), pH 5 (red), pH 6 (blue), pH 7 (green), pH 8 (black), excited at (λ_{exc}) **(a)** 340 nm and **(b)** 400 nm.

It is observed that the emission spectra of BTS have N* emitting around 400 nm and T* emitting around 500 nm. Based on reported literature values,[80] it is expected that the A* form of BTS would emit around ~550 nm. However, as the pH within the hydrogels was increased, no change in the emission spectra of BTS/F127 hydrogels was observed (figure 2.7a). This insensitivity of pH was further confirmed by observing the chromaticity diagram for the various pH values, where the CIE coordinates corresponding to different pH values are seen to overlap with each other (figure 2.8 and table S2.2). The hydrogels are seen to be light blue emitters

because of the high concentration of BTS within them (A_{335} = 1.1) (appendix A2.5). Selective excitation of the dianion (figure 2.7b) also shows that changing of the pH did not modulate the ground-state equilibrium between the N and A forms of BTS.

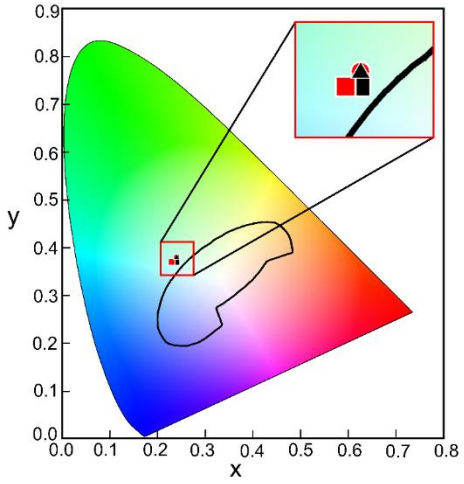

Figure 2.8: Chromaticity diagram (x, hue and y, saturation) of BTS emission (λ_{exc} = 340 nm) in 17% (w/w) F127 hydrogels with varying pH values from pH 4 to pH 8. The concentration of BTS at the different pH values is **(a)** A_{335} = 1.2 (black circle), **(b)** A_{335} = 1.2 (red circle), **(c)** A_{335} = 0.9 (black square), **(d)** A_{335} = 1.1 (red square) and **(e)** A_{335} = 1.2 (black triangle). Some of the symbols are not visible as they are overlapped by other symbols.

2.3.4 Identification of BTS isomers and their location within F127 hydrogels

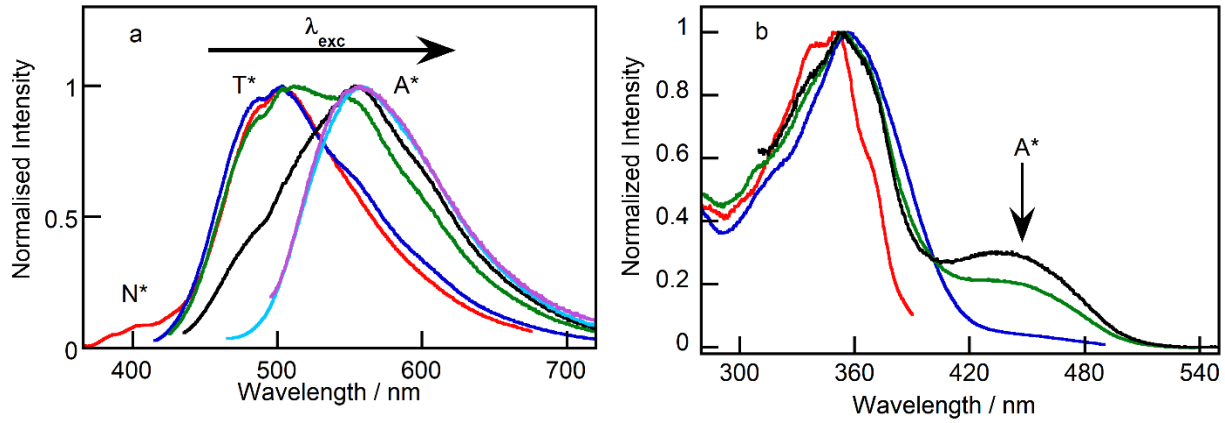

Figure 2.9: (a) Normalized steady-state emission spectra of BTS in 17% (w/w) at 30 °C excited at different wavelengths. (1) λ_{exc} = 340 nm (red) (2) λ_{exc} = 400 nm (blue) (3) λ_{exc} = 410 nm (green) (4) λ_{exc} = 420 nm (black) (5) λ_{exc} = 450 nm (cyan) λ_{exc} = 480 nm (purple) **(b)** Normalized excitation spectra of BTS in 17% (w/w) at 30 °C monitored at different wavelengths. (1) λ_{em} = 400 nm (red) (2) λ_{em} = 500 nm (blue) (3) λ_{em} = 550 nm (green) (4) λ_{em} = 600 nm (black).

To confirm the pH insensitive behaviour of BTS within F127 hydrogels, excitation spectra were collected to investigate the different isomeric forms of BTS contributing to the emission (figure S2.10). Emission spectra measured with incremental excitation wavelengths show a change in the peak position of BTS when the excitation wavelength moves above 400 nm indicating the presence of the dianion form (A) of BTS present in the ground state (figure 2.9a). Moreover, by collecting excitation spectra at the respective emission peaks, detailed information on the ground state species responsible for the emission can be obtained. As can be seen from figure 2.9b, the emission peaks observed at 400 nm and 500 nm corresponding to N* and T* respectively are formed by the same ground state species which is the N form. However, while the emission peak at 550 nm is seen to arise by the absorption of light by a different species, indicating the presence of the A form of BTS in the ground state.

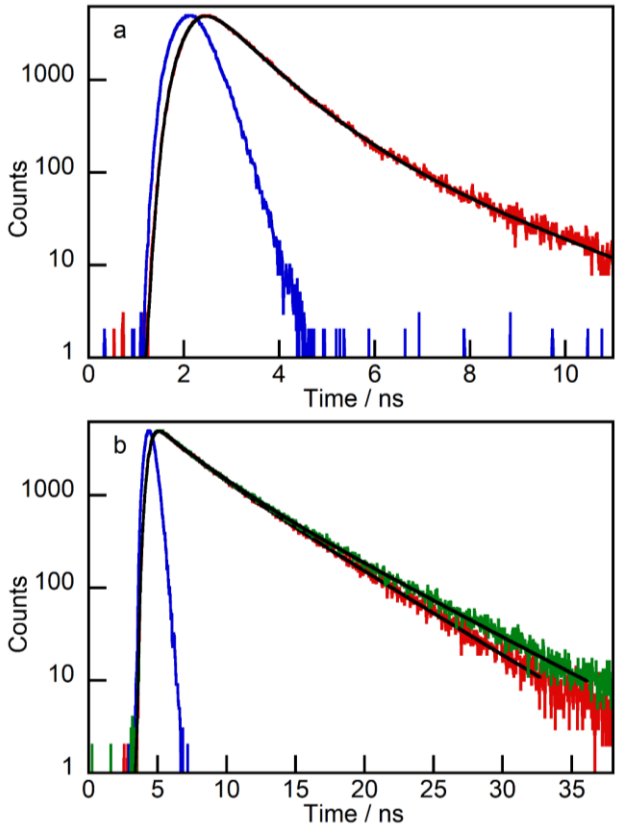

Figure 2.10: Time-resolved decay traces for singlet excited state of BTS in 17% (w/w) F127 hydrogels at 30 °C. (A) λ_{em} = 400 nm (red) (B) λ_{em} = 500 nm (red), λ_{em} = 550 nm (green). The solid blue line represents the IRF whereas the solid black line represents the fit to the decays.

The presence of the A form is further confirmed with the analysis of the time-resolved data for BTS containing F127 hydrogels. Time resolved studies have been shown to reveal guests localised in multiple microenvironments within a system. The decay traces for BTS were monitored at the emission maxima of the N^* (380 nm) and T^* (500 nm). To confirm our observations that the A^* was emitting, a decay trace was also collected at 550 nm. All the decay traces collected were fit to a multiexponential function to obtain three lifetimes for each wavelength (table 1.1 and appendix A2.7). A lifetime of 2.1 ns with a pre-exponential factor of 0.03 corresponding to 3% is observed when the decay trace is monitored at 380 nm. This lifetime corresponds to the singlet excited lifetime of N^*. However, such a low pre-exponential factor for N^* is seen due to the underlying emission from F127, which has the shortest lifetimes (τ_1)

observed at all the monitoring wavelengths (figure 2.10). Moreover, scattering contribution from the gel is expected to be higher at 380 nm since the monitoring wavelength is close to the excitation wavelength of the laser source. The above reasons combined with the ESIPT process that N^* undergoes, results in fewer photons from the N^* reaching the detector, and thus the contribution seen in the analysis may not represent the actual distribution of the N^* form of BTS in its excited state. As the monitoring wavelength is increased to 500 nm, a longer lifetime of 4.8 ns with a pre-exponential factor corresponding to 51% is observed which is assigned to the emission from the T^* form of BTS. Similar to the previous report for BTS,[80] a faster lifetime of 2.5 ns with a pre-exponential factor corresponding to 30% is attributed to the A^* form of BTS. When the emission decay is monitored at 550 nm, there is an increase in the contribution of A^* accompanied by a decrease in the pre-exponential factor of T^*, indicating the presence and contribution of the A^* form of BTS to the generation of white light emitting F127 hydrogels.

Table 2.1: Lifetimes (τ) and corresponding pre-exponential factors (A) for the emission of BTS in 17% F127 (w/w) at 20 °C and 30 °C for samples excited at 335 nm.[a]

T / °C	λ_{em} / nm[b]	A_1	τ_1 / ns	A_2	τ_2 / ns	A_3	τ_3 / ns
20	380	0.50 ± 0.04	0.2 ± 0.1	0.47 ± 0.05	0.8 ± 0.1	0.03 ± 0.03	2.1 ± 0.8
	500	0.17 ± 0.01	0.5 ± 0.2	0.30 ± 0.04	2.6 ± 0.2	0.54 ± 0.04	4.9 ± 0.1
	550	0.17 ± 0.03	0.5 ± 0.2	0.49 ± 0.06	3.3 ± 0.2	0.35 ± 0.08	6.0 ± 0.6
30	380	0.50 ± 0.03	0.2 ± 0.1	0.47 ± 0.03	0.8 ± 0.1	0.03 ± 0.03	2.1 ± 0.6
	500	0.19 ± 0.04	0.4 ± 0.1	0.30 ± 0.05	2.5 ± 0.2	0.51 ± 0.05	4.8 ± 0.2
	550	0.19 ± 0.04	0.5 ± 0.3	0.46 ± 0.05	2.9 ± 0.3	0.35 ± 0.06	5.5 ± 0.2

[a], Averages from five independent experiments; errors correspond to standard deviations. [b], wavelength for emission detection; ± 8 nm.

2.4 Discussion

As the absorption spectra for BTS are independent of the F127 phase transition, any changes in the emission spectra are a result of the excited state properties of the BTS species (N*, T* and A*) and are not due to a different distribution of species (N vs. A) in the ground state. This is because the same ratio of BTS fluorophores, i.e., N and A are present in the ground state irrespective of the phase of F127 (sol or gel). Unlike the BTS emission when dispersed in a polymer,[80] shoulders are observed for the emission maxima of the N* and T* forms of BTS in F127. In the polymer, most of the emission arises from T* and the emission maximum occurs at a longer wavelength (563 nm). This longer emission wavelength was proposed to be due to the presence of aggregates of BTS.[80] These differences suggest that the environment provided by the F127 micelles for BTS is heterogeneous and inhibits the aggregation of the chromophores. The similarity of the emission spectra of BTS in the sol and gel phases of F127 indicates that the colour of the emitted light does not depend on the phase of the system.

White light emitting BTS/F127 hydrogels were seen to be sensitive to the concentration of BTS incorporated within the hydrogels. The hydrogels can be seen to emit white light at low concentration of BTS loading within the hydrogel whereas, the color of emission changed to light blue when the concentration of BTS was sufficiently high (A_{335} = 1.1). The shift in emission color is a consequence of the higher contribution to the emission spectra from the T* form of BTS when the concentration is increased.

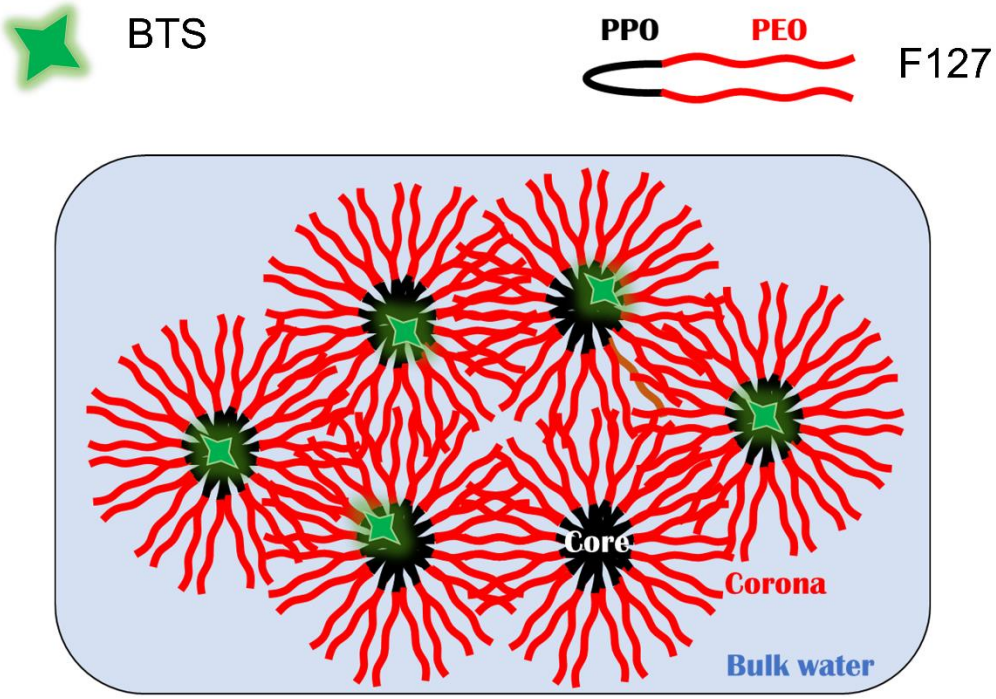

Figure 2.11: Schematic representation of BTS location within F127 hydrogels.

Previous studies have shown that the relative ratio of a fluorophore's acid and basic form can be used to change the color of F127 hydrogels based on the localization of the fluorophore, 4,4′-{(1E,1′E)-[2-(3-aminopropoxy)pyrimidine-4,6-diyl]bis(ethene-2,1-diyl)}-bis(*N*,*N*-diethylaniline) (PPBEN).[46] PPBEN was localized within the hydrophilic corona of the hydrogel, making it accessible to the free protons (H^+). This access to free H^+ ions allowed for modulation of the concentration between the emissive acid and base forms of PPBEN, thereby making the emission color of the hydrogel sensitive to pH. A similar effect should be expected for BTS as well if it is localized within the hydrophilic corona. However, when the pH of BTS/F127 hydrogels was changed, no such change in emission color of the hydrogels was observed. Moreover, the presence of the A* form of BTS contributing to the emission was also confirmed indicating that BTS was localized within a microenvironment of the hydrogel that protected it from H^+ ions. The only microenvironment that could allow for BTS to be protected from H^+ ions in such a way is the hydrophobic core of the micelle (figure 2.11).

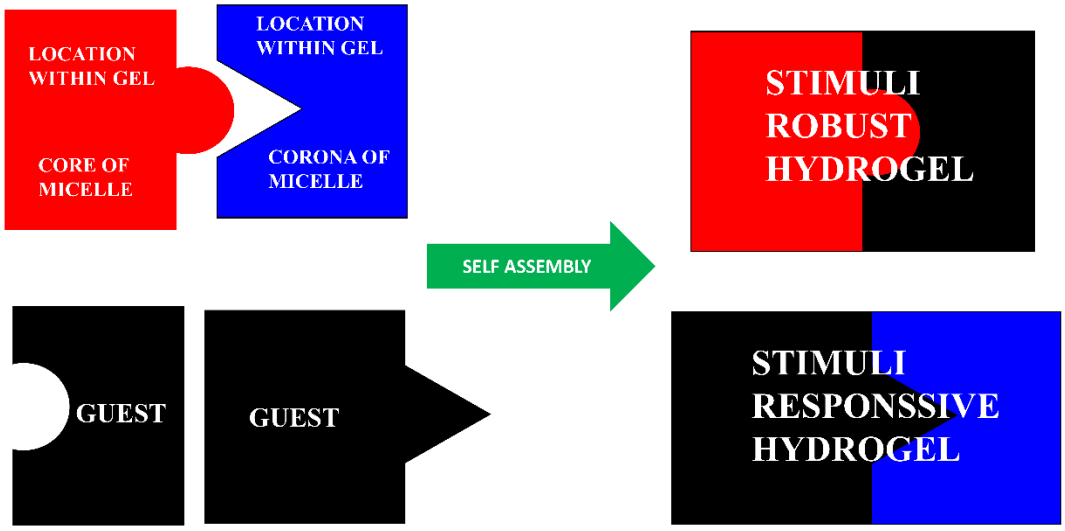

Figure 2.12: Schematic representation of how guest location within F127 hydrogels can dictate function.

2.5 Conclusion

A highly hydrophobic fluorophore was incorporated within F127 hydrogels to produce white light emitting hydrogels allowing for tuning of color from white to light blue by altering the fluorophore concentration. The hydrogel emission was seen to be insensitive to changes in pH due to the hydrophobic nature of the guest which when localized in the hydrophobic core of the micelles does not interact with the aqueous phase where the pH is changed. Depending on the molecular form of the guest, the guest could be localised either ‘exclusively in’ or ‘within both’ the hydrophobic as well as the hydrophilic microenvironments of the gel (figure 2.12). By being localized within the hydrophobic parts of the hydrogel, guest molecules can be protected from degradation by external stimuli within polymeric hydrogels to obtain robust hydrogel systems, whereas guest molecules localized within the hydrophilic parts of the hydrogel can yield stimuli sensitive systems. This knowledge can be exploited to design smarter and efficient hydrogel systems based on the desired application.

2.6 References

(1) Alexandridis, P.; Hatton, T. A. Poly(ethylene oxide)-poly(propylene oxide)-poly (ethylene oxide) Block Copolymer Surfactants in Aqueous Solutions and at Interfaces: Thermodynamics, Structure, Dynamics, and Modeling. *Colloids Surf., A* **1995,** *96*, 1–46.
(2) Kurahashi, M.; Kanamori, K.; Takeda, K.; Kaji, H.; Nakanishi, K. Role of Block Copolymer Surfactant on the Pore Formation in Methylsilsesquioxane Aerogel Systems. *RSC Adv.* **2012,** *2*, 7166–7173.
(3) Pitto-Barry, A.; Barry, N. P. E. Pluronic® Block-copolymers in Medicine: from Chemical and Biological Versatility to Rationalisation and Clinical Advances. *Polym. Chem.* **2014,** *5*, 3291–3297.
(4) Alexandridis, P.; Holzwarth, J. F.; Hatton, T. A. Micellization of Poly(ethylene oxide)-poly(propylene oxide)-poly(ethylene oxide) Triblock Copolymers in Aqueous Solutions: Thermodynamics of Copolymer Association. *Macromolecules* **1994,** *27*, 2414–2425.
(5) Tuzar, Z.; Kratochvíl, P. Block and Graft Copolymer Micelles in Solution. *Macromolecules* **1994,** *6*, 201–232.
(6) Alexandridis, P.; Lindman, B. *Amphiphilic Block Copolymers: Self-assembly and Applications*, 1st ed.; Elsevier: Amsterdam, 2000.
(7) Attwood, D.; Collett, J. H.; Tait, C. J. The Micellar Properties of the Poly(oxyethylene)-poly(oxypropylene) Copolymer Pluronic F127 in Water and Electrolyte Solution. *Int. J. Pharm.* **1985,** *26*, 25–33.
(8) Miller, S. C.; Drabik, B. R. Rheological Properties of Poloxamer Vehicles. *Int. J. Pharm.* **1984,** *18*, 269–276.
(9) Hamley, I. W. *The Physics of Block Copolymers*, Oxford University Press: New York, USA, 1998.
(10) Rassing, J.; Mackenna, W.; Bandopadhyay, S.; Eyring, E. Ultrasonic and ^{13}C-nmr Studies on Gel Formation in Aqueous Solutions of the ABA Block Polymer Pluronic F-127. *J. Mol. Liquid.* **1984,** *27*, 165–178.
(11) Turabee, M. D.; Jeong, T. H.; Ramalingam, P.; Kang, J. H.; Ko, Y. T. N,N,N-trimethyl Chitosan Embedded In Situ Pluronic F127 Hydrogel for the Treatment of Brain Tumor. *Carbohydr. Polym.* **2019,** *203*, 302–309.
(12) Miyazaki, S.; Tobiyama, T.; Takada, M.; Attwood, D. Percutaneous Absorption of Indomethacin from Pluronic F127 Gels in Rats. *J. Pharm. Pharmacol.* **1995,** *47*, 455–457.
(13) Peng, H.-S.; Stolwijk, J. A.; Sun, L.-S.; Wegener, J.; Wolfbeis, O. S. A Nanogel for Ratiometric Fluorescent Sensing of Intracellular pH Values. *Angew. Chem. Int. Ed.* **2010,** *49*, 4246–4249.
(14) Shibata, H.; Heo, Y. J.; Okitsu, T.; Matsunaga, Y.; Kawanishi, T.; Takeuchi, S. Injectable Hydrogel Microbeads for Fluorescence-based In Vivo Continuous Glucose Monitoring. *Proc. Natl. Acad. Sci. U.S.A.* **2010,** *107*, 17894–17898.
(15) Zhao, Y.; Shi, C.; Yang, X.; Shen, B.; Sun, Y.; Chen, Y.; Xu, X.; Sun, H.; Yu, K.; Yang, B.; Lin, Q. pH- and Temperature-sensitive Hydrogel Nanoparticles with Dual Photoluminescence for Bioprobes. *ACS Nano* **2016,** *10*, 5856–5863.
(16) Tsou, Y.-H.; Zhang, X.-Q.; Bai, X.; Zhu, H.; Li, Z.; Liu, Y.; Shi, J.; Xu, X. Dopant-free Hydrogels with Intrinsic Photoluminescence and Biodegradable Properties. *Adv. Funct. Mater.* **2018,** *28*, 1802607.

(17) Li, M.; He, P.; Li, S.; Wang, X.; Liu, L.; Lv, F.; Wang, S. Oligo(p-phenylenevinylene) Derivative-incorporated and Enzyme-responsive Hybrid Hydrogel for Tumor Cell-specific Imaging and Activatable Photodynamic Therapy. *ACS Biomater. Sci. Eng.* **2018,** *4*, 2037–2045.
(18) Chen, B.; Xie, H.; Wang, S.; Guo, Z.; Hu, Y.; Xie, H. UV Light-tunable Fluorescent Inks and Polymer Hydrogel Films based on Carbon Nanodots and Lanthanide for Enhancing Anti-counterfeiting. *Luminescence* **2019,** *34*, 437–443.
(19) Beneducci, A.; Cospito, S.; Deda, M. L.; Chidichimo, G. Highly Fluorescent Thienoviologen-based Polymer Gels for Single Layer Electrofluorochromic Devices. *Adv. Funct. Mater.* **2015,** *25*, 1240–1247.
(20) Wang, H.; Ji, X.; Li, Z.; Zhu, C. N.; Yang, X.; Li, T.; Wu, Z. L.; Huang, F. Preparation of a White-light-emitting Fluorescent Supramolecular Polymer Gel with a Single Chromophore and Use of the Gel to Fabricate a Protected Quick Response Code. *Mater. Chem. Front.* **2017,** *1*, 167–171.
(21) Paris, R.; Quijada-Garrido, I.; Garcia, O.; Liras, M. BODIPY-conjugated Thermo-sensitive Fluorescent Polymers Based On 2-(2-methoxyethoxy)ethyl methacrylate. *Macromolecules* **2011,** *44*, 80–86.
(22) Babu, S. S.; Praveen, V. K.; Ajayaghosh, A. Functional π-Gelators and Their Applications. *Chem. Rev.* **2014,** *114*, 1973–2129.
(23) Kim, T. H.; Seo, J.; Lee, S. J.; Lee, S. S.; Kim, J.; Jung, J. H. Strongly Fluorescent Hydrogel as a Blue-emitting Nanomaterial: An Approach toward Understanding Fluorescence−structure Relationship. *Chem. Mater.* **2007,** *19*, 5815–5817.
(24) Li, J.; Mooney, D. J. Designing Hydrogels for Controlled Drug Delivery. *Nat. Rev. Mater.* **2016,** *1*, 16071.
(25) Wei, S.; Li, Z.; Lu, W.; Liu, H.; Zhang, J.; Chen, T.; Tang, B. Z. Multicolor Fluorescent Polymeric Hydrogels. *Angew. Chem.* **2021,** *133*, 8690–8706.
(26) Zhao, Y.; Zhao, X.; Tang, B.; Xu, W.; Li, J.; Hu, J.; Gu, Z. Quantum-dot-tagged Bioresponsive Hydrogel Suspension Array for Multiplex Label-free DNA Detection. *Adv. Funct. Mater.* **2010,** *20*, 976–982.
(27) Zhang, J.; Jin, J.; Wan, J.; Jiang, S.; Wu, Y.; Wang, W.; Gong, X.; Wang, H. Quantum Dots-based Hydrogels for Sensing Applications. *Chem. Eng. J.* **2021,** *408*, 127351.
(28) Zhang, L.; Jean, S. R.; Ahmed, S.; Aldridge, P. M.; Li, X.; Fan, F.; Sargent, E. H.; Kelley, S. O. Multifunctional Quantum Dot DNA Hydrogels. *Nat. Commun.* **2017,** *29*, 381.
(29) Bhattacharya, S.; Nandi, S.; Jelinek, R. Carbon-dot–hydrogel for Enzyme-mediated Bacterial Detection. *RSC Adv.* **2017,** *7*, 588–594.
(30) Cayuela, A.; Kennedy, S. R.; Soriano, M. L.; Jones, C. D.; Valcárcel, M.; Steed, J. W. Fluorescent Carbon Dot–molecular Salt Hydrogels. *Chem. Sci.* **2015,** *6*, 6139–6146.
(31) Cayuela, A.; Soriano, M. L.; Kennedy, S. R.; Steed, J. W.; Valcárcel, M. Fluorescent Carbon Quantum Dot Hydrogels for Direct Determination of Silver Ions. *Talanta* **2016,** *151*, 100–105.
(32) Benson, K.; Ghimire, A.; Pattammattel, A.; Kumar, C. V. Protein Biophosphors: Biodegradable, Multifunctional, Protein-based Hydrogel for White Emission, Sensing, and pH Detection. *Adv. Funct. Mater.* **2017,** *27*, 1702955.
(33) Kotova, O.; Daly, R.; dos Santos, C. M. G.; Boese, M.; Kruger, P. E.; Boland, J. J.; Gunnlaugsson, T. Europium-directed Self-assembly of a Luminescent Supramolecular Gel from a Tripodal Terpyridine-based Ligand. *Angew. Chem. Int. Ed.* **2012,** *51*, 7208–7212.

(34) Chen, P.; Li, Q.; Grindy, S.; Holten-Anderson, N. White-light-emitting Lanthanide Metallogels with Tunable Luminescence and Reversible Stimuli-responsive Properties. *J. Am. Chem. Soc.* **2015,** *137*, 11590–11593.
(35) Wang, J.; Sun, S.; Wu, B.; Hou, L.; Ding, P.; Guo, X.; Stuart, M. A. C.; Wang, J. Processable and Luminescent Supramolecular Hydrogels from Complex Coacervation of Polycations with Lanthanide Coordination Polyanions. *Macromolecules* **2019,** *52*, 8643–8650.
(36) Zhang, Y.; Ding, Z.; Liu, Y.; Zhang, Y.; Jiang, S. White-light-emitting Hydrogels with Self-healing Properties and Adjustable Emission Colors. *J. Colloid and Interface Sci.* **2021,** *582*, 825–833.
(37) Bairi, P.; Roy, B.; Chakraborty, P.; Nandi, A. K. Co-assembled White-light-emitting Hydrogel of Melamine. *ACS Appl. Mater. Interfaces* **2013,** *5*, 5478–5485.
(38) Zhu, Q.; Zhang, L.; Vliet, K. V.; Miserez, A.; Holten-Anderson, N. White Light-emitting Multi-stimuli-responsive Hydrogel with Lanthanides and Carbon Dots. *ACS Appl. Mater. Interfaces* **2018,** *10*, 10409–10418.
(39) Rao, K. V.; Datta, K. K. R.; Eswaramoorthy, M.; George, S. J. Highly Pure Solid-state White-light Emission from Solution-processable Soft-hybrids *Adv. Mater.* **2013,** *25*, 1713–1718.
(40) Chen, B.; Feng, J. White-light-emitting Polymer Composite Film Based on Carbon Dots and Lanthanide Complexes. *J. Phys. Chem. C* **2015,** *119*, 7865–7872.
(41) Bhattacharya, S.; Samanta, S. K. Unusual Salt-induced Color Modulation through Aggregation-induced Emission Switching of a Bis-cationic Phenylenedivinylene-based π Hydrogelator. *Chem. Eur. J.* **2012,** *18*, 16632–16641.
(42) Galindo, J. M.; Leganés, J.; Patiño, J.; Rodríguez, A. M.; Herrero, M. A.; Díez-Barra, E.; Merino, S.; Sánchez-Migallón, A. M.; Vázquez, E. Physically Cross-linked Hydrogel Based on Phenyl-1,3,5-triazine: Soft Scaffold with Aggregation-induced Emission. *ACS Macro Lett.* **2019,** *8*, 1391–1395.
(43) Li, Z.; Liu, P.; Ji, X.; Gong, J.; Hu, Y.; Wu, W.; Wang, X.; Peng, H.-Q.; Kwok, R. T. K.; Lam, J. W. Y.; Lu, J.; Tang, B. Z. Bioinspired Simultaneous Changes in Fluorescence Color, Brightness, and Shape of Hydrogels Enabled by AIEgens. *Adv. Mater.* **2020,** *32*, 190649.
(44) Xia, Y.; Xue, B.; Qin, M.; Cao, Y.; Li, Y.; Wang, W. Printable Fluorescent Hydrogels Based on Self-assembling Peptides. *Sci. Rep.* **2017,** *7*, 9691.
(45) Xue, J.; Xu, X.; Zhu, Y.; Yang, D. Lanthanide Based White-light-emitting Hydrogel Mediated by Fluorescein and Carbon Dots with High Quantum Yield and Multi-stimuli Responsiveness. *J. Mater. Chem. C* **2020,** *8*, 3380–3385.
(46) Wang, J.; Tang, F.; Wang, Y.; Liu, S.; Li, L. Tunable Single-molecule White-light Emission in Stimuli-responsive Hydrogel. *Adv. Optical Mater.* **2020,** *8*, 1901571.
(47) Li, D.; Hu, W.; Wang, J.; Zhang, Q.; Cao, X.-M.; Ma, X.; Tian, H. White-light Emission from a Single Organic Compound with Unique Self-folded Conformation and Multistimuli Responsiveness. *Chem. Sci.* **2018,** *9*, 5709–5715.
(48) Liu, R.; Yang, Y.; Cui, Q.; Xu, W.; Peng, R.; Li, L. A Diarylethene-based Photoswitch and its Photomodulation of the Fluorescence of Conjugated Polymers. *Chem. Eur. J.* **2018,** *24*, 17756–17766.
(49) He, Z.; Zhao, W.; Lam, J. W. Y.; Peng, Q.; Ma, H.; Liang, G.; Shuai, Z.; Tang, B. Z. White Light Emission from a Single Organic Molecule with Dual Phosphorescence at Room Temperature. *Nat. Commun.* **2017,** *8*, 416.

(50) Zhu, C. N.; Bai, T.; Wang, H.; Bai, W.; Ling, J.; Sun, J. Z.; Huang, F.; Wu, Z. L.; Zheng, Q. Single Chromophore-based White-light-emitting Hydrogel with Tunable Fluorescence and Patternability. *ACS Appl. Mater. Interfaces* **2018,** *10*, 39343–39352.
(51) Scheiner, S. *Hydrogen Bonding: A Theoretical Perspective*, Oxford University Press: New York, USA, 1997.
(52) Ludwig, R. *Hydrogen-transfer Reactions*, 1st ed.; Wiley-VCH: Weinheim, Germany, 2007.
(53) Douhal, A.; Lahmani, F.; Zewail, A. H. Proton-transfer Reaction Dynamics. Chem. Phys. *Chem. Phys.* **1996,** *207*, 477–498.
(54) Arnaut, L. G.; Formosinho, S. J. Excited-state Proton Transfer Reactions I. Fundamentals and Intermolecular Reactions. *J. Photochem. Photobiol. A Chem.* **1993,** *75*, 1–20.
(55) Formosinho, S. J.; Arnaut, L. G. Excited-state Proton Transfer Reactions II. Intramolecular Reactions. *J. Photochem. Photobiol. A Chem.* **1993,** *75*, 21–48.
(56) Kosower, E. M.; Huppert, D. Excited State Electron and Proton Transfers. *Annu. Rev. Phys. Chem.* **1986,** *37*, 127–156.
(57) Förster, T. Diabatic and Adiabatic Processes in Photochemistry. *Pure Appl. Chem.* **1970,** *24*, 443–450.
(58) Sedgwick, A. C.; Wu, L.; Han, H.-H.; Bull, S. D.; He, X.-P.; James, T. D.; Sessler, J. L.; Tang, B. Z.; Tian, H.; Yoon, J. Excited-state Intramolecular Proton-transfer (ESIPT) Based Fluorescence Sensors and Imaging Agents. *Chem. Soc. Rev.* **2018,** *47*, 8842–8880.
(59) Wu, Y.; Peng, X.; Fan, J.; Gao, S.; Tian, M.; Zhao, J.; Sun, S. Fluorescence Sensing of Anions Based on Inhibition of Excited-state Intramolecular Proton Transfer. *J. Org. Chem.* **2007,** *72*, 62–70.
(60) Zhang, X.; Guo, L.; Wu, F.-Y.; Jiang, Y.-B. Development of Fluorescent Sensing of Anions under Excited-state Intermolecular Proton Transfer Signaling Mechanism. *Org. Lett.* **2003,** *5*, 2667–2670.
(61) Henary, M. M.; Wu, Y.; Fahrni, C. J. Zinc(II)-selective Ratiometric Fluorescent Sensors Based on Inhibition of Excited-state Intramolecular Proton Transfer. *Chem. Eur. J.* **2004,** *10*, 3015–3025.
(62) Mishra, H.; Misra, V.; Mehata, S. M.; Pant, T. C.; Tripathi, H. B. Fluorescence Studies of Salicylic Acid Doped Poly(vinyl alcohol) Film as a Water/Humidity Sensor. *J. Phys. Chem. A* **2004,** *108*, 2346–2352.
(63) Chen, L.; Ye, J.-W.; Wang, H.-P.; Pan, M.; Yin, S.-Y.; Wei, Z.-W.; Zhang, L.-Y.; Wu, K.; Fan, Y.-N.; Su, C.-Y. Ultrafast Water Sensing and Thermal Imaging by a Metal-organic Framework with Switchable Luminescence. *Nat. Commun.* **2017,** *8*, 15985.
(64) Catalán, J.; Fabero, F.; Guijarro, M. S.; Claramunt, R. M.; Maria, M. D.; Concepcion Foces-foces, M. D.; Cano, F. H.; Elguero, J.; Sastre, R. Photoinduced Intramolecular Proton Transfer as the Mechanism of Ultraviolet Stabilizers: A Reappraisal. *J. Am. Chem. Soc.* **1990,** *112*, 747–759.
(65) Acuña, A. U.; Costela, A.; Muñoz, J. M. A Proton-transfer Laser. *J. Phys. Chem. A* **1996,** *90*, 2807–2808.
(66) Acuña, A. U.; Amat-Guerri, F.; Costela, A.; Douhal, A.; Figuera, J. M.; Florido, F.; Sastre, R. Proton-transfer Lasing from Solid Organic Matrices. *Chem. Phys. Lett.* **1991,** *187*, 98–102.
(67) Chou, P.; McMorrow, D.; Aartsma, T. J.; Kasha, M. The Proton-transfer Laser. Gain Spectrum and Amplification of Spontaneous Emission of 3-Hydroxyflavone. *J. Phys. Chem.* **1984,** *88*, 4596–4599.
(68) Yan, C.-C.; Wang, X.-D.; Liao, L.-S. Organic Lasers Harnessing Excited State Intramolecular Proton Transfer Process. *ACS Photonics* **2020,** *7*, 1355–1366.

(69) Tsutsui, Y.; Zhang, W.; Ghosh, S.; Sakurai, T.; Yoshida, H.; Ozaki, M.; Akutagawa, T.; Seki, S. Electrically Switchable Amplified Spontaneous Emission from Liquid Crystalline Phase of an AIEE-active ESIPT Molecule. *Adv. Opt. Mater.* **2020,** *8*, 1902158.
(70) Lim, S.-J.; Seo, J.; Park, S. Y. Photochromic Switching of Excited-state Intramolecular Proton-transfer (ESIPT) Fluorescence: A Unique Route to High-contrast Memory Switching and Nondestructive Readout. *J. Am. Chem. Soc.* **2006,** *128*, 14542–14547.
(71) Sobolewski, A. L. Reversible Molecular Switch Driven by Excited-state Hydrogen Transfer. *Phys. Chem. Chem. Phys.* **2008,** *10*, 1243–1247.
(72) Tang, K.-C.; Chang, M.-J.; Lin, T.-Y.; Pan, H.-A.; Fang, T.-C.; Chen, K.-Y.; Hung, W.-Y.; Hsu, Y.-H.; Chou, P.-T. Fine Tuning the Energetics of Excited-state Intramolecular Proton Transfer (ESIPT): White Light Generation in a Single ESIPT System. *J. Am. Chem. Soc.* **2011,** *133*, 17738–17745.
(73) Moraes, E. S.; Duarte, L. G. T. A.; Germino, J. C.; Atvars, T. D. Z. Near Attack Conformation as Strategy for ESIPT Modulation for White-light Generation. *J. Phys. Chem. C* **2020,** *124*, 22406–22415.
(74) Serduik, I. E. Design and Emissive Features of Ionic White-light Fluorophore. *J. Phys. Chem. C* **2018,** *122*, 18615–18620.
(75) Padalkar, V. S.; Seki, S. Excited-state Intramolecular Proton-transfer (ESIPT)-inspired Solid State Emitters. *Chem. Soc. Rev.* **2016,** *45*, 169–202.
(76) Kwon, J. E.; Park, S. Y. Advanced Organic Optoelectronic Materials: Harnessing Excited-state Intramolecular Proton Transfer (ESIPT) Process. *Adv. Mater.* **2011,** *23*, 3615–3642.
(77) Thomas, S. S.; Hosseini-Nejad, H.; Bohne, C. Dynamics of Small Molecules within the F127 PEO–PPO–PEO Triblock Copolymer Gel and Sol Phases Studied at the Molecular Scale. *Soft Matter* **2022,** *18*, 1706–1714.
(78) Bohne, C. Supramolecular Dynamics. *Chem. Soc. Rev.* **2014,** *43*, 4037–4050.
(79) Pace, T. C. S.; Bohne, C. Dynamics of Guest Binding to Supramolecular Systems: Techniques and Selected Examples. *Adv. Phys. Org. Chem.* **2008,** *42*, 167–223.
(80) Duarte, L. G. T. A.; Germino, J. C.; Berbigier, J. F.; Barboza, C. A.; Faleiros, M. M.; Simoni, D. d. A.; Galante, M. T.; de Holanda, M. S.; Rodembusch, F. S.; Atvars, T. D. Z. White-light Generation from All-solution-processed OLEDs using a Benzothiazole–salophen Derivative Reactive to the ESIPT Process. *Phys. Chem. Chem. Phys.* **2019,** *21*, 1172–1182.
(81) Duarte, L. G. T. A.; Germino, J. C.; Mendes, R. A.; Berbigier, J. F.; Faleiros, M. M.; Rodembusch, F. S.; Atvars, T. D. Z. The Role of a Simple and Effective Salicylidene Derivative. Spectral Broadening and Performance Improvement of PFO-based All-solution Processed OLEDs. *Dye. Pigment.* **2019,** *171*, 107671.
(82) Duarte, L. G. T. A.; Germino, J. C.; Mendes, R. A.; Berbigier, J. F.; Moreira, K. S.; Faleiros, M. M.; de Freitas, J. N.; Burgo, T. A. L.; Rodembusch, F. S.; Atvars, T. D. Z. The Balance between Charge Mobility and Efficiency in All-solution Processed Organic Light-emitting Diodes of Zn(II) Coordination Compounds/PFO Composites. *J. Phys. Chem. C* **2020,** *124*, 21036–21046.
(83) *Color Calculator*, Osram Sylvania: 2021. https://www.osram.us/cb/tools-and-resources/applications/led-colorcalculator/index.jsp
(84) Smith, T.; Guild, J. The C.I.E. Colorimetric Standards and Their Use. *Trans. Opt. Soc.* **1931,** *33*, 73–134.
(85) Kelly, K. L. Color Designations for Lights. *J. Opt. Soc. Am.* **1943,** *33*, 627–632.

Chapter 3: Looking at Guest Localization in Low Molecular Weight Sodium Deoxycholate Hydrogels: From a Sol to a Gel Story.

3.1 Introduction

The role of non-covalent interactions in the formation of supramolecular gels results in these systems having complex molecular structures. In physical gels, there exist only two environments for guest localization, which are the core or corona of the micelles, irrespective of the phase of the system (sol or gel). However, supramolecular systems are more complex due to the inherent nature of the self-assembly processes involved. This complexity can result in structural changes within supramolecular systems when transitioning from the sol to the gel phase, affecting guest localization. The understanding of structural changes and how they may affect guest localization when supramolecular systems are converted from a sol to a gel can help in the efficient design of prospective supramolecular gel systems.

3.1.1 Bile salts and NaDC

Bile salts are an important class of amphiphilic compounds found in vertebrates. They are naturally produced by the liver and stored in the gallbladder, and typically found in bile. The function of bile salts is to facilitate fat and vitamin digestion by solubilizing these hydrophobic fats and vitamins in the intestines. The biological function of bile salts is predominantly dictated by the molecular structure and self-assembly behaviour of the bile salt.[1]

The molecular structure of bile salts consists of a rigid tetracyclic backbone with curved geometry. The R_1, R_2, and R_3 groups are either hydrogens or hydroxyl groups, whereas the R_4 group is a carboxylic acid or another terminal group (figure 3.1).[2] The hydrophilic hydroxyl groups are attached on the concave side of the steroidal structure, with the hydrophobic methyl groups on the convex side. This arrangement results in a facial amphiphilicity in bile salts, with a

concave polar face and a convex nonpolar face.[2] These structural properties of bile salt molecules allow them to aggregate in aqueous solutions.

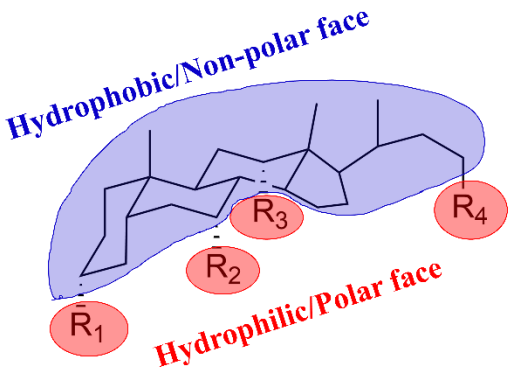

Name	R_1	R_2	R_3	R_4
Sodium Cholate	-OH	-OH	-OH	-COONa
Sodium Deoxycholate	-OH	-H	-OH	-COONa
Sodium Glycochlate	-OH	-OH	-OH	$-COONHCH_2COONa$
Sodium Chenodeoxycholate	-OH	-OH	-H	-COONa

Figure 3.1: Molecular structure of commonly investigated bile salts.

Bile salts self-assemble into aggregates, sometimes referred to as "micelles".[3] With increasing bile salt concentration, the molecules start to aggregate. Depending on the bile salt, the critical micelle concentration (CMC) may vary.[4-10] Aggregation in bile salts is largely driven by the hydrophobic association of the nonpolar faces of the molecular structure. This results in formation of primary aggregates.[11] In this structure, the hydrophilic acidic groups and hydroxyl groups point to the outside of the aggregate structure, shielding the hydrophobic core from water. Further aggregation can take place on increasing bile salt concentration. In this case, the primary aggregates which have the hydroxyl groups pointing outwards, associate with other primary aggregates in solution via hydrogen bonding resulting in elongated secondary aggregates.[11-13] In biology, bile salt aggregates act as lipid carriers or solubilizers by forming mixed micelles with fatty acids, cholesterol and monoglycerides.[14-16] These aggregation properties make bile salts adaptable hosts for guests with different polarities and sizes.[17-20]

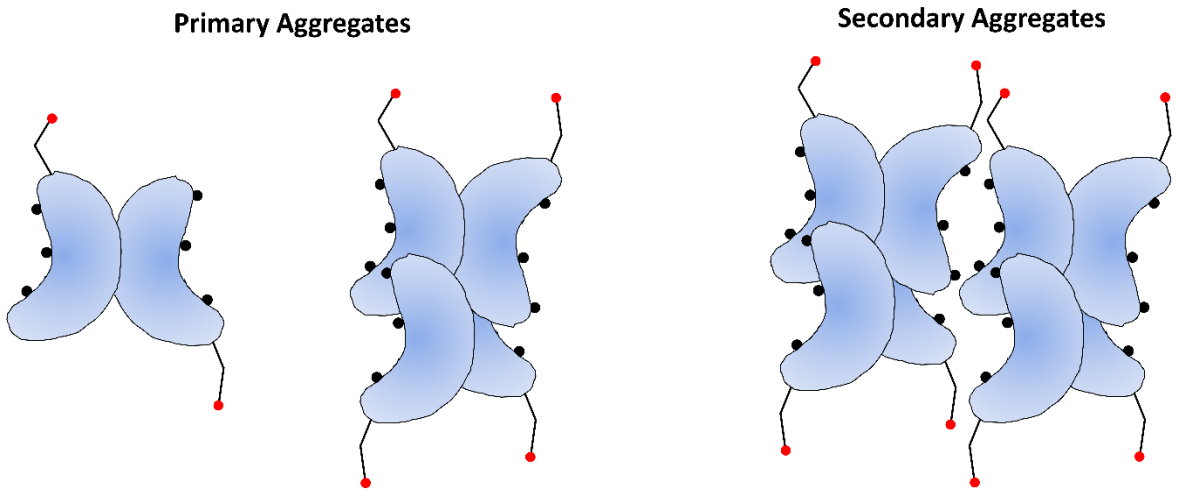

Figure 3.2: Cartoon representation of primary and secondary bile salt aggregates. The black dots represent the hydroxyl groups, and the red dot represents the carboxylate groups in bile salts.

The aggregation behaviour of bile salts is different from the aggregation behaviour of typical surfactants. Surfactants such as amphiphilic polymers (e.g. sodium dodecylsulfate) have a polar head and hydrophobic chain as a tail. The structural amphiphilicity of the steroidal backbone of bile salts, rather than the clear polarity difference between the polar groups and hydrophobic chain in typical surfactants makes the aggregation of bile salts more complex. This lack of a clear separation between the hydrophobic and hydrophilic parts in bile salts, contributes to their distinct aggregation properties.

Sodium deoxycholate (NaDC), shown in chart 3.1 is one of the most widely studied bile salts for its ability to form hydrogels at pH values close to neutrality.[21] At high pH values, the gel does not form and at low pH values, NaDC precipitates most likely due to protonation of the carboxylic acid group. NaDC gels are classified as supramolecular hydrogels and these hydrogels are known to possess thixotropic properties.[22-23] The biocompatibility possessed by NaDC hydrogels makes them prospective candidates for drug delivery, resulting in extensive work to understand the underlying forces responsible for gelation and how they can be modulated with external stimuli to design NaDC hydrogels with desired functionalities.

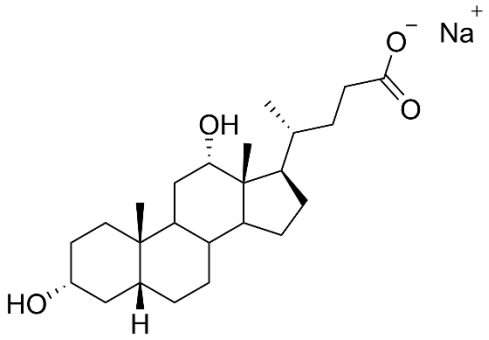

Chart 3.1: Structure of NaDC

Several models have suggested hydrogen bonding as the main driving force for gelation in NaDC hydrogels. Xu *et al*. observed that the addition of halide salts to the gel compressed the thickness of the electric double layer, thereby reducing electrostatic repulsions between the polar heads of NaDC.[24] This resulted in NaDC molecules coming closer to each other, which in turn favour intermolecular hydrogen bonding. These enhanced hydrogen bonding interactions resulted in an increase in the mechanical strength of the gels. On the other hand, the authors also showed that the addition of amino acids could break the hydrogen bonds resulting in weaker gels with low mechanical strength. These models were further supported by the work from Rodríguez Núñez *et al.* where the authors showed a decrease in the storage modulus of the gels with increasing temperatures, which is a result of the weakening of the hydrogen bonds.[25] Despite hydrogen bonding being suggested as the primary interaction responsible for gelation, other interactions such as electrostatic interactions between the deoxycholate anion and cations were also shown to affect mechanical properties of the hydrogel. The work from Rodríguez Núñez *et al.* showed that at constant pH and temperature, the storage modulus of NaDC hydrogels increases 100-fold, when the sodium ion (Na^+) concentration is increased from 0 to 0.6 M.[25] Moreover, the work by Zhang *et al.* has shown that the concentration of NaCl affected the pH and amount of NaDC required for gelation.[26] It was observed that in absence of Na^+ ions, a high

concentration of NaDC was required for gelation to take place. At constant NaDC concentration, the amount of Na^+ required for gelation was also seen to decrease with decreasing pH.

3.1.2 Fluorescence quenching

Fluorescence quenching refers to any process that decreases the fluorescence intensity of a fluorophore (F) containing sample. Quenching can occur via two different mechanisms, firstly collisional or dynamic quenching and the other being static quenching. In the case of dynamic quenching, the quencher (Q) needs to diffuse and encounter the excited state fluorophore before it decays to the ground state. Upon contact, the fluorophore returns to the ground state without the emission of a photon. In this kind of mechanism, quenching occurs without any permanent change to the molecule, that is in absence of a photochemical reaction. In static quenching, a non-fluorescent complex is formed between the quencher and fluorophore in the ground state.[27] For either static or dynamic quenching to take place, molecular contact between the fluorophore and quencher is necessary resulting in various applications of fluorescence quenching, such as studying the accessibility of a quencher to a protein or membrane bound fluorophore.[28-29] Additionally, the quenching rate constant can also be used to determine the diffusion coefficient of the quencher in the studied systems providing that the quenching is diffusion controlled.[30-34]

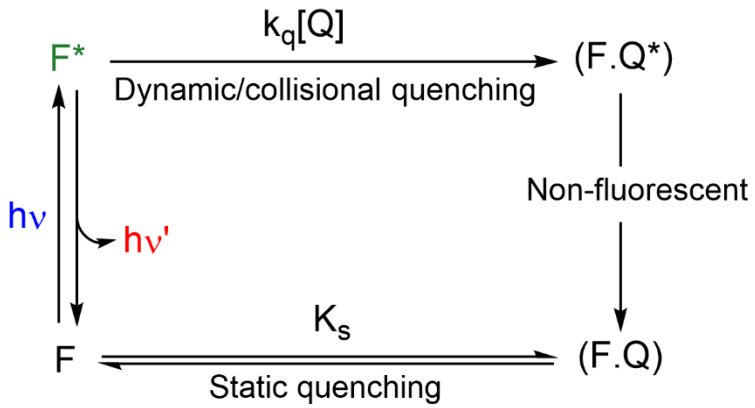

Figure 3.3: Schematic representation of fluorescence quenching, where F is the fluorophore and Q is the quencher.

Fluorescence quenching is typically described by the Stern-Volmer equation shown below.

$$\frac{I_0}{I} = \frac{\tau_0}{\tau} = 1 + k_q \tau_0 [Q] = 1 + K_{SV}[Q]$$

(Eq. 3.1)

In this expression, K_{SV} is the Stern-Volmer quenching constant, k_q is the bimolecular quenching rate constant, τ_0 and τ are the lifetime of the fluorophore in absence and presence of quencher, I_0 and I are the steady-state fluorescence intensities of the fluorophore in absence and presence of the quencher. Quenching data are usually presented as plots of I_0/I versus $[Q]$ because I_0/I is expected to be linearly dependent on the quencher concentration. A linear Stern-Volmer plot is generally indicative of a single class of fluorophores. However, if two fluorophore populations are present, with one inaccessible to the quencher, the Stern-Volmer plots deviate from linearity with a downward curvature, eventually becoming parallel to the *x-axis*.[27]

It is important to remember that linearity does not imply that the mechanism of quenching is dynamic. Static quenching is represented by the equation shown below.

$$\frac{I_0}{I} = 1 + K_S[Q]$$

(Eq. 3.2)

Similar to dynamic quenching, the dependence of I_0/I on $[Q]$ is observed to be linear, however, the quenching constant in this case represents the association constant between the fluorophore and quencher. The measurement of fluorescence lifetimes is the most definite method to distinguish between static and dynamic quenching. In dynamic quenching, a decrease in fluorescence lifetime with quencher concentration is observed because quenching is an additional process that depopulates the excited state affecting the overall decay rate constant, whereas static quenching removes a fraction of fluorophores from observation. The complexed fluorophores are non-fluorescent and only the fluorescence from the non-complexed fluorophores is observed. The non-complexed fraction of fluorophores is unperturbed and hence the lifetime for the non-complexed fluorophores stays the same and is τ_0. Therefore, for static quenching $\tau_0/\tau = 1$, whereas for dynamic quenching $\tau_0/\tau = I_0/I$.[27]

3.1.3 Binding response of fluorophores

Fluorophores are chemical compounds that emit light upon light excitation. These molecules absorb light of a specific wavelength and emit light at a longer wavelength. The absorbed wavelength and time before emission of the fluorophore depends on both the fluorophore structure and its chemical environment since the fluorophore interacts with its surrounding molecules. Such fluorophores when exposed to different chemical environments show a change in their fluorescence response, such as a shift in the emission wavelength or changes in the intensity of emitted light. The exposure of these fluorophores to different chemical environments can be a result of binding to macro- and biomolecules,[35] exposure to

solvents with varying polarity (solvatochromism)[36] and changes in ionic strength.[37] These characteristics have seen them used as dyes for staining tissues and cells,[38-39] probes and indicators,[40-42] or as materials in analytical techniques such as fluorescence imaging and spectroscopy.[43-44]

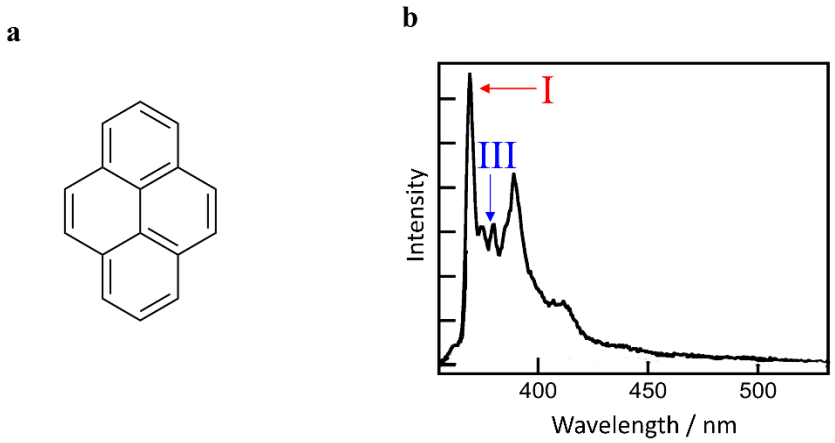

Figure 3.4: a) Molecular structure of pyrene. **b)** Steady-state fluorescence spectra of 0.5 μM pyrene showing the I and III peaks in water.

Pyrene is a polycyclic aromatic hydrocarbon obtained during the combustion of organic compounds. It is a highly symmetric molecule, that is aromatic despite not following Hückel's rule ($4n+2$) and having 16 π electrons (figure 3.3a).[45] The absorption and emission spectra of pyrene is well documented, with the earliest reports being by Jackson and coworkers who recorded its absorption in isooctane and the gas phase.[46] A similar investigation was done by Tanaka in n-heptane,[47] with this work being completed by Mangle and Topp when they investigated the gas-phase values of pyrene's absorption and emission spectra for its two lowest singlet states (S_1 and S_2).[48] In solution, pyrene has a high quantum yield and well-defined vibronic features in its emission spectrum. The emission spectrum of pyrene is constituted by five vibronic peaks, designated as I, II, III, IV and V. The intensity of peak I is known to increase with solvent polarity, whereas the intensity of peak III is solvent insensitive.[49-50] This has led to the ratio of these two peaks (I/III) being used to gain information on the polarity of the

environment close to molecular pyrene. In heterogenous systems where pyrene can be localized in multiple environments having varying polarity, the I/III ratio observed can be considered a weighted average of the values of each environment. For example, as shown in figure 3.5, in a non-polar homogenous system pyrene displays a I/III ratio of 1.0 (like n-butanol, p-xylene, diethyl ether),[50] whereas in a polar homogenous system this I/III ratio increases to 2.0 (like water, dimethylsulfoxide).[50] In a heterogenous system that contains both these microenvironments, if the pyrene is distributed equally, a I/III ratio of 1.5 will be observed (figure 3.5a). If the majority of the pyrene molecules experience a non-polar environment, a decreased value of the I/III ratio will be obtained (figure 3.5b). Alternately, if most of the pyrene molecules experience a polar environment, an increased value of the I/III ratio is obtained (figure 3.5c).

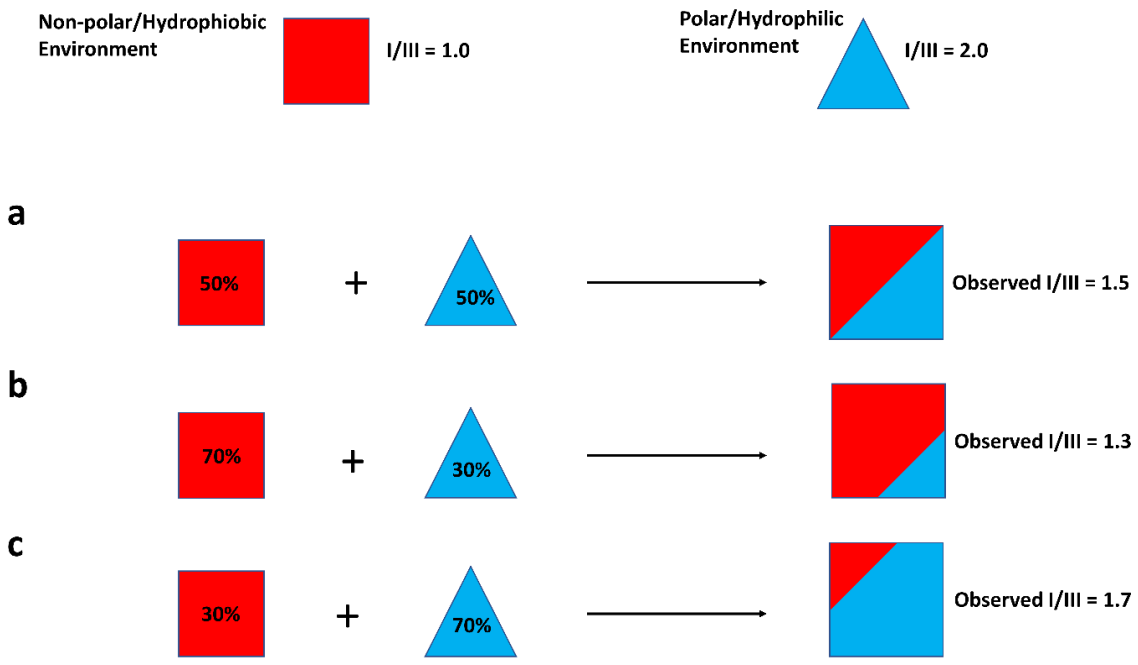

Figure 3.5: Schematic representation of the dependence of pyrene I/III ratio on its distribution in homogenous and heterogenous systems.

However, it is not just the steady-state fluorescence of pyrene that is sensitive to polarity. Changes in polarity experienced by pyrene also leads to changes in its fluorescence lifetime.

With an increase in polarity, the pyrene fluorescence lifetime is seen to decrease.[51] This steady-state and lifetime dependence of pyrene on the polarity of its microenvironment has been exploited to study various systems such as nanoparticles,[52] proteins,[53] nucleic acids,[54] lipids,[55] micelles,[56] and different macrocycles by either using pyrene or pyrene derivatives, or covalently attaching pyrene to the molecules to be investigated.[57]

3.1.4 Objective

Recent work in our group has shown that the addition of different types of cations affects the properties of NaDC hydrogels.[58] It was seen that addition of divalent cations like Ca^{2+} and Mg^{2+} resulted in the hydrogels having a lower sol-gel transition temperature than in presence of a monovalent cation like Na^{+}, K^{+}, NH_4^{+}. It was also seen that the addition of these cations affected the localization of guests within the hydrogel. With the addition of salts, pyrene localized within the hydrophobic regions of NaDC hydrogels was displaced to the hydrophilic region of the hydrogels. With the help of pyrene photophysics, it was observed that NaDC hydrogels possessed a minimum of two different microenvironments for pyrene to be localized in. One of these microenvironments behaved similarly to bulk water, whereas the other microenvironment was highly hydrophobic. However, these studies could only yield information around the polarity and not on the molecular structure of the microenvironments.

In my work, to attain a molecular picture of the different microenvironments present in NaDC hydrogels, pyrene was localized within these hydrogels and its fluorescence was quenched. The quenchers used in this study differ in their molecular characteristics, with one being ionic and another being neutral. The comparison of their quenching behaviour (mechanism of quenching and accessibility to pyrene) yielded information on the molecular structure of NaDC hydrogels.

3.2 Experimental

3.2.1 Materials

NaDC (Fluka, ≥ 98%), nitromethane (CH_3NO_2, Sigma-Aldrich, ≥ 98.5%), sodium iodide (NaI, Sigma-Aldrich, ≥ 99.999%) disodium phosphate (Na_2HPO_4, Anachemia, anhydrous, ≥ 99%), monosodium phosphate ($NaH_2PO_4 \cdot H_2O$, Anachemia, ≥ 99%), sodium chloride (NaCl, Sigma-Aldrich, BioXtra, ≥ 99%) and methanol (Fisher, spectral grade, ≥ 99.9%) were used as received. Pyrene (Sigma-Aldrich, ≥ 99%) was recrystallized from ethanol twice to obtain a white solid. Deionized water (Barnstead NANOpure deionizing systems, 17.8 MΩ cm) was used for the preparation of all solutions.

3.2.2 Sample Preparation

NaDC (416 mg) was dissolved in 5.0 mL of deionized water to obtain a 0.2 M stock solution. Pyrene (2.5 mg) was dissolved in 10.0 mL of methanol to obtain a 1.2 mM stock solution of pyrene. $NaH_2PO_4 \cdot H_2O$ (345.6 mg) in 5.0 mL of deionized water and Na_2HPO_4 (356.3 mg) in 5.0 mL of deionized water were dissolved to obtain 0.5 M solutions of each respectively. These were mixed in equal volume to obtain buffer with pH = 6.50 ± 0.01 at 21 °C. NaI (301.2 mg) was dissolved in 2.0 mL of deionized water to obtain 1 M stock NaI. NaCl (116.8 mg) was dissolved in 2.0 mL to obtain 1 M stock solution of NaCl. A 50 mM stock solution of CH_3NO_2 in deionized water was used for the experiments. Initially, 110 µL of CH_3NO_2 was dissolved in 2 mL of deionized water to obtain a 1 M CH_3NO_2 solution. Then, the 1 M CH_3NO_2 solution was further diluted with deionized water in a 2 mL volumetric flask to obtain a 50 mM CH_3NO_2 stock solution used during the experiments.

Preparation of NaDC gels without any quencher: Initially, 300 µL of 0.2 M NaDC and 1250 µL of deionized water were added to a vial and heated for 15 min at 60 °C. After 15 min, 2.5 µL of 1.2 mM pyrene, 200 µL of 0.5 M buffer (pH = 6.50 ± 0.01) and 250 µL of 1 M NaCl were added to keep the total volume as 2000 µL. This new solution was again heated for 15 min at 60 °C. After this, the solution from the vial was transferred to a triangular cell and allowed to sit for 20 h to form the gel before measurements were performed. The NaDC concentration was 30 mM. To prevent changes to the ionic strength when using NaI as a quencher, NaCl was added to keep the total Na^+ concentration constant at 305 mM. The pyrene concentration in the sample was 2.0 µM.

Preparation of NaDC gels with NaI as quencher: Initially, 300 µL of 0.2 M NaDC and 1250 µL deionized water were added to a vial and heated for 15 min at 60 °C. After 15 min, 2.5 µL of 1.2 mM, 200 µL of 0.5 M buffer (pH = 6.50 ± 0.01) along with the required volumes of 1 M NaI and 1 M NaCl (see table 3.1) was added to keep the total volume constant as 2000 µL. This new solution was again heated for 15 min at 60 °C. After this, the solution from the vial was transferred to a triangular cell and allowed to set for 20 h to form the gel before measurements were done. The NaDC concentration was 30 mM. To prevent changes to the Na^+ concentration on addition of NaI, NaCl was added keeping the total of NaI and NaCl added constant at 125 mM. The pyrene concentration in the samples was 2.0 µM, whereas the total Na^+ concentration was 305 mM.

Table 3.1: Preparation of experimental samples with varying iodide (I^-) concentrations.

NaI (mM)	Vol. of water (µL)	Vol. of NaDC (µL)	Vol. of buffer (µL)	Vol. of 1 M NaI (µL)	Vol. of 1 M NaCl (µL)	Final Vol. (µL)
0	1250	300	200	0	250	2000
5	1250	300	200	10	240	2000
10	1250	300	200	20	230	2000
15	1250	300	200	30	220	2000
20	1250	300	200	40	210	2000
25	1250	300	200	50	200	2000
50	1250	300	200	100	150	2000
75	1250	300	200	150	100	2000
100	1250	300	200	200	50	2000
125	1250	300	200	250	0	2000

Preparation of NaDC gels with CH_3NO_2 as quencher: Initially, 300 µL of 0.2 M NaDC and the required volume of deionized water were added to a vial and heated for 15 min at 60 °C. After 15 min, 2.5 µL of 1.2 mM pyrene, 200 µL of 0.5 M buffer (pH = 6.50 ± 0.01) along with the required volume of 50 mM CH_3NO_2 and 250 µL of 1 M NaCl were added to keep the total volume as 2000 µL. This new solution was again heated for 15 min at 60 °C. After this, the hot solution from the vial was transferred to a triangular cell and allowed to sit for 20 h to form the gel before measurements were performed. In the preparation method mentioned before, the required volume of deionized water is a compensation for the addition of quencher (solution in water), i. e., if 50 µL of quencher is going to be added, the volume of water added was adjusted to 1200 µL or if 150 µL of quencher is going to be added, the volume of water added is adjusted

to 1100 µL. This compensation is done to avoid dilution of pyrene due to a change in volume with quencher addition. A detailed description on how the volume of water is adjusted for each quencher concentration is shown in the table below (table 3.2). The NaDC concentration was 30 mM. NaCl (125 mM) was added to keep the ionic strength consistent with previous experiments where iodide was used as quencher. The pyrene concentration in the samples was 2.0 µM.

Table 3.2: Preparation of experimental samples with varying CH_3NO_2 concentrations.

CH_3NO_2 (mM)	**Vol. of water (µL)**	**Vol. of NaDC (µL)**	**Vol. of buffer (µL)**	**Vol. of 1 M CH_3NO_2 (µL)**	**Vol. of 1 M NaCl (µL)**	**Total Vol. (µL)**
0	1250	300	200	0	250	2000
0.25	1240	300	200	10	250	2000
0.50	1230	300	200	20	250	2000
0.75	1220	300	200	30	250	2000
1.00	1210	300	200	40	250	2000
1.25	1200	300	200	50	250	2000

3.2.3 Instrumentation

All samples were stored in a box to keep them in the dark before analysis to prevent photo-degradation of sodium iodide. Triangular cells were used to carry out all the photophysical experiments in the hydrogels. Steady-state emission studies were carried out on a PTI QM-40 spectrofluorometer. All samples were excited at 330 nm with slit bandwidths at 1.0 nm for both the excitation and emission monochromators and a 0.5 nm step count with 0.25 s averaging time. To account for scattering or residual emission from the gels, blanks were collected using 30 mM NaDC in water. The blanks were recorded in each cell, and the blank corresponding to each cell

was used for subtraction, e. g., blank collected in cell 1 was subtracted from the spectrum of the sample in cell 1, blank in cell 2 from the spectrum of sample in cell 2 and so on.

Single photon counting experiments were measured using an Edinburgh Instruments Ltd. OB920 setup. A 335 nm EPLED was used to excite all the samples and the emission decays were collected at 390 nm with a bandwidth of 16 nm for the emission monochromator. All decays were collected up to 100000 peak counts. The fits to the decay were done using the FAST software from Edinburgh Instruments Ltd. The tail fitting procedure available in the FAST software was used to fit the kinetics. Due to scattering, fitting of the kinetics was started 5–10 channels after the peak to remove the contribution from scattering. Fits with χ^2 values between 0.9–1.2 were deemed acceptable. The decays were fit to equation shown below.

$$I(t) = I(0)\sum_{i=1}^{n} A_i\, e^{-\frac{t}{\tau_i}}, \sum A_i = 1 \qquad \text{(Eq. 3.3)}$$

Where A_i and τ_i represent the pre-exponential factor and lifetime of the *i*th component respectively.

3.2.4 Methods

All quenching experiments were done as triplicates of independent experiments unless otherwise specified. For the quenching with sodium iodide, due to the limitation of the number of triangular cells available, only 6 quencher concentrations could be measured on a single day. The first experiment was done with quencher concentrations of 0, 5, 10, 15 and 25 mM. The next experiment was carried out using quencher concentrations of 0, 25, 50, 75, 100 and 125 mM. The point 0 mM and 25 mM were common between the two sets of experiments.

Steady-state Emission:

Emission spectra were integrated (A) over a wavelength range of 382–398 nm as this corresponded to the wavelength bandwidth for the time-resolved studies (390 ± 8 nm). The wavelength range ensured a good correlation between the steady-state and time-resolved studies for the Stern-Volmer plots (A_0/A) that were used to determine the mechanism of quenching for the different quenchers (appendix A3.1). The A_0/A values were calculated for each individual experiment, and then these values were averaged, which are the values used to construct the Stern-Volmer plots reported.

Time-resolved Emission:

All decay were fit to equation 3.3 yielding three lifetimes (τ_1, τ_2, τ_3). During the fitting process, τ_1 was assigned to free pyrene located in water and this value was fixed. The fixed value for τ_1 was calculated using the Stern-Volmer equation obtained by quenching pyrene with the relevant quencher in water (appendix A3.2). Initial results indicated that τ_3 was not being shortened in the presence of iodide ions (I^-) and thus, τ_3 was also fixed during the analysis. To establish the value of τ_3 that needed to be kept constant during the fitting process, initially the decay traces of a single experiment were fit to equation 3.3 keeping τ_1 constant. As mentioned earlier, a single experiment consisted of six quencher concentrations and therefore, this fitting process yielded six individual values for τ_3, corresponding to the respective quencher concentrations in that experiment. Based on the assumption that τ_3 is unquenched by iodide, the six τ_3 values were averaged to obtain an averaged $<\tau_3>_{avg}$ value for that experiment. Using this $<\tau_3>_{avg}$, the decay traces were refit to equation 3.3, by keeping τ_1 constant as before and fixing the value of τ_3 to $<\tau_3>_{avg}$ at all quencher concentrations involved in that experiment (appendix A3.3). This was repeated for all experiments where I^- was used to quench pyrene in NaDC

hydrogels. The quenching analysis for CH_3NO_2 did not require such a detailed methodology with the decay traces yielding three lifetimes with τ_1 fixed during the analysis (appendix A3.4).

Since the lifetime analysis for pyrene corresponded to a multiexponential function, average lifetimes ($<\tau>_{avg}$) were used to generate the time-resolved Stern-Volmer plots ($<\tau_0>_{avg}$ /$<\tau>_{avg}$), which were used to determine the quenching mechanism. The average lifetime was calculated using equation 3.4.[59] The $<\tau_0>_{avg}$ /$<\tau>_{avg}$ values were calculated for each experiment, and then these values were averaged. The averaged values were used to construct the Stern-Volmer plots.

$$\langle\tau\rangle_{avg} = \frac{\sum A_i \tau_i}{\sum A_i}$$

(Eq. 3.4)

3.3 Results

3.3.1 Steady-state emission results

The ratio of peak I and peak III for pyrene steady-state emission spectra is extensively used to characterize the polarity of the microenvironment experienced by pyrene within a system.[50] The I/III ratio of pyrene when distributed in highly polar medium like water is reported to be around ~1.9–2.0, whereas when pyrene is localized in a non-polar medium like cyclohexane, the I/III ratio of pyrene decreases to around 0.59.[50]

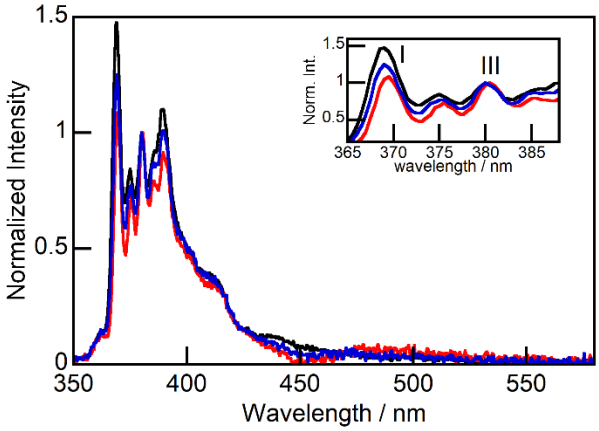

Figure 3.6: Steady-state emission of 2.0 μM pyrene in 30 mM NaDC hydrogels normalized at peak III with 0 mM quencher (black), 25 mM I^- (red) and 1.25 mM CH_3NO_2 (blue).

From figure 3.6, it can be observed that when pyrene is localized within NaDC hydrogels, it experiences a more hydrophobic microenvironment (I/III_{NaDC} = 1.4) in comparison to the reported value for pyrene in water. Moreover, the addition of different quenchers results in a decrease in the I/III ratio of pyrene with increasing quencher concentration (figure 3.6 and figure 3.7a). This decrease in the I/III ratio of pyrene irrespective of the quencher used indicates that in NaDC hydrogels, pyrene is localized in at least two different microenvironments with varying polarities. Moreover, the decrease of the I/III ratio of pyrene with increasing quencher concentrations indicates that the quencher is more accessible to the pyrene localized in the hydrophilic region of the hydrogel compared to the pyrene localized within the hydrophobic regions of the hydrogel.

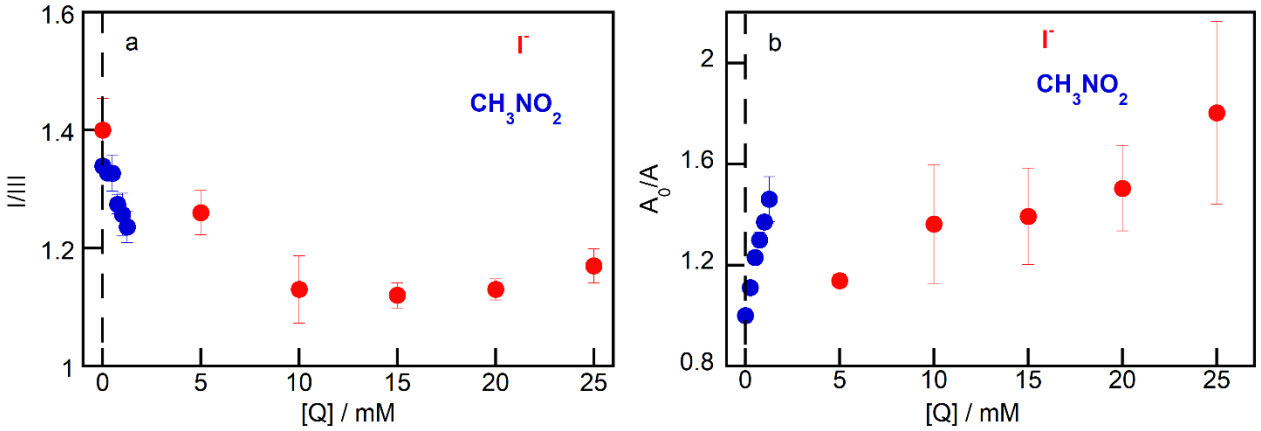

Figure 3.7: a) Changes in I/III ratios of 2.0 µM pyrene with increasing quencher concentrations in 30 mM NaDC hydrogels, **b)** Stern-Volmer plot for 2.0 µM pyrene with increasing quencher concentrations in 30 mM NaDC hydrogels. Values reported are averages of three individual experiments and two individual experiments for I^- and CH_3NO_2 respectively. The errors are the standard deviation of three individual experiments for I^- and the average deviation of two individual experiments for CH_3NO_2. The values reported for 0 and 25 mM I^- are averages of six individual experiments and the errors are the standard deviation of six individual experiments. The dashed black line indicates the origin on the concentration axis.

From figure 3.7a it can be observed that the addition of I^- as quencher results in a sharp decrease in the I/III ratio of pyrene before becoming constant at I^- concentrations equal to or greater than 10 mM. In comparison, when the quencher is changed to a neutral molecule like CH_3NO_2, a similar decrease in the I/III ratio of pyrene is observed but unlike for I^-, the curve is not observed to flatten out and reach a constant value. However, the concentrations of the two quenchers being compared in figure 3.7 are different making the previous comparison of the I/III ratio of limited value. For this reason, the I/III ratios for pyrene being quenched by the two quenchers were investigated when the two quenchers displayed a similar degree of quenching (A_0/A).

The relative quenching of fluorescence for each quencher (A_0/A) was derived using the steady-state Stern-Volmer plots of pyrene being quenched in NaDC hydrogels (figure 3.7b). At an A_0/A value of around 1.4, the quencher concentrations correspond to 10 mM I^- and 0.5–0.7 mM CH_3NO_2. At these respective quencher concentrations, it can be observed that I^- has already

quenched all the pyrene in the hydrophilic region of the hydrogel unlike CH_3NO_2. At the highest A_0/A value of 1.6 corresponding to 1.25 mM CH_3NO_2 and 20 mM I^-, the I/III ratio for CH_3NO_2 quenching still appears to be decreasing whereas, the I/III ratio for I^- quenching has reached a constant value.

3.3.2 Time-resolved studies

The fluorescence lifetime decay of pyrene is sensitive to its microenvironment, making it possible to differentiate the number of different microenvironments that pyrene maybe localized within NaDC hydrogels. In water, pyrene displays a single exponential lifetime of 133 ns. However, when pyrene is localized within NaDC hydrogels, the decay trace for pyrene fits to a multiexponential model yielding three lifetimes, namely τ_1, τ_2 and τ_3 (figure 3.8 and table 3.3). This indicates that pyrene exists in a minimum of three different microenvironments within NaDC hydrogels. Quenching studies have shown that fluorophores localized within different environments can exhibit the same lifetime, however, have varying accessibility to the quencher. These different microenvironments have been observed by increasing the quencher concentrations where the lifetime of the more accessible fluorophore shortens greatly in comparison to the fluorophore in the less accessible microenvironment.

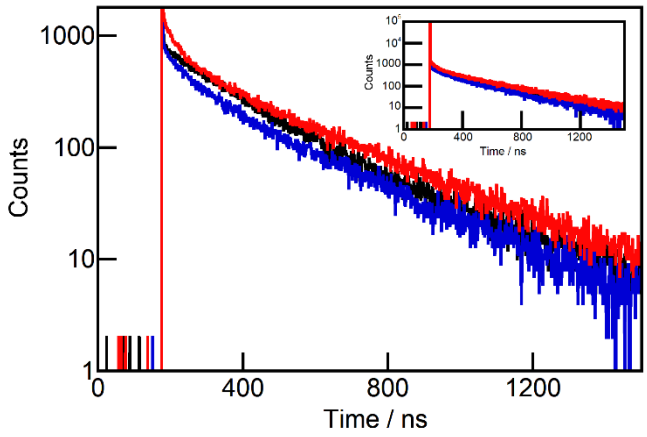

Figure 3.8: Time-resolved decay of 2.0 μM pyrene in 30 mM NaDC hydrogels with 0 mM quencher (black), 25 mM I^- (red) and 1.25 mM CH_3NO_2 (blue) without showing the initial scattering of light. Inset shows the full decay trace including the scattering of light for the decays shown in the main figure.

The shortest lifetime τ_1 is attributed to pyrene localized in the hydrophilic region of the hydrogel, where the microenvironment experienced by pyrene is similar to that in bulk water. The longest lifetime τ_3 is attributed to pyrene localized within the most hydrophobic region of the hydrogel. Moreover, the pyrene localized in this microenvironment seems to be inaccessible to the ionic quencher, I^-, as the lifetime remains unchanged with increasing quencher concentration (table 3.3 and table S3.8). However, when CH_3NO_2 is used as a quencher, this lifetime is observed to be quenched with increasing quencher concentration (table 3.3 and table S3.21). A third intermediate lifetime τ_2 is assigned to pyrene localized in an environment that is not as hydrophilic as the bulk water region of the gel nor as hydrophobic as the most hydrophobic region of the hydrogel.

Table 3.3: Lifetimes and pre-exponential factors of the singlet excited state of 2.0 μM pyrene in 30 mM NaDC hydrogels with varying quencher concentrations.[a]

A_0/A	[Q] / mM	A_1	τ_1 / ns[b]	A_2	τ_2 / ns	A_3	τ_3 / ns
				I^-			
1	0[c]	0.37 ± 0.09	133	0.3 ± 0.1	180 ± 20	0.33 ± 0.01	360 ± 20
1.2	5	0.37 ± 0.03	73.3	0.32 ± 0.05	200 ± 10	0.31 ± 0.02	378 ± 6
1.6	20	0.34 ± 0.01	31.2	0.30 ± 0.02	150 ± 10	0.36 ± 0.01	378 ± 6
				CH_3NO_2			
1	0	0.31 ± 0.01	133	0.31 ± 0.01	200 ± 10	0.38 ± 0.01	350 ± 10
1.2	0.5	0.31 ± 0.01	67.3	0.31 ± 0.01	160 ± 10	0.39 ± 0.01	320 ± 10
1.6	1.25	0.31 ± 0.01	37.8	0.31 ± 0.01	119 ± 2	0.38 ± 0.04	300 ± 10

[a], The total Na^+ concentration was kept constant at 305 mM. The values reported for I^- are averages of three individual experiments and the errors are the standard deviation for the three individual experiments. The values reported for CH_3NO_2 are averages of two individual experiments and the errors are the average deviation for the two individual experiments. [b], fixed values were obtained using equation S3.1 and S3.2. [c], average of six individual experiments and the errors are the standard deviation for the six individual experiments.

The lack of quenching of pyrene in a localized microenvironment in the time-resolved experiments is either indicative of quencher inaccessibility or that the quenching mechanism corresponds to static quenching. Therefore, to investigate the reason for the lack of quenching by I^- of the pyrene species corresponding to τ_3, Stern-Volmer plots were constructed using both steady-state and time-resolved data as shown in figure 3.9. The Stern-Volmer plots are seen to display predominantly a dynamic quenching mechanism, however, the lack of overlap between the steady-state and time-resolved Stern-Volmer plots indicates the presence of some static quenching taking place. Moreover, at I^- concentrations greater than 25 mM, static quenching becomes more predominant form of quenching taking place within NaDC hdyrogels (appendix

A3.5) The presence of this static quenching could be a result of the pyrene and the quencher being in close proximity in certain regions of the hydrogel. However, since we are interested in the mobility of the quenchers, the static mechanism of quenching provides no important insights as it has no effect on the I/III ratio of pyrene nor on the pyrene's lifetimes.

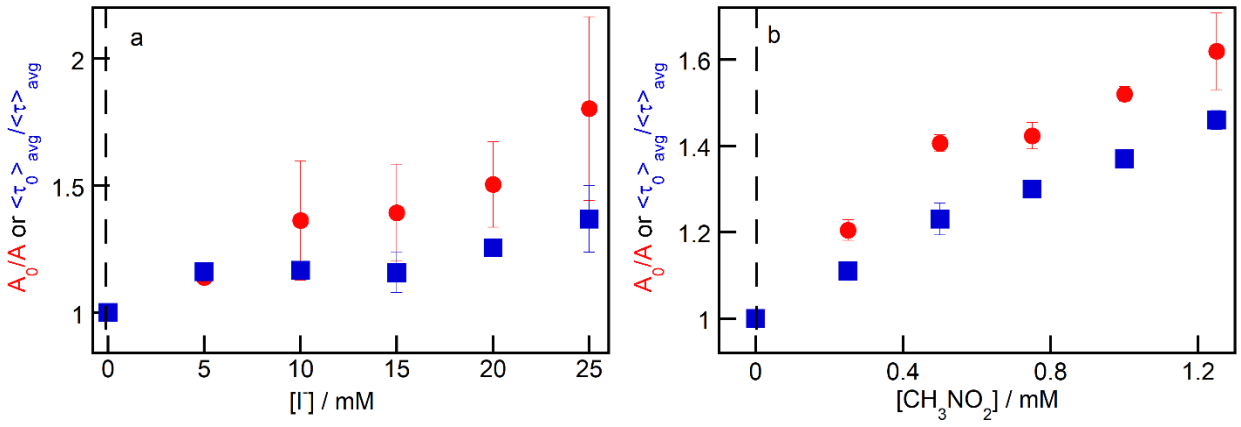

Figure 3.9: Stern-Volmer plot for 2.0 μM pyrene with increasing quencher **(A)** I^- **(B)** CH_3NO_2 concentrations in 30 mM NaDC hydrogels. The solid red circles represent the steady-state fluorescence, and the solid blue squares represent the time-resolved data. Values reported are averages of three individual experiments for I^- and two individual experiments for CH_3NO_2. The errors are the standard deviation of three individual experiments for I^- and the average deviation of two individual experiments for CH_3NO_2. The values reported for 0 and 25 mM I^- is an average of six individual experiments and the errors are the standard deviation of six individual experiments. The lifetime value for 10 mM I^- is an average of five individual experiments and the errors are the standard deviation of five individual experiments as one of the decay traces could not be fit (table S3.19). The dashed black line indicates the origin on the concentration axis.

3.4 Discussion

I^- and CH_3NO_2 behave differently as quenchers despite predominantly going through the dynamic mechanism of quenching of the pyrene molecules localized in NaDC hydrogels. In the case of I^- quenching, there exists a region within NaDC hydrogels that I^- is inaccessible to. The decrease in the I/III ratios for pyrene when the quencher concentration increases indicates that pyrene is present in multiple microenvironments, and that pyrene present in the hydrophilic regions of the hydrogel is quenched more efficiently by both the quenchers. However, as the

concentration of the two quenchers added to the hydrogel were different, to accurately compare the quenching effect of the two quenchers, the relative quenching of fluorescence was used (figure 3.10a). At A_0/A of 1.2, the I/III ratios are similar irrespective of the quencher used. As the A_0/A value increases, differences in the I/III ratio of pyrene are observed for the two quenchers. At A_0/A values greater than 1.4, the I/III ratio for I^- quenching has a lower value in comparison to the I/III ratio for CH_3NO_2 quenching in figure 3.10a. This result indicates that I^- is quenching the pyrene localized in the hydrophilic parts of the gel more efficiently in comparison to CH_3NO_2. This result also suggests that a region exists within NaDC hydrogels to which I^- is inaccessible.

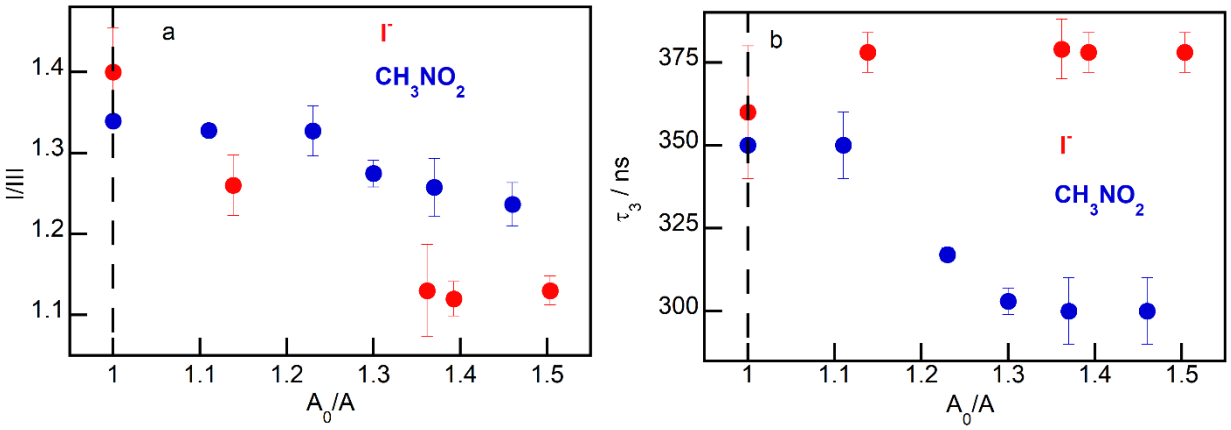

Figure 3.10: a) I/III ratio of 2.0 µM pyrene quenched by I^- and CH_3NO_2 as function of degree of quenching caused in the steady-state fluorescence (A_0/A). b) The variation of pyrene lifetime in the most hydrophobic region of the hydrogel (τ_3) quenched by I^- and CH_3NO_2 as function of degree of quenching caused in the steady-state fluorescence (A_0/A). Values reported are averages of three individual experiments and two individual experiments for I^- and CH_3NO_2 respectively. The errors are the standard deviation of three individual experiments for I^- and the average deviation of two individual experiments for CH_3NO_2. The values reported for A_0/A value of 0 for I^- is an average of six individual experiments and the errors are the standard deviation of six individual experiments. The dashed black line indicates the origin on the concentration axis.

The presence of multiple microenvironments for pyrene localization within NaDC hydrogels is confirmed by the multi-exponential decay traces obtained for pyrene through the time-resolved studies. The presence of three lifetimes indicates that there exist three distinctly

different microenvironments for pyrene to localize within NaDC hydrogels. The longer lifetime values of τ_2 and τ_3, in comparison to τ_1, is indicative of pyrene being localized within a more protective microenvironment. This lengthening in lifetime values is attributed to protection of pyrene from dissolved oxygen, observed previously for pyrene when localizing it within deoxygenated solvents, aqueous bile salt aggregates[60] and polymeric micelles.[56]

Comparing the effect of the two quenchers at similar A_0/A values, the longest lifetime (τ_3) which was assigned to pyrene in the most hydrophobic region of the hydrogel is unquenched by I^- but is quenched by CH_3NO_2 (figure 3.10b). Assuming a dynamic quenching mechanism for I^-, complexation between pyrene and I^- within a constrained microenvironment is not the dominant quenching process and the constant A_0/A values at higher concentrations (figure S3.7) confirms the inaccessibility of I^- to this hydrophobic region of the hydrogel. In comparison to I^-, CH_3NO_2 can quench all pyrene molecules with the three different lifetimes indicating that CH_3NO_2 has the ability to access pyrene in all locations within NaDC hydrogels. This lack of accessibility or protection offered to pyrene within a particular microenvironment of NaDC hydrogels to a negatively charged quencher (I^-) has been previously observed when quenching fluorophores localized within different bile salt aggregates in solution.[17-20] It was observed that the accessibility of anions to guests located in the primary binding site of bile salt aggregates was restricted in comparison to guests located in the secondary binding sites of the aggregates due to charge repulsion. This effect of charge repulsion on the accessibility of anions to guests within bile salt aggregates was further confirmed by studies done in different bile salts where the presence of taurine group in sodium taurocholate (NaTC) was shown to increase the accessibility of I^- to guests localized in NaTC aggregates compared to NaDC aggregates by reducing charge repulsion.[20] Furthermore, the quenching of pyrene by I^- and CH_3NO_2 has also been investigated

in a different bile salt, sodium cholate (NaC).[18] By increasing the Na^+ concentration, it was observed that access of pyrene to I^- was facilitated due to screening of the negative charges on the carboxylate groups of the aggregates. Concomitantly, this increase of Na^+ concentration resulted in hindered access of CH_3NO_2 to the pyrene localized in the aggregates indicating the formation of more compact aggregates.

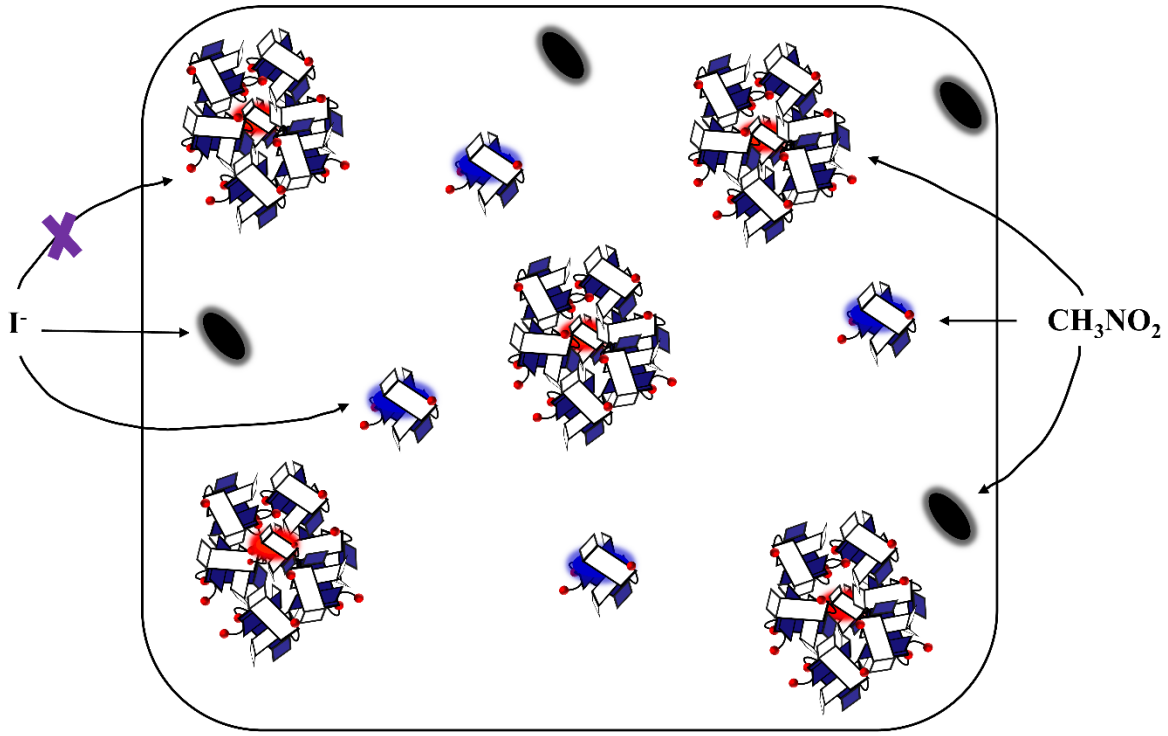

Figure 3.11: Schematic representation of the accessibility of different quenchers to pyrene localized in NaDC hydrogels (black is pyrene in the hydrophilic environment, blue corresponds to pyrene localized in sites with intermediate hydrophobicities and pyrene shown in red is localized in the most hydrophobic site of the gel.

Fluorescence correlation spectroscopy (FCS) studies in NaDC hydrogels have revealed the presence of two different types of aggregates, which can be attributed to larger immobile aggregates forming the gel microstructure and smaller aggregates diffusing in the aqueous phase.[58] The pyrene that is inaccessible to I^- (τ_3) is expected to be localized within the larger aggregates that are forming the gel microstructure. Due to the ionized nature of NaDC molecules at pH 6.5, the negative charge density in the larger aggregates forming the gel microstructure

will be much higher in comparison to the smaller aggregates. This high negative charge density causes I^- to be electrostatically repelled when trying to access pyrene localized within this charged microenvironment of NaDC hydrogels. The region where pyrene has the lifetime of τ_2 can be attributed to pyrene localized within the smaller aggregates, since these aggregates will have some access to I^- due to the lower negative charge density around them (figure 3.11). Moreover, the static quenching observed at I^- concentrations greater than 25 mM (figure S3.7) can be attributed to the compact nature of some of the aggregates in the hydrogel due to the high Na^+ concentration (305 mM), causing the pyrene and quencher to be localized in close proximity of each other within these compact aggregates.

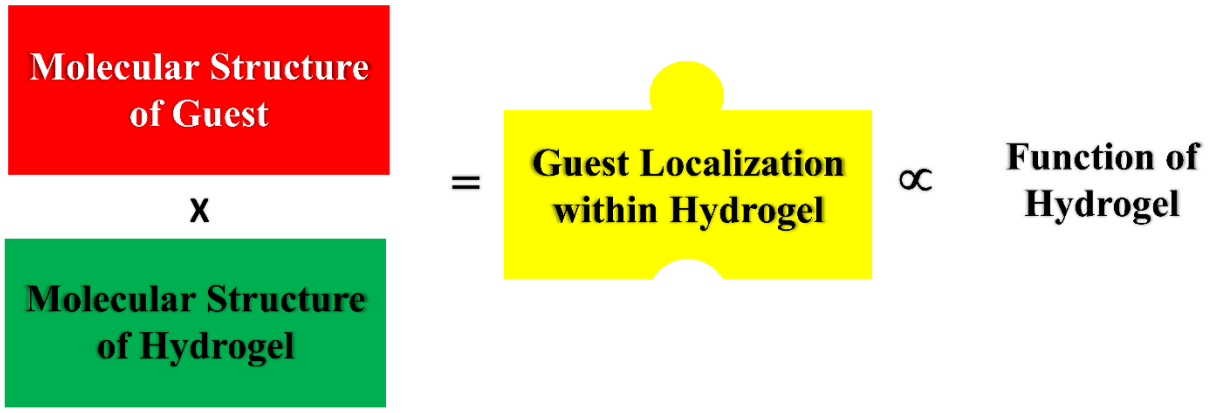

Figure 3.12: Schematic representation of how molecular structure of guest and hydrogel dictates hydrogel function.

The inability of negatively charged guests/quenchers to access certain microenvironments in NaDC hydrogels indicates that complementarity between the molecular structure of the guest and molecular structure of the hydrogel can play an important role when designing supramolecular hydrogel systems (figure 3.12). With NaDC hydrogels possessing a microenvironment that has a high negative charge density, the loading of neutral and positively charged molecules in this microenvironment will be higher than negatively charged molecules. Moreover, since the charge on the hydrogel microstructure is a function of the ionization of the

carboxylate groups of the bile salt, this loading efficiency could be further tuned by modulating the pH of the system. The change in pH could result in relocation of guests within the hydrogels, which is dependent on the guest's structure, with positively charged molecules able to access the hydrophobic regions of the gel more easily with increasing pH. This increase in accessibility of positively charged guests would be a result of the increased ionization of the carboxylic acid groups of NaDC resulting in the presence of more negatively charged gel microstructures. The pH dependent change in accessibility of guests to the various regions of the hydrogel affects the mobility of loaded guests within supramolecular hydrogel systems, resulting in the guests having different release kinetics due to the difference in their interactions with the various regions within NaDC hydrogels, which is a consequence of their localization within the hydrogels. This knowledge of guest interactions with the hydrogel dictates their localization within a heterogenous hydrogel system and could play an important role when determining the functional properties of hydrogels, such as the release kinetics of loaded guest molecules from within a hydrogel.

3.5 Conclusion

The accessibility to different microenvironments available in a supramolecular hydrogel depends on the molecular structure of the guest. This is evident from the difference in quenching behaviour seen for I^- and CH_3NO_2, despite both quenchers quenching pyrene localized in NaDC hydrogels with the same mechanism. NaDC hydrogels were seen to possess a minimum of three distinct microenvironments for the localization of pyrene. Firstly, a highly hydrophilic region (τ_1) that possesses characteristics like bulk water, where the pyrene is quenched most efficiently irrespective of the quencher used. A highly hydrophobic region (τ_3) where the pyrene is protected against quenching by a negatively charged quencher, I^-, but not a neutral quencher,

CH_3NO_2. This is because the negative charge density around this microenvironment inhibits I^- access through electrostatic repulsions. An intermediate polarity region (τ_2) is also present where pyrene is seen to localize in. The information from this work indicates that the ability of a hydrogel to adsorb and desorb guests not only depends on the molecular structure of the hydrogel but also depends on the molecular structure of the guest involved. These results shed light on the molecular structure of NaDC hydrogels, allowing for the development of functional supramolecular hydrogels using bile salts as the building block. Furthermore, the knowledge from this work also allows us to understand how the release kinetics of loaded guests from NaDC hydrogels could vary depending on the structural modifications of the guests.

3.6 References

(1) Mukhopadhyay, S.; Maitra, U. Chemistry and Biology of Bile Acids. *Current Science* **2004,** *87*, 1666–1683.
(2) Madenci, D.; Egelhaaf, S. U. Self-assembly in Aqueous Bile Salt Solutions. *Curr. Opin. Colloid Interface Sci.* **2010,** *15*, 109–115.
(3) Nair, P. P.; Kritchevsky, D.; Setchell, K. D. R. *The Bile Acids; Chemistry, Physiology, and Metabolism.*, Plenum Press: New York, 1971.
(4) Carey, M. C.; Montet, J.-C.; Small, D. M. Surface and Solution Properties of Steroid Antibiotics: 3-Acetoxylfusidic Acid, Cephalosporin P_1 and Helvolic Acid. *Biochemistry* **1975,** *14*, 4896–4905.
(5) Coello, A.; Meijide, F.; Núnez, E. R.; Tato, J. V. Aggregation Behavior of Bile Salts in Aqueous Solution. *J. Pharm. Sci.* **1996,** *85*, 9–15.
(6) Kratohvil, J. P.; DelliColli, H. T. Micellar Properties of Bile Salts. Sodium Taurodeoxycholate and Sodium Glycodeoxycholate. *Can. J. Biochem.* **1968,** *46*, 945–952.
(7) Matsuoka, K.; Moroi, Y. Micelle Formation of Sodium Deoxycholate and Sodium Ursodeoxycholate (Part 1). *Biochim. Biophys. Acta* **2002,** *1580*, 189–199.
(8) Meyerhoffer, S. M.; McGown, L. B. Critical Micelle Concentration Behavior of Sodium Taurocholate in Water. *Langmuir* **1990,** *6*, 187–191.
(9) Mukherjee, P.; Cardinal, J. Solubilization as a Method for Studying Self-association: Solubility of Naphthalene in the Bile Salt Sodium Cholate and the Complex Pattern of its Aggregation. *J. Pharm. Sci.* **1976,** *65*, 882–886.
(10) Ninomiya, R.; Matsuoka, K.; Moroi, Y. Micelle Formation of Sodium Chenodeoxycholate and Solubilization into the Micelles: Comparison with Other Unconjugated Bile Salts. *Biochim. Biophys. Acta* **2003,** *1634*, 116–125.
(11) Small, D. M.; Penkett, S. A.; Chapman, D. Studies on Simple and Mixed Bile Salt Micelles by Nuclear Magnetic Resonance Spectroscopy. *Biochim. Biophys. Acta* **1969,** *176*, 178–189.

(12) Small, D. M. The Physical Chemistry of Cholanic Acids. In *The Bile Acids; Chemistry, Physiology, and Metabolism*; Nair, P. P.; Kritchevsky, D., Eds.; Plenum Press: New York, 1971.
(13) Carey, M. C.; Small, D. M. Micellar Properties of Dihydroxy and Trihydroxy Bile Salts: Effects of Counterion and Temperature. *J. Colloid Interface Sci.* **1969,** *31*, 382–396.
(14) Carey, M. C.; Small, D. M. Micelle Formation by Bile Salts: Physical-chemical and Thermodynamic Considerations. *Arch. Intern. Med.* **1972,** *130*, 506–527.
(15) Carey, M. C.; Small, D. M. The Characteristics of Mixed Micellar Solutions with Particular Reference to Bile *Am. J. Med.* **1970,** *49*, 590–608.
(16) Weidman, T. S.; Kamel, L. Examination of the Solubilization of Drugs by Bile Salt Micelles. *J. Pharm. Sci.* **1973,** *91*, 1743–1764.
(17) Amundson, L. L.; Li, R.; Bohne, C. Effect of the Guest Size and Shape on Its Binding Dynamics with Sodium Cholate Aggregates. *Langmuir* **2008,** *24*, 8491–8500.
(18) Fuentealba, D.; Thurber, K.; Bovero, E.; Pace, T. C. S.; Bohne, C. Effect of Sodium Chloride on the Binding of Polyaromatic Hydrocarbon Guests with Sodium Cholate Aggregates. *Photochem. Photobiol. Sci.* **2011,** *10*, 1420–1430.
(19) Ju, C.; Bohne, C. Probing Bile Salt Aggregates by Fluorescence Quenching. *Photochem. Photobiol.* **1996,** *63*, 60–67.
(20) Li, R.; Carpentier, E.; Newell, E. D.; Olague, L. M.; Heafey, E.; Yihwa, C.; Bohne, C. Effect of the Structure of Bile Salt Aggregates on the Binding of Aromatic Guests and the Accessibility of Anions. *Langmuir* **2009,** *25*, 13800–13808.
(21) Sobotka, H.; Czeczowiczka, N. The Gelation of Bile Salt Solutions. *J. Colloid Sci.* **1958,** *13*, 188–191.
(22) Blow, D. M.; Rich, A. Studies on the Formation of Helical Deoxycholate Complexes. *J. Am. Chem. Soc.* **1960,** *82*, 3566–3571.
(23) Valenta, C.; Nowack, E.; Bernkop-Schnürch, A. Deoxycholate-hydrogels: Novel Drug Carrier Systems for Topical Use. *Int. J. Pharm.* **1999,** *185*, 103–111.
(24) Sun, X.; Xin, X.; Tang, N.; Guo, L.; Wang, L.; Xu, G. Manipulation of the Gel Behavior of Biological Surfactant Sodium Deoxycholate by Amino Acids *J. Phys. Chem. B* **2014,** *118*, 824–832.
(25) Jover, A.; Meijide, F.; Núñez, E. R.; Tato, J. V. Dynamic Rheology of Sodium Deoxycholate Gels. *Langmuir* **2002,** *18*, 987–991.
(26) Zhang, J.; Wang, H.; Li, X.; Song, S.; Song, A.; Hao, J. Two Gelation Mechanisms of Deoxycholate with Inorganic Additives: Hydrogen Bonding and Electrostatic Interactions. *J. Phys. Chem. B* **2016,** *120*, 6812–6818.
(27) Lakowicz, J. R. *Principle of Fluorescence Spectroscpy, 3rd Edition*, Springer: Berlin, 2006.
(28) Blatt, E.; Husain, A.; Sawyer, W. H. The Association of Acrylamide with Proteins: The Interpretation of Fluorescence Quenching Experiments. *Biochim. Biophys. Acta* **1986,** *871*, 6–13.
(29) Hannemann, F.; Bera, A. K.; Fischer, B.; Lisurek , M.; Teuchner, K.; Bernhardt, R. Unfolding and Conformational Studies on Bovine Adrenodoxin Probed by Engineered Intrinsic Tryptophan Fluorescence. *Biochemistry* **2002,** *41*, 11008–11016.
(30) Kasha, M. Collisional Perturbation of Spin-orbital Coupling and the Mechanism of Fluorescence Quenching: A Visual Demonstration of the Perturbation. *J. Chem. Phys.* **1952,** *20*, 71–74.
(31) Knibble, H.; Rehm, D.; Weller, A. Intermediates and Kinetics of Fluorescence Quenching by Electron Transfer. *Ber. Bunsenges. Phys. Chem.* **1968,** *72*, 257–263.

(32) Subczynski, W. K.; Hyde, J. S.; Kusumi, A. Oxygen Permeability of Phosphatidylcholine-cholesterol Membranes. *Proc. Natl. Acad. Sci. USA* **1989,** *86*, 4474–4478.
(33) Lakowicz, J. R. Fluorescence Spectroscopic Investigations of the Dynamic Properties of Proteins, Membranes, and Nucleic Acids. *J. Biochem. Biophys. Methods* **1980,** *2*, 90–119.
(34) Caputo, G. A.; London, E. Using a Novel Dual Fluorescence Quenching Assay for Measurement of Tryptophan Depth within Lipid Bilayers to Determine Hydrophobic α-Helix Locations within Membranes. *Biochemistry* **2003,** *42*, 3265–3274.
(35) Duan, Q.; Wang, F.; Lu, K. Recent Advances in Macrocyclic Arenes-based Fluorescent Indicator Displacement Assays. *Front. Chem.* **2022**, 7.
(36) Marini, A.; Muñoz-Losa, A.; Biancardi, A.; Mennucci, B. What is Solvatochromism? *J. Phys. Chem. B* **2010,** *114*, 17128–17135.
(37) Stepanenko, O. V.; Stepanenko, O. V.; Kuznetsova, I. M.; Verkhusha, V. V.; Turoverov, K. K. Sensitivity of Superfolder GFP to Ionic Agents. *PLoS ONE* **2014,** *9*, 1–10.
(38) Byvaltsev, V. A.; Bardonova, L. A.; Onaka, N. R.; Polkin, R. A.; Ochkal, S. V.; Shepelev, V. V.; Aliyev, M. A.; Potapov, A. A. Acridine Orange: A Review of Novel Applications for Surgical Cancer Imaging and Therapy. *Front. Oncol.* **2019,** *9*, 1–8.
(39) Tarnowski, B. I.; Spinale, F. G.; Nicholson, J. H. DAPI as a Useful Stain for Nuclear Quantitation. *Biotech. Histochem.* **1991,** *66*, 297–302.
(40) Kapuscinski, J. DAPI: A DNA-specific Fluorescent Probe. *Biotech Histochem.* **1995,** *70*, 220–233.
(41) Wu, S.-Y.; Shkolnikov, I.; Campbell, R. E. Fluorescent Indicators For Biological Imaging of Monatomic Ions. *Front. Cell Dev. Biol.* **2022,** *10*, 1–22.
(42) Miyawaki, A.; Llopis, J.; Heim, R.; McCaffery, J. M.; Adams, J. A.; Ikura, M.; Tsien, R. Y. Fluorescent Indicators for Ca^{2+}based on Green Fluorescent Proteins and Calmodulin. *Nature* **1997,** *388*, 882–887
(43) Yariv, A. *Optical Electronics in Modern Communications*, 5th ed.; Oxford University Press: New York, 1997.
(44) *Dye Lasers*. Schäfer, F. P., Ed. Springer: Berlin, 1973; Vol. 1.
(45) Randic, M. Aromaticity of Polycyclic Conjugated Hydrocarbons. *Chem. Rev.* **2003,** *103*, 3449–3605.
(46) Becker, R. S.; Singh, I. S.; Jackson, E. A. Comprehensive Spectroscopic Investigation of Polynuclear Aromatic Hydrocarbons. I. Absorption Spectra and State Assignments for the Tetracyclic Hydrocarbons and their Alkyl-substituted Derivatives. *J. Chem. Phys.* **1963,** *38*, 2144–2171.
(47) Tanaka, J. The Electronic Spectra of Pyrene, Chrysene, Azulene, Coronene and Tetracene Crystals. *Bull. Chem. Soc. Jpn.* **1965,** *38*, 86–102.
(48) Mangle, E. A.; Topp, M. R. Excited-state Dynamics of Jet-cooled Pyrene and Some Molecular Complexes. *J. Phys. Chem.* **1986,** *90*, 802–807.
(49) Nakajima, A. Fluorescence Spectra of Pyrene in Chlorinated Aromatic Solvents. *J. Lumin.* **1976,** *11*, 429–432.
(50) Kalyanasundaram, K.; Thomas, J. K. Environmental Effects on Vibronic Band Intensities in Pyrene Monomer Fluorescence and their Application in Studies of Micellar Systems. *J. Am. Chem. Soc.* **1977,** *99*, 2039–2044.
(51) Nakajima, A. Fluorescence Lifetime of Pyrene in Different Solvents. *Bull. Chem. Soc. Jpn.* **1973,** *46*, 2602–2604.

(52) Kim, D.; Amos, R.; Gauthier, M.; Duhamel, J. Applications of Pyrene Fluorescence to the Characterization of Hydrophobically Modified Starch Nanoparticles. *Langmuir* **2018,** *34*, 8611–8621.
(53) Bains, G.; Patel, A. B.; Narayanaswami, V. Pyrene: A Probe to Study Protein Conformation and Conformational Changes. *Molecules* **2011,** *16*, 7909–7935.
(54) Boyland, E.; Green, B. The Interaction of Polycyclic Hydrocarbons and Nucleic Acids. *Br. J. Cancer* **1962,** *16*, 507–517.
(55) Sahoo, D.; Narayanaswami, V.; Kay, C. M.; Ryan, R. O. Pyrene Excimer Fluorescence: A Spatially Sensitive Probe To Monitor Lipid-induced Helical Rearrangement of Apolipophorin III. *Biochemistry* **2000,** *39*, 6594–6601.
(56) Geiger, M. W.; Turro, N. J. Pyrene Fluorescence Lifetime as a Probe for Oxygen Penentration of Micelles. *Photochem. Photobiol.* **1975,** *22*, 273–276.
(57) Izatt, R. M.; Bradshaw, J. S.; Pawlak, K.; Bruening, R. L.; Tarbet, B. J. Thermodynamic and Kinetic Data for Macrocycle Interaction with Neutral Molecules. *Chem. Rev.* **1992,** *92*, 1261–1354.
(58) Seyedalikhani, M. Exploring the Binding of Small Guest Molecules in Sodium Deoxycholate Hydrogels. PhD University of Victoria, 2016. http://hdl.handle.net/1828/7615
(59) Sillen, A.; Engelborghs, Y. The Correct Use of "Average" Fluorescence Parameters. *Photochem. Photobiol.* **1998,** *67*, 475–486.
(60) Zana, R.; Guveli, D. Fluorescence Probing Study of the Association of Bile Salts in Aqueous Solutions. *J. Phys. Chem.* **1985,** *89*, 1687–1690.

Chapter 4: Molecular Interactions of Cucurbit[6]uril: A Tool for Controlling Function within Sodium Deoxycholate Hydrogels

4.1 Introduction

Significant work has been done in the field of supramolecular gels to develop structure property relationships to gain a better understanding on how the chemical structure of the gelator can be manipulated to control the properties of gels. Detailed structure property relationships are being developed for different classes of low molecular weight gels (LWMGs) such as metallogels,[1] sugars,[2] peptides,[3-4] dendritic systems,[5] and nucleobases[6-7] and the development of these structure property relationships will allow us to better control the function of LMWG hydrogel systems, through manipulation of the LMWG's chemical structure. An alternate approach to designing gels with desired properties is through the use of multi component gel systems.[8]

4.1.1 Effect of additives in gels

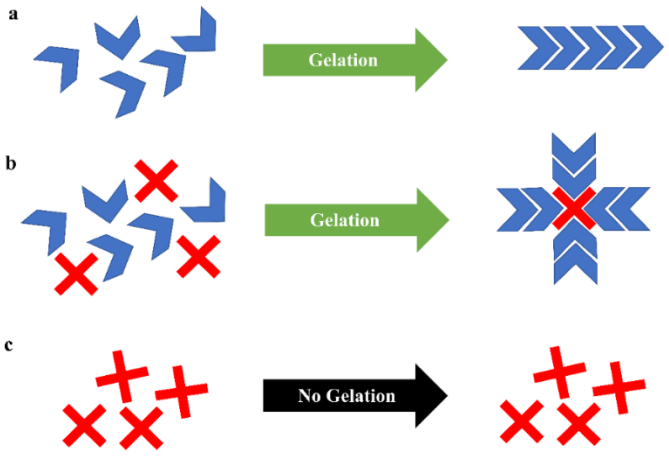

Scheme 4.1: Schematic representation of the gelation process for a) only gelator (blue), b) gelator and additive (red) and c) only additive.

The multi component strategy involves altering the ratio of the different components used to obtain tailor-made gels. This strategy involves the addition of a non-gelating compound

known as additive to a gelating medium. The additive is incapable of undergoing gelation in absence of the gelator (scheme 4.1). The addition of the additive results in changes in the thermochemical and functional properties of the gel, such as mechanical strength, stability, and rigidity of the gel, by impacting the self-assembly process of the gelator.[8-9] For example, Fuhrhop and coworkers demonstrated the improved stability of N-octyl-D-gluconamide gels using non-gellating additives.[10-11] N-octyl-D-gluconamide gels tend to undergo crystallization within a few hours. However, the incorporation of phosphotungstic acid (PTA) and sodium dodecylsulfate (SDS) enhanced the short-term and long-term stability of these gels, with the stabilization effect from SDS lasting for at least 5 months. The SDS micelles are hypothesized to solubilize any N-octyl-D-gluconamide crystal nuclei before macroscale crystallization can occur. Shirai and coworkers also showed improved mechanical strength in gels made from valine derivatives through the addition of polymers to the gelators.[12]

4.1.2 Additives in NaDC gels

In a similar way, additives have also been added to sodium deoxycholate (NaDC) hydrogels to modulate their functional properties. Use of halide salts like sodium chloride (NaCl) and sodium bromide (NaBr) have been shown to lead to formation of stiffer gels, with thicker fibers in the gel network.[13-14] The addition of NaCl has also been shown to improve the mechanical strength of NaDC hydrogels in absence of pH modulation.[15] Moreover, lanthanide salts were incorporated within NaDC hydrogels to obtain photoluminescent hydrogels with improved mechanical strength.[16] Apart from salts, graphene oxide was added to NaDC hydrogels, improving their mechanical strength by providing more hydrogen bonding sites in the gel network.[17] Tris(hydroxymethyl)aminomethane (TRIS) was used to induce gelation in NaDC at pH values above the pK_a of NaDC.[18-19] In these studies, the properties of NaDC hydrogels

were investigated as a function of pH and TRIS concentration. Changes in pH and TRIS concentration led to changes in the sol to gel transition temperatures and mechanical strength, because of changes in the crystallinity and structural rigidity of the gels. Polymers are another type of additive that have been used to improve the mechanical strength of NaDC hydrogels.[20] The addition of a linear polymer, poly(2-(2-methoxyethoxy)ethyl methacrylate-co-oligo-(ethylene glycol) methacrylate) to NaDC/Aspartine hydrogels showed a two-fold increase in their mechanical strength, whereas a 60-fold increase in mechanical strength was observed on the addition of a star shaped polymer, poly(2-(dimethylamino)ethyl methacrylate-b-2-(2-methoxyethoxy)ethyl methacrylate).

4.1.1 Cucurbiturils (CB[n]) as additives in gels

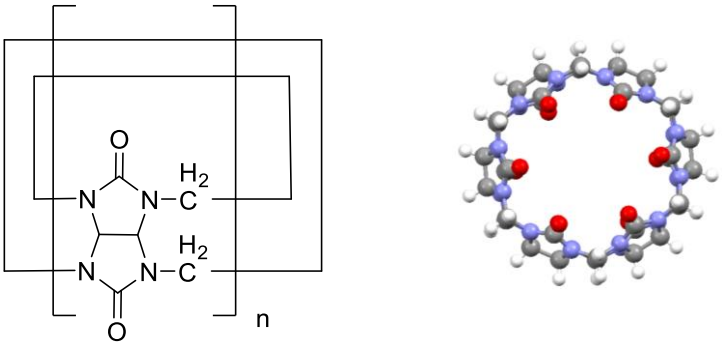

Chart 4.1: Molecular structure of CB[n] (left) and chemical structure of CB[6] (right).

Macrocycles are a new class of additives used to modulate the functional properties of supramolecular hydrogels.[21] Macrocycles exhibit distinct host-guest chemistry, due to their reversible binding of guest molecules. This nature of macrocyclic host-guest interactions allows them to serve different purposes depending on the desired outcome when used as additives in supramolecular gel systems. Macrocycles can act as scaffolds to direct binding sites into suitable positions to facilitate gelation.[9] Non-covalent macrocycle-guest interactions between the macrocycle and the gelator molecules can be manipulated to build the gel network through direct

incorporation of the macrocycles in the construction of the gel network.[9] In these scenarios, the macrocycle can serve as a tool for stimuli control. Lastly, they can be covalently attached to gelator molecules, wherein they do not take part in gelation process but act as binding sites for other guests such as drugs, cells, and ions.[9]

Cavitands are macrocyclic hosts with enforced cavities.[22] These cavities can act as binding sites for guests based on the complementarity between the cavity and the guest shape or size. Cucurbit[n]urils (CB[n]) are a class of cavitands composed of glycoluril subunits, where the 'n' (n = 5–8, 10 or 14) specifies the number of glycoluril units present (chart 4.1).[23-24] CB[n]s possess a cavity to accommodate hydrophobic hosts, whereas the portals at the interface can accommodate cationic guests, due to the negative charge density offered by the carbonyl groups. These aspects of CB[n]s coupled with their non-toxic nature have been extensively utilised by researchers to develop various supramolecular systems like rotaxanes and polymer-based gels.[25-28]

Gel formation by utilizing the unique host-guest interactions of CB[n]s is primarily achieved by covalently attaching a single guest or two different guests on the polymer. The addition of CB[n] results in complexation wherein the CB[n] encapsulates two molecules, establishing crosslinks which promote gel formation. The large cavity size of CB[8] has been extensively exploited to generate gels through this complexation methodology.[29-30] For example, Sherman and coworkers have used CB[8] to obtain cellulose-polyvinyl alcohol (PVA) gels by covalently crosslinking methyl viologen (MV) onto the PVA and a naphthyl (Np) moiety onto the cellulose.[31] In presence of CB[8], the MV and Np moieties are complexed within the CB[8] cavity resulting in gel formation. A similar strategy has been exploited by Tan and coworkers to obtain poly(*N*-(4-vinylbenzyl)-4,4′-bipyridinium dichloride-*co*-acrylamide) (P4VBAM) gels,

wherein MV was covalently attached to the polymer strands.[32] By adjusting the pH of the system, gelation is induced due to complexation of two MV moieties within the CB[8] cavity.

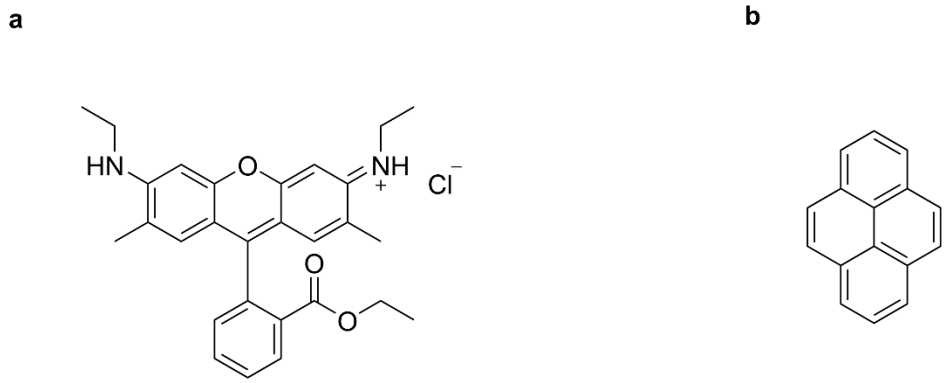

Chart 4.2: Molecular structure of (a) rhodamine 6G and (b) pyrene.

Apart from CB[8], other CB[n]s have also been explored for gelation purposes. Kim and coworkers have seen that CB[7] undergoes gelation in presence of dilute mineral acids at extremely low pH values between 0 and 2.[33] CB[6] has also been investigated to form gels with 1-aminium 4-methylbenzenesulphonate (BAMB) through the formation of CB[6]-BAMB pseudo rotaxane.[34] Kim and workers have also used the CB[6] host-guest interactions with polyamine conjugated hyaluronic acids to form a CB[6] based supramolecular gel for cellular engineering applications.[35]

4.1.2 Objectives

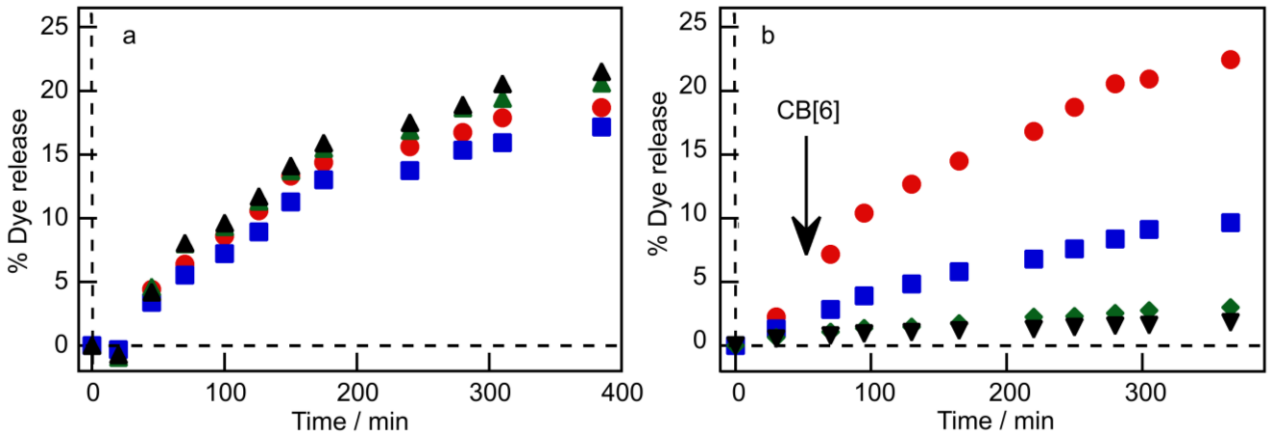

Figure 4.1: Release profile of fluorophores from NaDC gels (50 mM) with different CB[6]/NaDC ratios: 0 (red), 0.05 (blue), 0.1 (green), 0.15 (black). **a)** R6G **b)** pyrene. The dashed black line indicates the origin on the x- and y-axes. Modified and reproduced with permission from ref 37.

Recent work in our group has explored the role of CB[6] as an additive in sodium deoxycholate (NaDC) hydrogels.[36-37] Rheological experiments showed an increase in mechanical strength and an increase in the sol-gel transition temperature of the hydrogels when CB[6] is added. These functional changes to NaDC hydrogels on the addition of CB[6] were attributed to the increased hydrogen bonding between the gelator aggregates and carbonyl groups of the CB[6]. These interactions have been validated through confocal laser scanning microscopy (CLSM) studies. In these studies, the addition of CB[6] induced changes to the gel microstructure, where spherical microstructures of NaDC hydrogels changed to fibre shaped microstructures on addition of CB[6].[37] Steady-state and time-resolved fluorescence experiments were used to gather molecular level information of the NaDC-CB[6] system. Temperature dependent steady-state and time-resolved fluorescence experiments were used to gather molecular level information of the NaDC-CB[6], where relocation of pyrene between the aqueous phase of the gel and the gel microstructures was observed.[36] Dialysis studies on NaDC

hydrogels were conducted to investigate the release kinetics of the guests as a function of CB6] concentration.[37] The release kinetics of a cationic guest, rhodamine 6G (R6G), was observed to be independent of CB[6] concentration, whereas, for a neutral guest, pyrene, the release kinetics were seen to vary with different CB[6] concentrations (figure 4.1). The limited information on the molecular interactions of the respective guests (R6G, pyrene) with NaDC-CB[6] hydrogels, limited our understanding of the differences in the release kinetic of the guests, as a function of CB[6] concentration. The current investigation aims to correlate the changes occurring at the macroscopic level (change/no change in release kinetics) to the differences in the interaction of a guest (pyrene) with NaDC-CB[6] hydrogels at the molecular level.

4.2 Experimental

4.2.1 Materials

NaDC (Fluka, ≥ 98%), nitromethane (CH_3NO_2, Sigma-Aldrich, ≥ 98.5%), disodium phosphate (Na_2HPO_4) (Anachemia, anhydrous, ≥ 99%), monosodium phosphate ($NaH_2PO_4 \bullet H_2O$) (Anachemia, ≥ 99) and methanol (Fisher, spectral grade, ≥ 99.9%) were used as received. Pyrene (Sigma, ≥ 99%) was recrystallized from ethanol twice to obtain a white solid. CB[6] (CB[6]-AA-1) was synthesized and purified by me through modification of reported literature procedures (appendix A4.1 and A4.2). The purity (88%) was established spectroscopically using NMR, ESI-MS and steady-state fluorescence (appendix A4.3). Deionized water (Barnstead NANOpure deionizing systems, 17.8 MΩ cm) was used for the preparation of all solutions.

4.2.2 Sample Preparation

NaDC (416 mg) was dissolved in 5.0 mL of deionized water to obtain 0.2 M stock solution. Pyrene (2.5 mg) was dissolved in 10.0 mL of methanol to obtain 1.2 mM stock of

pyrene. $NaH_2PO_4•H_2O$ (345.6 mg) in 5.0 mL of deionized water and Na_2HPO_4 (356.3 mg) in 5.0 mL of water were dissolved to obtain 0.5 M solutions of each respectively. The stock solutions of Na_2HPO_4 and $NaH_2PO_4•H_2O$ were mixed in equal volumes to obtain 0.5 M buffer with pH = 6.50 ± 0.01 at 21 ºC. A CH_3NO_2 in water stock solution was used for all experiments. This stock solution was prepared by taking 110 µL of stock CH_3NO_2 in 2 mL of water to obtain a 1 M CH_3NO_2 in water solution. This 1 M CH_3NO_2 in water was diluted with water to obtain a 50 mM CH_3NO_2 stock solution used during the experiments. NaCl (116.8 mg) was dissolved in 2.0 mL to obtain a 1 M stock solution of NaCl.

Preparation of NaDC-CB[6] hydrogels: In sample vial, 6.8 mg of CB[6] was taken and to it was added 200 µL of buffer and required volume of deionized water to achieve a constant final volume. The volume of deionized water was adjusted to account for the addition of the quencher to the solution (table 4.1). For example, if 0 µL of quencher is added, then 1250 µL of water was added to keep the final volume as 2000 µL, whereas if 50 µL of quencher is added the volume of water added is adjusted to 1200 µL. The CB[6]-buffer-water solution was heated for 15 min at 60 ºC. After 15 min, 2.5 µL of pyrene stock, 300 µL of 0.2 M NaDC solution and 250 µL of 1M NaCl were added. This solution was heated at 60 ºC for 15 min, after which the hot solution was transferred to a triangular cell and allowed to set for 20 h before measurements. The NaDC concentration was 30 mM and the CB[6] concentration was 3 mM within the hydrogels. The total Na^+ concentration was kept constant at 305 mM in all samples. The pyrene concentration in the samples was 2.0 µM.

Table 4.1: Preparation of NaDC-CB[6] hydrogel samples with varying CH_3NO_2 concentrations.

CH_3NO_2 (mM)	**Wt. of CB[6] added (mg)**	**Vol. of water (µL)**	**Vol. of NaDC (µL)**	**Vol. of buffer (µL)**	**Vol. of 1 M CH_3NO_2 (µL)**	**Vol. of 1 M NaCl (µL)**	**Total Vol. (µL)**
0	6.8	1250	300	200	0	250	2000
0.25	6.8	1240	300	200	10	250	2000
0.50	6.8	1230	300	200	20	250	2000
0.75	6.8	1220	300	200	30	250	2000
1.00	6.8	1210	300	200	40	250	2000
1.25	6.8	1200	300	200	50	250	2000
1.50	6.8	1190	300	200	60	250	2000
2.00	6.8	1170	300	200	80	250	2000
2.50	6.8	1150	300	200	100	250	2000
3.00	6.8	1130	300	200	120	250	2000

4.2.3 Instrumentation

Gel samples: Steady-state emission studies were carried out using triangular cells on a PTI QM-40 spectrofluorometer. All samples were excited at 330 nm with slit bandwidths of 1.0 nm for both excitation and emission monochromators and a 0.5 nm step count with 0.25 s averaging time. To account for scattering or residual emission from the gels, blanks were collected using 30 mM NaDC in water. The blanks were recorded in each cell (2–7), and the blank corresponding to that cell was used for subtraction, i.e., blank collected in cell 2 was subtracted from spectra of sample in cell 2, blank in cell 3 from spectra of sample in cell 3 and so on. Emission spectra were

integrated from 382 nm to 398 nm for pyrene to obtain the total integrated peak area. Single photon counting experiments were done using an Edinburgh Instruments Ltd OB920 setup. For samples containing pyrene, a 335 nm nanoLED was used to excite all the samples and the emission decays were collected at 390 nm. All decays were collected up to 100000 peak counts. The fits to the decay were done using the FAST software from Edinburgh Instruments Ltd. Due to scattering, fitting of the traces was started 4–10 channels after the peak to remove the contribution from scattering using the tail fit method. The decays were fit to a distribution analysis using the maximum entropy method (MEM) proposed by Ware and coworkers.[38-39] The use of this method was required because the analysis used previously where the data were fit to a sum of exponentials was unable to deconvolute the number of lifetimes for the emission of pyrene in NaDC hydrogels containing 3 mM CB[6]. During the analysis, the lifetimes were fit between 20–600 ns, using 200 intervals. These settings were kept constant for all the decay traces analyzed. To obtain the *A* values for the *ith* time point, equation 4.1 was used.

$$A_i = \frac{Counts_i}{\sum Counts_i}, \ \sum A_i = 1$$

(Eq. 4.1)

Solution samples: Single photon counting experiments were done on an Edinburgh Instruments Ltd OB920 setup using a 335 nm EPLED to excite all the samples. The emission decays were collected at 390 nm up to 2000 peak counts. During the collection, the polarizer on the excitation side was kept constant at a vertical configuration (0°) and on the emission side at the magic angle configuration (55°) was used to eliminate anisotropic effects. The fits to the decays were done using the FAST software from Edinburgh Instruments Ltd. Due to scattering, fitting of the traces was started 4–10 channels after the peak to remove the contribution from scattering using the tail

fit method. The decays were fit to a distribution analysis using MEM and equation 4.1 was used to obtain the *A* values for the *ith* time point. The decays were also fit to a sum of exponentials using equation 4.2 to obtain quantitative values for the lifetimes.

$$I(t) = I(0)\sum_{i=1}^{n} a_i\, e^{-\frac{t}{\tau_i}}, \quad \sum a_i = 1$$

(Eq. 4.2)

4.3 Results

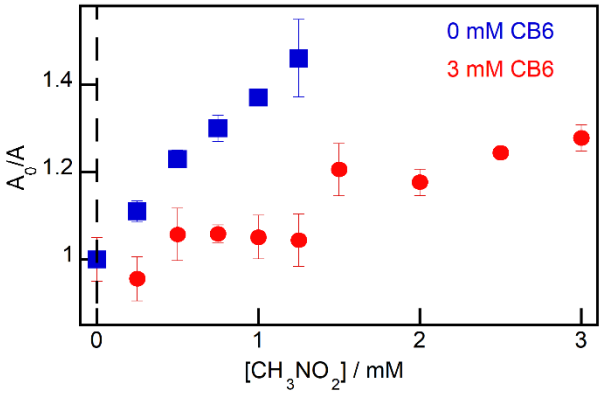

Figure 4.2: Steady-state Stern-Volmer plots for 2.0 μM pyrene using CH_3NO_2 as a quencher in 30 mM NaDC hydrogels in absence (blue) and presence of 3 mM CB[6] (red). The values reported for NaDC hydrogels are averages of two individual experiments and the errors are the average deviation of the two individual experiments. The values reported for NaDC-CB[6] hydrogels are average of three individual experiments and the errors are the standard deviation of the three individual experiments. The dashed black line indicates the origin on the concentration axis.

The access of CH_3NO_2 to excited-state pyrene within NaDC hydrogels varies on addition of CB[6] to the gels. It is observed that in the presence of CB[6], CH_3NO_2 has reduced access to the pyrene localized within NaDC hydrogels, seen by the lower A_0/A values at similar quencher concentrations. Moreover, even at high quencher concentrations (≥ 2.5 mM), the A_0/A values for pyrene quenched by CH_3NO_2 in NaDC-CB[6] hydrogels never reached the A_0/A values observed for pyrene quenching in NaDC hydrogels in absence of CB[6].

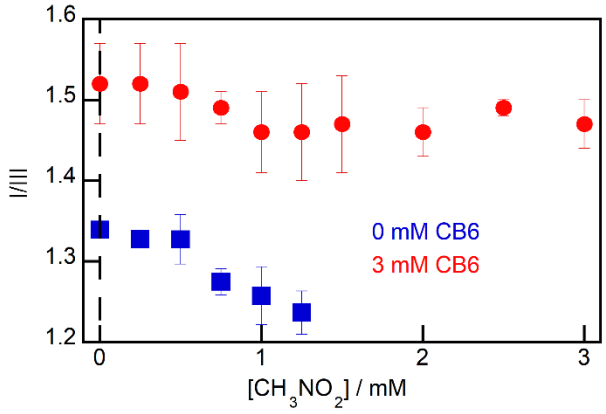

Figure 4.3: I/III ratios for 2.0 µM pyrene with increasing CH_3NO_2 concentrations in 30 mM NaDC hydrogels in absence (blue) and presence of 3 mM CB[6] (red). The values reported for NaDC hydrogels are averages of two individual experiments and the errors are the average deviation of the two individual experiments. The values reported for NaDC-CB[6] hydrogels are averages of three individual experiments and the errors are the standard deviation of the three individual experiments. The dashed black line indicates the origin on the concentration axis.

As discussed previously, the I/III ratio of pyrene's steady-state emission spectra is extensively used to characterise the polarity of the average microenvironment pyrene is localised in.[40] In NaDC hydrogels, it is observed that pyrene has a I/III ratio of around 1.35 ± 0.01. This I/III ratio is seen to decrease with increasing CH_3NO_2 concentration indicating that a higher degree of quenching occurs to the pyrene localized in the hydrophilic regions of the gel. However, when CB[6] is added to NaDC hydrogels, the I/III ratio increases to 1.52 ± 0.05, indicating the relocation of pyrene to a relatively more hydrophilic environment. Moreover, this I/III ratio is seen to not change with increasing CH_3NO_2 concentration, despite the relatively higher quencher concentrations used (I/III at highest concentration is 1.47 ± 0.03), indicating that pyrene is in a more protected microenvironment when CB[6] is present and possibly in a more homogenous microenvironment within the hydrogel.

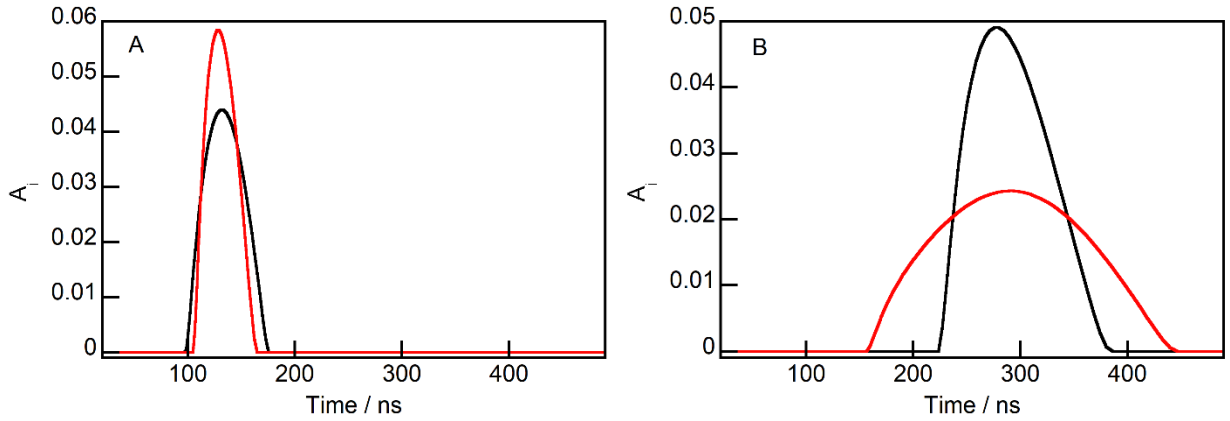

Figure 4.4: Lifetime distribution curves for 2.0 μM pyrene in 50 mM phosphate buffer, pH = 6.50 ± 0.01 in (A) absence and (B) presence of 3 mM CB[6] Each distribution curve corresponds to an individual experiment.

To elucidate the effect of CB[6] addition on the homogeneity of pyrene localization within the NaDC hydrogels, time-resolved studies were carried out. Typically, the decay traces obtained via time-resolved experiments are fit to a sum of exponentials (equation 4.2) to generate lifetime values. The number of different lifetimes obtained are an indication of the number of different microenvironments pyrene experiences within the hydrogel. However, on addition of CB[6] to NaDC hydrogels, the decay traces obtained are unable to yield lifetimes through the fitting of the decays using the sum of exponential analysis. For this purpose, the MEM analysis was employed to obtain lifetime distribution curves for pyrene which can provide information on the heterogeneity experienced by pyrene within NaDC hydrogels in absence and presence of 3 mM CB[6].

Table 4.2: Lifetime analysis for 0.5 μM pyrene in buffer obtained via the maximum entropy method and sum of exponentials fitting procedures.[a]

CB[6] / mM	τ_{MEM} / ns[b]	FWHM / ns[b]	τ / ns[c]
0	130 ± 1	44 ± 7	133 ± 1
3	283 ± 7	150 ± 50	290 ± 1

[a]values reported are the average of two individual experiments and the errors are the average deviation between the two individual experiments, [b]obtained through MEM, [c]obtained from the fit to a sum of exponentials.

Before analyzing the data for pyrene in NaDC hydrogels, the validity of the MEM was established by analyzing the fluorescence decays of pyrene in buffer and in presence of CB[6]. The distribution curve obtained for pyrene in buffer is narrow, quantified by the full-width half maxima (FWHM). The peak is observed to be centered around 130 ns, which is in agreement with the reported lifetime for pyrene in solution.[41-42] Moreover, this peak maximum of 130 ns obtained from the distribution curves was also seen to coincide with the lifetime value obtained through the sum of exponential fitting (τ = 133 ns) procedure showing the validity of the method (table 4.2).

The addition of CB[6] to pyrene in buffer results in a broadening of the lifetime distribution curve, with the FWHM increasing from 44 ns in buffer to 150 ns in presence of 3 mM CB[6]. The peak maxima obtained through the MEM (283 ns) and the lifetime obtained from the sum of exponential analysis (290 ns) are in good agreement. However, the distribution curves can be seen to be different between two individual experiments in presence of CB[6] indicated by the large error on the FWHM. This broad distribution and the high error on the FWHM is consistent with a high and inherent heterogeneity experienced by pyrene to CB[6] in buffer solutions, leading to different singlet excited-state pyrene lifetimes.

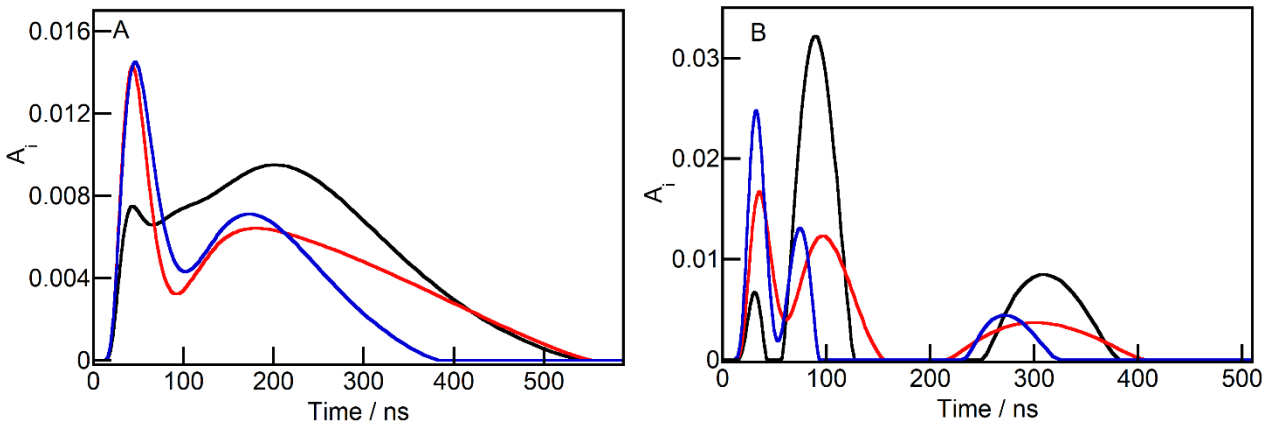

Figure 4.5: Lifetime distribution curves for 2.0 μM pyrene in 30 mM NaDC hydrogels containing (A) 0 mM and (B) 1.25 mM CH_3NO_2. Each distribution curve with a different color corresponds to an individual experiment.

The application of the MEM analysis to the fluorescence decays of pyrene localized in NaDC gels containing no CB[6] results in a broad distribution curve in absence of any quencher (figure 4.5A), which displays the heterogeneity experienced by pyrene within NaDC hydrogels. On increasing the quencher concentration, the broad distribution curve is seen to resolve into three separated peaks corresponding to the three different microenvironments for pyrene within NaDC hydrogels (figure 4.5B and appendix A4.4).

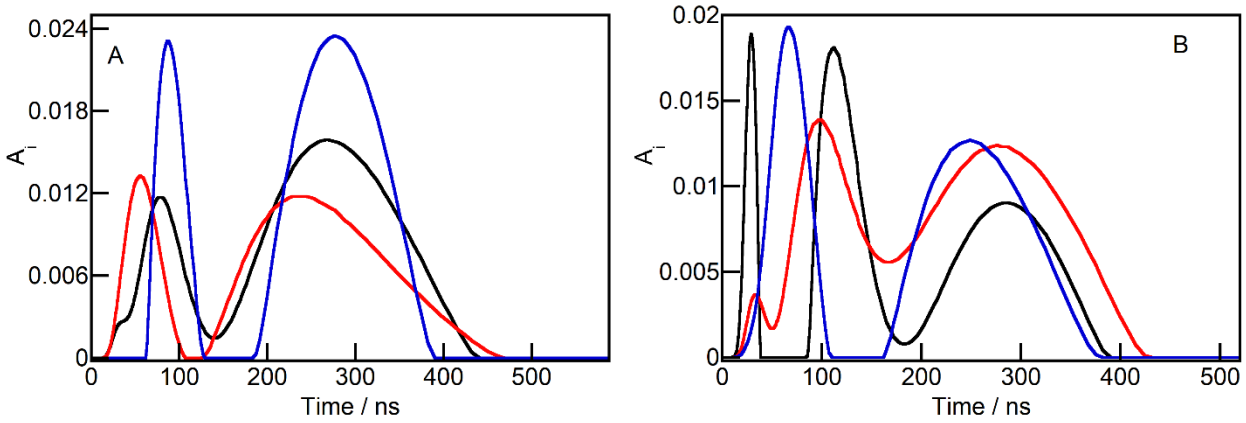

Figure 4.6: Lifetime distribution curves for 2.0 μM pyrene in 30 mM NaDC hydrogels in presence of 3 mM CB[6] containing (A) 0 mM and (B) 1.25 mM CH_3NO_2. Each distribution curve with a different color corresponds to an individual experiment.

On addition of CB[6], the lifetime distribution curve for pyrene in NaDC hydrogels maintains a similar broad shape in absence of any quencher and the distribution curve again is seen to resolve into three peaks with increasing quencher concentration (appendix A4.5). However, unlike in figure 4.5B, the peaks observed in figure 4.6B are not as well separated and overlap, indicating an enhancement of the heterogeneity experienced by pyrene within NaDC hydrogels with the addition of CB[6].

4.4 Discussion

Traditionally, the lifetimes of fluorophores are analyzed through the sum of exponentials method. However, as has been observed, the sum of exponentials works well if the fluorophore experiences discrete and relatively homogenous environments in the excited state. For systems where a fluorophore may experience high heterogeneity in its microenvironment, the MEM offers a suitable alternative. The suitability of the MEM was established by exciting pyrene in solution, in absence and presence of CB[6], and then applying both the sum of exponentials and MEM analysis to obtain information on the pyrene lifetimes. The narrow distribution curve with low error for the FWHM between the two individual experiments shows the reproducibility of

the MEM analysis in homogenous systems. Moreover, the lifetimes obtained via the MEM analysis and sum of exponential fitting procedures are in good agreement, indicated by the residuals from the two different fitting procedures being indistinguishable (figure S4.11–S4.12). On addition of CB[6], the distribution curves are seen to be broader, with a high error for the FWHM (figure 4.4B). This result, despite the lifetime values agreeing between the two different analysis methods (table 4.2), along with the indistinguishable residuals (figure S4.13–S4.14), indicates the failure of the sum of exponential analysis to properly reflect the heterogeneity of these systems. These results also indicate the inherent heterogeneity experienced for the binding of pyrene to CB[6], since more than one excited-state lifetime for pyrene is observed which indicates different binding modes of pyrene to CB[6]. These different binding modes of pyrene to CB[6] are a result of the weak binding of pyrene to CB[6] (K = (3.1±0.9) × 10^2 M^{-1} at 288K in 55% HCOOH (w/v) and 1% MeOH (v/v)), reported to proceed via a 1:1 complex formation and promoted by hydrophobic entropic factors and the size of pyrene preventing it from entering the CB[6] cavity. These factors cause the pyrene to interact either with the exterior wall of the CB[6] or form a partial inclusion/suspended complex when interacting to CB[6].[43]

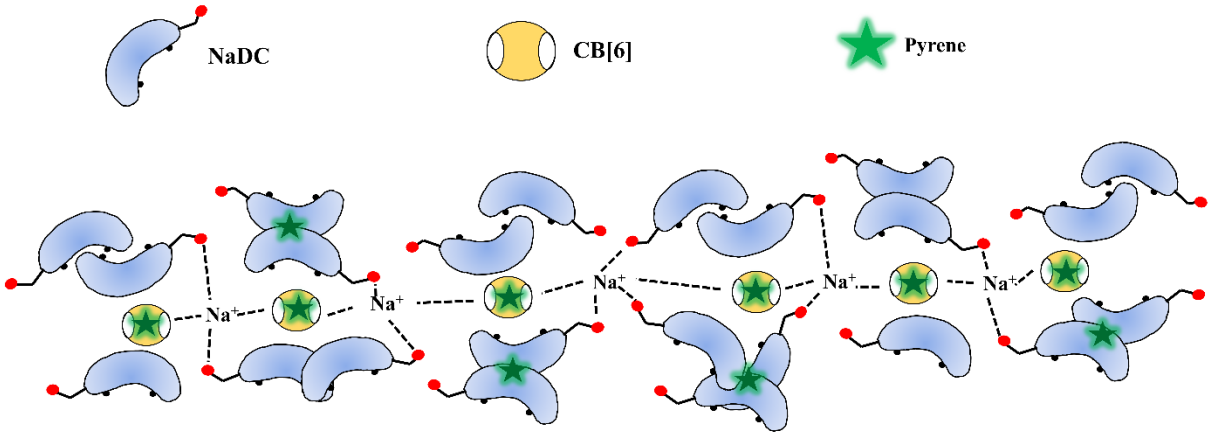

Scheme 4.2: Molecular picture of the fibre like NaDC-CB[6] hydrogels containing pyrene. The pyrene is bound to the exterior wall of the CB[6] as it is too big to go inside the cavity.

The requirement of a detailed and extensive methodology to obtain the three lifetimes for pyrene in NaDC gels in chapter 3 hints towards an inherent heterogeneity being experienced by pyrene in NaDC gels. These observations are confirmed when looking at the broad lifetime distribution curves obtained using the MEM analysis in absence of any quencher (figure 4.5A). On addition of quencher, the three microenvironments observed in chapter 3 are seen to resolve into their respective lifetime peaks, well separated from each other and centered around the expected lifetime values observed previously. The addition of CB[6] results in a less broad distribution curve in absence of quencher, indicating the relocation of pyrene from the hydrophilic region of the hydrogel to the hydrophobic region of the hydrogel. This relocation is supported by the change in the gel structure of NaDC hydrogels, going from spherical shapes of different sizes in absence of CB[6] to a fibrillar shape in presence of CB[6], suggested to happen due to the incorporation of the smaller NaDC aggregates in the aqueous phase being incorporated into the gel network.[37] However, the presence of overlapping peaks in the lifetime distribution of pyrene lifetimes in NaDC-CB[6] hydrogels indicate an increased heterogeneity in pyrene microenvironments in comparison to the microenvironments experienced by pyrene in NaDC hydrogels. This is reasonable since time-resolved information is more sensitive to the micro-

polarity of the fluorophore's environment than steady-state studies. A broad lifetime distribution curve is characteristic of the formation of pyrene-CB[6] complexes in solution as seen in figure 4.4B. The presence of this pyrene-CB[6] complex within both the gel network and the aqueous phase of NaDC gels amplifies the heterogeneity for the microenvironments around pyrene, resulting in the broad lifetime distribution curve with overlapping peaks, when 1.25 mM of CH_3NO_2 is added to pyrene localized within NaDC-CB[6] hydrogels. Moreover, the independence of the I/III ratio of pyrene steady-state emission to quencher concentration in NaDC-CB[6] hydrogels and the reduced A_0/A values for pyrene at similar quencher concentrations for NaDC-CB[6] hydrogels in comparison to NaDC hydrogels also indicates a relocation of pyrene to a more protected microenvironment within the hydrogel. The I/III ratio observed for pyrene in NaDC-CB[6] hydrogels is close to the reported value for the pyrene-CB[6] complex in aqueous solutions, indicating the presence of pyrene-CB[6] complex within the hydrogels.[36]

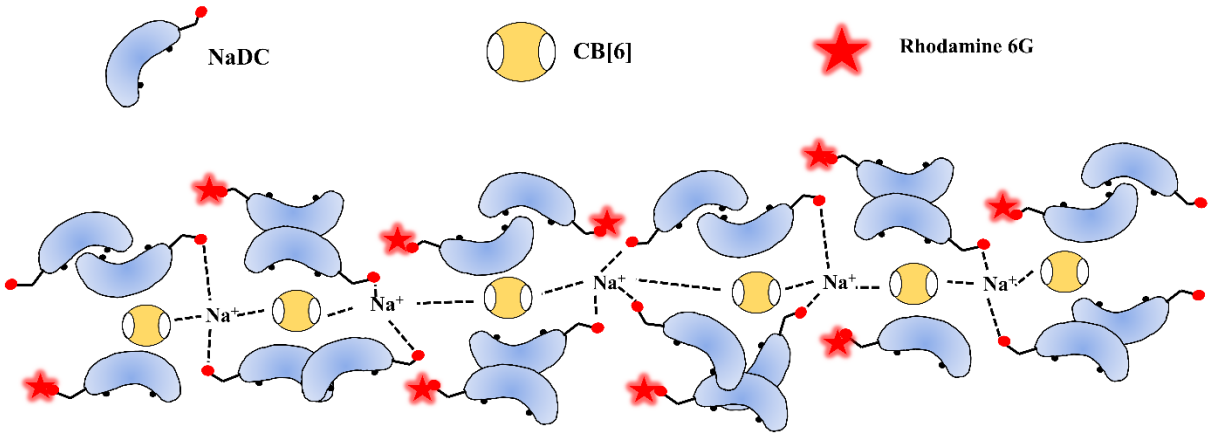

Scheme 4.3: Molecular picture of the fibre like NaDC-CB[6] hydrogels containing R6G.

The presence of the pyrene-CB[6] complex within NaDC-CB[6] hydrogels is the reason for the release kinetics of pyrene being dependent on CB[6] concentration in NaDC hydrogels

seen previously.[37] In comparison, the release kinetics of the cationic dye R6G were seen to be independent of CB[6] concentration in NaDC hydrogels.[37] Combining the structural information about NaDC-CB[6] hydrogels obtained via microscopy, the dependence of the release kinetics of pyrene and R6G on CB[6] concentration and detailed spectroscopic analysis of the current work, a molecular picture of the hydrogel emerges. The addition of CB[6] results in a pyrene-CB[6] complex, which is surrounded by NaDC molecules. Due to the pyrene-CB[6] complex, the pyrene is relocated from the hydrophilic regions of the hydrogel to the interior of the hydrogel, resulting in its release kinetics being altered (scheme 4.2). The size of pyrene prevents it from entering the CB[6] cavity, which results in pyrene interacting with the exterior wall of the CB[6] via the hydrophobic effect. To further decrease the interaction of pyrene with neighboring water molecules, the NaDC molecules are now expected to self-assemble around the pyrene-CB[6] complex. Previous work in our group has shown the role played by cations during CB[n] complexation,[44] which leads me to believe that sodium ions (Na^+) are involved in salt bridging interactions with the CB[6] as well as the surrounding NaDC molecules, resulting in fibre formation, observed through CLSM studies. This structural template of NaDC hydrogels in presence of CB[6] is also able to explain the independence of R6G release kinetics on the CB[6] concentration from NaDC hydrogels. The cationic nature of R6G leads this molecule to interact with the NaDC molecules that surround the CB[6], because at the pH of 6.5, the carboxylic acid groups are deprotonated and the electrostatic interaction between R6G and NaDC is preferred over the charge-dipole interaction of R6G and CB[6] portals. Therefore, in the absence or presence of CB[6], the R6G molecules are always interacting with NaDC molecules of the gel structure resulting in no alteration of the release kinetics of R6G molecules from NaDC

hydrogels on addition of CB[6] (scheme 4.3), making its release kinetics independent of CB[6] concentration in the hydrogels.

4.5 Conclusion

In this work, the role of molecular interactions of CB[6] with different guests (pyrene) has been explored as a tool to modulate function. Previous work in the group showed that the addition of CB[6] is known to affect release kinetics of the neutral molecule pyrene but not of the cationic molecule R6G from NaDC hydrogels.[37] By combining this previous knowledge and the detailed spectroscopic analysis from the current work, a molecular image of the hydrogel can be generated. The molecular interactions of the respective molecules are seen to play an important role in dictating the function of a system, in this case, the release rate of the guests from NaDC hydrogels. The specific interaction (hydrophobic effect) of pyrene with the exterior wall of CB[6] results in a pyrene-CB[6] complex, allowing it to localize within the fibrous gel network leading to the modulation the release of pyrene from NaDC gels by changing the CB[6] concentration in these gels. Conversely, the specific interaction (electrostatic) of the R6G with the NaDC molecules of the gel network is responsible for the release rate of R6G being unaffected on varying the CB[6] concentration in the gels. The understanding of these fundamental interactions at the molecular scale between guests and the building blocks of a supramolecular system could play an important role in predicting the macroscopic function of a supramolecular system, such as a hydrogel.

4.6 References

(1) Piepenbrock, M. O. M.; Lloyd, G. O.; Clarke, N.; Steed, J. W. Metal- and Anion-binding Supramolecular Gels. *Chem. Rev.* **2010,** *110*, 1990–2044.
(2) Gronwald, O.; Shinkai, S. Sugar-integrated Gelators of Organic Solvents. *Chem.–Eur. J.* **2001,** *7*, 4328–4334.
(3) Adams, D. J. Dipeptide and Tripeptide Conjugates as Low-molecular-weight Hydrogelators. *Macromol. Biosci.* **2011,** *11*, 160–173.
(4) Johnson, E. K.; Adams, D. J.; Cameron, P. J. Peptide based Low Molecular Weight Gelators. *J. Mater. Chem.* **2011,** *21*, 2024–2027.
(5) Smith, D. K. Dendritic Supermolecules – Towards Controllable Nanomaterials. *Chem. Commun.* **2006**, 34–44.
(6) Sivakova, S.; Rowan, S. J. Nucleobases as Supramolecular Motifs. *Chem. Soc. Rev.* **2005,** *34*, 9–21.
(7) Araki, K.; Yoshikawa, I. Nucleobase-containing Gelators. *Top. Curr. Chem.* **2005,** *256*, 133–165.
(8) Buerkle, L. E.; Rowan, S. J. Supramolecular Gels formed from Multi-component Low Molecular Weight Species. *Chem. Soc. Rev.* **2012,** *41*, 6089–6102.
(9) Qi, Z.; Schalley, C. A. Exploring Macrocycles in Functional Supramolecular Gels: From Stimuli Responsiveness to Systems Chemistry. *Acc. Chem. Res.* **2014,** *47*, 2222–2233.
(10) Fuhrhop, J.-H.; Schnieder, P.; Rosenberg, J.; Boekema, E. The Chiral Bilayer Effect Stabilizes Micellar Fibers. *J. Am. Chem. Soc.* **1987,** *109*, 3387–3390.
(11) Fuhrhop, J.-H.; Svenson, S.; Boettcher, C.; Roessler, E.; Vieth, H.-M. Long-lived Micellar N-alkylaldonamide Fiber Gels. Solid-state NMR and Electron Microscopic Studies. *J. Am. Chem. Soc.* **1990,** *112*, 4307–4312.
(12) Hanabusa, K.; Itoh, A.; Kimura, M.; Shirai, H. Terephthaloyal Derivatives as New Gelators; Excellent Gelation Ability and Remarkable Increase of Gel Strength by Adding Polymers. *Chem. Lett.* **1999,** *28*, 767–768.
(13) Blow, D. M.; Rich, A. Studies on the Formation of Helical Deoxycholate Complexes[1,2]. *J. Am. Chem. Soc.* **1960,** *82*, 3566–3571.
(14) Sun, X.; Du, Z.; Li, E.; Xin, X.; Tang, N.; Wang, L.; Yuan, J. Rheological Properties of the Gels of Biological Surfactant Sodium Deoxycholate/Amino Acids/Halide Salts System. *Colloids Surf., A* **2014,** *457*, 345–353.
(15) Zhang, J.; Wang, H.; Li, X.; Song, S.; Song, A.; Hao, J. Two Gelation Mechanisms of Deoxycholate with Inorganic Additives: Hydrogen Bonding and Electrostatic Interactions. *J. Phys. Chem. B* **2016,** *120*, 6812–6818.
(16) Wang, Y. T.; Xin, X.; Li, W. Z.; Jia, C. Y.; Wang, L.; Shen, J. L.; Xu, G. Y. Studies on the Gel Behavior and Luminescence Properties of Biological Surfactant Sodium Deoxycholate/Rare-earth Salts Mixed Systems. *J. Colloid Interface Sci.* **2014,** *431*, 82–89.
(17) Wang, L.; Xin, X.; Yang, M.; Ma, X.; Shen, J.; Song, Z.; Yuan, S. Effects of Graphene Oxide and Salinity on Sodium Deoxycholate Hydrogels and Their Applications in Dye Absorption. *Colloids Surf., A* **2015,** *483*, 112–120.
(18) Das, S.; de Rooy, S. L.; Jordan, A. N.; Chandler, L.; Negulescu, I. I.; El-Zahab, B.; Warner, I. M. Tunable Size and Spectral Properties of Fluorescent NanoGUMBOS in Modified Sodium Deoxycholate Hydrogels. *Langmuir* **2012,** *28*, 757–765.

(19) McNeel, K. E.; Das, S.; Siraj, N.; Negulescu, I. I.; Warner, I. M. Sodium Deoxycholate Hydrogels: Effects of Modifications on Gelation, Drug Release, and Nanotemplating. *J. Phys. Chem. B* **2015,** *119*, 8651–8659.
(20) Guo, Y.; Wang, R.; Shang, Y.; Liu, H. Effects of Polymers on the Properties of Hydrogels Constructed using Sodium Deoxycholate and Amino Acid. *RSC Adv.* **2018,** *8*, 8699–8708.
(21) Saji, V. S. Recent Updates on Supramolecular-based Drug Delivery – Macrocycles and Supramolecular Gels. *Chem. Rec.* **2022,** *22*, 1–20.
(22) Moran, J. R.; Karbach, S.; Cram, D. J. Cavitands: Synthetic Molecular Vessels[1]. *J. Am. Chem. Soc.* **1982,** *104*, 5826–5828.
(23) Freeman, W. A.; Mock, W. L.; Shih, N.-Y. Cucurbituril. *J. Am. Chem. Soc.* **1981,** *103*, 7367–7368
(24) Lee, J. W.; Samal, S.; Selvapalam, N.; Kim, H.-J.; Kim, K. Cucurbituril Homologues and Derivatives: New Opportunities in Supramolecular Chemistry. *Acc. Chem. Res.* **2003,** *36*, 621–630.
(25) Neira, I.; Peinador, C.; García, M. D. CB[7]- and CB[8]-based [2]-(Pseudo)rotaxanes with Triphenylphosphonium-capped Threads: Serendipitous Discovery of a New High-affinity Binding Motif. *Org. Lett. 2022* **2022,** *24*, 4491–4495.
(26) Zhang, Z.-Y.; Chen, Y.; Liu, Y. Cucurbiturils-based Pseudorotaxanes and Rotaxanes. In *Handbook of Macrocyclic Supramolecular Assembly*; Liu, Y.; Chen, Y.; Zhang, Z.-Y., Eds.; 2020; pp 759–786.
(27) Chen, H.; Hou, S.; Ma, H.; Li, X.; Tan, Y. Controlled Gelation Kinetics of Cucurbit[7]uril-adamantane Cross-linked Supramolecular Hydrogels with Competing Guest Molecules. *Sci. Rep.* **2016,** *6*, 20722.
(28) Wang, Z.; Sun, C.; Yang, K.; Chen, X.; Wang, R. Cucurbituril-based Supramolecular Polymers for Biomedical Applications. *Angew. Chem. Int. Ed.* **2022,** *61*, e20220673.
(29) Ding, Y.-F.; Wei, J.; Li, S.; Pan, Y.-T.; Wang, L.-H.; Wang, R. Host−guest Interactions Initiated Supramolecular Chitosan Nanogels for Selective Intracellular Drug Delivery. *ACS Appl. Mater. Interfaces* **2019,** *11*, 28665–28670.
(30) Rana, V. K.; Tabet, A.; Vigil, J. A.; Balzer, C. J.; Narkevicius, A.; Finlay, J.; Hallou, C.; Rowitch, D. H.; Bulstrode, H.; Scherman, O. A. Cucurbit[8]uril-derived Graphene Hydrogels. *ACS Macro Lett.* **2019,** *8*, 1629–1634.
(31) Appel, E. A.; Loh, X. J.; Jones, S. T.; Dreiss, C. A.; Scherman, O. A. Sustained Release of Proteins from High Water Content Supramolecular Polymer Hydrogels. *Biomaterials* **2012,** *33*, 4646–4652.
(32) Yang, H.; Chen, H.; Tan, Y. Cucurbit[8]uril Inducing Supramolecular Hydrogels by Adjusting pH. *RSC Adv.* **2013,** *3*, 3031–3037.
(33) Hwang, I.; Jeon, W. S.; Kim, H.-J.; Kim, D.; Kim, H.-J.; Selvapalam, N.; Fujita, N.; Shinkai, S.; Kim, K. Cucurbit[7]uril: A Simple Macrocyclic, pH-triggered Hydrogelator Exhibiting Guest-induced Stimuli-responsive Behavior. *Angew. Chem. Int. Ed.* **2007,** *46*, 210–213.
(34) Yang, H.; Tan, Y.; Wang, Y. Fabrication and Properties of Cucurbit[6]uril Induced Thermo-responsive Supramolecular Hydrogels. *Soft Matter* **2009,** *5*, 3511–3516.
(35) Park, K. M.; Yang, J. A.; Jung, H.; Yeom, J.; Park, J. S.; Park, K. H.; Hoffman, A. S.; Hahn, S. K.; Kim, K. In Situ Supramolecular Assembly and Modular Modification of Hyaluronic Acid Hydrogels for 3D Cellular Engineering. *ACS Nano* **2012,** *6*, 2960–2968.

(36) Seyedalikhani, M. Exploring the Binding of Small Guest Molecules in Sodium Deoxycholate Hydrogels. PhD University of Victoria, 2016. http://hdl.handle.net/1828/7615
(37) Talluri, S. G. Effect of Cucurbit[6]uril on the Structure and Dynamics of NaDC Gels. PhD University of Victoria, 2021. http://hdl.handle.net/1828/13847
(38) Siemiarczuk, A.; Wagner, B. D.; Ware, W. R. Comparison of the Maximum Entropy and Exponential Series Methods for the Recovery of Distributions of Lifetimes from Fluorescence Lifetime Data. *J. Phys. Chem.* **1990,** *94*, 1661–1666.
(39) Siemiarczuk, A.; Ware, W. R. A Novel Approach to Analysis of Pyrene Fluorescnece Decays in Sodium Dodecylsufate Micelles in the Presence of Cu^{2+} Ions based on the Maximum Entropy Method. *Chem. Phys. Lett.* **1989,** *160*, 285–290.
(40) Kalyanasundaram, K.; Thomas, J. K. Environmental Effects on Vibronic Band Intensities in Pyrene Monomer Fluorescence and their Application in Studies of Micellar Systems. *J. Am. Chem. Soc.* **1977,** *99*, 2039–2044.
(41) Xu, W.; Demas, J. N.; DeGraff, B. A.; Whaley, M. Interactions of Pyrene with Cyclodextrins and Polymeric Cyclodextrins. *J. Phys. Chem.* **1993,** *97*, 6546–6554.
(42) Yang, H.; Bohne, C. Effect of Amino Acid Coinclusion on the Complexation of Pyrene with β-Cyclodextrin. *J. Phys. Chem.* **1996,** *100*, 14533–14539.
(43) Sueldo Occello, V. N.; De Rossi, R. H.; Veglia, A. V. Complexation (Cucurbit[6]Uril-Pyrene): Thermodynamic and Spectroscopic Properties. *J. Lumin.* **2015,** *158*, 435–440.
(44) Vos, K. A. A Systems Chemistry Approach to Understanding Cucurbit[7]uril-guest Dynamics. PhD University of Victoria, 2020. http://hdl.handle.net/1828/11797

Chapter 5: Preliminary Exploration of the Host-guest Chemistry of Cucurbit[6]uril as a Handle to Modulate Function within Urea Based Hydrogels

5.1 Introduction

Most functional systems are developed to be thermodynamically stable, where the building block interactions are either strong covalent bonds as seen in chemical gels or physical crosslinking between the microstructures such as in physical gels. However, supramolecular systems are made up of weak non-covalent interactions between the building blocks. The dynamic nature of the building block interactions in supramolecular systems provides a prospective avenue to modulate function, like uptake and release of molecules to or from a supramolecular hydrogel.

5.1.1 Host-guest chemistry of CB[n]

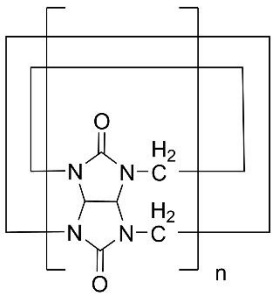

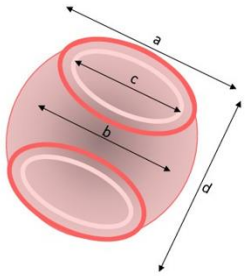

		CB[5]	CB[6]	CB[7]	CB[8]
Outer Diameter (Å)	a	13.1	14.4	16.0	17.5
Cavity (Å)	b	4.4	5.8	7.3	8.8
	c	2.4	3.9	5.4	6.9
Height (Å)	d	9.1	9.1	9.1	9.1
Cavity volume (Å^3)	-	82	164	279	479

Figure 5.1: Tabulation of the sizes of the different CB[n] homologues.[1]

Cucurbit[n]urils (CB[n]s) belong to a family of macrocycles made from the reaction of glycoluril and paraformaldehyde.[1] These molecules possess a highly rigid structure, containing a cavity capable of binding hydrophobic guests. Moreover, the carbonyl lined portals of CB[n]s are

capable of binding to positively charged guests or stabilizing cationic charges on a guest through ion-dipole interactions.[2] The stabilization of cationic charges can result in pK_a shifts of guest molecules when bound to CB[n].[3-6] The size of the CB[n] cavity imparts an inherent selectivity to the nature of molecular interactions of the different homologues of CB[n].[1] For example, CB[5] is the smallest known member of the CB[n] family and can form exclusion complexes. In these exclusion complexes, the aromatic or aliphatic group of the molecule remains exposed to the solvent with the cationic charge stabilised by the carbonyl portals.[7] The larger CB[6] is known to be selective towards the binding of alkyl-ammonium cations as well as small aromatic ammonium cations like benzyl-ammonium.[1, 7-8] CB[7] due to its larger cavity size is able to bind larger aromatic guests and form complexes with high equilibrium constants.[6, 9-11] Lastly, the large cavity of CB[8] is capable of forming 1:1:1 guest:guest:host complexes, where the two guests can either be two of the same molecules or two different molecules.[12-14] Beyond the selectivity however, there is limited knowledge pertaining to the relationship between molecular structure of guest with the rate constants of association and dissociation of guests with CB[n]s.[6, 15-17] Varying these rate constants could play a key role in influencing the supramolecular function of a supramolecular system built on a CB[n] template.

Researchers have tried to better understand the relationship between molecular structure of guests and their binding kinetics with CB[n]s.[6, 9, 15-21] The complexation dynamics of guests like amines is known to be affected by the charge on the amine, wherein neutral amines are known to bind faster to CB[n]s in comparison to cationic amines which bind slowly due to formation of an external complex before internalisation to the CB[n] cavity.[6, 16, 20-21] Recent work in our group focused on dicationic guests (dibenzylamines) having structural similarities, however the position of cationic charge was different in the guests investigated.[17] All the guests

investigated displayed difference in binding kinetics with CB[7] despite having similar structure and equilibrium constants. Moreover, one of the guest studied in this work, 2,7'-dimethyl-diazapyrenium was seen to form oligomeric assemblies via an external complex at higher CB[7] concentrations.[17]

5.1.2 Urea based gelators

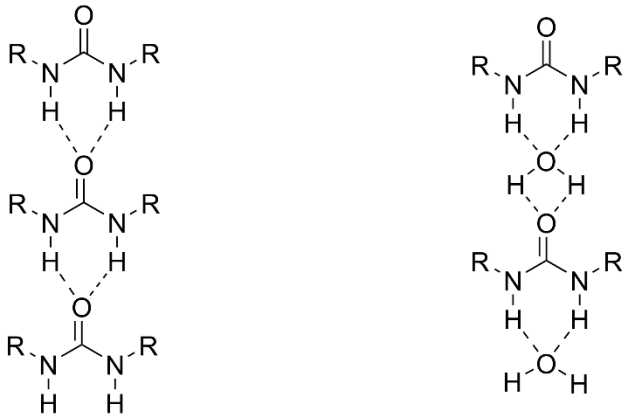

Figure 5.2: Two differernt hydrogen-bonded structures of a urea derivative.

Ureas are one of the smallest gelators known, with N-alkyl, N, N'-dialkyl and N,N-dialkyl ureas capable of gelating in organic solvents.[22] The ability of the ureide group to interact with each other through hydrogen bonds between the two NH atoms and the carbonyl groups provides directional self assembly (figure 5.2), making the ureide group a prospective candidate for constructing supramolecular architectures.[23] These properties of ureas have been extensively utilized to synthesize mono, bis, tri or tetrakis urea organo- and hydrogelators.[23-29] Moreover, the addition of multiple ureide groups to a low molecular weight gel (LMWG) offers a potential route to modifying the strength and morphology of the gel because of the increased number of hydrogen bonding sites.

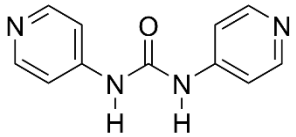

Chart 5.1: Molecular structure of urea **1**.

One of the smallest known urea based hydrogelator is N,N'-bis(4-pyridyl)urea (**1**), with a sol to gel transition temperature of 90 °C.[30] Molecule **1** was seen to form pH sensitive hydrogels in a pH range from 8.3–10. However, no gelation is observed when the pH is decreased to 5.3. This non gelation behaviour was attributed to the protonation of the pyridyl nitrogens, and confirmed by using the monohydrochloride salt which inhibited the gelation of **1**. The development of **1**, its acid derivatives and the non-gellating isomer, N,N'-bis(3-pyridyl)urea has led to the formation of a class of supramolecular hydrogels.[22-23, 25]

5.1.3 Objective

The objective of this study was to modulate the association and dissociation rate constants of CB[6] with urea based gelators and to correlate this change in rate constants with the release kinetics of a guest (pyrene) from the urea based hydrogel. This modulation of rate constants is achieved by functionalizing the urea with different handles (R group on NH) (figure 5.2). The ureide group is expected to provide us with a hierarchical assembly through hydrogen bonding that would help in the gelation of these molecules in aqueous solutions containing CB[6]. Changing the functional group on the ureide moiety is expected to impact the dynamics of binding between the urea and CB[6].

5.2 Experimental

5.2.1 Materials

4-aminopyridine (4-AP) and 1,1'-carbonyldimidazole (CDI) were obtained from Merck and used as received. Tetrahydrofuran (THF) (99.9%) was obtained from Caledon labs, dichloromethane (DCM, HPLC grade, 99.9%) and methanol (spectral grade, ≥ 99.9%) was obtained from Fischer chemicals, toluene (HPLC grade, 99.9 %), hexane (HPLC grade, 99.9 %) and dimethyl sulfoxide-d_6 (DMSO-d_6, 99.9% atom) were obtained from Sigma Aldrich and all solvents were used as received. Sodium chloride (NaCl) was obtained from Sigma and used as received. Ethyelene glycol (EG, anhydrous, 99.8%, Sigma) was borrowed from the Hicks group and used as received. Deionized water (Branstead NANOpure deionizing system ≥ 17.8 MΩ cm) was used for preparation of all aqueous solutions. Urea **1** was synthesized and purified using reported procedures, and purity confirmed through ^{1}H and ^{13}C nuclear magnetic resonance (NMR) (appendix A5.1).[31-33]

5.2.2 Sample Preparation

The NMR samples were prepared by dissolving 2.0 mg of compound in 1 mL of DMSO-d_6 in a volumetric flask before transferring the solution to an NMR tube. A 3.7 mM stock solution of **1** was prepared by dissolving 3.9 mg of **1** in 5 mL of methanol. This stock was used to prepare the solutions for the spectroscopic experiments.

Binding isotherm: In a 5 mL volumetric flask, 16 μL of stock solution of **1** and 29.2 mg of NaCl was added and the volumetric flask was filled with deionized water to obtain a 12.3 μM solution of urea **1** in 0.1 M NaCl. Now, 3 mL of this solution was added to quartz cuvette and absorbance measurements were collected (sample).

A mass of 8 mg of CB[6], 29.2 mg of NaCl and 16 μL of stock solution of **1** were added to a different 5 mL volumetric flasks, and these were filled with deionized water to obtain a 1.61 mM CB[6] solution in 0.1 M NaCl (titrant). The addition of 12.3 μM of **1** to this titrant solution prevented any dilution effects from affecting the binding experiments.

Kinetic experiments: For the kinetic experiments, equal volumes of two solutions are mixed before the data collection is carried out. For this reason, the prepared solutions had twice the concentration needed. For example, to obtain a 12.3 μM solution of **1** and 100 mM NaCl after mixing, the pre-mixed solutions contained 24.6 μM of **1** in water and 200 mM NaCl in water.

Similarly, for the mixing of urea **1** and CB[6], the solutions prepared were also twice the desired final concentrations. However, for these experiments, all the solutions were prepared using 0.1 M NaCl in water as solvent to prevent changes in NaCl concentration after mixing.

Inverted vial test for gelation: For these experiments, a 0.8 % (w/v) solution of **1** was prepared for each sample. This was done by taking 20 mg of **1** in a sample vial with 2 mL of water (solution 1). This solution was then heated at 90 °C in a water bath for 30 min. After 30 min, the sample vial was taken out and allowed to cool at room temperature overnight. This heating and cooling process was repeated for all samples being investigated for gelation. To prepare samples of **1** with 5 mM CB[6], 10 mg of CB[6] was added to the solution 1 before the heating and cooling process was undertaken. Similarly, for samples containing 100 M NaCl, 12 mg of NaCl was added to the solution before heating. To create samples in 20% aqueous EG, instead of adding 2 mL of water to the sample, 0.2 mL of EG and 1.8 mL of water was added. This procedure kept the final volume as 2 mL. To confirm gelation, the samples were inverted 20 h after the cooling process had begun. If the sample on vial inversion did not fall, a gel had formed. If the sample on vial inversion, fell, no gelation had taken place. In certain cases, the

sample was seen to fall on vial inversion, however, not all of the sample had completely fallen. Small parts of the sample were seen to be stuck on the base of the vial on inversion. These samples were assumed to undergo partial gelation. Moreover, after a week, the non-gellating sample were seen to precipitate out of solution, however, this was not the case for the partially gellating samples where a colloid dispersion is observed (appendix A5.2).

5.2.3 Instrumentation

All NMR spectra were obtained on a Bruker AVANCE I 500MHz NMR spectrometer operating at 500.27 MHz frequency with a BBO probe. The spectra were acquired using 30^{o} pulse angle and a 10 s relaxation delay. The T_1 was estimated to be $\leq$ 1.3 s via the T_1 null in the inversion recovery sequence for the peaks of interest. For ^{1}H NMR a total of 128 scans of the sample were taken, whereas for ^{13}C NMR a total of 1024 scans were taken.

Absorption spectra were collected on a CARY 100 Varian spectrometer at a scan rate of 600 nm/min. The long-time scale (0–30 min) kinetic experiments were done on a CARY 100 Varian spectrometer, using the time scan configuration. In this configuration, the multi-cell holder was used, with one cell containing the urea-CB[6] sample after mixing and the other cell containing a reference sample containing 0.1 M NaCl in water. The scans were collected at 285 nm over a period of 30 min with an averaging time of 2 s and dwell time, which is the time after which the collection switches between the sample cell to the reference cell and vice versa, that was set to 30 s. All experiments on the CARY 100 were carried at a constant temperature of 25 °C. The short-time scale (0–90 s) experiments were collected on an Applied Photophysics SX20 stopped-flow system operating with a Hg-Xe vapour lamp by mixing two solutions with a 1:1 volume ratio inside the mixing chamber. A baseline was collected using 10 mM NaCl solutions.

The absorbance modality of the stopped-flow was used for the experiments, where the sample was irradiated at 286 nm and amount of light transmitted through the sample was detected.

For the kinetic experiments on the CARY 100, all the solutions made for mixing were kept in a water bath, with the temperature of the water bath set at 25 °C and monitored with a thermometer. This was done to prevent temperature equilibration from affecting the kinetic trace collection. After mixing 1.5 mL each from the necessary solutions in a quartz cuvette, the sample was shaken thoroughly to for 30 s. After 30 s, the cuvette was transferred to the cell holder in the CARY 100, which was pre-set to 25 °C. After 90 s, the collection of the kinetic traces was started.

5.3 Results

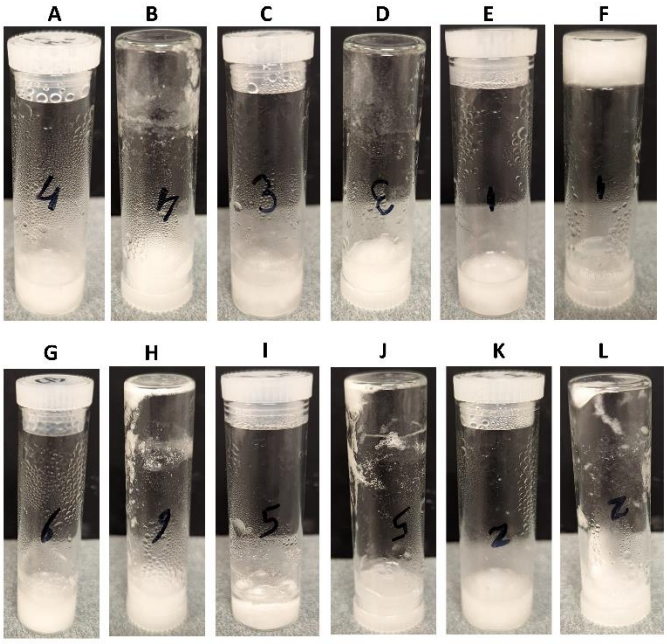

Figure 5.3: Images of the gel inversion tests for urea **1** (0.8% w/v) at different conditions. A) Upright image of **1** in water. B) Inverted setup of A. C) Upright image of **1** and 5 mM CB[6] in water. D) Inverted setup of C. E) Upright image of **1** in 20% aqueous EG. F) Inverted setup of E. G) Upright image of **1** and 5 mM CB[6] in 20% aqueous EG. H) Inverted setup of G. I) Upright image of **1** and 5 mM CB[6] in 0.1 mM NaCl. J) Inverted setup of I. K) Upright image of **1**, 5mM CB[6] and 0.1 M NaCl in 20% aqueous EG. L) Inverted setup of K.

To correlate the effect of kinetics between the urea and CB[6] to the release kinetics of an external guest, it is important to produce hydrogels between urea **1** and CB[6]. For this reason, the gelation of urea **1** was investigated under different conditions to explore the effect of CB[6] (table 5.1). It is observed that in an aqueous medium, in absence and presence of CB[6], the urea is incapable of gelation (figure 5.3A–B). However, the addition of EG to solution results in urea **1** forming gels (figure 5.3E–F). Moreover, the addition of NaCl and CB[6] are seen to induce partial gelation of urea **1** in both pure aqueous medium and in 20% aqueous EG solutions.

Table 5.1: The gelation behaviour of urea **1** when exposed to different conditions in water and 20% aqueous EG corresponding to the images in figure 5.3.

Conditions	Corresponding upright image	Corresponding inverted image	Gelation/ Partial Gelation/ No Gelation
Aqueous medium			
1	A	B	No Gelation
1 + 5 mM CB[6]	C	D	Partial Gelation
1 + 5 mM CB[6] + 100 mM NaCl	I	J	Partial Gelation
20% aqueous EG			
1	E	F	Gelation
1 + 5 mM CB[6]	G	H	Partial Gelation
1 + 5 mM CB[6] + 100 mM NaCl	K	L	Partial Gelation

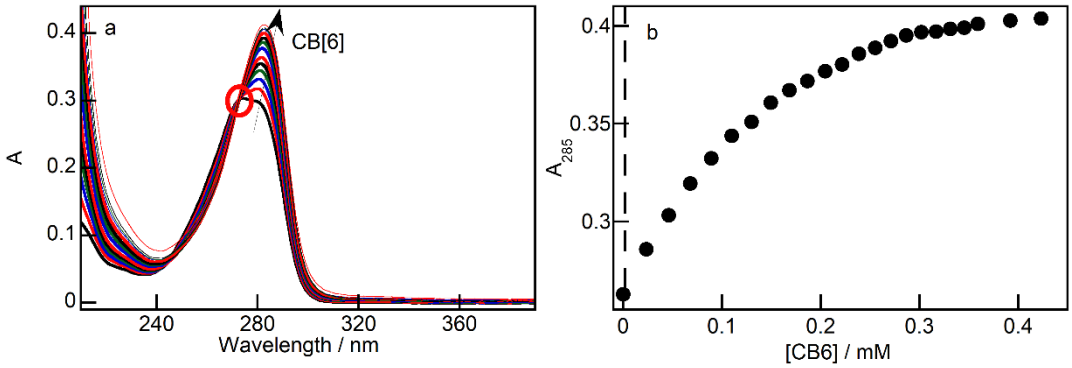

Figure 5.4: a) Absorption spectra of 12.3 μM of **1** in 100 mM NaCl with increasing CB[6] concentration. **b)** Change in absorbance of 12.3 μM of **1** at 285 nm in 100 mM NaCl with increasing CB[6] concentrations. The dashed black line in figure 5.3B indicates the origin on the concentration axis.

The gelation studies showed that there is some interaction happening between **1** and CB[6] in solution. Therefore, to investigate the magnitude of the interaction between urea **1** and

CB[6], binding studies were carried out using absorption spectroscopy (figure 5.4). The absorption maxima of urea **1** was seen to shift from 272 nm in water to 282 nm, accompanied by an increase in absorbance at this wavelength, when increasing concentrations of NaCl (figure S5.11) is added. The addition of CB[6] to urea **1** in 100 mM NaCl results in an additional shift of the absorption maxima to 283 nm (figure 5.4a and figure S5.12), along with an increase in the absorption at this wavelength indicating the presence of a binding interaction between urea **1** and CB[6].

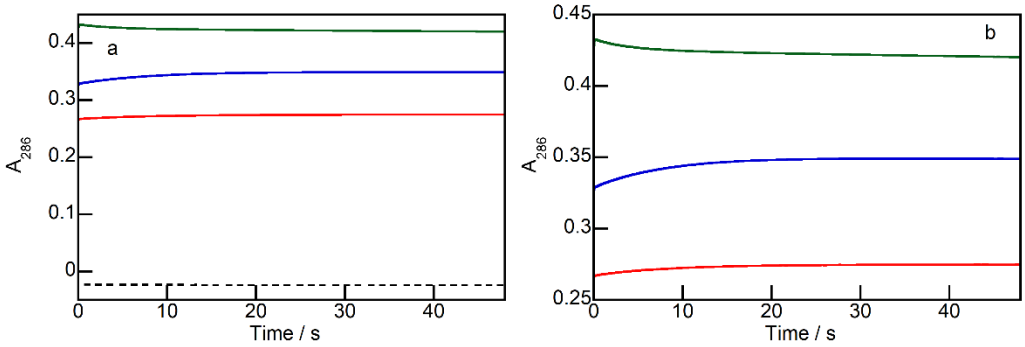

Figure 5.5: a) Stopped-flow traces for the mixing of 12.3 μM of **1** in 100 mM NaCl with increasing CB[6] concentrations. (1) 0 mM CB[6] (red), (2) 100 mM CB[6] (blue), (3) 300 mM CB[6] (green). The dotted line represents the trace for mixing of 100 mM NaCl with 100 mM NaCl. **b)** Expanded version of panel a showing only the kinetic traces for the mixing of urea with CB[6].

Preliminary stopped-flow experiments showed an offset in the kinetic traces on increasing the CB[6] concentration (figure 5.5). This is expected as the absorbance of **1** is seen to increase when binding to CB[6] in presence of 100 mM NaCl. The kinetic traces are seen to possess a growth profile when mixing **1** with 100 mM NaCl (red trace in figure 5.5), indicating that an interaction between **1** and NaCl occurs. This interaction between **1** and NaCl has been seen previously, wherein **1** was seen to bind to Cl^- ions in acetonitrile solutions.[31] This interaction was also investigated in this work to establish the maximum concentration of NaCl to be added for CB[6] solubilization, before studying the binding interactions between **1** and CB[6] (figure S5.11).

The addition of 100 mM CB[6] results in an increase in the offset of the kinetic traces with a similar growth profile for the kinetic trace (blue trace in figure 5.5) in absence of CB[6[(red trace in figure 5.5). However, when the CB[6] concentration is further increased to 300 mM, the profile of the kinetic trace possess a decay profile, which is in contrast to the results of the binding isotherm where the addition of CB[6] led to an increase in absorbance (green trace in figure 5.5). Moreover, at this concentration of CB[6], a slow process is seen to arise in the kinetic trace that requires investigation in a longer time scale (figure S5.13).

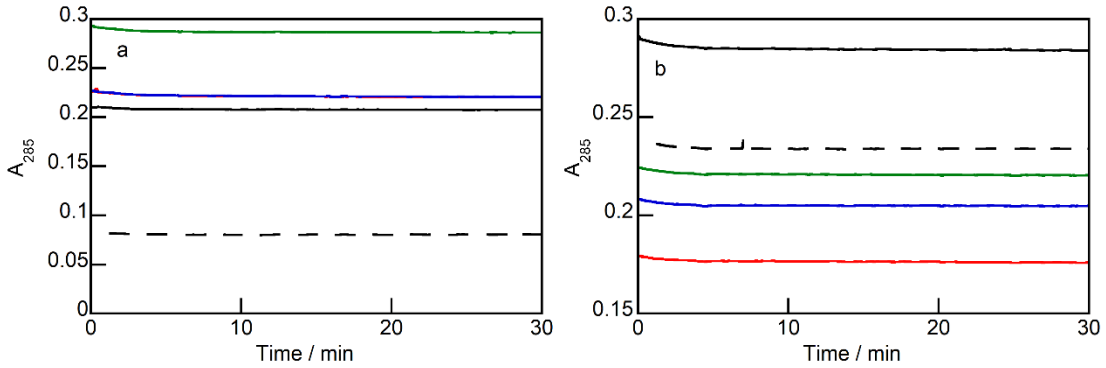

Figure 5.6: Kinetic traces for the mixing of 12.3 μM of **1** with various NaCl concentrations. Concentrations of NaCl presented are 0 mM (dashed black), 60 mM (red), 100 mM (blue), 200 mM (green) and 500 mM (black). The red and blue traces are overlayed. Panels **a** and **b** correspond to two individual experiments.

To qualitatively understand the switch in the kinetics from a growth to a decay profile, initially the binding kinetics between **1** and NaCl were investigated. In absence of NaCl, the decay trace is expected to show a flat line, however, as is observed in figure 5.6, in the absence and presence of NaCl, the kinetic traces show a decay profile. The qualitative behaviour of the kinetics is the same, but the observed offsets were not reproducible. These results indicate that there is an underlying process that takes place when mixing **1** with water. Ureas are known to aggregate in aqueous medium,[34-37] and therefore, this kinetic process being observed when mixing **1** and water could be a result of deaggregation of **1** on mixing, assisted by the addition of NaCl.

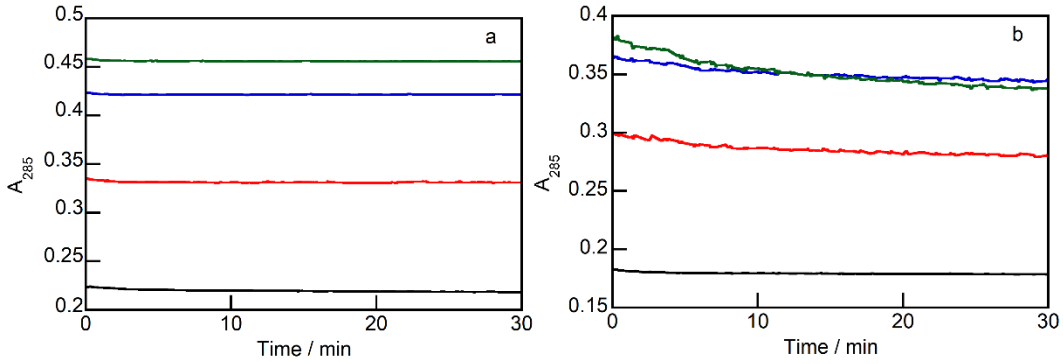

Figure 5.7: Kinetic traces for the mixing of 12.3 μM of **1** with various CB[6] concentrations in 100 mM NaCl. Concentrations of CB[6] presented are 0 mM (black), 0.8 mM (red), 1.5 mM (blue), 2.0 mM (green). Panel **a** and **b** correspond to two individual experiments.

Further investigations into the interactions between **1** and CB[6] were carried out by conducting kinetic experiments by mixing **1** and CB[6] in aqueous 100 mM NaCl solutions. The kinetic traces displayed similar changes in the amplitude to the binding isotherm between **1** and CB[6] (figure 5.4b), along with a decay profile for the kinetic traces over a longer time scale (figure 5.7). The results from figure 5.7 in conjunction with figure 5.4 indicate that there is an interaction happening between **1** and CB[6] in presence of 100 mM NaCl.

5.4 Discussion

Preliminary results from this study have shown that there exist interactions between urea **1** and CB[6] that affect the gelation behaviour of **1** in water and 20% EG solutions. However, the interactions of urea **1** are not exclusive to CB[6] since urea **1** also interacts with NaCl in aqueous solutions, an interaction seen previously in organic solvents.[31]. Additionally, the kinetic experiments indicate that the principle behind the objective for this project related to the kinetic kinetic studies between ureas and CB[6] to modulate the release of guest molecules from a urea-CB[6] system maybe achievable and suggest a need to redesign the project.

In aqueous solutions, ureas are known to either form hydrogen bonds with water or exist in a dimerized or oligomerized state via self-aggregation. The presence of both urea-water

clusters and the self-aggregated ureas has been explored through thermodynamic, two dimensional (2D)-infrared spectroscopy and molecular dynamic simulations studies.[37-40] As mentioned earlier, when urea **1** is mixed with water, the kinetic trace displays a decay profile. The presence of the decay profile on mixing **1** with water seems to be a result of deaggregation of either the urea-water clusters or urea self-aggregates due to dilution on mixing (figure 5.6). Furthermore, the addition of NaCl is seen to show a similar decay profile for the kinetic traces (figure 5.6), indicating that the binding of **1** to NaCl may assist in this deaggregation process.

The presence of NaCl in the urea-CB[6] system is necessitated due to the low solubility of CB[6] in water. The concentration of NaCl required was established through the binding experiments between urea **1** and NaCl (figure S5.11). The concentration of 100 mM NaCl was chosen to achieve complete binding of **1** and Cl^-. The differences in the observable trends in figure 5.6 is probably a result of the aggregation number of urea **1**, not being the same between the two individual experiments. Moreover, these experiments were carried out in aqueous solutions of uncontrolled pH, which may also be contributing to the different aggregation behaviour of the urea across the individual experiments, resulting in the differences in the observable trends seen in figure 5.6.

Stopped-flow experiments showed that the binding kinetics between **1** and CB[6] possess a growth profile within the time range investigated (0–50 s). However, as the concentration of CB[6] is increased to 300 mM CB[6], the kinetic trace is seen to possess a decay profile along with the presence of a slow kinetic process (figure S5.13). This slow kinetic process could be a result of the binding between CB[6] and Na^+ ions in solution acting as a competitor to the binding interaction between **1** and CB[6]. Such a slowdown of the kinetics of host-guest binding on the addition of cations has been seen previously.[17] Another reason for the slowdown of the

kinetics could be the formation of an inclusion complex between urea **1** and CB[6] that may or may not be capped by Na^+ at the opposite portal occupied by the urea. The investigations on the longer time scale (figure 5.7) confirm the presence of urea **1** and CB[6] interactions, with the order of the amplitude changes being roughly consistent across the two individual experiments.

The differences in the gelation behaviour of urea **1** on addition of 100 mM NaCl and CB[6] in water and 20% aqueous EG (table 5.1 and figure 5.3) can be attributed to the nature of the interactions taking place between **1** and the respective binding partners (Cl^- ions or CB[6]). Urea **1** has been reported to form gels at 0.8% (w/v) in water and aqueous EG solutions.[30] It was seen that the gelation of urea **1** is a result urea-solvent interactions taking place in solution. Using crystallographic studies, the authors observed that the water molecules interact with the pyridyl nitrogen and carbonyl groups through hydrogen bonding, whereas the ethylene glycol interacts with the other pyridyl nitrogen and the nitrogens (-NH) of the ureide group through hydrogen bonding interactions. Based on the interactions between urea **1** with different anions in acetonitrile,[31] it is expected that the Cl^- ions would now bind to ureide nitrogens (-NH), breaking the interactions between the urea and the solvent resulting in the alteration of the gelation behaviour of urea **1** in water and 20% EG. The presence of CB[6] is expected to cause a similar effect since CB[6] are known to bind to amines.[6-7, 16-18, 20-21] The secondary amine groups at both the pyridyl nitrogen and the ureide group are prospective binding sites for CB[6], thereby reducing the number of urea-solvent interactions, resulting in the partial gelation behaviour (table 5.3) and formation of a colloidal dispersion (appendix A5.2) of urea **1** in 20% EG. Moreover, an encapsulation of the pyridyl groups by CB[6] through internalization in the CB[6] cavity, accompanied by the ureide (NH)-Cl^- interactions, would result in the loss of urea to form my proposed self-assembled microstructures. The information from these preliminary

experiments with urea **1** would suggest a need to redesign the urea to achieved he intended objectives for this project.

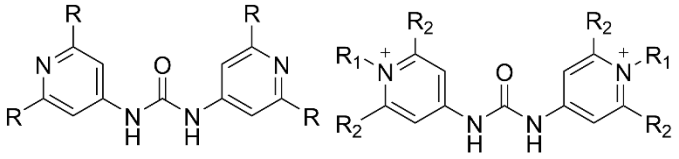

1
a - R = H
b - R = CH_3

2
a - R_1 = CH_3, R_2 = H
b - R_1 = $CH(CH_3)_2$, R_2 = H
c - R_1 = CH_3, R_2 = CH_3

Chart 5.2: Structures of proposed monourea derivatives.

For this purpose, different functionalized ureas are proposed to be synthesized as shown in chart 5.2. To prevent the CB[6] from interacting with the ureide group and interrupting the hierarchical self-assembly of the urea, I propose the designing of cationic ureas. This structural modification is proposed to be achieved through further functionalization leading to the addition of alkyl substituents on the pyridyl nitrogens (molecule **2**). The addition of functional groups on the pyridyl nitrogen (molecule **2**) is also expected to improve the solubility of the ureas in water due to the presence of two cationic charges. These cationic charges are also expected to favour the ion-dipole interactions between the cationic pyridyl nitrogen and carbonyl groups of the CB[6], over the dipole-dipole interactions taking place in urea **1**. Additionally, since CB[n]s are known to stabilise charges through their carbonyl portals,[2] the charged ureas may favour the formation of an external complex, leading to a 2D network in conjugation with the hierarchical assembly of the urea. Another strategy that could be used to favour external complexation, is by increasing the bulk on the pyridyl ring (molecule **1b** and **2c**). By investigating the binding interactions between the different ureas and CB[6] through kinetic and thermodynamic studies, and correlating them to release kinetics of guests from the urea-CB[6] gel systems, we can

understand the role played by the interactions between the building blocks of a system on its functional properties.

5.5 Conclusion

The experiments in this work explore the feasibility of carrying out kinetic experiments to determine the kinetics of building block interactions that make up a supramolecular system. The urea used in this work is seen to show some interactions with a macrocycle, CB[6], that affect gelation behaviour of the urea in water and 20% aqueous EG. Moreover, the binding kinetics between the urea and CB[6] are seen to show both slow, over time scale of 0–15 min and fast kinetic process, over time scale of 0–50 s. The faster kinetic process is also observed when mixing urea **1** with water and with increasing NaCl concentrations, indicating that this fast process could be a result of urea deaggregation, which is suggested to occur because of the specific interactions possible between the different binding motifs in the urea with CB[6] and Cl^- ions in solution. The preliminary results in this study validate the idea behind the project, i.e., to investigate building block interactions and provide a framework on which further experimental work can be explored through design optimization of the experiments and the structure of the ureas.

5.6 References

(1) Lee, J. W.; Samal, S.; Selvapalam, N.; Kim, H.-J.; Kim, K. Cucurbituril Homologues and Derivatives: New Opportunities in Supramolecular Chemistry. *Acc. Chem. Res.* **2003,** *36*, 621–630.
(2) Freeman, W. A.; Mock, W. L.; Shih, N.-Y. Cucurbituril. *J. Am. Chem. Soc.* **1981,** *103*, 7367–7368
(3) Montes-Navajas, P.; Garcia, H. Complexes of Basic Tricyclic Dyes in their Acid and Basic Forms with Cucurbit[7]uril: Determination of pK_a and Association Constants in the Ground and Singlet Excited State *J. Photochem. Photobiol. A* **2009,** *204*, 97–101.
(4) Saleh, N. i.; Koner, A. L.; Nau, W. M. Activation and Stabilization of Drugs by Supramolecular pK_a Shifts:Drug-delivery Applications Tailored for Cucurbiturils. *Angew. Chem. Int. Ed.* **2008,** *47*, 5398–5401.
(5) Shaikh, M.; Dutta Choudhury, S.; Mohanty, J.; Bhasikuttan, A. C.; Nau, W. M.; Pal, H. Modulation of Excited-state Proton Transfer of 2-(2'-Hydroxyphenyl)benzimidazole in a Macrocyclic Cucurbit[7]uril Host Cavity:Dual Emission Behavior and pK_a Shift. *Chem. Eur. J.* **2009,** *15*, 12362–12370.
(6) Thomas, S. S.; Bohne, C. Determination of the Kinetics Underlying the pKa Shift for the 2-aminoanthracenium Cation Binding with Cucurbit[7]uril. *Faraday Discuss.* **2015,** *185*, 381–398.
(7) Jansen, K.; Buschmann, H.-J.; Wego, A.; Döpp, D.; Mayer, C.; Drexler, H.-J.; Holdt, H.-J.; Schollmeyer, E. Cucurbit[5]uril, Decamethylcucurbit[5]uril and Cucurbit[6]uril. Synthesis, Solubility and Amine Complex Formation. *J. Incl. Phenom. Macrocycl. Chem.* **2001,** *39*, 357–363.
(8) Hoffmann, R.; Knoche, W.; Fenn, C. Host–guest Complexes of Cucurbituril with the 4-Methylbenzylammonium lon, Alkali-metal Cations and NH_4^+ *J. Chem. Soc., Faraday Trans.* **1994,** *90*, 1507–1511
(9) Tang, H.; Fuentealba, D.; Ko, Y. H.; Selvapalam, N.; Kim, K.; Bohne, C. Guest Binding Dynamics with Cucurbit[7]uril in the Presence of Cations. *J. Am. Chem. Soc.* **2011,** *133*, 20623–20633.
(10) Cao, L.; Šekutor, M.; Zavalij, P. Y.; Mlinarić-Majerski, K.; Glaser, R.; Isaacs, L. Cucurbit[7]uril·Guest Pair with an Attomolar Dissociation Constant. *Angew. Chem. Int. Ed.* **2014,** *53*, 988–993.
(11) Mohanty, J.; Pal, H.; Ray, A. K.; Kumar, S.; Nau, W. M. Supramolecular Dye Laser with Cucurbit[7]uril in Water. *ChemPhysChem* **2007,** *8*, 54–56.
(12) Appel, E. A.; Biedermann, F.; Rauwald, U.; Jones, S. T.; Zayed, J. M.; Scherman, O. A. Supramolecular Cross-linked Networks via Host-guest Complexation with Cucurbit[8]uril. *J. Am. Chem. Soc.* **2010,** *132*, 14251–14260.
(13) Appel, E. A.; Loh, X. J.; Jones, S. T.; Dreiss, C. A.; Scherman, O. A. Sustained Release of Proteins from High Water Content Supramolecular Polymer Hydrogels. *Biomaterials* **2012,** *33*, 4646–4652.
(14) Appel, E. A.; Loh, X. J.; Jones, S. T.; Biedermann, F.; Dreiss, C. A.; Scherman, O. A. Ultrahigh-water-content Supramolecular Hydrogels Exhibiting Multistimuli Responsiveness. *J. Am. Chem. Soc.* **2012,** *134*, 11767–11773.
(15) Assaf, K. I.; Nau, W. M. Cucurbiturils: From Synthesis to High-affinity Binding and Catalysis. *Chem. Soc. Rev.* **2015,** *44*, 394–418.

(16) Márquez, C.; Hudgins, R. R.; Nau, W. M. Mechanism of Host−guest Complexation by Cucurbituril. *J. Am. Chem. Soc.* **2004,** *126*, 5806–5816.
(17) Vos, K. A. A Systems Chemistry Approach to Understanding Cucurbit[7]uril-guest Dynamics. PhD University of Victoria, 2020. http://hdl.handle.net/1828/11797
(18) Thomas, S. S.; Tang, H.; Bohne, C. Noninnocent Role of Na^+ Ions in the Binding of the N-Phenyl-2-naphthylammonium Cation as a Ditopic Guest with Cucurbit[7]uril. *J. Am Chem. Soc.* **2019,** *141*, 9645–9654.
(19) Barrow, S. J.; Kasera, S.; Rowland, R. J.; del Barrio, J.; Scherman, O. A. Cucurbituril-based Molecular Recognition. *Chem. Rev.* **2015,** *115*, 12320–12406.
(20) Marquez, C.; Nau, W. M. Two Mechanisms of Slow Host–guest Complexation between Cucurbit[6]uril and Cyclohexylmethylamine: pH-Responsive Supramolecular Kinetics. *Angew. Chem. Int. Ed.* **2001,** *40*, 3155–3160.
(21) Miskolczy, Z.; Megyesi, M.; Toke, O.; Biczók, L. Change of the Kinetics of Inclusion in Cucurbit[7]uril upon Hydrogenation and Methylation of Palmatine. *Phys. Chem. Chem. Phys.* **2019,** *21*, 4912–4919.
(22) George, M.; Tan, G.; John, V. T.; Weiss, R. G. Urea and Thiourea Derivatives as Low Molecular-mass Organogelators. *Chem. Eur. J.* **2005,** *11*, 3243–254.
(23) Yamanaka, M. Urea Derivatives as Low-molecular-weight Gelators. *J. Incl. Phenom. Macrocycl. Chem.* **2013,** *77*, 33–48.
(24) de Loos, M.; Friggeri, A.; van Esch, J.; Kellogg, R. M.; Feringa, B. L. Cyclohexane Bis-Urea Compounds for the Gelation of Water and Aqueous Solutions. *Org. Biomol. Chem.* **2005,** *3*, 1631–1639.
(25) Estroff, L. A.; Hamilton, A. D. Water Gelation by Small Organic Molecules. *Chem. Rev.* **2004,** *104*, 1201–1216.
(26) de Loos, M.; Feringa, B. L.; van Esch, J. Design and Application of Self-assembled Low Molecular Weight Hydrogels. *Eur. J. Org. Chem.* **2005,** *2005*, 3615–3631.
(27) Babu, S. S.; Praveen, V. K.; Ajayaghosh, A. Functional π-Gelators and Their Applications. *Chem. Rev.* **2014,** *114*, 1973–2129.
(28) James, S. J.; Perrin, A.; Jones, C. D.; Yufit, D. S.; Steed, J. W. Highly Interlocked Anion-bridged Supramolecular Networks from Interrupted Imidazole-urea Gels. *Chem. Commun.* **2014,** *50*, 12851–12854.
(29) Rodriguez-Llansola, F.; Hermida-Merino, D.; Nieto-Ortega, B.; Ramirez, F. J.; Navarrete, J. T. L.; Casado, J.; Hamley, I. W.; Escuder, B.; Hayes, W.; Miravet, J. F. Self-assembly Studies of a Chiral Bisurea-based Superhydrogelator. *Chem. Eur. J.* **2012,** *18*, 14725–14731.
(30) Kumar, D. K.; Jose, A. A.; Das, A.; Dastidar, P. First Snapshot of a Nonpolymeric Hydrogelator Interacting with its Gelling Solvents. *Chem. Commun.* **2005**, 4059–4061.
(31) Baggi, G.; Boiocchi, M.; Fabbrizzi, L.; Mosca, L. Moderate and Advanced Intramolecular Proton Transfer in Urea–anion Hydrogen-bonded Complexes. *Chem. Eur. J.* **2011,** *17*, 9423–9439.
(32) Weilandt, T.; Troff, R. W.; Saxell, H.; Rissanen, K.; Schalley, C. A. Metallo-supramolecular Self-assembly: The Case of Triangle-square Equilibria. *Inorg Chem.* **2008,** *47*, 7588–7598.
(33) Wu, J.; Wang, C.; Leas, D.; Vargas, M.; White, K. L.; Shackleford, D. M.; Chen, G.; Sanford, A. G.; Hemsley, R. M.; Davis, P. H.; Dong, Y.; Charman, S. A.; Keiser, J.; Vennerstorm, J. L. Progress in Antischistosomal N,N'-Diarylurea SAR. *Bioorg. Med. Chem. Lett.* **2018,** *28*, 244–248.

(34) Frank, H. S.; Franks, F. Structural Approach to the Solvent Power of Water for Hydrocarbons; Urea as a Structure Breaker *J. Chem. Phys.* **1968,** *48*, 4746–4757.
(35) Schellman, J. A. The Stability of Hydrogen-bonded Peptide Structures in Aqueous Solution. *C. R. Trav. Lab. Carlsberg, Ser. Chim.* **1955,** *29*, 230–259.
(36) Kreschek, G. C.; Scheraga, H. A. The Temperature Dependence of the Enthalpy of Formation of the Amide Hydrogen Bond; the Urea Model[1]. *J. Phys. Chem.* **1965,** *69*, 1704–1706.
(37) Stokes, R. H. Thermodynamics of Aqueous Urea Solutions. *Aust. J. Chem.* **1967,** *20*, 2087–2100.
(38) Abu-Hamdiyyah, M. The Effect of Urea on the Structure of Water and Hydrophobic Bonding[1]. *J. Phys. Chem.* **1965,** *69*, 2720–2725.
(39) Jung, Y. M.; Matusewicz, B. C.; Kim, S. B. Characterization of Concentration-dependent Infrared Spectral Variations of Urea Aqueous Solutions by Principal Component Analysis and Two-dimensional Correlation Spectroscopy. *J. Phys. Chem. B* **2004,** *108*, 13008–13014.
(40) Stumpe, M. C.; Grubmüller, H. Aqueous Urea Solutions: Structure, Energetics, and Urea Aggregation. *J. Phys. Chem. B* **2007,** *111*, 6220–6228.

Chapter 6: Summary

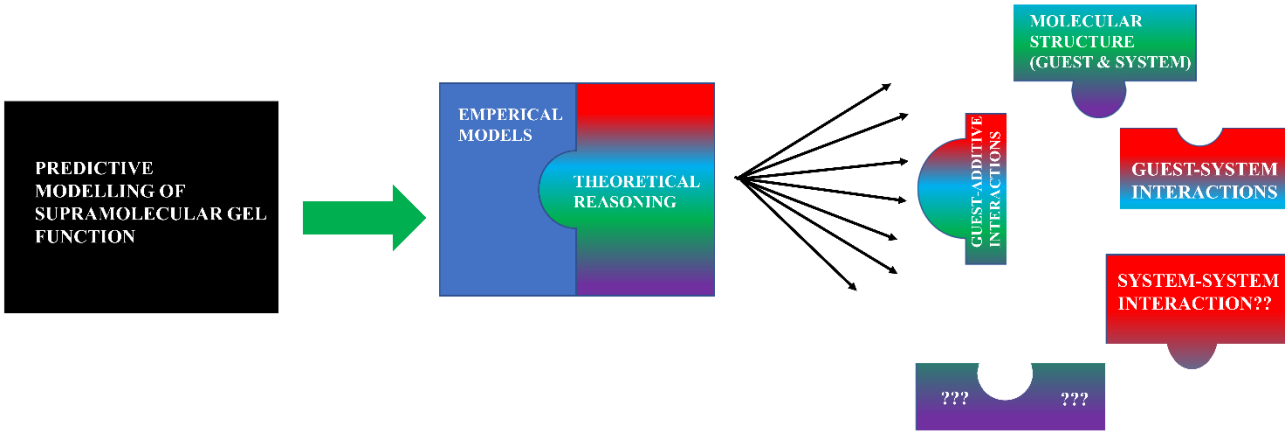

Figure 6.1: Schematic representation of the complementarity of empirical models and the possible theoretical concepts required for predicting supramolecular function.

This dissertation aims to utilize the known theoretical concepts and explore new theoretical concepts that can influence the function of supramolecular systems, specifically supramolecular hydrogels. The development of pH resistant emissive F127 hydrogels exploited the known theoretical concepts around polymeric gels formed via micellization. In these micellar systems, a guest molecule only has two possible localization environments, a hydrophilic corona, and a hydrophobic core. The structural characteristics of our fluorophore, BTS, utilizes this information to leverage the hydrophobic effect, confining BTS into the core of the micelles, where its emission is seen to be protected from the changes in pH. Through fluorescence quenching experiments of fluorophores in NaDC hydrogels in the presence and absence of CB[6], a molecular understanding of the hydrogels was obtained. This understanding revealed why the release kinetics of certain molecules from NaDC hydrogels, such as pyrene, is affected by the addition of CB[6], while for others like R6G the release kinetics remain unaffected. These new insights into the molecular interactions between the guests and the NaDC and NaDC-CB[6] systems could not have been achieved solely through empirical models. Additionally, the design

of the urea-CB[6] system was intended to examine how the kinetics between the building blocks of a system affect the release kinetics of guests, which would not have been feasible through empirical methods alone. Through preliminary experiments, the impact of various binding interactions of the urea with the solvent, NaCl and CB[6] on the urea's gelation behaviour is utilized to design prospective functionalized ureas. The newly proposed ureas are expected to display improved water solubility and gelation behaviour in presence of CB[6], that can be utilized to study the binding kinetics between the urea and CB[6] and correlate the binding kinetics to the release kinetics of guest from various urea-CB[6] hydrogels. The findings in this dissertation aim to provide the necessary theoretical understanding around supramolecular systems, that can be integrated with empirical models to develop more accurate predictions for function in supramolecular systems (figure 6.1).

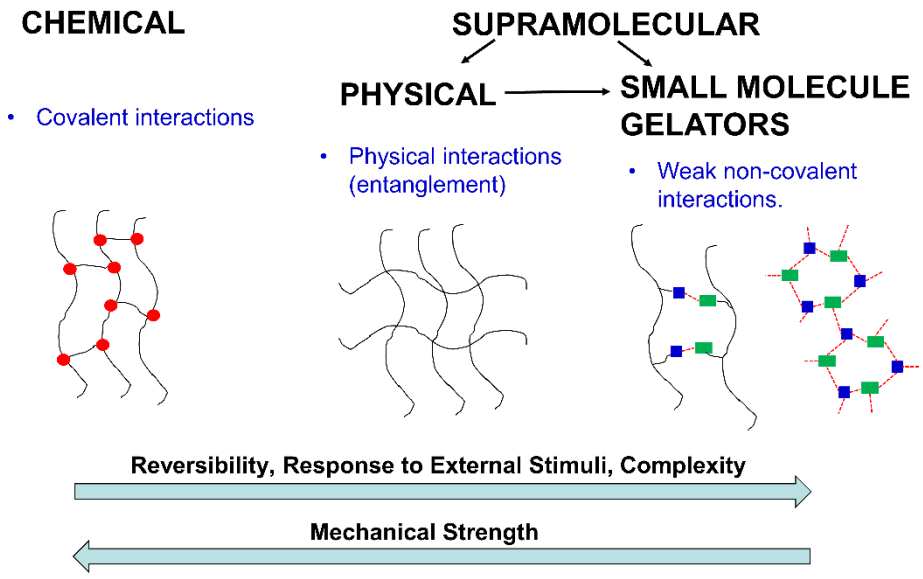

Figure 6.2: Schematic representation of the dependence of various characteristics across the different classes of hydrogels.

Another aspect of this work focused on exploring the significance of complexity in supramolecular gel chemistry. Complexity refers to intricate systems characterized by interconnected relationships, processes, and components that influence each other in a non-linear manner. Understanding and predicting the behavior of complex systems can be challenging, making them less attractive for functional system development. The self-assembled microstructures of F127 hydrogels, with only two possible environments for guest localization, are ideal for functional systems. By localising the guest in the hydrophilic corona of F127 hydrogels, stimuli-responsive sensing systems can be developed, whereas by localizing the guest within the core of F127 micelles, guests can be protected from external stimuli and degradation to develop robust functional systems. However, NaDC hydrogels have a more complex self-assembling mechanism, making them more challenging to understand. Nevertheless, by

comprehending the role of molecular interactions in the self-assembly of NaDC hydrogels, this increased complexity can be harnessed. The addition of CB[6] to NaDC hydrogels allows the development of stronger hydrogels without affecting the release kinetics of cationic molecules, while for neutral molecules, CB[6] not only strengthens the gel but also slows down their release. Achieving the results seen through addition of CB[6] in NaDC hydrogels would require additional synthetic effort when designing chemical gels to serve a similar purpose. Conversely, physical gels like F127 would exhibit a more consistent response regardless of the guest used. Therefore, the studies in this dissertation aim to demonstrate how complexity can be utilized as a tool for achieving a desired functionality when designing and developing functional supramolecular systems.

The integration of empirical models with experimentally gained theoretical concepts can lead to the development of more robust and accurate predictive models. With the empirical model approach using pattern recognition and observed data to establish correlation between variables, and the theoretical reasoning approach using fundamental scientific understanding to provide insights into underlying mechanisms and relationships within a system, the two approaches can complement each other and accelerate the discovery of prospective drug delivery systems. The development of functionalized ureas and the kinetic investigations of their binding to CB[6] is aimed at providing another theoretical concept that could impact the release of guests from a hydrogel without the guest having to interact with the system, as was the case for the release of pyrene from NaDC-CB[6] hydrogels. Furthermore, the increased understanding of these theoretical concepts will allow us to exploit the complexity offered by supramolecular systems to achieve the desired functionality within our hydrogel system. This increased control over complexity within supramolecular systems can allow us to develop multifunctional

hydrogel systems, wherein we can obtain hydrogels with desired mechanical strength as well as desired release behaviour for external guests.

Appendix

Chapter 2

A2.1 ^{1}H NMR for BTS in DMSO-d_6

The ^{1}H NMR spectrum of BTS was measured in DMSO-d_6 (Figure S2.1).

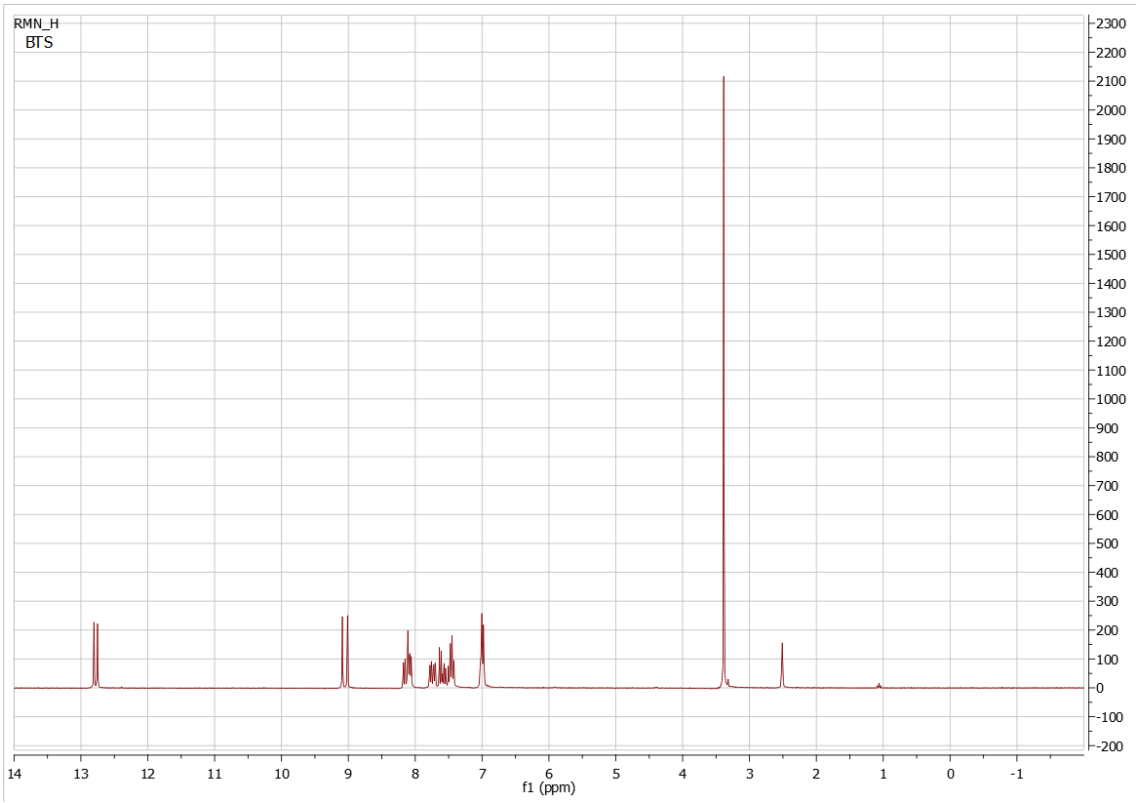

Figure S2.1: ^{1}H NMR spectrum of BTS in DMSO-d_6.

^{1}H NMR (400 MHz, DMSO-d6): δ 12.76-12.80 (s, 1H), 12.72-12.76 (s, 1H), 9.08-9.10 (s, 1H), 9.01-9.03 (s, 1H), 8.15-8.19 (d, 1H, J=8.0 Hz), 8.07-8.13 (t, 3H, J=7.5 Hz), 7.75-7.78 (dd, 1H, J=7.5 Hz and J=1.5 Hz), 7.70-7.73 (dd, 1H, J=7.5 Hz and J=1.5 Hz), 7.62-7.66 (d, 1H, J=8.5 Hz), 7.55-7.60 (t, 1H, J=7.5 Hz), 7.47-7.51 (t, 1H, J=7.5 Hz), 7.42-7.47 (t, 2H, J=8.0 Hz), 6.97-7.02 (m, 4H).

A2.2 Steady-state emission spectra of BTS in F127 hydrogels excited at different wavelengths.

The normalized steady-state emission spectra for BTS in 17% (w/w) F127 hydrogels at 30 °C were excited at wavelengths with a 10 nm increment from 300 to 480 nm. The normalized spectra highlight that N is primarily excited at the shorter wavelengths, while above 400 nm A is selectively excited.

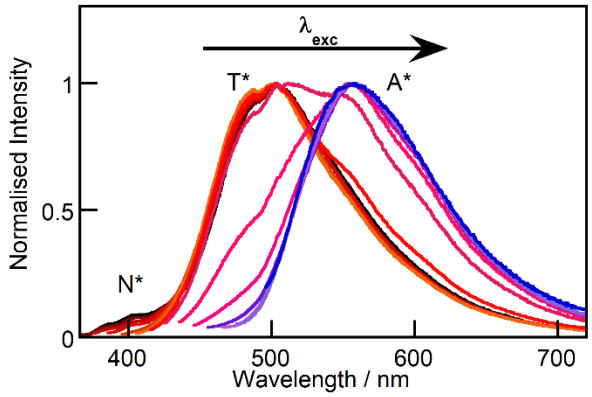

Figure S2.2: Normalised steady-state emission spectra of BTS in 17% (w/w) F127 at 30 °C excited within a wavelength range of 300 nm to 480 nm with a 10 nm increment (black to red to blue).

A2.3 Steady-state emission spectrum for BTS in the F127 hydrogel

The steady-state emission spectrum for 17% (w/w) F127 hydrogel at 30 °C, in the absence and presence of BTS shows that the contribution from the emission of impurities in F127 does not change the shape of the BTS emission spectrum.

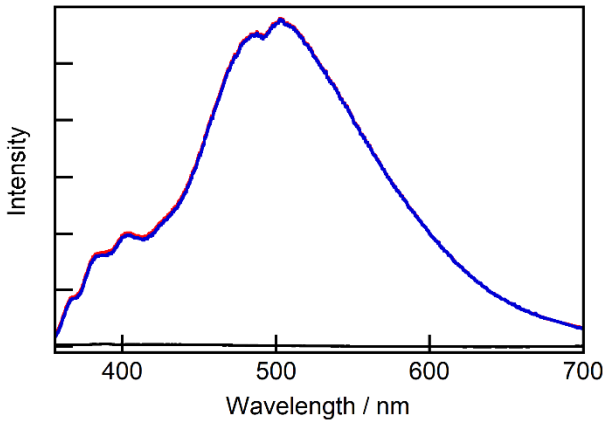

Figure S2.3: Steady-state emission spectra (λ_{exc} = 340 nm) of BTS (A_{335} = 0.2) in 17% (w/w) F127 at 30 °C uncorrected (red) and corrected (blue) for the emisson from F127 impurities and for light scattering (black).

A2.4 CIE chromaticity coordinates for varying BTS concentrations in F127 hydrogels and for BTS in F127 hydrogels at different pH values

The CIE chromaticity coordinates at varying BTS concentrations in 17% (w/w) F127 hydrogels and for BTS in 17% (w/w) F127 hydrogels at different pH values were determined from the from the emission spectra of the gels (tables S2.1 and S2.2).

Table S2.1: CIE coordinates for 17% (w/w) F127 hydrogels containing BTS at 30 °C shown in Figure 2.6. BTS concentration is represented as the absorbance of the sample at 335 nm.

A_{335}	Point in figure 2	x	y
0.2	Black circle	0.24	0.33
0.4	Red circle	0.25	0.36
0.6	Black square	0.23	0.34
0.8	Red square	0.23	0.34
1.1	Black Triangle	0.22	0.38

Table S2.2: CIE coordinates for 17% (w/w) F127 hydrogels containing BTS at 30 °C at different pH values shown in figure 2.8. BTS concentration is represented as the absorbance of the sample at 335 nm.

A_{335}	pH	Point in figure 2.8	x	y
1.2	4	Black circle	0.24	0.38
1.2	5	Red circle	0.24	0.38
0.9	6	Black square	0.24	0.37
1.1	7	Red square	0.23	0.37
1.2	8	Black Triangle	0.24	0.38

A2.5 Absorbance for BTS in F127 hydrogels at different pH.

The absorbance spectra for BTS in 17% F127 hydrogels at different pH values (figures 2.4-2.8). Since for each pH an individual sample was used, the absorbance at 335 nm was used to quantify the concentration of BTS within the hydrogels. A sharp jump seen around 355 nm is the point of the lamp change on the instrument which could not be eliminated even after subtracting the blank. This lack of lamp jump correction could be because of the high concentration of BTS (A_{335} > 1.0) within the hydrogels. A difference in shape of the absorption spectra is also observed for the BTS in 17% F127 hydrogel sample at pH 6 at shorter wavelengths (figure 2.9) which was not followed up on since the emission spectra were not affected by this change.

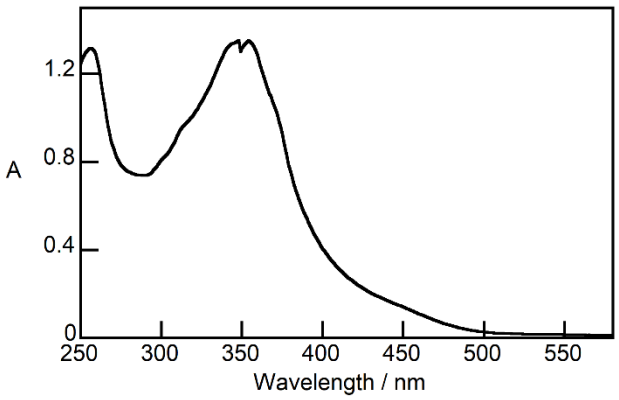

Figure S2.4: Absorbance of BTS in 17% (w/w) F127 at 30 °C at pH 4.

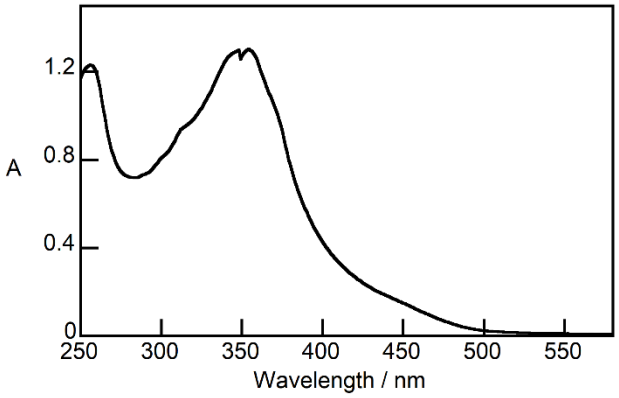

Figure S2.5: Absorbance of BTS in 17% (w/w) F127 at 30 °C at pH 5.

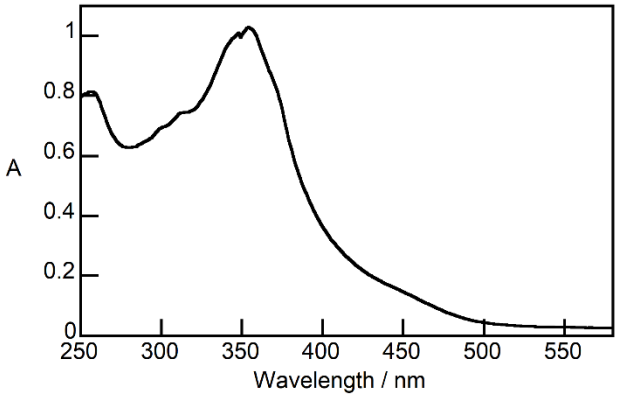

Figure S2.6: Absorbance of BTS in 17% (w/w) F127 at 30 °C at pH 6.

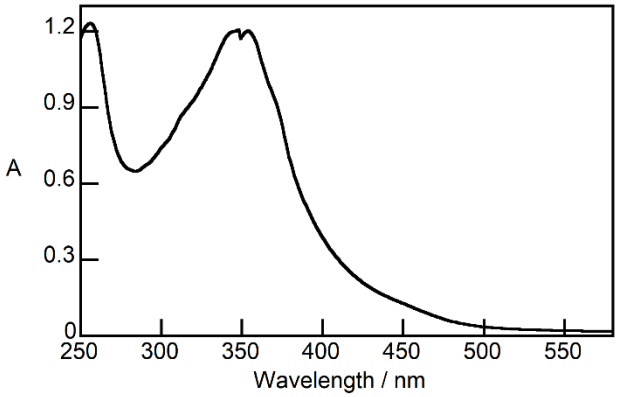

Figure S2.7: Absorbance of BTS in 17% (w/w) F127 at 30 °C at pH 7.

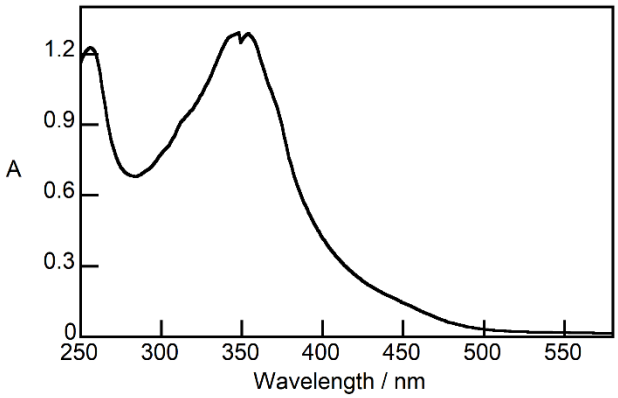

Figure S2.8: Absorbance of BTS in 17% (w/w) F127 at 30 °C at pH 8.

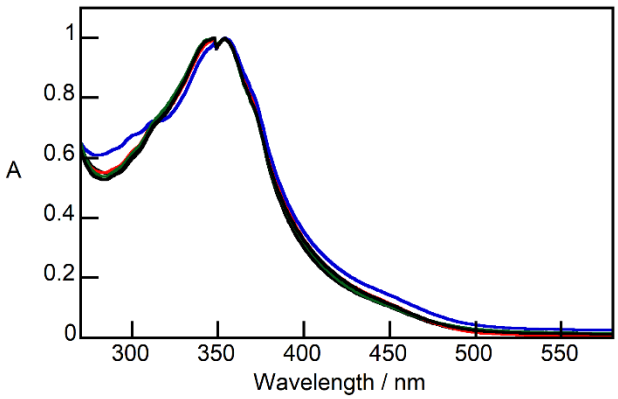

Figure S2.9: Absorbance of BTS normalized at 335 nm in 17% (w/w) F127 at 30 °C at various pH : pH 4 (black), pH 5 (red), pH 6 (blue), pH 7 (green), pH 8 (black).

A2.6 Excitation spectra for BTS in F127 hydrogels monitored at different emission wavelengths.

The normalized excitation spectra measured at different emission wavelengths show the presence of different forms of BTS in 17% (w/w) F127 hydrogels at 30 °C along with the absorbance spectrum for the same sample at 30 °C.

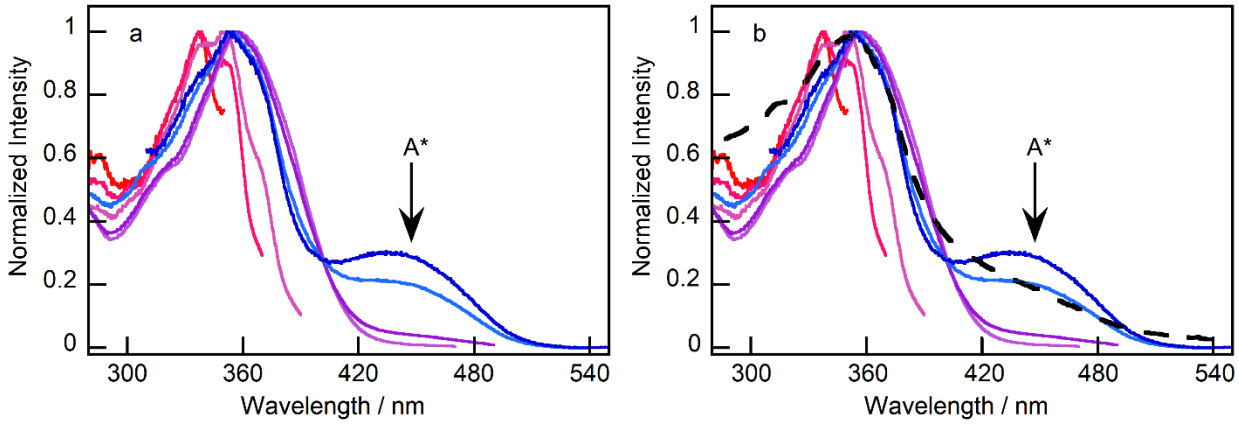

Figure S2.10: (a) Normalized excitation spectra of BTS in 17% (w/w) F127 at 30 °C monitored at different wavelengths. The emission monochromator was fixed at the following wavelengths λ_{em} = 360 nm, 380 nm, 396 nm, 480 nm, 500 nm, 550 nm, and 600 nm (red to blue). (b) The normalized excitation spectra overlapped with the normalized absorption spectra of BTS in 17% (w/w) F127 at 30 °C. The dashed black line represents the absorption spectra of the sample.

A2.7 Time-resolved experiments for the decay of singlet excites state BTS in F127 hydrogels.

The lifetime values for different BTS concentrations in 17% (w/w) F127 hydrogels at 20 °C and 30 °C were determined at different emission wavelengths from the fitting of the fluorescence decays to a sum of exponentials (Table S2.3–S2.8). The lifetimes for individual experiments were averaged since these lifetimes did not change with BTS concentration. The impurity emission from F127 have lifetimes in the same range as for the emission of BTS (Table S2.9). However, the contribution from this impurity emission to the decay of the excited state of

BTS is minimal since the overall intensity of the emission from the F127 impurities is very low compared to the intensity for the BTS emission (Figure 2.3).

Table S2.3: Lifetimes (τ) and corresponding pre-exponential factors (A) for the emission of BTS in 17% F127 (w/w) at 20 °C and 30 °C for samples excited at 335 nm.[a]

T / °C	λ_{em} / nm[b]	A_1	τ_1 / ns	A_2	τ_2 / ns	A_3	τ_3 / ns
20	360	0.61 ± 0.05	0.2 ± 0.1	0.37 ± 0.04	0.8 ± 0.1	0.02 ± 0.02	3 ± 2
20	380	0.49 ± 0.03	0.2 ± 0.1	0.49 ± 0.05	0.8 ± 0.1	0.03 ± 0.03	2.1 ± 0.9
20	400	0.48 ± 0.04	0.2 ± 0.1	0.48 ± 0.04	0.9 ± 0.1	0.04 ± 0.01	2.2 ± 0.2
20	450	0.39 ± 0.04	0.5 ± 0.1	0.33 ± 0.04	1.9 ± 0.1	0.28 ± 0.01	4.6 ± 0.1
20	480	0.26 ± 0.03	0.4 ± 0.2	0.29 ± 0.03	2.3 ± 0.5	0.46 ± 0.03	4.8 ± 0.2
20	500	0.17 ± 0.01	0.5 ± 0.2	0.31 ± 0.03	2.6 ± 0.2	0.52 ± 0.02	4.9 ± 0.1
20	550	0.16 ± 0.03	0.5 ± 0.2	0.49 ± 0.07	3.3 ± 0.2	0.35 ± 0.09	5.9 ± 0.6
20	600	0.18 ± 0.09	0.4 ± 0.2	0.51 ± 0.07	3.2 ± 0.1	0.31 ± 0.03	6.4 ± 0.2
30	360	0.61 ± 0.05	0.2 ± 0.1	0.37 ± 0.03	0.8 ± 0.1	0.02 ± 0.02	2.0 ± 0.7
30	380	0.50 ± 0.04	0.2 ± 0.1	0.47 ± 0.03	0.8 ± 0.1	0.03 ± 0.03	2.0 ± 0.7
30	400	0.50 ± 0.02	0.2 ± 0.1	0.46 ± 0.02	0.8 ± 0.1	0.03 ± 0.01	2.3 ± 0.3
30	450	0.41 ± 0.05	0.4 ± 0.1	0.33 ± 0.03	1.8 ± 0.2	0.27 ± 0.03	4.6 ± 0.1
30	480	0.26 ± 0.02	0.4 ± 0.2	0.26 ± 0.04	2.3 ± 0.3	0.48 ± 0.02	4.7 ± 0.1
30	500	0.19 ± 0.04	0.4 ± 0.1	0.31 ± 0.04	2.5 ± 0.3	0.51 ± 0.05	4.8 ± 0.2
30	550	0.19 ± 0.04	0.5 ± 0.4	0.46 ± 0.05	2.9 ± 0.3	0.34 ± 0.06	5.5 ± 0.3
30	600	0.16 ± 0.03	0.5 ± 0.1	0.55 ± 0.03	3.0 ± 0.1	0.29 ± 0.02	6.0 ± 0.2

[a], Averages from five independent experiments; errors correspond to standard deviations. [b], wavelength for emission detection; ± 8 nm.

Table S2.4: Lifetimes (τ) and corresponding pre-exponential factors (A) for the emission of BTS in 17% F127 (w/w) at 20 °C and 30 °C for samples excited at 335 nm at BTS concentration of A_{335} = 0.4.[a]

T / °C	λ_{em} / nm[b]	A_1	τ_1 / ns	A_2	τ_2 / ns	A_3	τ_3 / ns	χ^2
20	360	0.63±0.01	0.24±0.01	0.37±0.02	0.92±0.01	≤ 0.01	5±1	1.121
20	380	0.47±0.01	0.24±0.02	0.53±0.01	0.89±0.02	0.01±0.01	3±1	1.052
20	400	0.43±0.01	0.22±0.03	0.54±0.01	0.86±0.02	0.04±0.01	2.3±0.1	1.004
20	450	0.39±0.01	0.42±0.05	0.34±0.01	1.65±0.09	0.27±0.01	4.61±0.04	0.937
20	480	0.28±0.01	0.25±0.07	0.26±0.01	2.0±0.1	0.46±0.01	4.80±0.04	1.045
20	500	0.19±0.01	0.30±0.09	0.28±0.01	2.4±0.2	0.53±0.01	4.93±0.05	0.977
20	550	0.19±0.01	0.57±0.09	0.51±0.01	3.5±0.2	0.30±0.01	6.3±0.2	0.966
20	600	0.18±0.01	0.40±0.08	0.49±0.01	3.2±0.1	0.32±0.01	6.6±0.1	1.023
30	360	0.62±0.01	0.15±0.01	0.36±0.01	0.77±0.03	0.03±0.01	1.3±0.1	1.119
30	380	0.50±0.01	0.24±0.03	0.50±0.01	0.87±0.03	≤ 0.01	2.8±0.7	0.974
30	400	0.48±0.01	0.2±0.2	0.47±0.01	0.81±0.02	0.05±0.01	2.11±0.08	1.008
30	450	0.46±0.01	0.37±0.03	0.32±0.01	1.75±0.08	0.22±0.01	4.58±0.05	0.893
30	480	0.27±0.01	0.29±0.07	0.27±0.01	2.0±0.1	0.46±0.01	4.66±0.04	0.907
30	500	0.26±0.01	0.23±0.06	0.29±0.01	2.4±0.1	0.45±0.01	4.81±0.06	1.069
30	550	0.21±0.01	0.30±0.07	0.42±0.01	2.6±0.1	0.37±0.01	5.54±0.07	0.945
30	600	0.20±0.01	0.42±0.01	0.49±0.01	2.89±0.09	0.31±0.01	6.13±0.09	0.938

[a], Errors obtained from the software during the fitting process. [b], wavelength for emission detection; ± 8 nm.

Table S2.5: Lifetimes (τ) and corresponding pre-exponential factors (A) for the emission of BTS in 17% F127 (w/w) at 20 °C and 30 °C for samples excited at 335 nm at BTS concentration of A_{335} = 0.8.[a]

T / °C	λ_{em} / nm[b]	A_1	τ_1 / ns	A_2	τ_2 / ns	A_3	τ_3 / ns	χ^2
20	360	0.57±0.01	0.17±0.02	0.40±0.01	0.81±0.04	0.03±0.01	1.7±0.3	0.938
20	380	0.47±0.01	0.21±0.03	0.51±0.01	0.85±0.04	0.02±0.01	1.8±0.5	1.063
20	400	0.48±0.01	0.21±0.02	0.48±0.01	0.97±0.03	0.03±0.01	2.2±0.2	1.161
20	450	0.37±0.01	0.48±0.06	0.34±0.01	1.9±0.1	0.29±0.01	4.57±0.06	0.931
20	480	0.28±0.01	0.73±0.08	0.31±0.01	3.2±0.5	0.41±0.01	5.1±0.2	0.955
20	500	0.15±0.01	0.5±0.1	0.37±0.01	2.8±0.2	0.48±0.01	5.0±0.1	1.019
20	550	0.17±0.01	0.26±0.09	0.49±0.01	3.1±0.1	0.35±0.01	5.9±0.1	1.035
20	600	0.13±0.01	0.3±0.1	0.56±0.01	3.27±0.09	0.31±0.01	6.6±0.1	0.994
30	360	0.53±0.01	0.19±0.03	0.41±0.01	0.76±0.06	0.06±0.01	1.4±0.2	1.048
30	380	0.46±0.01	0.20±0.03	0.49±0.01	0.80±0.06	0.05±0.01	1.5±0.3	0.932
30	400	0.49±0.01	0.17±0.02	0.48±0.01	0.82±0.02	0.03±0.01	2.2±0.1	0.917
30	450	0.40±0.01	0.37±0.04	0.34±0.01	1.82±0.09	0.26±0.01	4.63±0.05	0.965
30	480	0.24±0.01	0.47±0.08	0.27±0.01	2.5±0.2	0.49±0.01	4.76±0.07	0.945
30	500	0.19±0.01	0.4±0.1	0.30±0.01	2.5±0.2	0.51±0.01	4.79±0.07	1.053
30	550	0.22±0.01	0.35±0.07	0.53±0.01	3.2±0.1	0.26±0.01	5.9±0.2	0.960
30	600	0.17±0.01	0.39±0.09	0.56±0.01	3.05±0.09	0.27±0.01	6.1±0.1	0.937

[a], Errors obtained from the software during the fitting process. [b], wavelength for emission detection; ± 8 nm.

Table S2.6: Lifetimes (τ) and corresponding pre-exponential factors (A) for the emission of BTS in 17% F127 (w/w) at 20 °C and 30 °C for samples excited at 335 nm at BTS concentration of A_{335} = 0.2.[a]

T / °C	λ_{em} / nm[b]	A_1	τ_1 / ns	A_2	τ_2 / ns	A_3	τ_3 / ns	χ^2
20	360	0.69±0.01	0.14±0.01	0.30±0.01	0.87±0.01	0.01±0.01	3.3±0.2	0.995
20	380	0.50±0.01	0.16±0.02	0.48±0.01	0.86±0.01	0.02±0.01	2.6±0.2	1.131
20	400	0.52±0.01	0.17±0.02	0.44±0.01	0.88±0.02	0.05±0.01	2.47±0.07	1.029
20	450	0.35±0.01	0.39±0.05	0.35±0.01	2.0±0.1	0.29±0.01	4.57±0.06	0.961
20	480	0.25±0.01	0.22±0.07	0.29±0.01	2.3±0.1	0.46±0.01	4.48±0.05	0.995
20	500	0.18±0.01	0.3±0.1	0.29±0.02	2.5±0.2	0.53±0.01	4.91±0.06	0.935
20	550	0.16±0.01	0.6±0.1	0.58±0.01	3.6±0.1	0.25±0.01	6.6±0.2	1.025
20	600	0.18±0.01	0.28±0.09	0.48±0.01	3.18±0.09	0.34±0.01	6.51±0.09	0.970
30	360	0.67±0.01	0.14±0.01	0.32±0.01	0.85±0.01	0.01±0.01	3.1±0.2	1.051
30	380	0.52±0.01	0.18±0.02	0.47±0.01	0.87±0.02	0.02±0.01	2.6±0.3	1.188
30	400	0.52±0.01	0.19±0.02	0.45±0.01	0.89±0.02	0.03±0.01	2.6±0.1	1.046
30	450	0.36±0.01	0.59±0.06	0.35±0.01	2.1±0.2	0.29±0.01	4.72±0.08	0.906
30	480	0.23±0.01	0.43±0.09	0.31±0.01	2.6±0.2	0.46±0.01	4.88±0.08	1.003
30	500	0.17±0.01	0.5±0.1	0.37±0.01	3.0±0.2	0.46±0.01	5.0±0.1	0.912
30	550	0.24±0.01	0.25±0.08	0.41±0.01	2.71±0.09	0.35±0.01	5.55±0.07	0.994
30	600	0.18±0.01	0.44±0.08	0.54±0.01	3.06±0.09	0.28±0.01	6.2±0.1	0.954

[a], Errors obtained from the software during the fitting process. [b], wavelength for emission detection; ± 8 nm.

Table S2.7: Lifetimes (τ) and corresponding pre-exponential factors (A) for the emission of BTS in 17% F127 (w/w) at 20 °C and 30 °C for samples excited at 335 nm at BTS concentration of A_{335} = 0.6.[a]

T / °C	λ_{em} / nm[b]	A_1	τ_1 / ns	A_2	τ_2 / ns	A_3	τ_3 / ns	χ^2
20	360	0.57±0.01	0.21±0.02	0.40±0.01	0.81±0.05	0.03±0.01	1.7±0.4	1.001
20	380	0.44±0.01	0.19±0.03	0.51±0.01	0.77±0.05	0.05±0.01	1.5±0.2	0.966
20	400	0.46±0.01	0.22±0.03	0.51±0.01	0.85±0.02	0.04±0.01	2.25±0.09	0.964
20	450	0.37±0.01	0.47±0.05	0.36±0.01	1.9±0.1	0.27±0.01	4.65±0.06	0.929
20	480	0.22±0.01	0.36±0.09	0.32±0.01	2.2±0.1	0.46±0.01	4.83±0.05	0.964
20	500	0.16±0.01	0.8±0.2	0.32±0.01	2.7±0.4	0.51±0.01	4.9±0.1	0.986
20	550	0.16±0.01	0.30±0.09	0.48±0.01	3.1±0.1	0.36±0.01	4.9±0.1	0.992
20	600	0.32±0.01	0.16±0.05	0.41±0.01	3.05±0.08	0.27±0.01	6.22±0.09	0.975
30	360	0.61±0.01	0.16±0.02	0.38±0.01	0.80±0.03	0.01±0.01	1.8±0.3	1.008
30	380	0.47±0.01	0.16±0.04	0.45±0.01	0.73±0.05	0.08±0.01	1.4±0.1	1.100
30	400	0.48±0.01	0.20±0.03	0.48±0.01	0.86±0.02	0.03±0.01	2.4±0.1	1.171
30	450	0.36±0.01	0.37±0.05	0.36±0.01	1.61±0.08	0.28±0.01	4.47±0.04	1.033
30	480	0.24±0.01	0.25±0.09	0.28±0.01	1.9±0.1	0.48±0.01	4.64±0.04	0.968
30	500	0.14±0.01	0.4±0.1	0.32±0.01	2.3±0.2	0.54±0.01	4.72±0.06	1.020
30	550	0.14±0.01	0.4±0.2	0.44±0.01	2.7±0.1	0.42±0.01	5.21±0.08	0.966
30	600	0.15±0.01	0.5±0.1	0.58±0.01	2.97±0.09	0.27±0.01	6.0±0.1	0.993

[a], Errors obtained from the software during the fitting process. [b], wavelength for emission detection; ± 8 nm.

Table S2.8: Lifetimes (τ) and corresponding pre-exponential factors (A) for the emission of BTS in 17% F127 (w/w) at 20 °C and 30 °C for samples excited at 335 nm at BTS concentration of A_{335} = 1.1.[a]

T / °C	λ_{em} / nm[b]	A_1	τ_1 / ns	A_2	τ_2 / ns	A_3	τ_3 / ns	χ^2
20	360	0.57±0.01	0.19±0.03	0.39±0.01	0.73±0.06	0.04±0.01	1.4±0.2	0.971
20	380	0.53±0.01	0.14±0.03	0.40±0.01	0.73±0.06	0.07±0.01	1.3±0.2	0.996
20	400	0.51±0.01	0.15±0.02	0.46±0.01	0.79±0.02	0.03±0.01	1.9±0.2	0.981
20	450	0.45±0.01	0.55±0.06	0.25±0.01	1.8±0.2	0.30±0.01	4.52±0.06	0.981
20	480	0.24±0.01	0.4±0.1	0.27±0.01	2.0±0.2	0.49±0.01	4.69±0.04	0.934
20	500	0.17±0.01	0.5±0.1	0.30±0.01	2.5±0.2	0.54±0.01	4.80±0.07	1.004
20	550	0.12±0.01	0.6±0.2	0.40±0.04	3.4±0.2	0.48±0.02	5.8±0.2	0.942
20	600	0.09±0.01	0.6±0.2	0.60±0.01	3.4±0.1	0.31±0.01	6.3±0.2	0.940
30	360	0.61±0.01	0.18±0.02	0.38±0.01	0.79±0.03	0.01±0.01	2.3±0.7	0.965
30	380	0.55±0.01	0.14±0.02	0.43±0.01	0.78±0.03	0.01±0.01	1.7±0.4	1.079
30	400	0.53±0.01	0.15±0.02	0.44±0.01	0.78±0.03	0.03±0.01	1.9±0.2	1.156
30	450	0.45±0.01	0.48±0.05	0.27±0.01	1.7±0.1	0.27±0.01	4.50±0.05	1.047
30	480	0.29±0.01	0.7±0.1	0.19±0.01	2.5±0.6	0.51±0.01	4.5±0.1	1.002
30	500	0.18±0.01	0.5±0.1	0.25±0.01	2.4±0.3	0.57±0.01	4.51±0.07	1.019
30	550	0.17±0.01	1.2±0.3	0.52±0.01	3.4±0.5	0.32±0.01	5.4±0.5	1.074
30	600	0.12±0.01	0.6±0.2	0.57±0.01	3.0±0.1	0.32±0.01	5.7±0.1	0.995

[a], Errors obtained from the software during the fitting process. [b], wavelength for emission detection; ± 8 nm.

Table S2.9: Lifetimes (τ) and corresponding pre-exponential factors (A) for the emission of 17% F127 (w/w) at 20 °C and 30 °C for samples excited at 335 nm.[a]

T / °C	λ_{em} / nm[b]	A_1	τ_1 / ns	A_2	τ_2 / ns	A_3	τ_3 / ns	χ^2
20	360	1.0±0.2	0.01±0.01	≤ 0.01	2.5±0.1	≤ 0.01	9±1	1.040
20	380	0.84±0.01	0.16±0.01	0.15±0.01	2.36±0.03	0.02±0.01	9.5±0.1	1.148
20	400	0.57±0.01	0.44±0.02	0.39±0.01	2.56±0.03	0.04±0.01	10.0±0.2	1.092
20	450	0.58±0.01	0.46±0.02	0.37±0.01	2.55±0.04	0.05±0.01	8.5±0.2	1.206
20	480	0.60±0.01	0.45±0.02	0.36±0.01	2.74±0.04	0.05±0.01	9.4±0.2	1.101
30	360	1.00±0.01	0.01±0.01	≤ 0.01	2.61±0.09	≤ 0.01	10±1	1.172
30	380	0.87±0.03	0.12±0.01	0.11±0.01	2.35±0.02	0.01±0.01	9.5±0.1	1.061
30	400	0.59±0.01	0.31±0.02	0.37±0.01	2.42±0.03	0.04±0.01	9.4±0.1	1.184
30	450	0.55±0.01	0.40±0.02	0.40±0.01	2.56±0.04	0.05±0.01	8.2±0.2	1.059
30	480	0.61±0.01	0.49±0.02	0.35±0.01	2.73±0.04	0.05±0.01	9.6±0.2	1.131

[a], Errors obtained from the software during the fitting process. [b], wavelength for emission detection; ± 8 nm.

Chapter 3

A3.1 Choosing of the wavelength range 382–398 nm for the steady-state Stern-Volmer analysis.

Control experiments were conducted to establish the correct methodology for data analysis to verify the authenticity of the quenching mechanism observed when quenching pyrene with I^- due to the possibility of artifacts resulting from the molecular structure of both the species and polarity sensitive nature of pyrene. As discussed earlier, the intensity of peak I of pyrene emission spectra is sensitive to polarity. This relative variability for the intensity of peak I of pyrene results in Stern-Volmer plots with possible artifacts. Observation of a static quenching mechanism between pyrene and I^-, would indicate a ground-state complexation between pyrene and I^-, which is unlikely based on the structure of both the species involved. Control experiments were done to establish the correct methodology for data analysis since a change of the relative intensity for the I peak could distort the A_o/A values. Pyrene was quenched by I^- in 15 mM NaDC solutions where it was observed that pyrene is present in two microenvironments (water and aggregates). The steady-state spectra of pyrene were integrated over multiple wavelength ranges and compared to the average lifetime ratio (average lifetime calculated using equation 3.4 and tables S3.1–S3.4) in the Stern-Volmer plots (figures S3.1 and S3.2). The optimal wavelength range for integration of fluorescence area was 382–398 nm (figures S3.3 and S3.4), which corresponded to the bandwidth (16 nm) used on the single photon counter (16 nm) when monitoring the fluorescence decays. When pyrene is in the homogeneous aqueous environment the wavelength range chosen for integration does not matter (figure 3.4) as expected for an experiment where the I/III ratio remains constant, showing that the wavelength range and bandwidth chosen for steady-state Stern-Volmer plots should be the same as those for the time-

resolved studies for pyrene is in a microenvironment with sites with different polarities (tables S3.5 and S3.6).

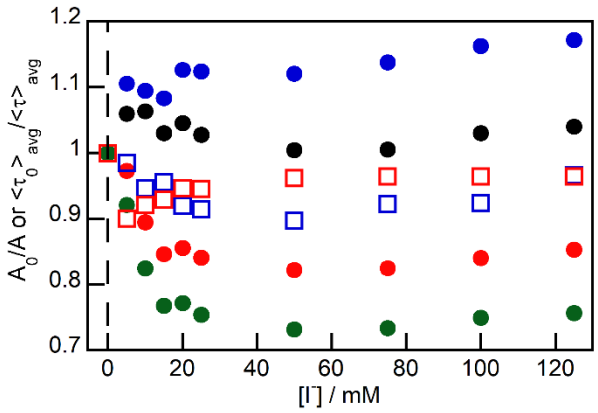

Figure S3.1: Stern-Volmer plot for 2.0 µM pyrene in 15 mM NaDC solution using I^- as a quencher (Control 1). The steady-state values (A_0/A) are shown as filled symbols and the time-resolved values are shown as unfilled symbols. (1) 367–410 nm area ratio (red circle) (2) 367–372 nm area ratio (blue circle) (3) 382–398 nm area ratio (black circle) (4) 378–383 nm area ratio (green circle) (5) $\langle\tau_0\rangle_{avg}/\langle\tau\rangle_{avg}$ using table S3.1 (blue square) (6) $\langle\tau_0\rangle_{avg}/\langle\tau\rangle_{avg}$ using table S3.2 (red square). The dashed black line indicates the origin on the concentration axis.

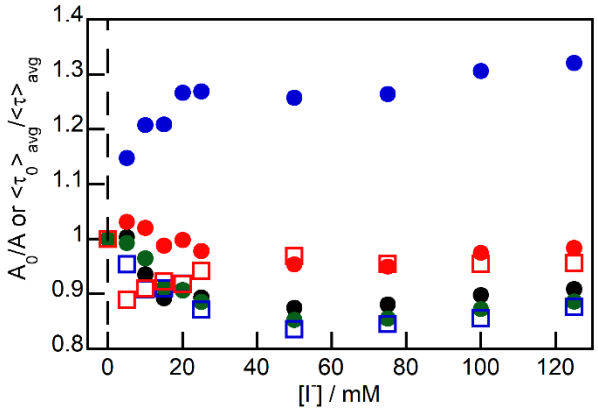

Figure S3.2: Stern-Volmer plot for 2.0 µM pyrene in 15 mM NaDC solution using I^- as a quencher (Control 2). The steady-state values (A_0/A) are shown as filled symbols and the time-resolved values are shown as unfilled symbols. (1) 367–410 nm area ratio (black circle) (2) 367–372 nm area ratio (blue circle) (3) 382–398 nm area ratio (red circle) (4) 378–383 nm area ratio (green circle) (5) $\langle\tau_0\rangle_{avg}/\langle\tau\rangle_{avg}$ using table S3.3 (blue square) (6) $\langle\tau_0\rangle_{avg}/\langle\tau\rangle_{avg}$ using table S3.4 (red square). The dashed black line indicates the origin on the concentration axis.

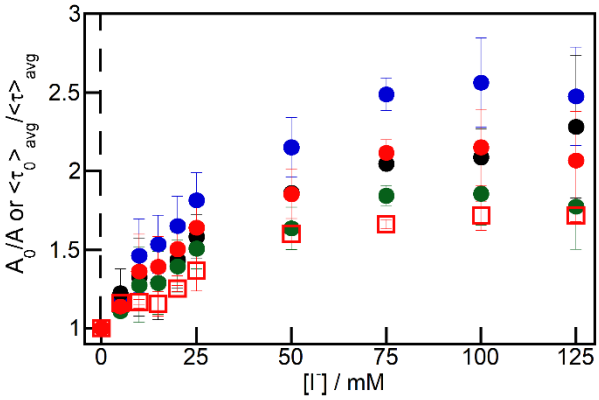

Figure S3.3: Stern-Volmer plot for 2.0 µM pyrene in 30 mM NaDC hydrogels having [Na^+] = 305 mM using I^- as a quencher. The steady-state values (A_0/A) are shown as filled symbols and the time-resolved values are shown as unfilled symbols. (1) 367–410 nm area ratio (black circle) (2) 367–372 nm area ratio (blue circle) (3) 382–398 nm area ratio (red circle) (4) 378–383 nm area ratio (green circle) (5) $\langle\tau_0\rangle_{avg}/\langle\tau\rangle_{avg}$ (red square). Values reported are averages of three individual experiments and the errors are the standard deviation of three individual experiments. The values reported for 0 and 25 mM I^- is an average of six individual experiments and the errors are the standard deviation of six individual experiments. The dashed black line indicates the origin on the concentration axis.

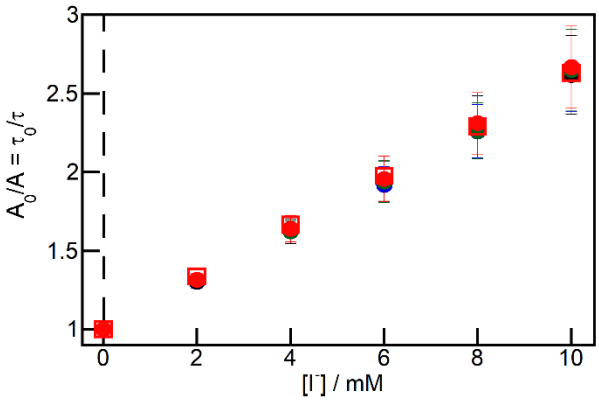

Figure S3.4: Stern-Volmer plot for 0.5 µM pyrene in water using I^- as a quencher. The steady-state values (A_0/A) are shown as filled symbols and the time-resolved values are shown as unfilled symbols. (1) 367– 410 nm (black circle) (2) 367–372 nm area ratio (blue circle) (3) 382–398 nm area ratio (red circle) (4) 378–383 nm area ratio (green circle) (5) $\langle\tau_0\rangle_{avg}/\langle\tau\rangle_{avg}$ (red square). Values reported are averages of three individual experiments and the errors are the standard deviation of three individual experiments. The dashed black line indicates the origin on the concentration axis.

Table S3.1: Lifetimes and pre-exponential factor values for 2.0 μM pyrene in a 15mM NaDC solution with increasing I^- concentrations of control 1.

I^- / mM	A_1[b]	τ_1 /ns[a]	A_2[b]	τ_2 / ns[c]	χ^2
0	0.45	133	0.55	364	1.062
5	0.29	73.3	0.71	342	1.065
10	0.23	50.5	0.77	342	1.160
15	0.22	38.6	0.78	338	1.160
20	0.19	31.2	0.81	342	1.173
25	0.19	26.2	0.81	345	1.097
50	0.2	14.6	0.8	359	1.162
75	0.2	10.1	0.8	350	1.174
100	0.2	7.7	0.8	350	1.058
125	0.23	6.2	0.77	348	1.103

[a], fixed during analysis with values obtained from equation S3.1. [b], fixed during analysis. [c], error on the value is ± 1 and obtained from the fitting software.

Table S3.2: Lifetime and pre-exponential factor values for 2.0 μM pyrene in a 15mM NaDC solution with increasing I^- concentrations of control 1.

I^- / mM	A_1[a]	τ_1 /ns	A_2[a]	τ_2 / ns[a]	χ^2
0	0.46	140. ± 1	0.54	350	1.193
5	0.25	76.2 ± 0.1	0.75	350	1.143
10	0.25	51.5 ± 0.1	0.75	350	1.158
15	0.25	41.7 ± 0.1	0.75	350	1.163
20	0.25	21.6 ± 0.1	0.75	350	1.174
25	0.25	22.2 ± 0.1	0.75	350	1.193
50	0.25	4.2 ± 0.1	0.75	350	1.095
75	0.25	1.8 ± 0.1	0.75	350	1.101
100	0.25	1.8 ± 0.1	0.75	350	1.005
125	0.25	1.8± 0.1	0.75	350	1.014

[a], fixed during analysis.

Table S3.3: Lifetime and pre-exponential factor values for 2.0 μM pyrene in a 15mM NaDC solution with increasing I^- concentrations of control 2.

I^- / mM	A_1[b]	τ_1 /ns[a]	A_2[b]	τ_2 / ns[c]	χ^2
0	0.46	133	0.54	352	1.117
5	0.29	73.3	0.71	341	1.173
10	0.24	50.5	0.76	348	1.150
15	0.23	38.6	0.77	347	1.102
20	0.24	31.2	0.76	350	1.174
25	0.21	26.2	0.79	358	1.191
50	0.16	14.6	0.84	355	1.117
75	0.16	10.1	0.84	352	1.008
100	0.16	7.7	0.84	348	1.129
125	0.16	6.2	0.84	340	1.160

[a], fixed during analysis with values obtained from equation S3.1. [b], fixed during analysis. [c], error on the value is ± 1 and obtained from the fitting software.

Table S3.4: Lifetime and pre-exponential factor values for 2.0 μM pyrene in a 15mM NaDC solution with increasing I^- concentrations of control 2.

I^- / mM	A_1[a]	τ_1 /ns	A_2[a]	τ_2 / ns[a]	χ^2
0	0.46	135 ± 1	0.54	351	1.098
5	0.25	78.8 ± 0.1	0.75	351	1.191
10	0.25	53.4 ± 0.1	0.75	351	1.106
15	0.25	38 ± 1	0.75	351	1.166
20	0.24	31 ± 1	0.76	351	1.165
25	0.25	15.4 ± 0.1	0.75	351	1.248
50	0.26	0.09 ± 0.1	0.74	351	1.087
75	0.25	1.04 ± 0.1	0.75	351	0.960
100	0.25	0.9 ± 0.1	0.75	351	1.089
125	0.25	0.05 ± 0.05	0.75	351	1.089

[a], fixed during analysis.

Table S3.5: I/III ratios for 2.0 μM pyrene in a 15 mM NaDC solution with increasing I^- concentrations of control 1. No errors reported as this is an independent experiment.

I^- / mM	I/III
0	1.19
5	1.00
10	0.92
15	0.87
20	0.82
25	0.80
50	0.79
75	0.78
100	0.77
125	0.77

Table S3.6: I/III ratios for 2.0 μM pyrene in a 15 mM NaDC solution with increasing I^- concentrations of control 2. No errors reported as this is an independent experiment.

I^-/ mM	**I/III**
0	1.26
5	0.99
10	0.90
15	0.85
20	0.83
25	0.81
50	0.78
75	0.77
100	0.78
125	0.78

A3.2 Quenching of pyrene in water by I^- and CH_3NO_2.

Pyrene was quenched by I^- (figure S3.5) and CH_3NO_2 (figure S3.6) in water, from which Stern-Volmer quenching plots were generated. The Stern-Volmer constant (K_{SV}) and the quenching rate constants (k_q) obtained (table S3.7) were used to generate equations S3.1 and S3.2 for the respective quenchers. These equations were then used to calculate the theoretical lifetime values for pyrene in water at the relevant quencher concentrations used to quench pyrene in 30 mM NaDC hydrogels. These theoretical values obtained were kept constant when fitting the lifetime decay traces for pyrene in 30 mM NaDC hydrogels (τ_1).

Table S3.7: Stern-Volmer constants (K_{SV}) and quenching rate constants (k_q) for pyrene quenched by different quenchers in water.[a]

[Q]	$\boldsymbol{K_{sv}}$ **/ M^{-1}**	$\boldsymbol{k_q}$ **/ 10^9 M^{-1} s^{-1}**
I^-	161 ± 1	1.2 ± 0.1
CH_3NO_2	107 ± 1	7.7 ± 0.3

[a]The values reported are the average of two individual experiments and the errors are the average deviation between the two individual experiments.

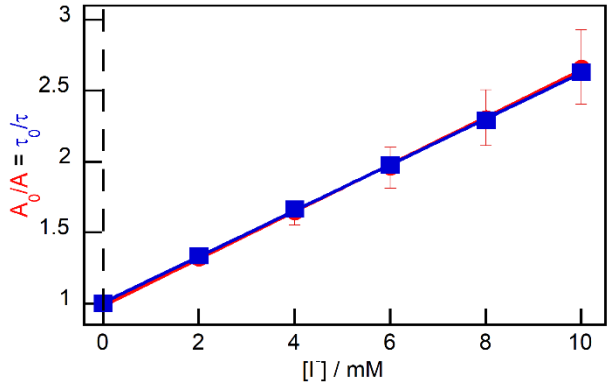

Figure S3.5: Stern-Volmer quenching plot for 0.5 µM pyrene in water using I^- as quencher. The values reported are for two independent experiments and the errors are the average deviation of two experiments. The red line corresponds to the steady-state Stern-Volmer plot and the blue line corresponds to the time-resolved Stern-Volmer plot. The dashed black line indicates the origin on the concentration axis.

$$k_{obs} = (7.6 \times 10^6) + (1.2 \times 10^9)[NaI] \quad \text{(Eq. S3.1)}$$

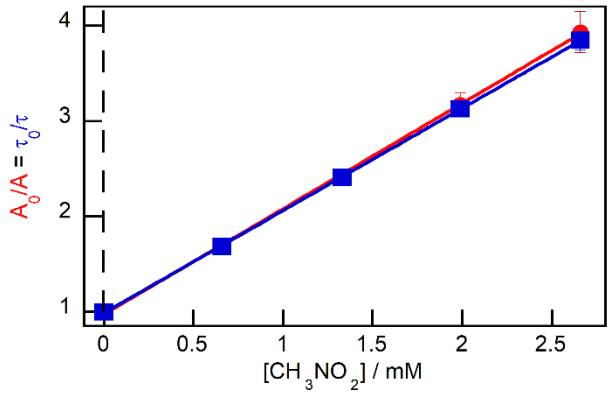

Figure S3.6: Stern-Volmer quenching plot for 0.5 µM pyrene in water using CH_3NO_2 as quencher. The values reported are for two independent experiments and the errors are the average deviation of two experiments. The red line corresponds to the steady-state Stern-Volmer plot and the blue line corresponds to the time-resolved Stern-Volmer plot. The dashed black line indicates the origin on the concentration axis.

$$k_{obs} = (7.6 \times 10^6) + (7.7 \times 10^9)[CH_3NO_2] \quad \text{(Eq S3.2)}$$

A3.3 Analysis of time-resolved lifetime data for excited pyrene quenched in NaDC hydrogels by I^-.

In table S3.8, the lifetime values obtained for pyrene when I^- is used as quencher are reported. These values are averages for the individual experiment and the errors are the standard deviation for those experiments. During the analysis of a single experiment, τ_1 and the A_1, A_2 and A_3 values were fixed to obtain values τ_2 and τ_3 (tables S3.9, S3.11, S3.13, S3.15, S.17 and S3.19). The A_1, A_2 and A_3 values indicate the contribution of the differently localized pyrene species to the decay trace. In static quenching, the fraction of fluorophore available for excitation decreases with increasing quencher concentration. This would result in the statically quenched fluorophore to contribute less to the decay trace, which should be visible via a decrease in the A value corresponding to the statically quenched fluorophore with increasing quencher concentration. However, during the initial fitting process the value of A_1, which belongs to pyrene in water was seen to decrease with increasing quencher concentration. Based on figure S3.5, the mechanism of quenching pyrene in water by I^- is mostly dynamic and this result prompted us to modify our analysis procedure into fixing the A_1, A_2 and A_3 values. In the initial fittings where τ_1 and the A_1, A_2 and A_3 values were fixed, it was observed that τ_3 was not being quenched by I^-, therefore, the τ_3 value was averaged for the individual experiment to obtain a $<\tau_3>_{avg}$ value. This initial analysis was based on assumptions which limited our ability to interpret the results. Firstly, by fixing the A_i values at all quencher concentrations we assume that only dynamic quenching takes place within the hydrogels irrespective of quencher concentration. As seen from figure S3.7 (see figure in the next section below), this is not the case at higher quencher concentrations. Secondly, the lack of quenching of τ_3 could be because of pyrene being in a microenvironment that is inaccessible to I^- or pyrene localized in a highly constrained microenvironment being statically

quenched by I^-. However, the contribution from static quenching is assumed to be small. Therefore to experimentally elucidate the reasons for τ_3 being unquenched, the analysis was further modified. The τ_3 values obtained for an individual experiment at different quencher concentrations were averaged to obtain a $<\tau_3>_{avg}$ value. This allowed a fit where only two values were kept constant (τ_1 and τ_3) and the rest of the values were recovered from the fit allowing me to overcome the limitations posed by my initial analysis. The decay traces of the individual experiment were then refitted using equation 3.3 by fixing τ_1 to the value obtained via equation S3.1 and fixing τ_3 to the $<\tau_3>_{avg}$ value for each experiment. The new fitted values obtained (tables S3.10, S3.12, S3.14, S3.16, S.18 and S3.20) were averaged and the errors reported in table S3.8 and table 3.3.

Table S3.8: Lifetimes and pre-exponential factors for the emission from the singlet excited state of 2.0 μM pyrene in 30 mM NaDC hydrogels with varying I^- concentrations.[a] The values reported are the averages for the data in tables S3.10, S3.12, S3.14, S3.16, S.18 and S3.20.

I^- / mM	A_1	τ_1 /ns[b]	A_2	τ_2 / ns	A_3	τ_3 / ns
0[c]	0.37 ± 0.09	133	0.3 ± 0.1	180 ± 20	0.38 ± 0.01	360 ± 20
5	0.37 ± 0.03	73.3	0.32 ± 0.05	200 ± 10	0.31 ± 0.02	378 ± 6
10[d]	0.32 ± 0.01	50.5	0.30 ± 0.01	160 ± 10	0.38 ± 0.01	379 ± 9
15	0.32 ± 0.01	38.6	0.27 ± 0.04	150 ± 10	0.41 ± 0.04	378 ± 6
20	0.34 ± 0.01	31.2	0.30 ± 0.02	150 ± 10	0.36 ± 0.01	378 ± 6
25[c]	0.38 ± 0.07	26.2	0.27 ± 0.03	130 ± 10	0.35 ± 0.04	360 ± 20
50	0.44 ± 0.01	14.6	0.25 ± 0.01	102 ± 3	0.31 ± 0.01	350 ± 10
75	0.44 ± 0.02	10.1	0.25 ± 0.01	92 ± 8	0.30 ± 0.01	350 ± 10
100	0.46 ± 0.03	7.7	0.24 ± 0.02	93 ± 6	0.30 ± 0.01	350 ± 10
125	0.45 ± 0.01	6.2	0.25 ± 0.01	89 ± 5	0.30 ± 0.01	350 ± 10

[a], The total Na^+ concentration was kept constant at 305 mM. The values reported are averages of three individual experiments and the errors are standard deviation for the three individual experiments. [b], fixed values were obtained using equation S3.1. [c], average of six individual experiments. [d], average of two individual experiments and errors are the average deviation of two individual experiments.

Table S3.9: Lifetimes and pre-exponential factors for the emission from the singlet excited state of 2.0 μM pyrene in 30 mM NaDC hydrogels with varying I^- concentrations for a single quenching experiment.[a]

I^- / mM	A_1[b]	τ_1 /ns[c]	A_2[b]	τ_2 / ns	A_3[b]	τ_3 / ns[d]
0	0.31	133	0.32	161 ± 1	0.37	340
25	0.31	26	0.32	104 ± 1	0.37	346
50	0.31	14.6	0.32	102 ± 1	0.37	338
75	0.31	10.1	0.32	86.8 ± 0.1	0.37	339
100	0.31	7.7	0.32	87.6 ± 0.1	0.37	336
125	0.31	6.2	0.32	96.3 ± 0.1	0.37	338

[a], The total Na^+ concentration was kept constant at 305 mM. [b], fixed during analysis. [c], fixed values were obtained using equation S3.1. [d], error for these values is ± 1 which were obtained from the fitting software.

Table S3.10: Lifetimes and pre-exponential factors for the emission from the singlet excited state of 2.0 μM pyrene in 30 mM NaDC hydrogels with varying I^- concentrations for a single quenching experiment.[a]

I^- / mM	A_1[d]	τ_1 /ns[b]	A_2[d]	τ_2 / ns	A_3[d]	τ_3 / ns[c]	χ^2
0	0.20	133	0.44	161 ± 1	0.36	339.5	1.143
25	0.43	26	0.24	109 ± 1	0.33	339.5	1.031
50	0.45	14.6	0.25	101 ± 1	0.30	339.5	1.092
75	0.42	10.1	0.27	85.1 ± 0.1	0.31	339.5	1.051
100	0.49	7.7	0.23	95.9 ± 0.1	0.28	339.5	1.049
125	0.43	6.2	0.27	87.3 ± 0.1	0.30	339.5	1.173

[a], The total Na^+ concentration was kept constant at 305 mM. [b], fixed values were obtained using equation S3.1. [c], fixed values obtained from averaging the τ_3 values of table S3.9. [d], error for these values is ± 0.01 which were obtained from the fitting software.

Table S3.11: Lifetimes and pre-exponential factors for the emission from the singlet excited state of 2.0 μM pyrene in 30 mM NaDC hydrogels with varying I^- concentrations for a single quenching experiment.[a]

I^- / mM	A_1[b]	τ_1 /ns[c]	A_2[b]	τ_2 / ns	A_3[b]	τ_3 / ns[d]
0	0.31	133	0.32	167 ± 1	0.37	349
25	0.31	26	0.32	102 ± 1	0.37	335
50	0.31	14.6	0.32	92.5 ± 0.1	0.37	348
75	0.31	10.1	0.32	89.2 ± 0.1	0.37	346
100	0.31	7.7	0.32	87 ± 1	0.37	348
125	0.31	6.2	0.32	93.6 ± 0.1	0.37	346

[a], The total Na^+ concentration was kept constant at 305 mM. [b], fixed during analysis. [c], fixed values were obtained using equation S3.1. [d], error for these values is ± 1 which were obtained from the fitting software.

Table S3.12: Lifetimes and pre-exponential factors for the emission from the singlet excited state of 2.0 μM pyrene in 30 mM NaDC hydrogels with varying I^- concentrations for a single quenching experiment.[a]

I^- / mM	A_1[d]	τ_1 /ns[b]	A_2[d]	τ_2 / ns	A_3[d]	τ_3 / ns[c]	χ^2
0	0.38	133	0.24	167 ± 1	0.38	345	1.085
25	0.43	26.2	0.26	121 ± 1	0.30	345	1.039
50	0.44	14.6	0.25	98.6 ± 0.1	0.31	345	0.999
75	0.45	10.1	0.25	89.5 ± 0.1	0.30	345	1.157
100	0.46	7.7	0.24	86.6 ± 0.1	0.30	345	1.083
125	0.45	6.2	0.26	84.6 ± 0.1	0.30	345	1.146

[a], The total Na^+ concentration was kept constant at 305 mM. [b], fixed values were obtained using equation S3.1. [c], fixed values obtained from averaging the τ_3 values of table S3.11. [d], error for these values is ± 0.01 which were obtained from the fitting software.

Table S3.13: Lifetimes and pre-exponential factors for the emission from the singlet excited state of 2.0 μM pyrene in 30 mM NaDC hydrogels with varying I^- concentrations for a single quenching experiment.[a]

I^- / mM	A_1[b]	τ_1 /ns[c]	A_2[b]	τ_2 / ns	A_3[b]	τ_3 / ns[d]
0	0.31	133	0.32	165 ± 1	0.37	358
25	0.31	26	0.32	105 ± 1	0.37	355
50	0.31	14.6	0.32	95 ± 1	0.37	360
75	0.31	10.1	0.32	93.1 ± 0.1	0.37	357
100	0.31	7.7	0.32	98.7 ± 0.1	0.37	360
125	0.31	6.2	0.32	96.6 ± 0.1	0.37	363

[a], The total Na^+ concentration was kept constant at 305 mM. [b], fixed during analysis. [c], fixed values were obtained using equation S3.1. [d], error for these values is ± 1 which were obtained from the fitting software.

Table S3.14: Lifetimes and pre-exponential factors for the emission from singlet excited state of 2.0 μM pyrene in 30 mM NaDC hydrogels with varying I^- concentrations for a single quenching experiment.[a]

I^- / mM	A_1[d]	τ_1 /ns[b]	A_2[d]	τ_2 / ns	A_3[d]	τ_3 / ns[c]
0	0.46	133	0.16	165 ± 1	0.38	359
25	0.45	26.2	0.24	124 ± 1	0.31	359
50	0.44	14.6	0.24	105 ± 1	0.32	359
75	0.46	10.1	0.24	101 ± 1	0.30	359
100	0.43	7.7	0.26	97.4 ± 0.1	0.31	359
125	0.46	6.2	0.24	94.9 ± 0.1	0.30	359

[a], The total Na^+ concentration was kept constant at 305 mM. [b], fixed values were obtained using equation S3.1. [c], fixed values obtained from averaging the τ_3 values of table S3.13. [d], error for these values is ± 0.01 which were obtained from the fitting software.

Table S3.15: Lifetimes and pre-exponential factors for the emission from the singlet excited state of 2.0 µM pyrene in 30 mM NaDC hydrogels with varying I^- concentrations for a single quenching experiment.[a]

I^- / mM	A_1[b]	τ_1 /ns[c]	A_2[b]	τ_2 / ns[d]	A_3[b]	τ_3 / ns[d]
0	0.31	133	0.32	212	0.37	386
5	0.31	73.3	0.32	182	0.37	377
10	0.31	50.5	0.32	165	0.37	389
15	0.31	38.6	0.32	161	0.37	390
20	0.31	31.2	0.32	141	0.37	378
25	0.31	26.2	0.32	141	0.37	389

[a], The total Na^+ concentration was kept constant at 305 mM. [b], fixed during analysis. [c], fixed values were obtained using equation S3.1. [d], error for these values is ± 1 which were obtained from the fitting software.

Table S3.16: Lifetimes and pre-exponential factors for the emission from the singlet excited state of 2.0 µM pyrene in 30 mM NaDC hydrogels with varying I^- concentrations for a single quenching experiment.[a]

I^- / mM	A_1[d]	τ_1 /ns[b]	A_2[d]	τ_2 / ns[e]	A_3[d]	τ_3 / ns[c]	χ^2
0	0.40	133	0.21	212	0.39	385	1.143
5	0.40	73.3	0.29	214	0.31	385	1.155
10	0.33	50.5	0.30	168	0.37	385	0.972
15	0.33	38.6	0.29	141	0.39	385	1.193
20	0.33	31.2	0.32	167	0.34	385	1.090
25	0.32	26.2	0.30	128	0.38	385	1.200

[a], The total Na^+ concentration was kept constant at 305 mM. [b], fixed values were obtained using equation S3.1. [c], fixed values obtained from averaging the τ_3 values of table S3.15. [d], error for these values is ± 0.01 which were obtained from the fitting software. [e], error for these values is ± 1 which were obtained from the fitting software.

Table S3.17: Lifetimes and pre-exponential factors for the emission from the singlet excited state of 2.0 µM pyrene in 30 mM NaDC hydrogels with varying I^- concentrations for a single quenching experiment.[a]

I^- / mM	A_1[b]	τ_1 /ns[c]	A_2[b]	τ_2 / ns[d]	A_3[b]	τ_3 / ns[d]
0	0.31	133	0.32	187	0.37	375
5	0.31	73.3	0.32	163	0.37	372
10	0.31	50.5	0.32	182	0.37	364
15	0.31	38.6	0.32	260	0.37	363
20	0.31	31.2	0.32	174	0.37	378
25	0.31	26.2	0.32	170	0.37	383

[a], The total Na^+ concentration was kept constant at 305 mM. [b], fixed during analysis. [c], fixed values were obtained using equation S3.1. [d], error for these values is ± 1 which were obtained from the fitting software.

Table S3.18: Lifetimes and pre-exponential factors for the emission from the singlet excited state of 2.0 µM pyrene in 30 mM NaDC hydrogels with varying I^- concentrations for a single quenching experiment.[a]

I^- / mM	A_1[d]	τ_1 /ns[b]	A_2[d]	τ_2 / ns[e]	A_3[d]	τ_3 / ns[c]	χ^2
0	0.42	133	0.19	187	0.39	373	1.063
5	0.39	73.3	0.28	186	0.33	373	1.114
10	0.32	50.5	0.30	158	0.38	373	1.173
15	0.32	38.6	0.22	167	0.46	373	1.156
20	0.36	31.2	0.28	141	0.37	373	1.16
25	0.37	26.2	0.26	141	0.37	373	1.202

[a], The total Na^+ concentration was kept constant at 305 mM. [b], fixed values were obtained using equation S3.1. [c], fixed values obtained from averaging the τ_3 values of table S3.17. [d], error for these values is ± 0.01 which were obtained from the fitting software. [e], error for these values is ± 1 which were obtained from the fitting software.

Table S3.19: Lifetimes and pre-exponential factors for the emission from the singlet excited state of 2.0 µM pyrene in 30 mM NaDC hydrogels with varying I^- concentrations for a single quenching experiment.[a]

I^- / mM	A_1[b]	τ_1 /ns[c]	A_2[b]	τ_2 / ns[d]	A_3[b]	τ_3 / ns[d]
0	0.31	133	0.32	193	0.37	370
5	0.31	73.3	0.32	177	0.37	352
10	0.31	50.5	0.32	217	0.37	410
15	0.31	38.6	0.32	180	0.37	366
20	0.31	31.2	0.32	153	0.37	377
25	0.31	26.2	0.32	144	0.37	385

[a], The total Na^+ concentration was kept constant at 305 mM. [b], fixed during analysis. [c], fixed values were obtained using equation S3.1. [d], error for these values is ± 1 which were obtained from the fitting software.

Table S3.20: Lifetimes and pre-exponential factors for the emission from the singlet excited state of 2.0 µM pyrene in 30 mM NaDC hydrogels with varying I^- concentrations for a single quenching experiment.[a]

I^- / mM	A_1[d]	τ_1 /ns[b]	A_2[d]	τ_2 / ns[e]	A_3[d]	τ_3 / ns[c]	χ^2
0	0.39	133	0.24	193	0.37	377	1.091
5	0.34	73.3	0.38	199	0.28	377	1.099
10				Could not be fit			
15	0.31	38.6	0.31	149	0.39	377	1.127
20	0.33	31.2	0.30	150	0.37	377	1.044
25	0.29	26.2	0.32	148	0.39	377	0.957

[a], The total Na^+ concentration was kept constant at 305 mM. [b], fixed values were obtained using equation S3.1. [c], fixed values obtained from averaging the τ_3 values of table S3.19. [d], error for these values is ± 0.01 which were obtained from the fitting software. [e], error for these values is ± 1 which were obtained from the fitting software.

A3.4 Analysis of time-resolved lifetime data for excited pyrene quenched in NaDC hydrogels by CH_3NO_2.

The lifetimes obtained for pyrene when quenched by CH_3NO_2 in 30 mM NaDC hydrogels is shown in table S3.21. The individual experiments that were averaged to obtain the average values and errors for table S3.21 are also shown below (tables S3.22–S3.23).

Table S3.21: Lifetimes and pre-exponential factors for the emission from the singlet excited state of 2.0 μM pyrene in 30 mM NaDC hydrogels with varying CH_3NO_2 concentrations.[a] The values reported are the averages of the data from tables S3.21 and S3.22.

CH_3NO_2 / mM	A_1	τ_1 /ns[b]	A_2	τ_2 / ns	A_3	τ_3 / ns
0	0.31 ± 0.01	133	0.31 ± 0.01	200 ± 10	0.38 ± 0.01	350 ± 10
0.25	0.31 ± 0.01	91.1	0.31 ± 0.01	170 ± 20	0.38 ± 0.01	350 ± 10
0.50	0.31 ± 0.01	67.3	0.31 ± 0.01	160 ± 10	0.39 ± 0.01	317 ± 2
0.75	0.31 ± 0.01	53.4	0.31 ± 0.01	159 ± 7	0.39 ± 0.01	303 ± 4
1.00	0.31 ± 0.01	44.2	0.31 ± 0.01	141 ± 1	0.39 ± 0.01	300 ± 10
1.25	0.31 ± 0.01	37.8	0.31 ± 0.01	119 ± 2	0.38 ± 0.01	300 ± 10

[a], The total Na^+ concentration was kept constant at 305 mM. The values reported are averages of two individual experiments and the errors are average deviation for the two individual experiments. [b], fixed values were obtained using equation S3.2.

Table S3.22: Lifetimes and pre-exponential factors for the emission from the singlet excited state of 2.0 µM pyrene in 30 mM NaDC hydrogels with varying CH_3NO_2 concentrations for a single quenching experiment.[a]

CH_3NO_2 / mM	A_1[c]	τ_1 /ns[b]	A_2[c]	τ_2 / ns[d]	A_3[c]	τ_3 / ns[d]
0	0.31	133	0.31	199	0.38	343
0.25	0.31	91.1	0.31	155	0.38	363
0.50	0.3	67.3	0.3	157	0.4	319
0.75	0.3	53.4	0.3	152	0.4	299
1.00	0.3	44.2	0.3	141	0.4	291
1.25	0.31	37.8	0.31	117	0.38	287

[a], The total Na^+ concentration was kept constant at 305 mM. [b], fixed values were obtained using equation S3.2. [c], error for these values is ± 0.01 which were obtained from the fitting software. [d], error for these values is ± 1 which were obtained from the fitting software.

Table S3.23: Lifetimes and pre-exponential factors for the emission from the singlet excited state of 2.0 µM pyrene in 30 mM NaDC hydrogels with varying CH_3NO_2 concentrations for a single quenching experiment.[a]

CH_3NO_2 / mM	A_1[c]	τ_1 /ns[b]	A_2[c]	τ_2 / ns[d]	A_3[c]	τ_3 / ns[d]
0	0.31	133	0.31	201	0.38	364
0.25	0.31	91.1	0.31	188	0.38	337
0.50	0.31	67.3	0.31	162	0.38	314
0.75	0.31	53.4	0.31	165	0.38	306
1.00	0.31	44.2	0.31	140	0.38	309
1.25	0.31	37.8	0.31	121	0.38	312

[a], The total Na^+ concentration was kept constant at 305 mM. [b], fixed values were obtained using equation S3.2 [c], error for these values is ± 0.01 which were obtained from the fitting software. [d], error for these values is ± 1 which were obtained from the fitting software.

A3.5 Static quenching of pyrene by I^- in NaDC hydrogels.

The quenching mechanism of I^- as a quencher was observed to be dynamic at quencher concentrations of 0–25 mM. When the quencher concentration was increased further, a static quenching mechanism is observed as is evident from the lack of overlap between the two Stern-Volmer plots in figure S3.7. Moreover, we observe both the Stern-Volmer plots becoming parallel to the concentration axis, indicating that I^- has quenched only a fraction of the pyrene to which I^- had access to and there exists a fraction of pyrene within NaDC hydrogels that is inaccessible to I^-.

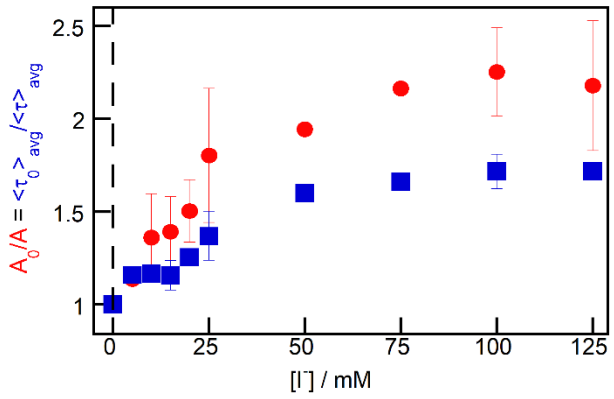

Figure S3.7: Stern-Volmer plot for 2.0 µM pyrene using I^- as a quencher in 30 mM NaDC hydrogels. The solid red circles represent the steady-state fluorescence data, and the solid blue squares represent the time-resolved data. Values reported are averages of three individual experiments and the errors are the standard deviations of three individual experiments. The values reported for 0 and 25 mM I^- are an average of six individual experiments and the errors are the standard deviation of six individual experiments. The dashed black line indicates the origin on the concentration axis.

Chapter 4.

A4.1 Synthesis of CB[6]

1.1 Materials:

Formic acid (HCOOH, 90%), 35% deuterium chloride in D_2O (Sigma, 99% D atom), hydrochloric acid (HCl, 36.5%) glycoluril (Sigma, 97%), paraformaldehyde (Sigma, 95%) and sodium chloride (NaCl,) (Sigma, BioXtra ≥ 99.9%) were used as received. Deionized water (Barnstead NANO pure deionizing system ≥ 17.8 MΩ cm) was used for preparation of the solutions. 4-(1H-imidazol-1-yl)aniline (API) and diaminohexane (DAH) were recrystallized using reported literature procedures in the group.[1] Ultrapure CB[n]s (UpCB[n]) were obtained from Kimoon Kim, Dept. of Chemistry, Pohang University.

1.2 Synthesis of CB[6]:

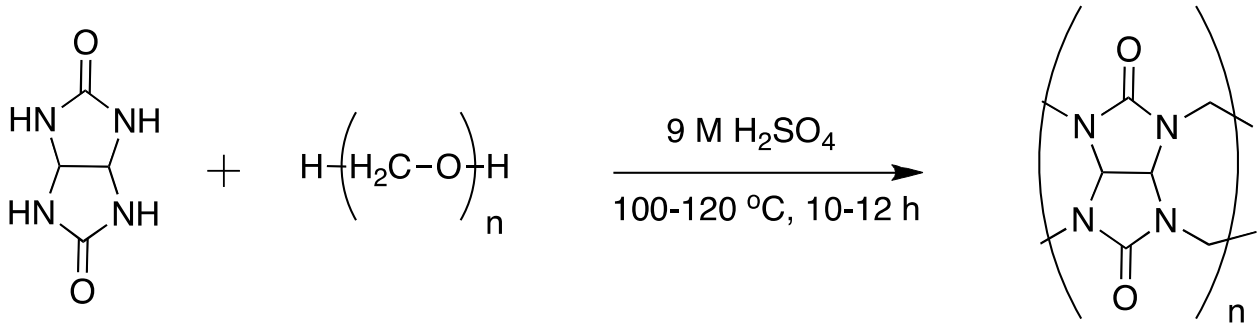

Chart S4.1: Synthesis of CB[n]

In a 100 mL two-necked round bottom flask, glycoluril (10.0 g, 70.04 mmol) is dissolved in 9 M H_2SO_4 (80-90 mL) at room temperature with the help of sonication. A condenser is connected to one of the mouths of the flask whereas the other mouth was connected to a $CaCl_2$ guard column. Once completely dissolved, solid paraformaldehyde is added (4.2 g, 140.08 mmol) slowly and the solution is mixed immediately with the help of a magnetic stirrer. No gel formation is observed. The mixture is initially heated to 60 °C for 2 h before increasing the

temperature to 110 °C and the reaction is run at this temperature for 10–12 h. Subsequently, the reaction is cooled to room temperature. Once cooled, the reaction mixture is poured into cold methanol (150 mL) to precipitate the CB[n]s. This mixture contains CB[5], CB[6], CB[7], CB[8], iCB[n] and CB[5]•CB[10]. This mixture is stored in the fridge overnight to ensure complete precipitation of CB[n]s before purification is undertaken to extract CB[6].

A4.2 Purification of CB[6]

The precipitate stored in the fridge after synthesis is first filtered on a vacuum pump. The solid residue obtained after vacuum filtration is added to 100 mL water and magnetically stirred for 3 h at 60 °C. This aqueous solution is filtered hot on a vacuum pump to obtain a solid residue (residue 1). The filtrate obtained in this step can be used to obtain CB[5] and CB[7], by adding the filtrate into 100 mL of cold methanol to precipitate the aforementioned CB[5] and CB[7] (fraction 1). Residue 1 is again added to 100 mL water, magnetically stirred at 60 °C for 3 h and filtered hot on a vacuum pump to obtain a solid residue (residue 2). Similar to residue 1, residue 2 is also added to 100 mL water, magnetically stirred at 60 °C for 3 h and filtered hot to ensure complete removal of CB[5] and CB[7] yielding residue 3. Residue 3 is expected to contain CB[6], CB[8] and CB[5]•CB[10], and is thus further purified to obtain CB[6]. The mass of 1 g of residue 3 is dissolved in 40 mL of 3 N HCl. This acidic mixture is magnetically stirred at room temperature for 2 h. The insoluble solid is removed by gravity filtration. The filtrate obtained is then evaporated to dryness on a rotary evaporator to obtain a solid, which is reported to be CB[6].[2] This CB[6] was vacuum dried for 6–8 h. If the solid obtained after vacuum drying is not white, it is added to 25 mL of water and stirred for 2 h. This step is repeated until only white solid is obtained. The white solid is filtered on a vacuum pump and vacuum dried for 6–8 h to yield CB[6]-AA-1.

A4.3 Spectroscopic determination of the CB[6] purity

3.1 Methods:

Nuclear Magnetic Resonance (NMR) studies were done with the help of Chris Barr. ^{1}H NMR was collected on a Bruker AVANCE I 500 MHz NMR spectrometer operating at 500.27 MHz frequency using a BBO probe. The spectrum was acquired using a 30° pulse angle and a 10 s relaxation delay. The T_1 was estimated to be ≤ 1.3 s via T_1 null in the inversion recovery sequence for the peaks of interest. Mass spectroscopy studies were done by Hongwen Chen at Simon Fraser University. Low-resolution electrospray ionization-mass spectrometry (ESI-MS) spectra were obtained using a Bruker micrOTOF instrument equipped with an ESI source.

Fluorescence emission studies were done on a PTI QM-40 spectrofluorometer. All samples were excited at 280 nm, and emission spectra were collected from 295–550 nm. The monochromator bandwidths were kept at 2 nm for both excitation and emission monochromators. A 0.5 nm step size and 0.25 s integration time settings were used when collecting each spectrum.

For the steady-state fluorescence titration of CB[6], the total integrated area of emission (integrated from 330–550 nm) was plotted against the concentration of DAH and the data points above zero were fit to a linear equation. The intercept with the X-axis corresponds to the actual CB[6] concentration of the sample. The percent purity of CB[6] was determined by dividing the actual concentration CB[6] concentration obtained from the intercept with the CB[6] concentration calculated from the mass used to prepare the solutions.

3.2 Sample Preparation:

For ^{1}H NMR studies, 18 mg of CB[6]-AA-1 was dissolved in 1 mL of 35% DCl in D_2O. A reference sample was made using ultrapure CB[n]s synthesized by Kimoon Kim. In the reference sample 17.1 mg of CB[6], 12.3 mg of CB[5], 12.2 mg of CB[7] and 11.4 mg of CB[8] provided by Kim were dissolved in 1 mL of 35% DCl in D_2O.

Samples for mass spectrometry were made in 20% HCOOH. This 20% HCOOH solution was made by mixing 22 mL of 90% HCOOH and 88 mL of deionized water in a 100 mL volumetric flask. Two standard solutions were made using UpCB[n], the first one containing 60 μM each of UpCB[5], UpCB[6] and UpCB[7] in 20% HCOOH, whereas the other standard sample contained 60 μM each of UpCB[6] and UpCB[8] in 20% HCOOH. These standards allowed us to establish the different CB[n] peaks to be expected in our sample, if it contained other CB[n] homologues. A 100 μM CB[6]-AA-1 in 20% HCOOH sample was made to check for presence of other CB[n] homologues and establish its purity.

A 0.1 M stock solution of NaCl was prepared by dissolving 0.15 g of the salt in deionized water. A stock solution of CB[6] (0.5 mM) was prepared by weighing 2.5 mg of CB[6] and dissolving it in 5 mL of 0.1 M NaCl solution. Weighing 9.5 mg of DAH.2HCl salt and dissolving it into 5 mL of deionized water prepared a 10 mM stock solution of DAH.2HCl. A 10 mM API.HCl stock solution was prepared by dissolving 9.8 mg of the salt in 5 mL of deionized water. Multiple dilutions of 36.5% HCl using deionized water allowed me to obtain a 1 mM stock solution of HCl, which was used for further sample preparation. In a 10 mL volumetric flask, 20 μL of the API stock solution and 200 μL of the CB[6] stock solution in NaCl were taken and diluted up to the mark using 1 mM HCl. The final concentrations of API and CB[6] in this mixture was 20 μM and 10 μM respectively. The concentration of Na^{+} was 10 mM whereas that

of H^+ was 1 mM. Adding 500 µL of stock DAH.2HCl in a 5 mL volumetric flask and diluting to the mark with 1 mM HCl prepared a 1 mM DAH solution. For the determination of the spectrum for baseline corrections of the emission spectra a 10 µM CB[6] solution in 1mM HCl was prepared.

3.3 Results

3.3.1 NMR

The possible impurities present in CB[6] could be trace quantities of other CB homologues (CB[5], CB[7] and CB[8]). Thus the NMR of not just CB[6]-AA-1, but of a mixture of UpCB[n] was carried out. This experiment allowed us to observe the peaks obtained for an impure CB[6] sample. A pure CB[n] sample is expected to show three sets of peaks in the NMR spectrum which can be seen for CB[6]-AA-1in figure S4.1.[3-4] The singlet at 2.19 is attributed to the hydrogen from the methylene bridge that is present in the plane of the CBs (H_b) (labeling shown in figure S4.1). The doublet at 0.95 results from the methylene bridge hydrogen present in the plane perpendicular to CBs (H_c) and the doublet at 2.05 corresponds to the hydrogen from the glycoluril subunits (H_a).[3] By comparing the spectra of CB[6]-AA-1 and that of a mixture of CB[n]s, we determined that no other CB[n] homologues were present for the CB[6]-AA-1 sample within the NMR detection limit. The downfield shift in the peak positions for the mixture of UpCB[n]'s in comparison the CB[6] peaks is possibly due to intermolecular interactions between the different CB[n]s in the mixture. These intermolecular interactions could be hydrogen bonding or dipole-dipole interactions that cause a shielding of the protons resulting in the downfield shift seen in figure S4.1.

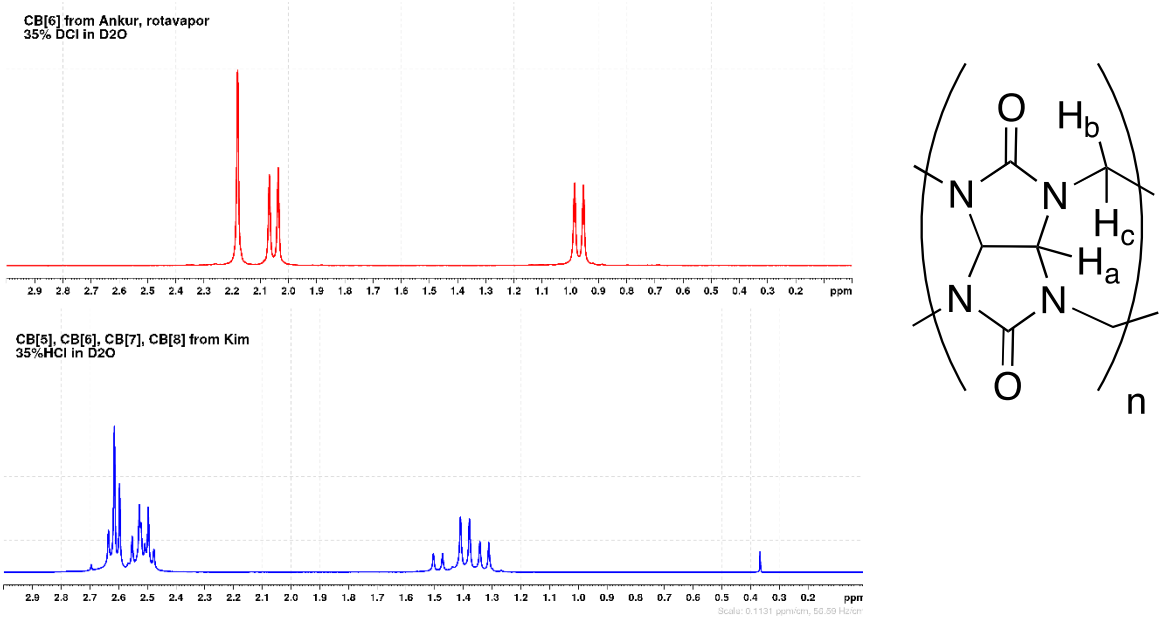

Figure S4.1: ^{1}H NMR of CB[6]-AA-1 (top red) and UpCB[n], n=5, 6, 7, 8 from Kim (bottom blue).

3.3.2 ESI-MS

Mass spectra were collected for CB[6]-AA-1 and a series of CB[n] mixtures to verify the purity of synthesized CB[6]-AA-1. The various peaks obtained in the mass spectra for each sample are detailed in table S4.1. The assignment of all the peaks obtained during the mass spectrometry experiments are shown in table S4.2. The mass spectra peaks for CB[6]-AA-1 were seen to be devoid of peaks characteristic to other CB[n]s, indicating the absence of other CB[n] homologues in our sample.

Table S4.1: Peaks obtained for samples in ESI-MS

Sample (in 20% HCOOH)	**Peak position**
100 μM CB[6]-AA-1	1019, 1035, 1077
60 μM UpCB[5], UpCB[6] & UpCB[7]	853, 921, 1019, 1035, 1081, 1185
60 μM UpCB[6] & UpCB[8]	1019, 1035, 1081, 1351

Table S4.2: Assignment of peaks obtained in ESI-MS

Peak Position	**Assignment**
853	CB[5]•Na^+
921	NH_4Cl•CB[5]•K^+ or KCl•CB[5]•NH_4^+
1019	CB[6]•Na^+
1035	CB[6]•K^+
1077	NaCl•CB[6]•K^+
1081	CB[6]@HCOOH•K^+
1185	CB[7]•Na^+
1351	CB[8]•Na^+

@inclusion complex, •capped exclusion complex with cation at the portal

3.3.3 Steady-state fluorescence

The spectroscopic titration done to determine the purity of CB[6]-AA-1 relies on the difference in binding affinity of API and DAH to CB[6]. In the binding of CB[6] and API the charged anilinium cation interacts with the partially charged carbonyl groups at the portals with a binding constant (K) of $(8 \pm 2) \times 10^4$ M^{-1}, pH ~ 5.7.[5] This binding is weaker in comparison to the binding of the DAH with CB[6] ($K = (2.9 \pm 0.2) \times 10^8$ M^{-1}, 0.05 M NaCl).[6] It is reported that

CB[6] shows strongest binding to penta- ($K = (1.5 \pm 0.1) \times 10^8$ M^{-1}, 0.05 M NaCl) and hexa-bridged ($K = (2.9 \pm 0.2)$ x 10^8 M^{-1}, 0.05 M NaCl) diamonium functionalities as is the case with DAH.[6-8] API shows weak fluorescence in aqueous 1 mM HCl solution, however, on addition of CB[6], the fluorescence intensity of API increases significantly due to formation of the CB[6]@API complex. On addition of DAH, the CB[6]@API complex dissociates and API is displaced from CB[6] with DAH now binding to the host. The CB[6]@DAH complex has a 1:1 stoichiometry and thus, the amount of DAH required to completely displace API from the complex leads to the fluorescence decrease. Thus, the amount of CB[6] present in the solution corresponds to the added DAH concentration when the fluorescence intensity reaches zero.[9-10] Using this method, the purity of CB[6]-AA-1 was determined to be 88%. All experiments requiring CB[6] were carried out within 1 month of spectroscopically determining the purity.

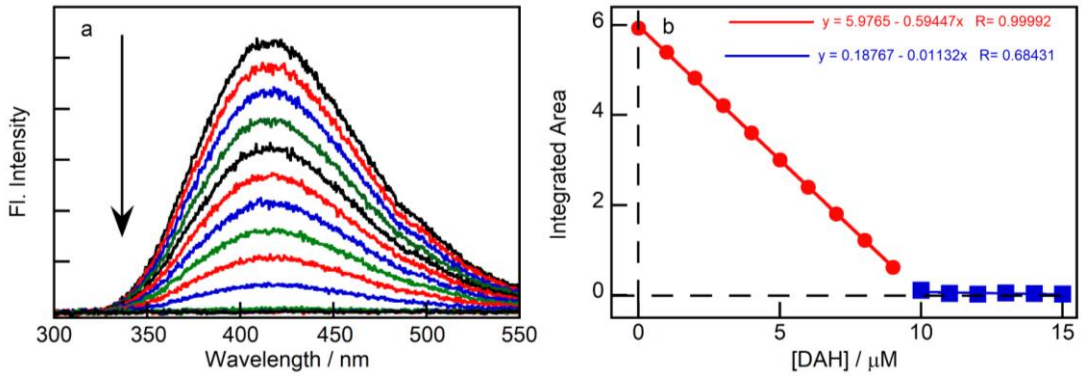

Figure S4.2: (A) Emission spectra of the CB[6]-API complex with increasing DAH concentration **(B)** plot of the total integrated area of CB[6]-API complex emission against the DAH concentration to obtain the actual CB[6] concentration. The dashed black line indicates the origin on both the integrated area and concentration axis.

A4.4 Lifetime distribution analysis for pyrene quenched by CH_3NO_2 in NaDC hydrogels.

The lifetime distribution curves for pyrene quenched in NaDC hydrogels with CH_3NO_2 concentrations other than 0 and 1.25 mM showing the separation of distribution peaks for different quencher concentrations (figure S4.3–S4.6).

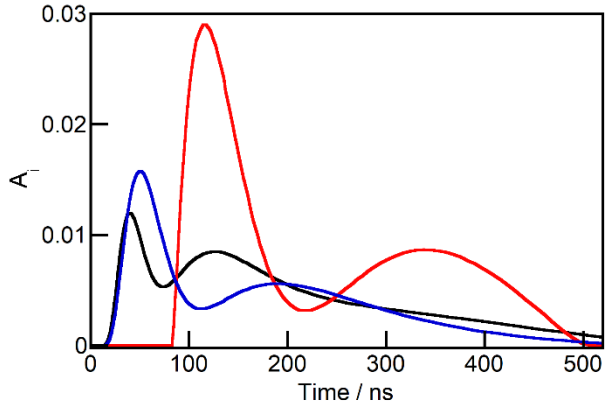

Figure S4.3: Lifetime distribution curves for 2.0 μM pyrene in 30 mM NaDC hydrogels containing 0.25 mM CH_3NO_2. Each distribution curve corresponds to an individual experiment.

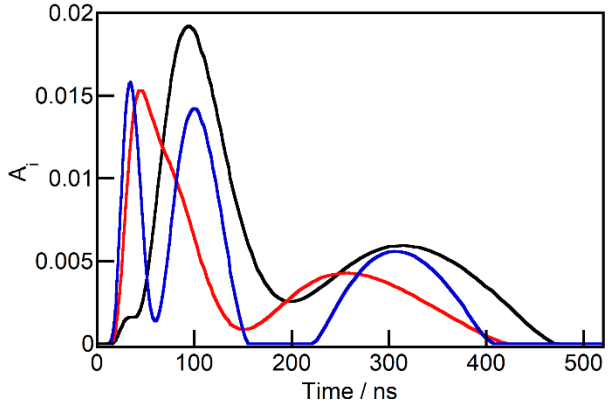

Figure S4.4: Lifetime distribution curves for 2.0 μM pyrene in 30 mM NaDC hydrogels containing 0.50 mM CH_3NO_2. Each distribution curve corresponds to an individual experiment.

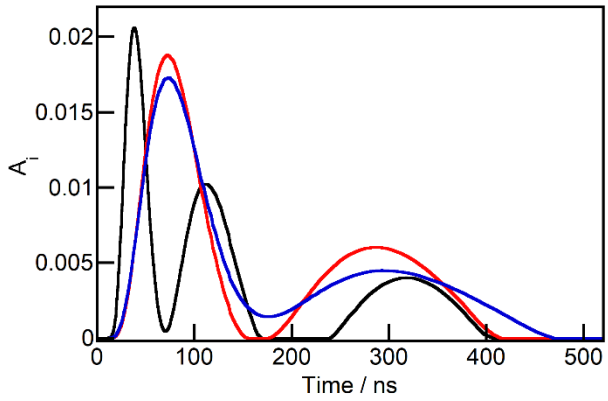

Figure S4.5: Lifetime distribution curves for 2.0 μM pyrene in 30 mM NaDC hydrogels containing 0.75 mM CH_3NO_2. Each distribution curve corresponds to an individual experiment.

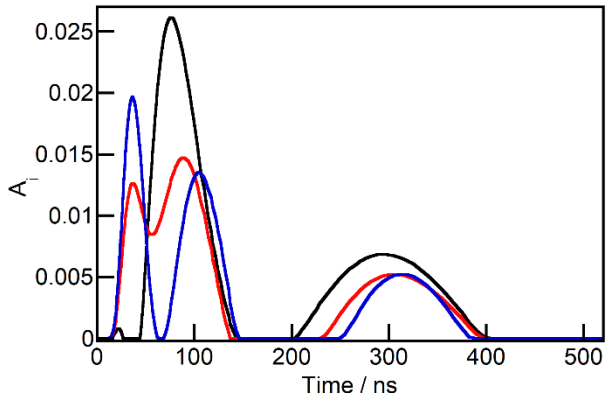

Figure S4.6: Lifetime distribution curves for 2.0 μM pyrene in 30 mM NaDC hydrogels containing 1.00 mM CH_3NO_2. Each distribution curve corresponds to an individual experiment.

A4.5 Lifetime distribution analysis for pyrene quenched by CH_3NO_2 in NaDC-CB[6] hydrogels.

The lifetime distribution curves for pyrene quenched in NaDC-CB[6] hydrogels with CH_3NO_2 concentrations other than 0 and 1.25 mM showing the increased heterogeneity in pyrene lifetimes in presence of CB[6] as the width of the distribution peaks increase (figure S4.7–S4.10).

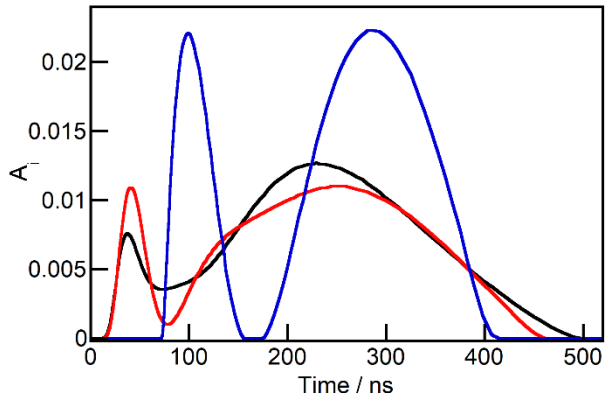

Figure S4.7: Lifetime distribution curves for 2.0 μM pyrene in 30 mM NaDC hydrogels in presence of 3 mM CB[6] containing 0.25 mM CH_3NO_2. Each distribution curve corresponds to an individual experiment.

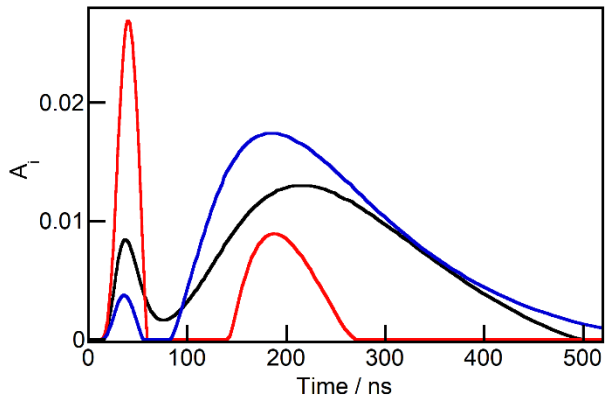

Figure S4.8: Lifetime distribution curves for 2.0 μM pyrene in 30 mM NaDC hydrogels in presence of 3 mM CB[6] containing 0.50 mM CH_3NO_2. Each distribution curve corresponds to an individual experiment.

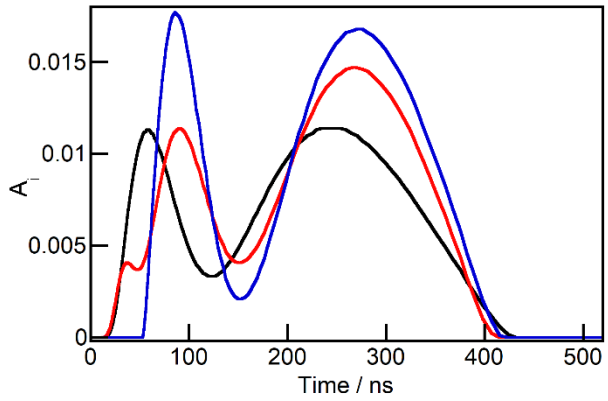

Figure S4.9: Lifetime distribution curves for 2.0 μM pyrene in 30 mM NaDC hydrogels in presence of 3 mM CB[6] containing 0.75 mM CH_3NO_2. Each distribution curve corresponds to an individual experiment.

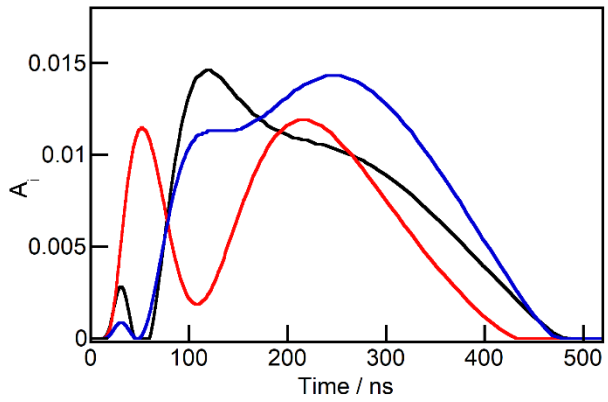

Figure S4.10: Lifetime distribution curves for 2.0 μM pyrene in 30 mM NaDC hydrogels in presence of 3 mM CB[6] containing 1.00 mM CH_3NO_2. Each distribution curve corresponds to an individual experiment.

A4.6 Lifetime distribution analysis of pyrene in buffer with and without CB[6]

The validity of the MEM analysis was determined by comparing the residuals obtained when fitting the pyrene lifetime data through both, the MEM and sum of exponential methods. It was observed, that in absence of CB[6], the residuals seen are indistinguishable for each one of the analysis methods. Moreover, the addition of CB[6] displayed similar indistinguishable

residuals, however, as seen previously in figure 4.4B, the lifetime distribution curve was observed to be different for two individual experiments.

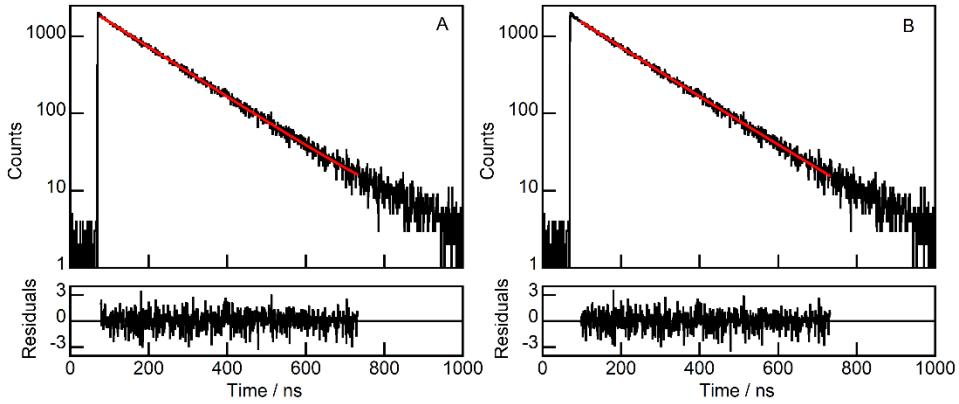

Figure S4.11: (A) Decay trace for 0.5 µM pyrene in 50 mM phosphate buffer (black). The solid red line corresponds to the fit done using MEM. The lower panel corresponds to the residuals obtained for the fit. (B) Decay trace for 0.5 µM pyrene in 50 mM phosphate buffer (black). The solid red line corresponds to the fit done using a sum of exponential analysis. The lower panel corresponds to the residuals obtained for the fit.

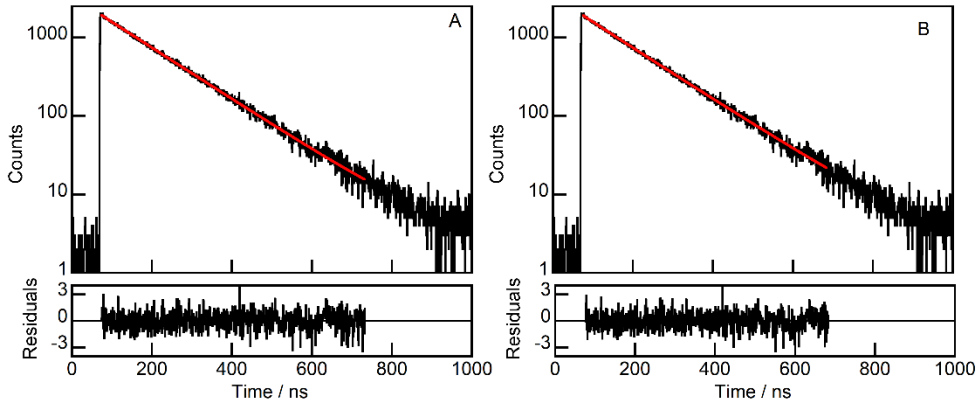

Figure S4.12: (A) Decay trace for 0.5 µM pyrene in 50 mM phosphate buffer (black). The solid red line corresponds to the fit done using MEM. The lower panel corresponds to the residuals obtained for the fit. (B) Decay trace for 0.5 µM pyrene in 50 mM phosphate buffer (black). The solid red line corresponds to the fit done using sum of exponential analysis. The lower panel corresponds to the residuals obtained for the fit.

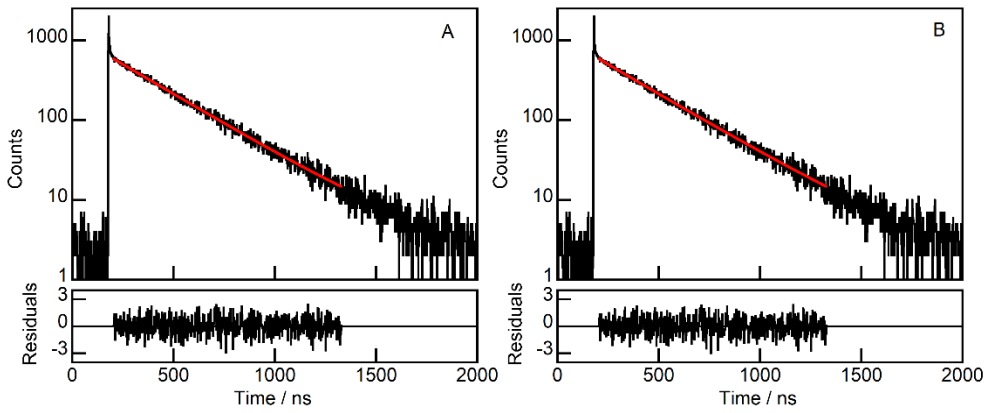

Figure S4.13: (A) Decay trace for 0.5 μM pyrene with 3 mM CB[6] in 50 mM phosphate (black). The solid red line corresponds to the fit done using MEM. The lower panel corresponds to the residuals obtained for the fit. (B) Decay trace for 0.5 μM pyrene in 50 mM phosphate buffer (black). The solid red line corresponds to the fit done using exponential analysis. The lower panel corresponds to the residuals obtained for the fit.

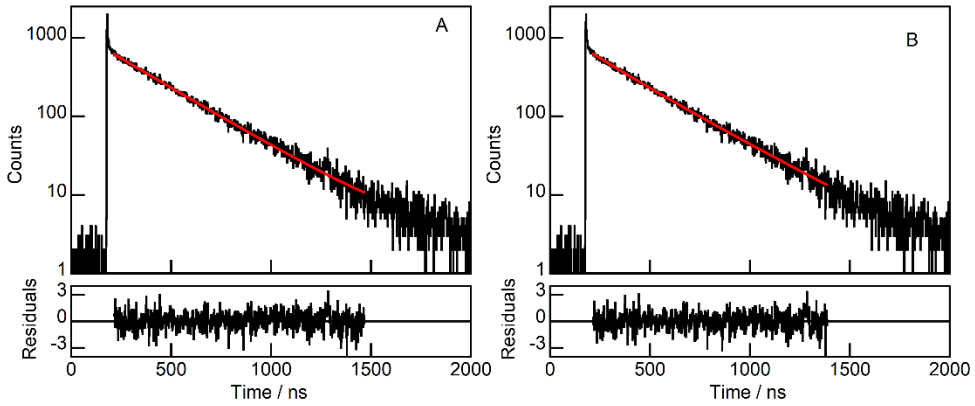

Figure S4.14: (A) Decay trace for 0.5 μM pyrene with 3 mM CB[6] in 50 mM phosphate (black). The solid red line corresponds to the fit done using MEM. The lower panel corresponds to the residuals obtained for the fit. (B) Decay trace for 0.5 μM pyrene in 50 mM phosphate buffer (black). The solid red line corresponds to the fit done using exponential analysis. The lower panel corresponds to the residuals obtained for the fit.

A4.7 References

(1) Talluri, S. G. Effect of Cucurbit[6]uril on the Structure and Dynamics of NaDC Gels. PhD University of Victoria, 2021. http://hdl.handle.net/1828/13847
(2) Huang, W.-H.; Liu, S.; Isaacs, L. Cucurbit[n]urils. In *Modern Supramolecular Chemistry: Strategies for Macrocycle Synthesis*; Diederich, F.; Stang, P. J.; Tykwinski, R. R., Eds.; Wiley-VCH Verlag GmbH & Co.: Weinheim, 2008; pp 113–142.
(3) Jiao, D.; Scherman, O. A. Isolation of Cucurbit[n]uril Homologues with Imidazolium Salts in a Recyclable Manner. *Green Chem.* **2012,** *14*, 2445–2449.
(4) Haouaj, M.; Ko, Y. H.; Luhmer, M.; Kim, K.; Bartik, K. NMR Investigation of the Complexation of Neutral Guests by Cucurbituril. *J. Chem. Soc., Perkin Trans.* **2001,** *2*, 2104–2107.
(5) Feng, Y.; Xue, S.-F.; Fan, Z.-F.; Zhang, Y.-Q.; Zhu, Q.-J.; Tao, Z. Host–guest Complexes of Some Cucurbit[n]urils with the Hydrochloride Salts of Some Imidazole Derivatives. *J. Incl. Phenom. Macrocycl. Chem.* **2009,** *64*, 133–133.
(6) Rekharsky, M. V.; Ko, Y. H.; Selvapalam, N.; Kim, K.; Inoue, Y. Complexation Thermodynamics of Cucurbit[6]uril with Aliphatic Alcohols, Amines, and Diamines. Supramolecular Chemistry 2007, 19, 39-46. *Supramol. Chem.* **2007,** *19*, 39–46.
(7) Barrow, S. J.; Kasera, S.; Rowland, M. J.; del Barrio, J.; Scherman, O. A. Cucurbituril-based Molecular Recognition. *Chem. Rev.* **2015,** *115*, 12320–12406.
(8) Assaf, K. I.; Nau, W. M. Cucurbiturils: From Synthesis to High-affinity Binding and Catalysis. *Chem. Soc. Rev.* **2015,** *44*, 394–418.
(9) Lee, S. J. C.; Lee, J. W.; Lee, H. H.; Seo, J.; Noh, D. H.; Ko, Y. H.; Kim, K.; Kim, H. I. Host−guest Chemistry from Solution to the Gas Phase: An Essential Role of Direct Interaction with Water for High-Affinity Binding of Cucurbit[n]urils. *J. Phys. Chem. B* **2013,** *117*, 8855–8864.
(10) Freeman, W. A.; Mock, W. L.; Shih, N.-Y. Cucurbituril. *J. Am. Chem. Soc.* **1981,** *103*, 7367–7368.

Chapter 5.

A5.1 Synthesis of Urea 1

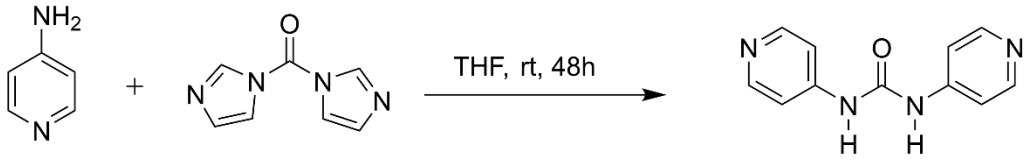

Chart S5.1: Synthetic route to obtain **1**.

In a 100 mL round bottom flask 2.0 g of 4-AP and 1.4 g of CDI were added along with a magnetic stirrer to ensure proper mixing of the solids, after which 60 mL of THF was added to the flask. The flask was then sealed with a stopper and the reaction stirred for 48 h. After 48 h, the reaction mixture was poured into a beaker containing 200 mL of water which resulted in the formation of a white precipitate. This white solid was extracted via vacuum filtration and washed with 50 mL of toluene and then 50 mL of DCM according to reported procedures. The purity was checked by ^{1}H and ^{13}C NMR.

^{1}H NMR (DMSO-d_6): δ 7.45 (d, J=6.3 Hz, 4H, H_a), 8.40 (d, J=6.3 Hz, 4H, H_b), 9.33 (s, 2H, H_c).

^{13}C NMR (DMSO-d_6): δ 113.0 (C_a), 146.5 (C_c), 150.7 (C_b), 152.3 (C_d).

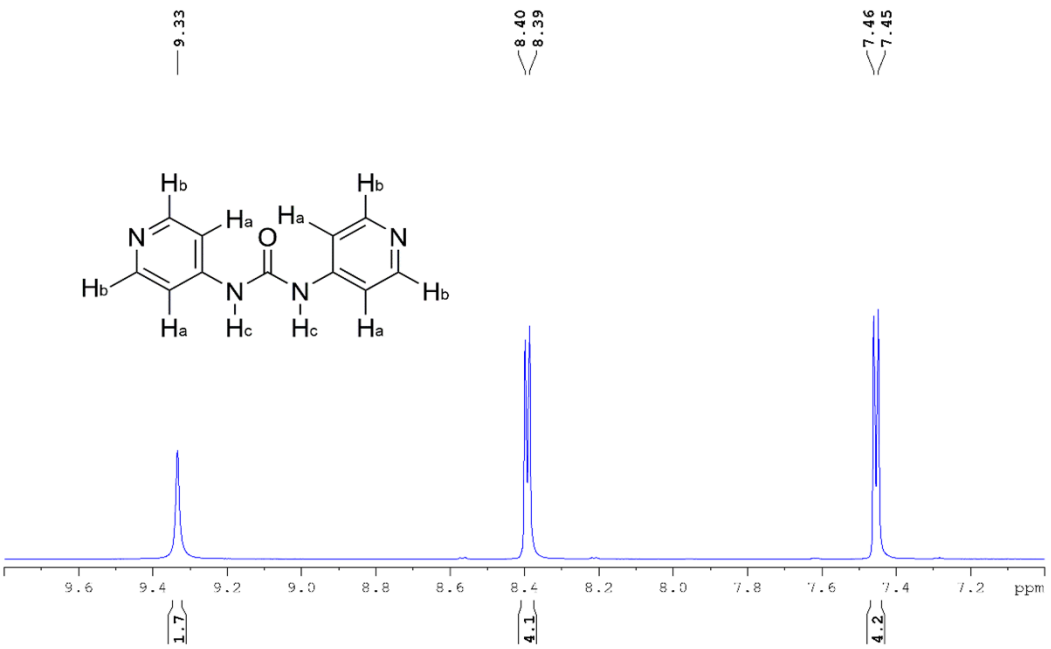

Figure S5.1: ^{1}H NMR spectra (500 MHz) of **1** in DMSO-d_6.

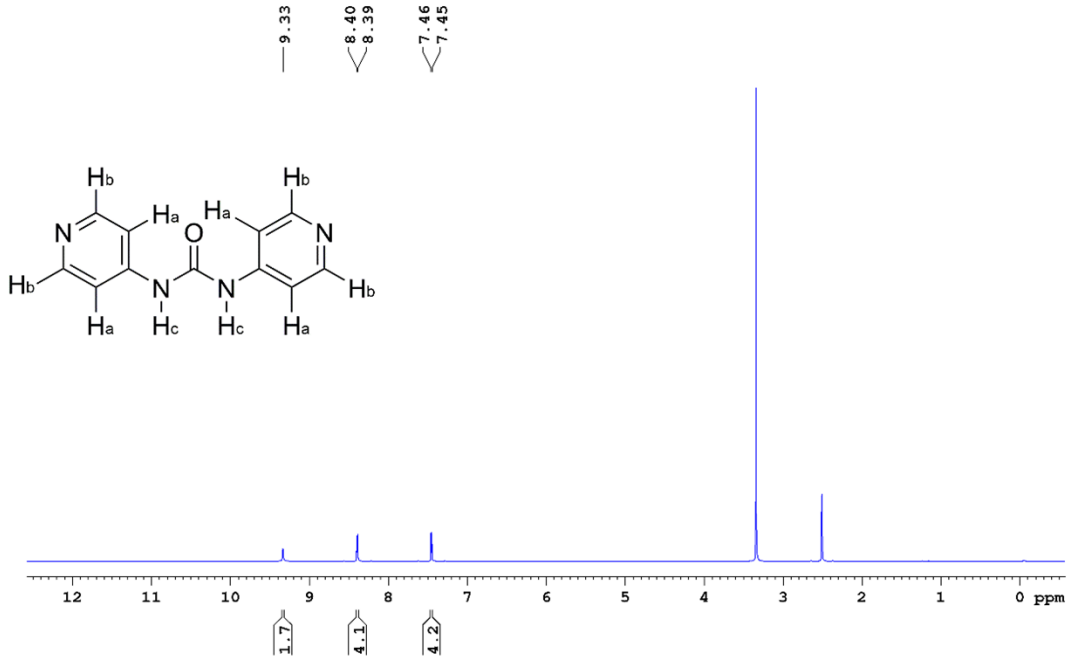

Figure S5.2: Full view of the ^{1}H NMR spectra (500 MHz) of **1** in DMSO-d_6. The peak around δ 3.3 ppm corresponds to water and the peak at δ 2.5 ppm corresponds to DMSO.

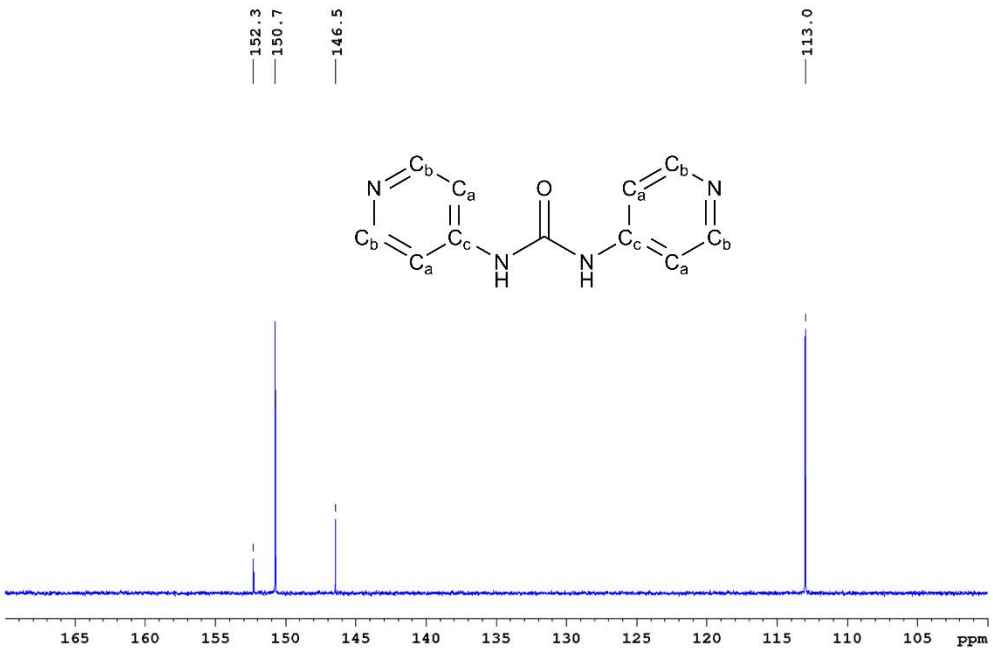

Figure S5.3: ^{13}C NMR spectra (500 MHz) of **1** in DMSO-d_6.

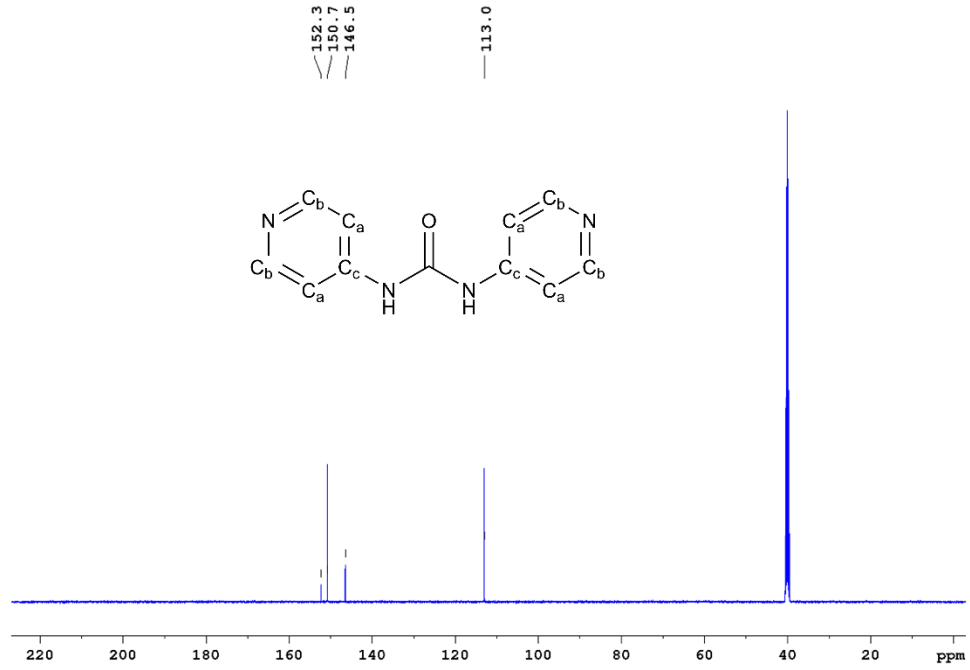

Figure S5.4: Full view of the ^{13}C NMR spectra (500 MHz) of **1** in DMSO-d_6. The peak at δ 40 ppm corresponds to DMSO.

A5.2 Inverted Vial Tests.

The sample for the inverted vial tests were monitored a week after gelation to confirm the gelation behaviour of all the samples. Only the sample containing **1**, 5 mM CB[6] and 100 mM NaCl in water (figure S5.5) was seen to settle down as a precipitate confirming no gelation had taken place. For all the other samples that did not undergo gelation, a colloid dispersion was observed after a week which was assumed to indicate partial gelation had occurred in these samples (figure S5.6-S5.10).

Figure S5.5: Image of **1** (0.8% w/v), 5mM CB[6] and 100 mM NaCl in water, 1 week after gelation experiment.

Figure S5.6: Image of **1** (0.8% w/v) in 20% aqueous EG, 1 week after gelation experiment.

Figure S5.7: Image of **1** (0.8% w/v), 5mM CB[6] and 100 mM NaCl in 20% aqueous EG, 1 week after gelation experiment.

Figure S5.8: Image of **1** (0.8% w/v) in water, 1 week after gelation experiment.

Figure S5.9: Image of **1** (0.8% w/v) and 5mM CB[6] in water, 1 week after gelation experiment.

Figure S5.10: Image of **1** (0.8% w/v) in water, 1 week after gelation experiment.

A5.3 Binding isotherm of urea 1 with increasing NaCl concentrations.

The changes in binding of **1** with increasing NaCl concentrations is shown below. The addition of NaCl resulted in change in the peak maximum of urea **1** accompanied by an increase in absorbance at this new peak maximum as shown in figure S5.11.

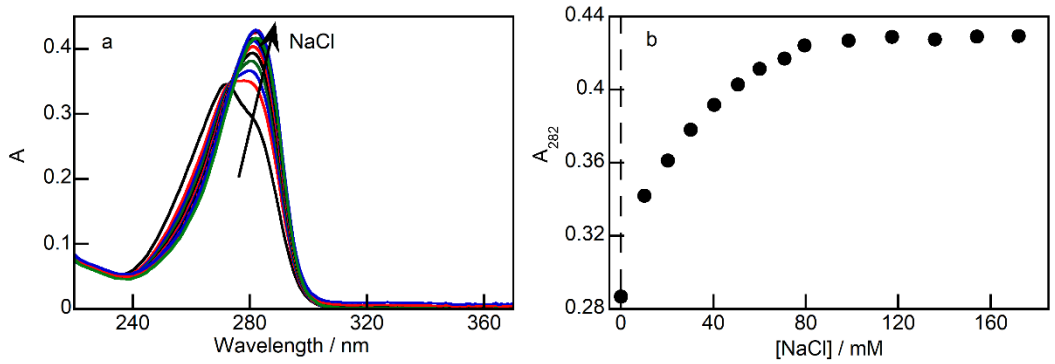

Figure S5.11: a) Absorption spectra of 12.3 μM of **1** in water with increasing NaCl concentration. **b)** Change in absorbance of 12.3 μM of **1** at 282 nm in water with increasing NaCl concentrations. The dashed black line in figure S5.11B indicates the origin on the concentration axis.

A5.4 Change in absorption maximum of urea 1 in presence of NaCl and CB[6]

To show the shift in the absorption maximum of urea **1**, the normalized absorbance spectra of urea **1** when subjected to the different conditions is shown below in figure S5.12.

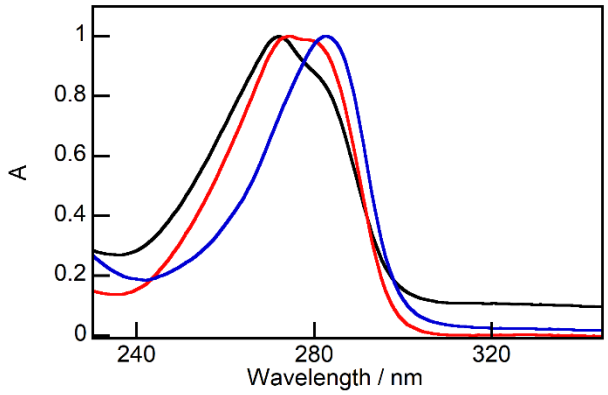

Figure S5.12: Normalized absorption spectra of 12.3 μM urea **1** in water (black), in aqueous 100 mM NaCl (red) and in presence of 100 mM NaCl and 0.4 M CB[6] (blue).

A5.5 Changes in stopped-flow kinetic traces on mixing urea 1 and CB[6]

To observe the change in the profile of the kinetic traces as well as the onset of the slow process in the binding kinetics when mixing urea **1** and CB[6], the stopped-flow traces were normalized for their amplitudes (figure S5.13).

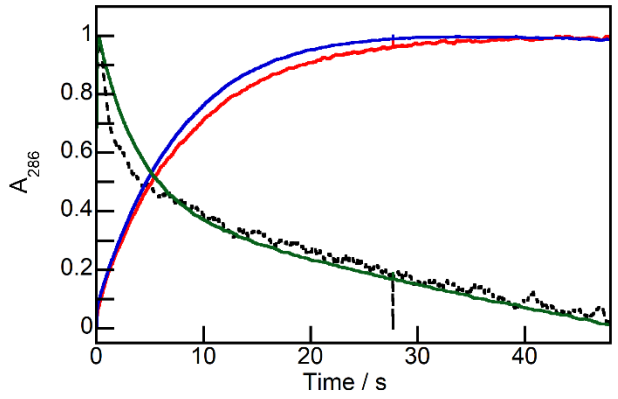

Figure S13: Amplitude normalized stopped-flow traces for the mixing of 12.3 μM of **1** in 100 mM NaCl with increasing CB[6] concentrations. (1) 0 mM CB[6] (red), (2) 100 mM CB[6] (blue), (3) 300 mM CB[6] (green). The dotted line represents the trace for mixing of 100 mM NaCl with 100 mM NaCl.